UNIVERSITY OF SOUTHAMPTON

Spectroscopic Analysis of Nanodielectric Interfaces

by

Celia Yeung

A thesis submitted for the
degree of Doctor of Philosophy

in the
Faculty of Physical Sciences and Engineering
Department of Electronics and Computer Science

August 2013

UNIVERSITY OF SOUTHAMPTON

ABSTRACT

FACULTY OF PHYSICAL SCIENCES AND ENGINEERING
DEPARTMENT OF ELECTRONICS AND COMPUTER SCIENCE

Doctor of Philosophy

by Celia Yeung

Polymeric nanocomposites have received an exceptional amount of attention over the recent years as they have the ability to possess enhanced properties. The use of nanosized phases in composite materials, as opposed to their microsized counterpart, delivers characteristics which allow nanodielectric systems to operate at an increased performance and improved efficiency. The requirements of the polymeric system can easily be tailored to suit specific applications with as little as 2 wt.% filler loading, whilst maintaining the typical weight of the virgin material.

With the transition from micrometric to nanomeric phases, the volume of the interfacial region increases dramatically and this is where the mechanisms behind nanocomposite behaviour are believed to occur. As the potential for nanodielectrics is endless, the importance of in-depth studies into the filler-matrix interface is fundamental. Many studies have already partaken in research which uses organosilanes as a coupling agent, however few the quantity of organosilane as a variable parameter, or compared the use of hydrous and anhydrous functionalisation methods. This study investigates the consequences of introducing differently functionalised nanosilicas into epoxy systems; a number of spectroscopic techniques (Raman spectroscopy, Fourier transform infrared spectroscopy and combustion analysis) were employed to quantify the level of surface modification on the surface of silica nanoparticles, before mixing methods were developed in an attempt to reach nanoparticle homogeneity in an epoxy matrix. Scanning electron microscopy was employed to investigate the dispersion state of the filler with respect to the degree of functionalisation, whilst data from AC breakdown studies, differential scanning calorimetry and dielectric spectroscopy were analysed to determine the effects of differently functionalised nanosilica in a dielectric system. The investigation shows how condensation reactions within the interphase has an influence dielectric behaviour, and highlights how changes in the stoichiometry of the epoxy system alters the polymer architecture to have an effect on the electrical properties of the nanocomposites.

Further studies explore the use of confocal Raman spectroscopy as a tool in probing the nanofiller-matrix interface. A simulation based on the scattering of incident photons was compared with empirical data from a range of dielectric films; modifications to the scattering photon approach relates physically obtained values for bulk attenuation directly to those observed in confocal Raman depth profiles. Although it was found that the revised model was able to produce confocal Raman depth profiles that closely match experimental data from the nanocomposite films, the nature of nanoparticle agglomeration during functionalisation and the typical resolution of confocal Raman systems do not allow for the detection of chemical changes on the filler.

Contents

Declaration Of Authorship

I, Celia Yeung, declare that the thesis entitled "Spectroscopic Analysis of Nanodielectric Interfaces" and the work presented in the thesis are both my own, and have been generated by me as the result of my own original research. I confirm that:

- this work was done wholly or mainly while in candidature for a research degree at this University;
- where any part of this thesis has previously been submitted for a degree or any other qualification at this University or any other institution, this has been clearly stated;
- where I have consulted the published work of others, this is always clearly attributed;
- where I have quoted from the work of others, the source is always given. With the exception of such quotations, this thesis is entirely my own work;
- I have acknowledged all main sources of help;
- where the thesis is based on work done by myself jointly with others, I have made clear exactly what was done by others and what I have contributed myself;
- parts of this work have been published as;

    1. C. Yeung, G. Gherbaz and A. S. Vaughan, 'On the use of Raman and FTIR Spectroscopy for the Analysis of Silica-based Nanofillers', *IEEE International Conference on Electrical Insulation and Dielectric Phenomena, pp. 319-323, (2010)*

2. C. Yeung and A. S. Vaughan, ‘A study of how varying degrees of functionalised nanofiller have an effect on nanodielectrics’, *IEEE International Conference on Electrical Insulation and Dielectric Phenomena, pp. 526-530, (2012)*

Signed: ....

Date ....

Acknowledgements

I would like to thank my supervisor Professor Alun Vaughan for his enthusiasm, support and invaluable discussions. My thanks extends to Professor Paul Lewin for all the encouragement, patience and general guidance.

My sincerest appreciation goes to Dr Paul Hoy for his assistance with the Fourier transform infrared spectrometer, and Mr Neil Sessions, Mr Alistair Clark and Dr Shuncai Wang for their technical support with the scanning electron microscopes. I would like to further my gratitude to Dr Lynda Brown and Dr Alex Holt for sharing their extensive knowledge in the field of Chemistry. Thank you to Dr Harry Rose for his patience and advise when coding in Matlab.

I am indebted to many people within the High Voltage group, past and present. I am particularly grateful to the High Voltage workshop, Dr Ian Hosier and Dr Martin Morgan-Reading for their expertise and patience. A special acknowledgment goes to the PhD students whom I've had the pleasure of working with; Dr Nicola Freebody, Dr Dao Ngoc Long, Dr Jack Hunter, Dr Van Nguyen, and Dr Linh Truong. Thank you for your much needed advice, humour and friendship, I wish you all the best for the future.

A massive shout out to my amazing badminton friends! Thank you for the sporting challenges and lunchtime laughter. Ying, James and Charles, thanks for the training and feeding when I needed it the most. You have helped me more than you know.

Finally, a big thank you to Chris, your constant reassurance and never-ending smile has been with me through the good times and the bad. You have made me a better person.

For My Parents

Words cannot describe how your continuous nuturing, encouragement and endless patience has had a positive impact on my life. I can never thank you enough for your infinite support and your relentless endurance during phone-calls.

Chapter 1

Introduction

The continuous need for new technologies with enhanced functionality and improved efficiency has driven science to develop extraordinary materials. As the world population increases, electrical power industries strive to meet ever-growing demand, our current needs for superior materials have meant the traditional roles of ‘conductor’ and ‘insulator’ have become the most basic of requirements. Conventional polymeric composites have long been established as excellent insulators for many high voltage applications and the properties of each insulator have been tailored to meet specific needs; this may include a high resistance to partial discharge, low dielectric loss, mechanical robustness and improved thermal conductivity. Despite this, emerging nanodielectrics have the potential to supersede current insulating systems by performing at higher levels of stress whilst maintaining its insulative integrity, and therefore the last two decades has seen a surge in interest in nanocomposite systems due to their ability to exhibit exceptional properties [1]. This new class of material differs from conventional systems as they contain phases which measure a maximum of 100 nm in at least one of its dimensions. Although the mechanisms behind such phenomena remain poorly understood, in marked contrast to macroscopic multi-component systems, the matrix-filler interface in nanocomposites dominates a significant proportion of the total composite volume, it is therefore of common belief that nanodielectric properties stem from their sizeable interfacial region. This has led to intensive research in improving the quality of the interface and the analysis of the phenomena which may occur within it.

1.1 Nanocomposites

Examples of nanodielectric materials date back thousands of years and have known to be used as early as the Song Dynasty (960 - 1279 AD), where nanomeric metal oxides were introduced into porcelain glazes to produce shades of blue and green in Jun ware [2]. Other examples of early nanotechnology include the Lycurgus cup (290 - 325 AD), which is a unique diatretum that possesses dichroic properties with the addition of gold nanoparticles into glass [3], and Damascus steel (17th century) where sharp, shatter resistant blades and distinctive patterns were a result of processing carbon nanotubes and cementite nanowires within the steel matrices, Figure 1.1 [4]. The 1900s saw a rise in the use of carbon black and nanoclays as reinforcing agents in rubbers and elastomers respectively [5, 6], where the former example produced products with increased wear resistance making them ideal for use in vehicle tyres.

FIGURE 1.1: The distinctive pattern of a Damascus blade [7].

Despite this, it was not until the late 1980s that The Toyota Research Group made a significant impact on nanocomposite history when they patented their montmorillonite/nylon-6 nanocomposite. Their material contained a 4.2 wt.% filler loading which saw a 80 °C increase in the heat distortion temperature of the host polyamide [1, 8]. Subsequently, the product was utilised in their vehicle engines as cam belt covers and since then, a number of publications have reported how the addition of the correct nanofiller can modify or induce material properties; for example, Sumita *et al* reported a 30% improvement in yield stress and a 170% increase in the Young's modulus in a nanosilica-polypropylene composite [9], whereas Agag *et al* reported a 12.1 GPa increase in the tensile modulus of a polyamide system with the addition of 2 wt.% montmorillonite clay [10].

1.2 Electrical properties of nanodielectrics

Much of the initial effort in nanotechnology was focused on generating composite materials with improved thermal and mechanical properties, however this concept quickly became an interest in the field of electrical insulation. In 1988, Johnston *et al* patented their research on the positive effects of introducing "*fine alumina or silica of critical particle size*" into polymer resins [11], where an increased resistance to corona discharge was observed when subjected to high voltages. Unfortunately these marked findings were overlooked until the early 1990s, when Lewis introduced the concept of the 'nanodielectric'.

Since then, a number of groups have produced and investigated the electrical response of dielectric systems. For example, some authors have explored and published findings on the resistance to partial discharge; Henk *et al* showed how the presence of nanoparticle silica improved the voltage endurance of epoxy resin by twenty-fold [12], suggesting that damage due to partial discharge was limited by the filler acting as a heat sink to remove excess energy and provided thermal stability at higher temperatures. They also found that the addition of nanofiller had the advantage of reducing the physical shrinkage of the system during the cure which lowered stress on the system upon the application of mechanical strain. Layered silicates have also seen to improve erosion depths caused by partial discharge, Kozako *et al* used scanning electron microscopy (SEM) and atomic force microscopy (AMF) to quantify the surface characteristics of polyamide composites [13]. Their analysis revealed that although a 2 wt.% filler loading showed no improvement to surface roughness, it was assumed that the filler had a significant effect on the manner in which the polymer matrix crystallised at the interface. The crystalline volume around the filler provided a greater resistance to partial discharge than amorphous regions and the silicate layers were considered to act as shields at the surface of the nanocomposite to reduce surface erosion. Similarly, Fuse *et al* later discussed the possible mechanisms that resulted in the resistance to partial discharge in high voltage applications [14]. Their publication stated that the nanofiller rearranges at the composite surface and serves to increase the bond strength between the polymeric host and filler, consequently increasing the durability against partial breakdown phenomena. The benefits of combining nanomeric fillers into polymer matrices have also been also observed and discussed by other groups using nanosilica [12, 15]. Whilst some groups studied the resistance to partial discharge, the relative permittivity of nanodielectrics has been under keen investigation. Typically the relative permittivity of the virgin matrix will change according to the relative permittivity of the filling phase. For example, if the addition of filler with a higher relative permittivity is added, the overall permittivity is observed to increase, conversely the combination of a filler of lower relative permittivity will result in a permittivity decrease. A comparison between micro-fillers and nanofillers was published by Nelson *et al* who compare titania composites containing fillers of micrometric and nanomeric sizes. They discuss how the relative permittivity of titania-epoxy nanocomposite is higher than the microcomposite equivalent, which is assumed to be a product of restricted overall mobility of the dipolar movements due to the reduced size of the nanofiller [16]. Nelson *et al* publish permittivity values of 9.99 for the base resin at 1 kHz, whereas the micro and nanocomposites possess permittivity values of 13.8 amd 8.49 respectively. Furthermore, the DC breakdown strength of nanocomposites has also been under examination, for example, Roy *et al* found an incremental increase in DC breakdown strength with the addition of treated nanofillers in their cross-linked polyethylene matrix in comparison to the virgin material. Similar to studies regarding resistance to partial discharge [14, 13], the degree of crystallinity was reported as a possible origin for this behaviour; the publication discusses how the increase in breakdown strength may be a product of path discontinuity due to nanoparticles scattering charges in the crystalline phase. In contrast, studies by Lau *et al* show a reduction in DC dielectric strength of silica filled polyethylene nanocomposites, claiming that the filler may introduce trapping sites within the interphase and produce space charge effects [17].

It is important to note that the dissimilarity between these publications are not uncommon, for example there have also been a difference in research that examine the AC breakdown strengths of nanodielectric materials. Singha *et al* show a reduction in the dielectric strength under an AC field with the addition of 0.1 to 10% of nanomeric titanium dioxide (approximately 50 nm) in a bisphenol-A epoxy resin, whereas Li *et al* observes a general increase of AC breakdown strength with the addition of low filler loadings of the same nanofiller (20 - 25 nm) [18]. Singha *et al* comments on the differences between AC breakdown data where they conclude that the particle size and sample thickness might have a significant effect. Amongst these parameters, the various combinations of filler loading and polymer matrices has led to a saturation in publications in the high voltage field, this contributes further difficulty in establishing the mechanisms behind nanodielectric phenomena.

Although the above publications focused on the electrical properties of nanodielectrics, it must not be forgotten that all materials have a multifunctionality and the performance of high voltage systems cannot solely rely on electrical capabilities; many factors contribute to the failure of high voltage insulation including impurities in processing, mechanical stresses and thermal properties. Chaing *et al* published a report on thermosetting systems and compared unfilled epoxies with those which had been filled with modified silicon and phosphorous nanofillers [19]. At low temperatures, the group observed a negligible difference in thermal stability, whereas at temperatures above 800 °C, the modified systems possessed a higher flame retardancy and retained thermal stability. Similarly, Motori *et al* shared their findings on the effects of dispersing layered silicates into a polypropylene matrix. They used thermogravimetric analysis (TGA) to demonstrate how a 6 wt.% loading increased the potential operating temperature of the material [20]. Further examples of nanodielectrics systems and their impressive properties are described in a review by Tanaka, which includes combinations of layered silicates, silica and titania nanofillers in epoxy, silicone rubbers and polyimide matrices [21].

1.3 Polymer matrices and nanofillers

The properties of composite materials are heavily dependent upon the nature of both the host matrix and the reinforcing filler. For example, metals are renowned for their ability to operate at high temperatures and may therefore be combined with a fibrous filler to produce a material with high mechanical strength and high melting point; whereas ceramics exhibit a high resistance to weathering and corrosion, and can therefore be blended with metallic fibres to overcome fracturing or brittleness [22]. Polymer matrix composites are often favoured in the field of high voltage insulation, not only for their insulative capabilities as thermal and electrical insulation, but also due to their desirable weight to strength ratio, low manufacturing costs and versatility in many industrial sectors.

1.3.1 Polyepoxides

Polymers range from the most basic linear skeletal structures (e.g. polyvinyl chloride) to those with architectures involving rings, side-branches, cross-linking bonds (e.g. Bakelite). They can be chemically engineered to meet the requirements of many applications by polymerising specific monomers; for example, polystyrene is formed from breaking a double bond in a styrene monomer unit and processing it such that it bonds with another styrene monomer which has also had its double bond broken. Polystyrene is an example of polymer which is classed as a thermoplastic, which indicates that the system can be remoulded upon the application of heat and it retain specific shapes from remoulding. In contrast, thermosetting polymers are those which have the inability to be reshaped; typically polymers are processed to form bonds between neighbouring polymer chains and act inhibit the individual freedom of each chain. This process is known as cross-linking which is seen to increase the overall stability of the system.

Polyepoxides, or epoxies are a good example of cross-linked polymers. This class of amorphous polymer is characterised by one or more oxirane ring (where one oxygen atom and two carbon atoms bond to form a three-membered ring) that is cross-linked with a curing agent and occasionally with the addition of a hardener. Its thermosetting nature means that these types of polymers cannot be melted and remoulded once formed which makes them suitable for applications that require high thermal stability [23]. There are a wide variety of epoxy resins with a range of functionalities available for commercial use and those with a greater number of reactive sites will result in a highly cross-linked network that increases heat resistance and density. As an example, TGE-6F (triglycidyl ether of 1,3,5-tris(2 hydro hexafluoro-2-propyl)benzene) is a trifunctional resin that is readily cured to increase production output and therefore has financial benefit [24].

The curing agent is chosen such that its functional groups are completely compatible with the epoxy resin where the reactive nature of the oxirane rings favours reactions with nucleophiles such as hydroxyl or amine groups. The curing agent cross-links with the resin to form a continuous three-dimensional network that reduces the mobility of the chains. The properties of the system can be adjusted by varying the stoichiometry or cross-linked polymer chain length, both of which will determine the overall properties of the system. Typically, the system is polymerised with the application heat or a chemical catalyst, where achieving an optimum temperature for the cure is vital for the system to react completely and successfully; if the applied temperature is below the system's ultimate glass transition temperature, T_g, the epoxy will vitrify but remain in an uncured state. This is an issue as this glassy state will retard the cross-linking process and increase the time for the epoxy to cure fully [25, 26, 27].

1.3.2 Epoxy resin reactions with amine based curing agents

This study uses D.E.R 332 from Sigma-Aldrich, which is a diepoxide chemical containing four aromatic rings and an epoxide group at either end of the polymer chain. The curing agent is a polyetheramine obtained from Huntsman; Jeffamine D-230 is composed of an oxyproplene backbone with two amine groups available for cross-linking. The process in which these chemicals react is shown below [24].

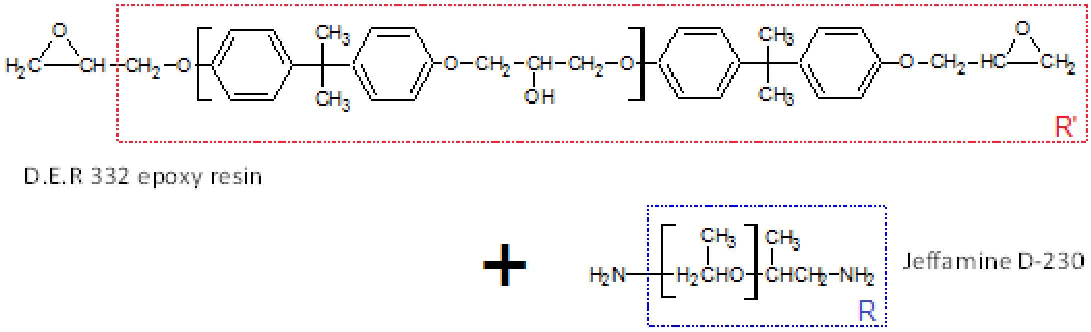

Figure 1.2: The chemical structure of D.E.R 332 epoxy resin (above) and Jeffamine D-230 hardener (below).

The reaction between these two compounds begin as the primary aliphatic amine from the hardener reacts with an epoxide group in the resin. Each of the amine groups provides two active hydrogen atoms for reaction, these hydrogen atoms have an affinity towards bonding with the oxygen atom in the oxirane ring.

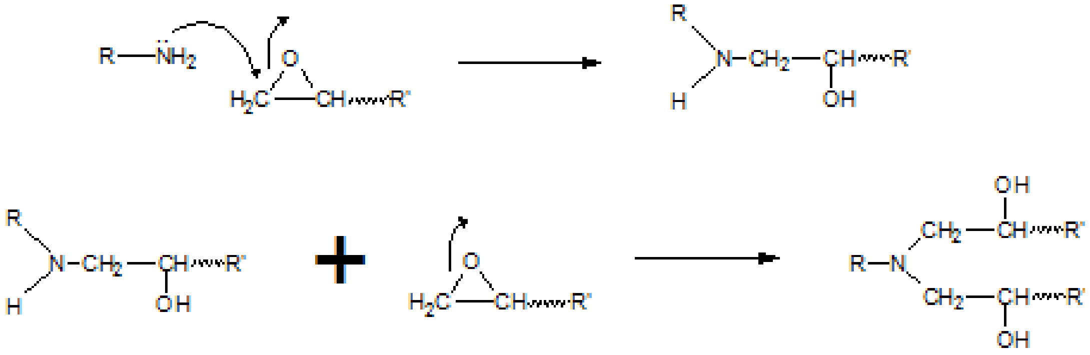

Figure 1.3: Opening of epoxide ring due to active hydrogen atom in the amine (above) followed by the bonding of the second hydrogen atom with an epoxide group from an alternative D.E.R 332 molecule.

The second aliphatic amine group from the curing agent will then proceed to react with another two epoxide rings via the same mechanism. The unreacted epoxide groups (on the ends of R′) will then continue react with other amine groups which in turn perpetuates further cross-linking.

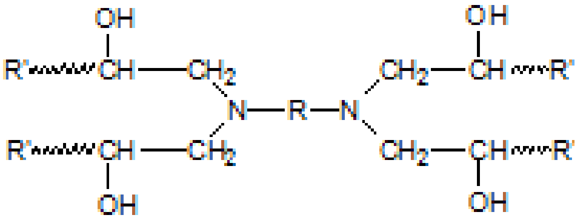

Figure 1.4: The product of crosslinking one Jeffamine D-230 monomer with four D.E.R 332 monomers.

Any hydroxyl groups generated during the curing process will result in alternative cross-linking reactions; for example, they may react with epoxide rings to form ether bonds. This process of etherfication competes with the epoxy-amine cure which is dependent on the stoichiometric ratio of resin to hardener used. Any alcohol bi-products produced act as catalysts to promote the curing process.

Epoxy resins may contain aromatic, aliphatic or cycloaliphatic chains and have been developed with varying molecular weights. Combined with the correct curing agent, properties such as water resistance, heat resistance, anti-chemical corrosion characteristics and a high strength to weight ratio can be induced [28]. The versatility of this class of material has seen an explosion in their consumption since the 1940s [29] and they are now utilised in industries from communications to biomedicine [24]. Epoxies have also been documented to possess excellent dielectric properties and are renowned in the electrical industry for their dielectric strengths in the region of 120 to 180 kVmm^{-1}, dielectric permittivities in the range of 3 to 6 at low frequencies and tan δ values between 10^{-3} to 10^{-2} at 60 to 1000 Hz [24]. Epoxies are therefore an extremely popular material in the electrical power and electronics industries and are often employed for potting, embedding or encapsulation of electronic components on circuit boards [29].

1.3.3 Nanofillers

For a composite material to be classified as a nanocomposite, one of its filling phases must measure a maximum of 100 nm in at least one of its dimensions. Such fillers are typically introduced into polymer matrices at loadings of 1 to 10 wt.% and can be grouped with respect to their dimensions. The filling phases for nanocomposite systems can vary greatly in their shape (including (quasi-) spherical particles, fibres and laminas), aspect ratio and intrinsic properties, it is therefore of great importance to select the appropriate nanofiller to promote the desired properties for any application. The dispersion of one type of nanofiller can have a number of positive and/or negative effects, the most common nanofillers used in dielectric systems are described below;

- **Nanoclays** are natural or synthetic plate-like clay particles that are part of the phyllosilicate family [1]. These silicate layers possess a Si_2O_5 crystalline tetrahedron structure, where each tetrahedral is typically bonded to metal cations to neutralise the excess negative charge. For example, aluminium, magnesium or sodium cations may bond with the crystalline structures to form silicates such as kaolinite ($Al_2Si_2O_5(OH)_4$), lizardite ($Mg_3Si_2O_5(OH)_4$) and Montmorillonite (Al, $Mg_2)Si_4O_{10}(OH)_2.nH_2O$. Montmorillonite (MMT) is one of the most popular nanoclays used, as it has the potential to be exfoliated such that its aspect ratio is increased by a thousand fold. This has been shown to improve thermal, electrical and mechanic properties of nanocomposites [30, 31].

- **Metal oxides and hydroxides** are hygroscopic in nature and therefore have an affinity for mixing with polar matrices [1]. There are a number of materials that fall into this category, including zinc oxide (ZnO), titanium dioxide (titania, TiO_2), aluminium oxide (alumina, Al_2O_3) and boehmite ($Al_2O(OH)$), all of which can change the electrical properties of polymer systems. Nanomeric silicas are commonly used as additives in epoxy resins to improve thermal conductivity and act to promote a positive effect on the dielectric response of the system [1, 32]. Silicon dioxides are amongst the most abundant material on earth as they can be found in quartz and sand, however they are often synthesised via pyrogenic or precipitation methods and engineered with a porous surface to increase their surface area for specific application. Publications have reported how the introduction of nanosilica into dielectric phases have an effect on a number of properties including the electrical breakdown strength [17, 33] and increased resistance to partial discharge [34, 35]. As the compatibility of silicas with polar matrices are poor, they are often functionalised with the use of organosilane chemistries; this takes advantage of the hydroxyl groups on the surface of the filler by coupling an intermediate polymer between the filling phase and matrix.

- **Carbon nanotubes** are formed from hexagonal networks of carbon atoms and can be prepared as single-walled or multi-walled, as seen in Figure 1.5. The surface modification of carbon nanotubes is often required as they tend to agglomerate which can lead to electrical failure in insulating systems [36, 37]; the dispersion via ultrasonication methods can prove problematical as such techniques may damage the nanofiller and have a negative effect on the aspect ratio [38, 39]. Carbon nanotubes have been of great interest in the field of nanotechnology as their electrical properties are dependent upon the chirality of the structure; their conductive or insulative characteristics can be modified by changing the way in which the tubes are rolled [1].

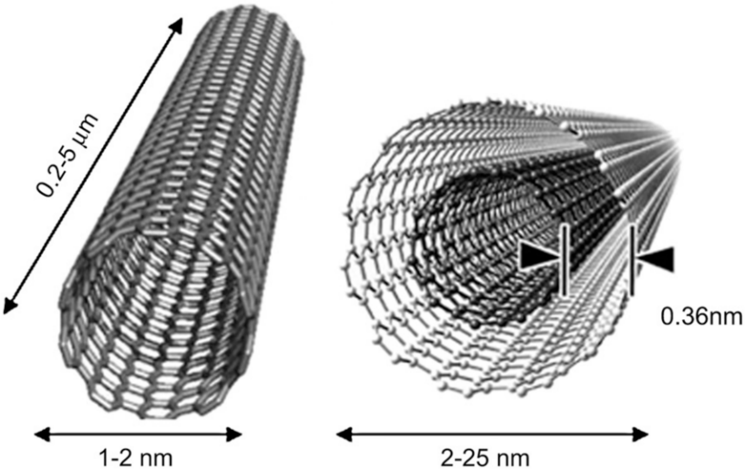

Figure 1.5: Single-walled carbon nanotube (left) and multiwalled carbon nanotube (right). Reprinted from [40].

The intention of introducing these types of fillers into virgin materials is to enhance material characteristics, however positive effects are not always the case, detrimental effects are thought to be due to a number of parameters, including defects in virgin materials [32], filler size [16, 32] and weight loading [41]. One of the most common factors which are seen to negatively influence nanocomposite behaviour is the agglomeration of nanofiller due to poor dispersion [42, 43]; the reduction of the interfacial region between matrix and filler is thought to have a fundamental role on material properties [33, 44] and this remains to be an issue for all classes of nanocomposites.

1.4 Nanofiller mixing and functionalisation

1.4.1 Dispersion methods

As a consequence of their nanomeric size, filler particles in nanocomposite systems tend to agglomerate either before or during nanocomposite production. Conventional mixing techniques such as shear mixing may not be able to overcome the high surface energies and the electrostatic forces within the system and typical processing methodologies are in constant competition with the low entropic drive for mixing [45]. Agglomerations of nanofiller within a polymer system have been seen to be detrimental in enhancing composite properties and a number of methods have been used to provide a well dispersed system [46, 47]. Whilst magnetic mixing has been shown to distribute micro-sized phases in polymer matrices to a satisfactory uniform manner [48], nanofillers require more rigorous methods to overcome the electrostatic forces between particles such that a homogenous dispersion can be achieved. Shear mixing is a popular method that reach speeds of up to 5,000 rpm; however the technique is not without its disadvantages, this method may require long periods to achieve an acceptable degree of homogeneity [49] and is only successful if the viscosity of the sample is sufficient to retain the dispersion. One of the most popular techniques of dispersion is ultrasonication, where pulses of ultrasonic waves are used to break up existing filler agglomerations. The application of an ultrasonic pulse through liquid media results in instantaneous cavitation, where the system is violently compressed and is followed by a sudden drop in pressure as rarefaction occurs; these processes causes micro bubbles that expand and contract rapidly with the frequency of the ultrasonic pulse and acts to homogenise the medium. Ultrasonication can be applied in one of two ways, via an ultrasonic bath or using an ultrasonic probe. Standard laboratory water bath sonicators have the ability of operating at 20 to 24 Hz with powers less than 100 W [49], whereas probe sonicators can apply up to 1500 W with a variable pulse setting and amplitude [50]. Of the two methods, ultrasonication in a water bath is preferred as prolonged exposure to ultrasonication via a probe can result in filler damage and degradation of the matrix; this is a particular issue for carbon nanotubes [38, 49]. As this study employs the use of ultrasonication both via a water bath and a probe, the two will be differentiated by using the term *ultrasonication* to describe the former and *sonication* to represent the latter.

1.4.2 Surface modification

In addition to mechanical mixing, researchers have developed chemical methods to promote dispersion. Surface functionalisation involves modifying the surface of nanofillers such that they are compatible with the composite matrix. Coupling agents can be used to overcome the immiscibility of the filling phase and the matrix phase, where one end of the agent bonds to the surface of the nanofiller and the other is bonds with the molecules within the matrix. A variety of coupling agents are available, each containing various functional groups suited for different purposes. Titanate couplers are those which bond directly to inorganic substrates via its monoalkoxy (or neoalkoxy) group. Organotitanates are typically used in materials that require the ability to operate in high temperature conditions as neoalkoxy titanates possess a thermally stable structure [51] and are most effective with carbon black and carbonate fillers. Due to the instability of titanium with carbon, any functional group must be bonded to the titanium atom via an oxygen atom, this will increase the length of the organotitanate chain which may have affect the composite properties (i.e. increase thickness or free volume within the interface) [52]. It has also been found that discolouration may occur in the presence of phenols as a result of the reactivity of titanium-oxygen bonds, therefore zirconate coupling agents may be used as an alternative. Zirconate couplers have a similar chemical formula to titanate couplers and have been used to promote adhesion in printing ink formulations [53].

One of the most popular coupling agents in the electrical industry are organosilanes. Their affinity for reaction with hydroxyl groups makes them suitable for treating mineral surfaces and renders the filler hydrophobic. These qualities have ensured their increase use in the polymer industry over the last 50 years [24] and has been used in high voltage applications for the development of insulative materials. Research has been published on how organosilane coupling agents have improved nanofiller dispersion and provide a greater bond strength between the filling and matrix phases; for example, the General Electric Company USA patented the use of vinyl silane coupling agent formulations for their extruded XLPE cable insulation materials [54], they found use of vinyl silane provided stable covalent bonding between polyethylene, silica and other inorganic fillers, cross-linked using a dicumyl peroxide catalyst; the resulting polymer composite showed significant improvements against electrical and water treeing, and increased high temperature performance [54].

1.5 The nanocomposite interface

There has been much discussion regarding the mechanisms that govern nanodielectric behaviour, where the main focus has been concentrated on the sizeable interfacial volume. Lewis describes how, assuming that the interfaces were determined only by short range forces, composites containing filler(s) with dimensions of 5 nm or less would result in the interfacial region occupying at least 50% of the total volume [55].

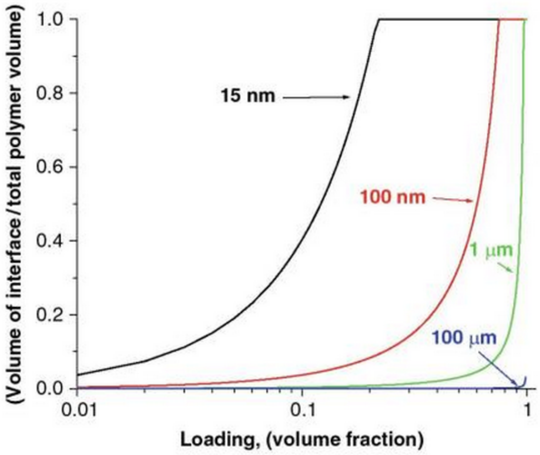

FIGURE 1.6: The interfacial region occupies a greater volume fraction with decreasing filler size and increased loading. Repinted from [1].

Figure 1.6 shows how a greater volume fraction could be occupied by the interphase with decreasing nanofiller size and an increased weight loading. As a consequence, a number of studies revolve around the nature of the interfacial region. Many have come to believe that the matrix-filler interface provides an 'interaction zone', in which the mobility of polymer chains are altered and results in the enhancement of nanodielectric properties [21, 56]. Theories regarding the interfacial region have been proposed by a number of authors.

1.5.1 Lewis' Intensity Model

In 2004, Lewis introduced the concept that the interface is a region that possesses modified electrochemical and electromechanical characteristics [57]. This region is influenced by a combination of short and long range forces between the filler and matrix that manifest themselves via any of the following; the concentration of atomic, molecular and ionic species, electron concentration, energy density or dielectric polarisability. As the intensity of the forces overlap, they interact and have the potential to modify the system both physically and chemically.

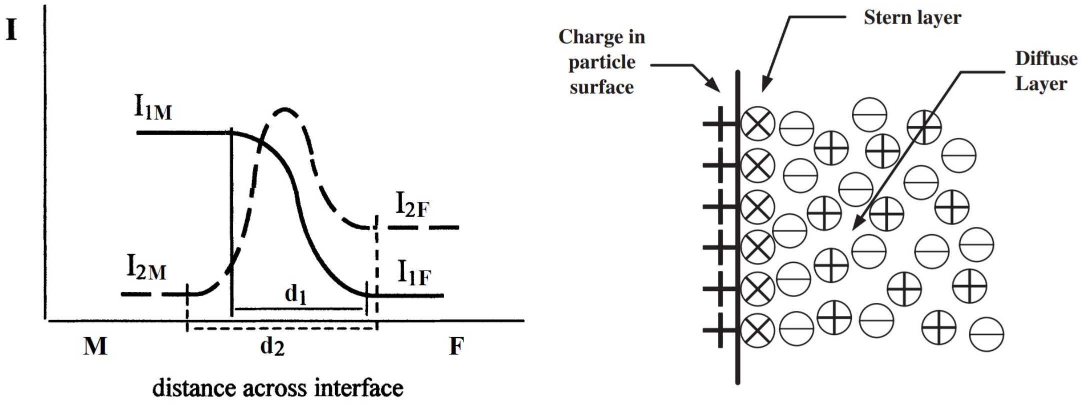

(a)

(b)

FIGURE 1.7: a) The interaction intensities of phases M and F b) Stern and diffuse Gouy-Chapman layer surrounding a nanoparticle. Edited and reprinted from [57].

Figure 1.7(a) represents Lewis' concept where the intensities of a property from species F and species M decrease over distances d_1 and d_2. The Intensity Model describes the formation of a Stern layer around the nanofiller that acts to counteract the charges within the filling phase. The surrounding charges within the matrix are then displaced to compensate for the concentration of negative or positive charges on the filler surface and form a diffuse Gouy-Chapman layer, Figure 1.7(b). These properties dictate the dielectric behaviour of the nanocomposite. As the filler loading increases, there is an increased overlap of the diffuse layer which acts to amplify or induce changes in the dielectric properties of the system [57]. Although this model is nondescript, this generalised model illustrates the possible interactions that occur at the interface and aids the visualisation of phenomena which may occur around the filling particulates.

1.5.2 Tanaka's Multicore Model

Tanaka *et al* proposed their Multicore Model in 2005 [15]. The detailed model takes the simple case of a spherical nanoparticle and assumes there are three concentric layers bound to the surface, each with specific properties. The closest 'bonded layer' is an estimated 1 nm in thickness and is believed to represent a transitional region that strongly binds the organic and inorganic parts of the system. These bonds are formed with the aid of a coupling agent and are either (or a combination of) covalent bonds, van der Waals forces or hydrogen bonds. The second 'bound layer' is described to contain polymer chains that interact strongly with the first layer and the surface of the particle. The polymer chains align perpendicularly to particle surface to form a region with an estimated thickness of 2 to 9 nm. The interaction strength between filler and matrix is assumed to be proportional to the thickness of the bound polymer fractions. The final 'loose layer' is composed of polymer chains with dissimilar chain conformation to the second layer, it is loosely coupled to the second layer and possesses different properties including chain mobility, free volume and crystallinity. Tanaka *et al* published an additional paper to show how the Multicore Model can be used to explain various nanocomposite phenomena in a number of dielectric systems [21]; having applied the model to data obtained from a number of papers (published up to 2003), Tanaka *et al* concluded that although some electrical behaviours of the nanodielectric systems could be successfully explained via their theory, there were still data that proved contradictory.

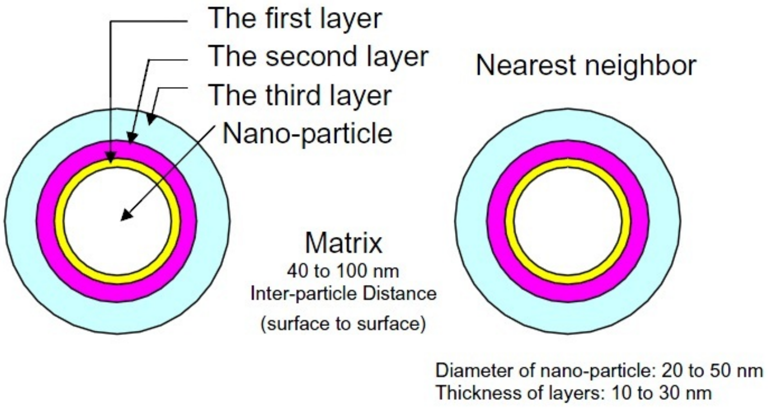

FIGURE 1.8: Schematic diagram of Tanaka's Multicore Model. Reprinted from [15].

This concept of concentric rings is convenient as it does not contradict ideas regarding the electric double layer, however there is no suggestion that the three surrounding regions are strictly discrete as implied by the authors. Furthermore, the entropy in the system will dictate the manner in which the chains align at the surface of the filler and influence nanodielectric behaviour, there is therefore no guarantee a specific configuration will be adopted and the chain configurations about the filler may vary according to the conditions in which the materials are prepared. This may explain any contradictions between model and experimental data [21].

1.5.3 Zou's Water-shell Model

Following a study of nanosilica filled epoxy, the Water-shell Model was proposed by Zou *et al* [58]. Based on the concept that water occupies the interfacial region around the filler, the model is a function of a number of layers in which the first layer surrounding the nanoparticle 'core' is formed from 5 to 10 water molecules (of size 0.278 nm) and is tightly bound to the surface of the filler. In comparison, the second layer is believed to be loosely bonded to the first layer via van der Waals forces and provides a conductive region around the particle(s). The remaining water in the system is considered to exist freely in the bulk. As an example, in the case of an epoxy which is subjected to relatively high humidity conditions, the overlap of the layers will provide conduction channels for charges or carriers that will contribute to epoxy degradation and decrease the breakdown strength. However, it must be noted that Zou's Water-shell Model is based on the assumption that water is distributed uniformly around each nanoparticle, for applications such as nanodielectric cable insulation, this is highly unlikely. Additional investigations by Fabiani *et al* [59] have come to similar conclusions when they performed water-uptake studies on polymer matrices.

1.5.4 Other models

A number of alternative theories have been proposed regarding the effects of the interface in nanodielectric composites. Rätzke *et al* introduced the Interphase Volume Model, where the interface should be considered as the 'interphase' as this better defines the region surrounding the nanofiller composed of polymer chains [60]. The extent to which enhanced properties are induced are reliant upon the optimum interphase content, which is dictated by the size of the nanofiller, the loading weight and the thickness of the interphase created. The system was visualised as a body-centered cubic lattice structure, where the model specifically shows a relationship between the filler loading and the total volume fraction and how this may contribute to resistance to electrical treeing and partial discharge. The authors discussed how the greatest improvement in such properties were attained when the interface volume was at an optimum [60]. Ciprari *et al* have reported that the interfacial region is not a continuous layer of polymer chains attached to the surface of the nanofiller [61], but an area in which segments of polymer chains are able to anchor themselves to the surface via bonding. Limitations in the interactions between matrix and filler result in partial adsorption, whilst the remainder of the polymer chains interact and entangle amongst themselves. Their publication presents data obtained from techniques including transmission electron microscopy (TEM), scanning electron microscopy (SEM), Fourier transfer infrared analysis (FTIR) and thermogravimetric analysis (TGA), and includes mathematical methods to calculate the number of anchored sites. Their studies concluded that the interfacial regions are not of a uniform thickness and may possess areas of low density of anchored sites around nanofiller particles. In contrast, Tsagaropoulos *et al* explained how glass transition temperature behaviour in silica-polymer nanocomposites implies that there are two influential layers surrounding the nanofiller [62, 63]. The outer layer, bound to the inner layer is thought to possess its own glass transition characteristics and has been confirmed by the presence of two tan δ peaks in polystyrene, polymethyl methacrylate and polydimethylsiloxane composite systems.

The models presented in this section define concepts in attempt to illustrate behaviour at or within the interface; however, although descriptions of physical structures and chemical bonding are suggested, no suggested model to date can fully account for enhanced nanocomposite properties.

1.6 Aims of the thesis

Whether the nanofiller is nanoscopic in three dimensions (particles), two dimensions (fibres and tubes) or in one (sheets and platelets), the existence of at least one nanoscale dimension results in a large interfacial region (hundreds of m^2g^{-1} [64]) and this is assumed to play a fundamental role in nanocomposite behaviour [65, 66]. The aggregation of nanofillers therefore, has practical consequences in nanocomposite systems and many groups have shown how agglomeration can undo all the potential benefits of a well dispersed system [46, 47]. Evidence exists to show that the aggregation of nanofiller can, for example, dramatically reduce the breakdown strength of a system [65] or promote deterioration of mechanical properties [67]. Much of the early Toyota work was focused on nanocomposites based upon nanoclays and polyamides due to their polar nature, where the strong interactions between the two components favoured mixing. However, since both nanoparticle and polymer molecule are relatively large, the entropic drive for mixing is low and as a result, the dispersion state of the nanofiller is strongly affected by the chemical interactions that occur within the interface [45]. For many dielectric applications, non-polar materials such as polyethylene have been increasingly popular, but obtaining a uniform distribution of polar fillers (such as nanosilica) then proves problematical. Consequently, the concept of functionalising nanoparticles to aid mixing is an attractive one. Many groups have shown how the use of coupling agents can change the surface chemistry of the nanofiller to exhibit an amphiphilic character such that one end reacts with an inorganic surface whilst the other is compatible with the polymeric host [68, 69, 42]. By using such technologies, it is possible to modify the chemistry and the extent of the interphase regions such that dispersion can be improved.

Whilst the notion of surface functionalisation is not new, there have been few detailed studies in which this has been treated as a variable parameter in nanodielectric systems. This thesis sets out to show how nanosilica surface chemistry can be modified to varying degrees and how this will affect nanofiller and matrix mixing. The surface modifications will be measured and quantified using a range of spectroscopic techniques to prove how the interface may be optimised to meet demanding dielectric requirements. As thermosetting epoxies are extremely versatile and a popular choice of material in the area of electrical systems and electronics [24], this work studies a range of silica-epoxy nanocomposites. The objectives of this study were;

- Produce differently functionalised nanosilicas, via both hydrous and anhydrous methods of surface modification, whilst varying the quantities of coupling agent in the modification process.
- Quantify the degree of nanoparticle modification using Raman spectroscopy and Fourier transform infrared spectroscopy.
- Develop a method to successfully introduce differently functionalised nanosilicas into an epoxy system, such that dispersion is uniform.
- Investigate how the differently modified nanosilica, and its dispersion has an effect on the dielectric properties of an epoxy system using AC breakdown studies, differential scanning calorimetry and dielectric spectroscopy.

1.7 Thesis Contents

Chapter 1 includes an introduction into nanocomposite materials, the possible benefits of nanodielectrics in high voltage systems and a review of proposed theories that attempt to explain enhanced nanodielectric characteristics.

Chapter 2 describes the optical and electrical techniques used in this study. Preliminary studies which dictate the final sample preparation methods are also detailed.

Chapter 3 presents a method of nanosilica functionalisation using hydrous solvents and discusses the spectroscopic data obtained from epoxy samples with the addition of the differently functionalised nanosilica.

Chapter 4 describes an anhydrous method of nanosilica functionalisation and presents spectroscopic data that quantifies the degree of functionalisation and the electrical effects of introducing the filler into epoxy.

Chapter 5 analyses confocal Raman spectroscopy as a tool for studying dielectrics, comparing results from vertically depth profiling different polymer systems with simulated data.

Chapter 6 is an overview of the study and compares the differences in functionalising nanosilica via a hydrous and anhydrous route. Conclusions and future work are also included.

Chapter 2

Spectroscopic Techniques and Preliminary Studies

2.1 Methods of spectroscopy

The scope of nanocomposite research is vast and the focus on this class of material can be divided into two areas; some groups specialise in designing and developing new nanodielectrics with novel characteristics, whilst others invest their time in understanding the basic physical and chemical concepts that lead to nanocomposite phenomena. The two areas of research are complimentary and both should be studied to gain a complete understanding of nanodielectric materials. The following sections describe the spectroscopic techniques used to study the nanocomposite systems prepared for this thesis.

2.2 Raman spectroscopy

There are a number of ways in which bonds can vibrate, these include symmetrical or asymmetrical stretching, scissoring, rocking, wagging and twisting (Figure 2.1); each represented by peaks or troughs in infrared spectra that can be analysed to interpret the chemical composition of the material [70, 71].

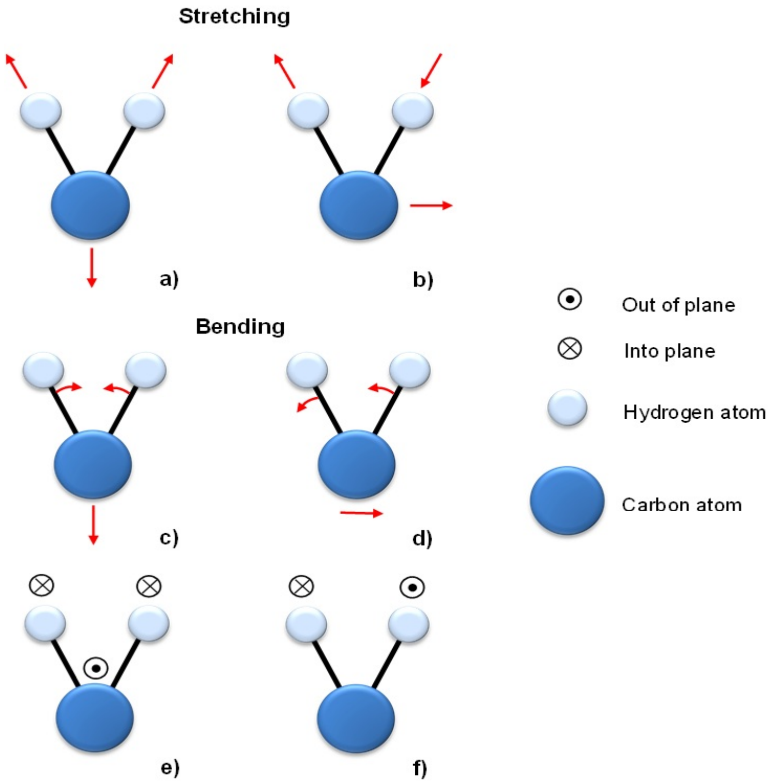

Figure 2.1: The stretching and bending of CH_2. a) symmetric, b) asymmetric; in-plane bending c) scissoring, d) rocking; out-of-plane bending e) wagging, f) twisting. Redrawn from [71].

Raman spectroscopy is a unique spectroscopic technique that is often used to identify the chemical composition of a material by probing these vibrational modes and interpreting the spectra obtained via the Raman effect. This phenomenon was originally envisaged by Smekal in 1923 [72] but was attributed to Raman and Krishnan in 1928 [73], and occurs due to the inelastic interactions between matter and light. Whilst the majority of incident light maintains its direction of propagation and travels through the medium, a small percentage will be scattered in various directions. The main scattering process, Rayleigh scattering, occurs when radiation is scattered elastically. The alternative scattering mechanisms are inelastic and typically follow one of two processes; Brillion scattering arises from the changes in translational energy in the lattice of solids due to acoustic modes, as the medium is compressed, light bends accordingly with the change in the refractive index causing shifts in the frequency of light. These shifts are proportional to the velocity of the acoustic mode affecting the medium [74]. The second, weaker form of inelastic scattering is Raman scattering; of the total incident radiation, only 10^{-7} is scattered via this process [75]. As a consequence of the vibrational variations in a system, the frequency of the incident light is shifted; this gives rise to Stokes and anti-Stokes lines in Raman spectra, where the frequency change corresponds to particular vibrational transitions. The mechanisms for the Raman effect can be described by classic theory or quantum mechanics.

2.2.1 Classical theory

Consider a wave of electromagnetic light incident on a medium, where upon its oscillating electric field will have an influence on the electron densities that surround molecule nuclei. This will cause the electrons to deviate from equilibrium, induce a dipole moment, μ, and induces variations in the polarisability, η. The change in dipole moment leads to a change in the energy of the radiation and results in a shift in its frequency. This can be explained mathematically by manipulating the equations for the electric field and the polarisability to arrive at the expression below (equation 2.1) [76].

$$\mu = \eta_0 E_0 \cos(2\pi\nu_i t) + \frac{1}{2} E_0 Q_{max} \left(\frac{\partial \eta}{\partial Q}\right) \{\cos\left[2\pi(\nu_i + \nu)t\right] + \cos\left[2\pi(\nu_i - \nu)t\right]\} \tag{2.1}$$

here η_0 is the polarisation of the molecule in equilibrium, E_0 describes the amplitude of the applied electric field, Q_{max} is the maximum vibrational amplitude of the molecule, whilst ν_i and ν represent the frequencies of the incident radiation and that of the vibrating molecule respectively [76]. In this expression, the first term relates to Rayleigh scattering as the frequency remains unchanged. However, the second term is associated with Raman scattering, where $\cos\left[2\pi\left(\nu_i + \nu\right)t\right]$ denotes Stokes scattering with frequency $(\nu_i + \nu)$ and $\cos\left[2\pi\left(\nu_i - \nu\right)t\right]$ represents anti-Stokes scattering with frequency $(\nu_i - \nu)$. In addition, this equation highlights the fact that a sample must be Raman active to obtain Raman spectra from the system; that is to say there must be a change in the molecule's polarisability with respect to position from equilibrium, Q. [77]. In other words,

$$\frac{\partial \eta}{\partial Q} \neq 0 \tag{2.2}$$

2.2.2 Quantum mechanics

The quantum mechanical approach describes the incoming light in terms of photons. When these photons interact with atoms or molecules in a medium, the system is excited from the ground state to a virtual energy state. In the case where the system returns to its original state, Rayleigh scattering is observed. However, Raman scattering is observed when an excited system relaxes into an energy state higher than its initial state, energy is transferred from the photons to the molecules in the medium. This is known as Stokes scattering. The emitted photon will have a frequency lower than that of the incident photon and produce a Stokes line in the Raman spectrum. Conversely, anti-Stokes scattering occurs when the molecule relaxes into a state that is lower in energy than its original state [75].

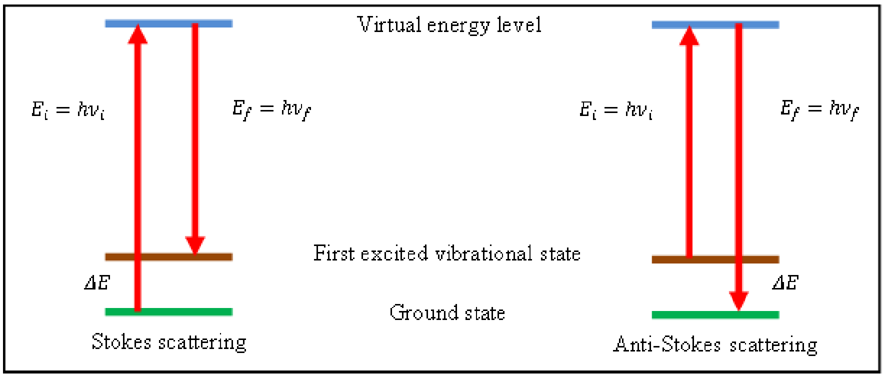

FIGURE 2.2: Energy diagram representing Stoke and anti-Stokes Raman scattering.

The emitted photon gains energy from the medium and therefore has a higher frequency than the incident photon. The energy gained or lost by a photon is given by;

$$\Delta E = h\left(\nu_i - \nu_f\right) \tag{2.3}$$

where h is Planck's constant, ν_i and ν_f are the incident and final frequencies of the photons respectively.

The intensity of the Stokes spectrum is generally higher than the anti-Stokes, as fewer molecules exist in excited vibrational states. The ratio of Stokes to anti-Stokes scattering is determined by the Boltzmann distribution,

$$\frac{N_l}{N_0} = \frac{g_l}{g_0}\exp\left(-\frac{E_\nu}{kT_A}\right) \tag{2.4}$$

where N_l and N_0 represent the number of atoms in the lower and higher vibrational states respectively, g_l and g_0 are the degeneracy of the lower and higher vibrational states, E_ν is the energy difference between vibrational levels, k is the Boltzmann constant and T_A is the absolute temperature.

Raman spectroscopy is an extremely versatile tool, it has been adapted with a series of methods to produce new techniques such as surface enhanced Raman scattering (SERS), tip-enhanced Raman spectroscopy (TERS) and coherent anti-Stokes Raman spectroscopy (CARS), all of which have different characteristics that suit different applications.

2.3 Fourier transform infrared spectroscopy

Infrared spectroscopy is a method of absorption spectroscopy that utilises the infrared region of the electromagnetic spectrum to characterise the molecular composition of a system. For temperatures above absolute zero, the atoms and molecules within a system are in constant motion. Atoms are described to possess three translational degrees of motion and polyatomic molecules have three rotational degrees of freedom in addition to their $3n'$ degrees of translational motion (n' is the number of atoms in the molecule). Linear molecules have $3n'$ - 5 normal modes of vibration and non-linear possess $3n'$ - 6 (due to the asymmetry). In some cases, these vibrational motions result in a change in dipole moment which gives rise to infrared activity and therefore when an infrared active material is exposed to infrared light, frequencies that are resonant to vibrational modes will result in light absorption. Infrared spectroscopy uses a combination of the near-infrared (14000 to 4000 cm^{-1}), mid-infrared (4000 to 400 cm^{-1}) and far-infrared (400 to 10 cm^{-1}) wavelengths to excite a molecular system. Resonant frequencies are absorbed which are characteristic of specific functional groups and this allows the chemical structure of the specimen to be determined [78]. Spectra are generally presented in either absorption, A, or transmittance, T, with respect to either wavenumber $\tilde{\nu}$, or wavelength λ. The transmittance is calculated as $\left(\frac{I}{I_0}\right)$, the ratio of power transmitted through the sample, I, and the power of the incident light on the sample, I_0. The relationship between this and the absorption is given as [79],

$$A = \log_{10}\left(\frac{I_0}{I}\right) \tag{2.5}$$

Unlike conventional dispersive infrared methods, where the incident beam is split into two such that one traverses the path length of a sample and the other acts as reference, Fourier transform spectroscopy involves irradiating a sample with a polychromatic infrared source. Within the spectrometer, each wavelength produces part of a broad-spectrum interferogram, every component is summed and Fourier transform mathematics are applied to convert the raw signal into recognisable infrared spectra [80]. As Fourier transform infrared spectroscopy analyses a sample over a range of infrared frequencies simultaneously, it is more efficient than dispersive (monochromatic) infrared spectroscopy and provides a higher signal-to-noise ratio to give clearer spectra [81]. However there are disadvantages, if one region produces noise, the whole spectrum will be affected as the data is recorded simultaneously. Furthermore, spectra obtained via this technique is likely to be prone to artefacts due to changes in atmospheric changes. As the background spectra and sample spectra are acquired at different times, even the smallest change in water vapour of CO_2 will contaminate the spectra [82].

2.4 Ultraviolet-visible spectroscopy

UV-visible spectroscopy is a simple tool that is used to study the absorption properties of a material when subjected to electromagnetic radiation in the spectral ultra-violet and visible frequency range. Frequencies from these regions of the electromagnetic spectrum are energetic enough to excite the material and cause it to experience electronic transitions. Much like infrared spectroscopy, incident radiation that is resonant to specific bonds will be absorbed and provide information about the chemical composition of the system [83]. The attenuation coefficient of the absorbing species can be calculated by measuring the transmittance and using the Beer-Lambert law (equation 2.6) [79, 84, 85].

$$T = \frac{I}{I_0} = C\exp(-az) \tag{2.6}$$

This equation shows the relationship between the radiation transmitted, T, with respect to its absorption coefficient, a. The absorption coefficient subsumes both turbidity and absorption effects. Again, I_0 is the value of the intensity radiation before it passes through the material whilst I is the intensity that is detected after traversing path length z. C is a constant.

When incoming electromagnetic radiation strikes the interface between two media of differing refractive indices, optical effects such as reflection, refraction and transmission are observed. Part of the radiation is reflected at the angle of incidence to the normal (as given by the law of reflection) and part of the radiation is refracted and continues to travel at an angle dictated by Snell's law [73],

$$n_i \sin\theta_i = n_t \sin\theta_t \tag{2.7}$$

where n_i is the refractive index of the medium before encountering the interface and n_t is the refractive index of the medium after passing through the interface. θ_i corresponds to the angle of incidence and θ_t is the angle at which the light is refracted.

The amount of reflected and transmitted light at the interface is dependent on the reflectance, R_f, and transmittance, T, which are the ratios of the reflected power to the incident power, and the ratio of the transmitted power to the incident power respectively [73]. These values vary with the angle of incidence, the material's refractive index and its polarisation properties. In the case of dielectrics, the electric component of electromagnetic radiation will cause the material to polarise and this will have an effect on the reflectance and transmittance. The reflectance and transmittance are calculated from the amplitude reflection coefficient, r, and the amplitude transmission coefficient, t', which are derived using the Fresnel equations [73, 86]. When the incident electric field is perpendicular to the plane of incidence, the amplitude reflection coefficient and amplitude transmission coefficient are [73];

$$r_{\perp} = \frac{E_{0r}}{E_{0i}}_{\perp} = -\frac{\sin(\theta_i - \theta_t)}{\sin(\theta_i + \theta_t)} \tag{2.8}$$

$$t'_{\perp} = \frac{E_{0t}}{E_{0i}}_{\perp} = \frac{\tan(\theta_i - \theta_t)}{\tan(\theta_i + \theta_t)} \tag{2.9}$$

However, when the incident electric field is parallel to the plane of incidence, the amplitude reflection and transmission coefficients are written;

$$r_{\parallel} = \frac{E_{0r}}{E_{0i}}_{\parallel} = \frac{2\sin\theta_t\cos\theta_i}{\sin(\theta_i + \theta_t)} \tag{2.10}$$

$$t'_{\parallel} = \frac{E_{0t}}{E_{0i}}_{\parallel} = \frac{2\sin\theta_t\cos\theta_i}{\sin(\theta_i + \theta_t)\cos(\theta_i - \theta_t)} \tag{2.11}$$

where E_{0i}, E_{0r} and E_{0t} are the amplitudes for the incident, reflected and transmitted electric fields respectively. Therefore, the reflectance, R_f, and transmittance, T, values can be obtained;

$$R_f = \left(\frac{E_{0r}}{E_{0i}}^2\right) = r^2 \tag{2.12}$$

$$T = \frac{n_t\cos\theta_t}{n_i\cos\theta_i}\left(\frac{E_{0t}}{E_{0i}}\right)^2 = \left(\frac{n_t\cos\theta_t}{n_i\cos\theta_i}\right)t'^2 \tag{2.13}$$

In the case where the incident light is perpendicular to the sample specimen, $\theta_i = \theta_t = 0$, where there is no distinction between the perpendicular and parallel components. Therefore the two parameters are derived as,

$$R_f = R_{f\parallel} = R_{f\perp} = \left(\frac{n_t - n_i}{n_t + n_i}\right)^2 \tag{2.14}$$

$$T = T_{\parallel} = T_{\perp} = \frac{4n_t n_i}{(n_t + n_i)^2} \tag{2.15}$$

2.5 Scanning electron microscopy

The spectral analysis of specimens can often be supported with the use of an electron microscope. Electron microscopes were developed in the early 1930s to overcome the limitations in microscopes that used visible light. By replacing visible light with an electron source, a higher resolution can be achieved as the electrons are not limited by the physical wavelength of light. From diffraction theory, the resolution obtained from electron microscopy has the potential to be 400,000 times greater than optical microscopy [87]. This theoretical value is achievable providing incident electrons are not scattered by gases in their trajectory; sample chambers within electron microscopes are usually evacuated to pressures of 10^{-2} Pa or less to reduce this problem.

Scanning electron microscopy is a method used to study the topological characteristics of a sample. Typically current passes through a tungsten filament cathode which is heated to temperatures in excess of 2527 °C such that electrons are thermionically emitted with an energy of 2 to 40 eV. These electrons pass through condenser and objective lenses and are directed towards the specimen. The beam is rastered across the sample via deflection coils and the electrons interact with the material to produce various emissions that are detected by the instrument.

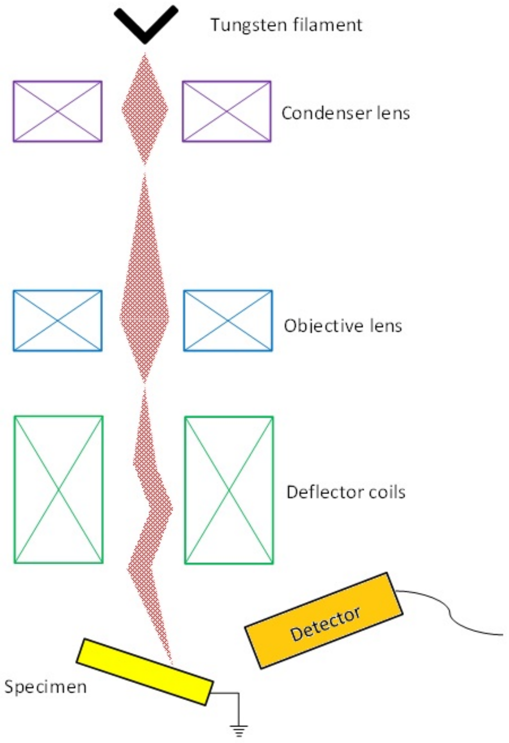

FIGURE 2.3: Schematic of scanning electron microscope instrument, the red shaded area shows the paths of the electrons.

Inelastic interactions between the incident electrons and the specimen provide information about the sample. The incident electrons may give rise to secondary or backscattered electrons that are formed in the interaction volume, as seen in Figure 2.4; Auger and X-ray radiation may also be emitted. Secondary electrons result predominantly from primary and Auger electrons that have transferred energy to the sample system and emerge from the interaction volume with energies of 50 eV or less. This occurs within close proximity of the sample surface and therefore strongly contribute to topographical images of the sample. Backscattered electrons, however, are electrons that have escaped the specimen with energies greater than 50 eV; the production of backscattered electrons is strongly dependent upon the atomic number of the sample, where materials with a high atomic number will generally scatter the electrons to a greater degree. This is beneficial in scanning electron microscopy as these areas are bright regions due to higher electron emission and contrast with darker regions for materials with low atomic numbers [88].

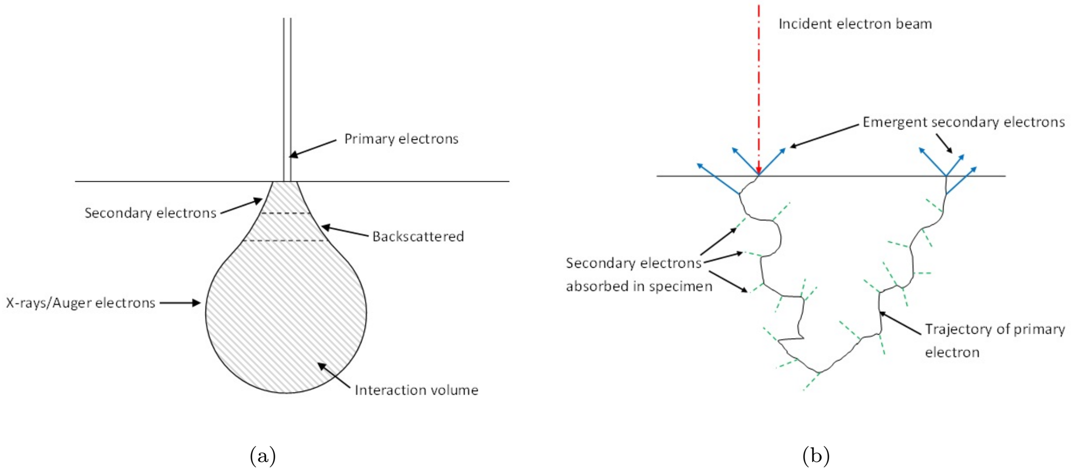

(a) (b)

FIGURE 2.4: a) Interaction volume within the bulk of the specimen, b) production of secondary electrons. Redrawn from [88].

2.6 Differential scanning calorimetry

Differential scanning calorimetry (DSC) is a simple thermoanalytical method that is used to study material properties based on their melting temperature, T_m, crystallisation temperature, T_c, and glass transition temperature, T_g [8]. This method of calorimetry compares the heat flow of two pans, one which contains the specimen and the other acts as a reference; the temperature of both pans are increased at the same rate and the heat flow is monitored, as the sample undergoes phase transition(s), the system will adjust the power accordingly to maintain the temperature of the pans such that they remain ideally equivalent. By plotting the heat flow within a pan against the temperature, the temperature at which a phase transition occurs can be identified and analysed [89]. Typically isothermal DSC is used, where the temperature of the two systems are quickly brought to a chosen temperature and thermal analysis is carried out as a function of increasing temperature, or as a function of time [90]. Isothermal DSC has the benefits of controlling and holding the temperature precisely with no drift, however it must be noted that it is unsuitable for measuring reactions which have a short time frame (i.e. fast curing reactions in epoxies) as the system takes time to stabilise the temperature.

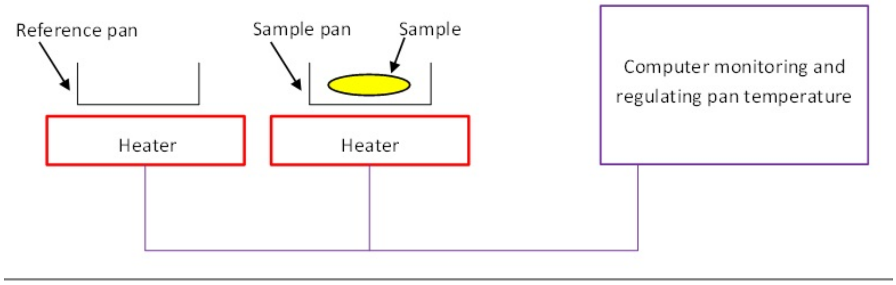

FIGURE 2.5: Schematic of a differential scanning calorimeter.

Figure 2.6 is a schematic plot of heat flow with respect to temperature for a typical polymer system. Below T_g, the thermal energy of the system is low and the polymer chains within the system have little mobility. As the temperature is increased to T_g, a stepped increase is observed as energy is absorbed to change the state of the system. At T_c there is a significant increase in enthalpy due to a change in the crystallinity of the system and is represented by a trough. In contrast, a peak is visible when a greater amount of energy is required to increase the temperature of the polymer system through its melting point.

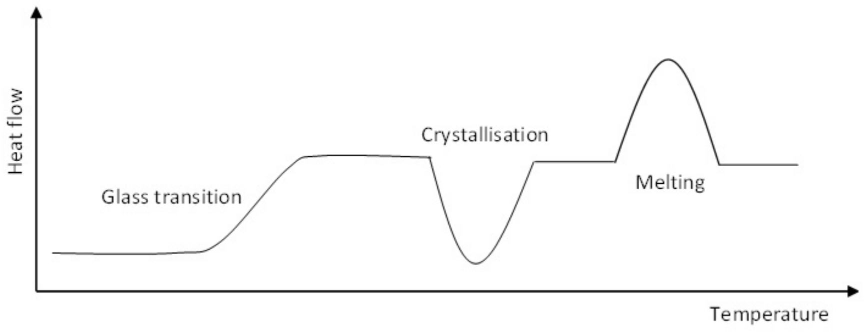

FIGURE 2.6: Typical features in a DSC curve obtained from a semi-crystalline polymer undergoing thermal transitions.

As amorphous polymers (such as epoxies) do not have a melting or crystallisation temperature, neither of these transitions will be visible in DSC studies. However, a feature representing the T_g will be observed. Enthalpy relaxation effects are removed by repeating a scan and only taking into account the second set of data [91, 92].

2.7 Dielectric spectroscopy

For a more detailed understanding of dielectric phenomena, one must consider the interactions between dielectrics and applied electric fields at a range of frequencies. Whilst optical spectroscopies (including Raman, infrared and UV-visible) are capable of observing resonance phenomena that occur when incident frequencies of 10^{12} Hz are applied, such methods are unsuitable for analysing the effect of electric fields which possess frequencies in the range of 10^{-6} to 10^{12} Hz [93]. Dielectric spectroscopy is such a technique, which analyses the effects of an applied electric field within this range. The application of an electric field will cause permanent and/or induced dipoles to orientate themselves with respect to the field, however the molecules may experience lag and therefore can only reach equilibrium over time; this technique measures the real relative permittivity, ε', which is related to how much energy is stored from the applied field, and the imaginary relative permittivity, ε'', which describes how much energy is dissipated in the system.

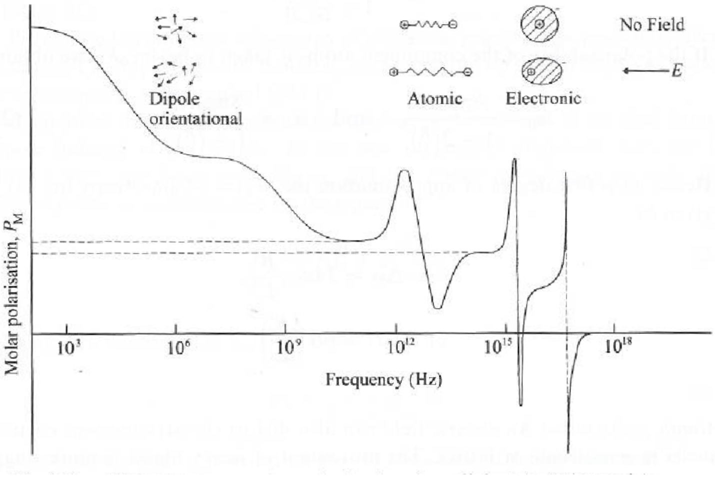

FIGURE 2.7: Schematic diagram of types of polarisation with respect to frequency. Reprinted from [94].

To understand the mathematics behind such mechanisms, consider a dielectric sample which is subjected to an electric field, E = $E_0\cos(\omega t)$. The dipoles within the system are disturbed and dielectric displacement, D, is observed,

$$\begin{aligned} \mathrm{D} &= D_0\cos(\omega t - \delta) \\ &= D_0\cos(\omega t)\cos(\delta) + \sin(\omega t)\sin(\delta) \\ &= D_1\cos(\omega t) + D_2\sin(\omega t) \end{aligned} \tag{2.16}$$

where $D_1 = D_0\cos(\delta)$ and $D_2 = D_0\sin(\delta)$. As the displacement in a linear, isotropic dielectric can also be written as D = $\varepsilon^*\varepsilon_0$E, where ε^* is the complex relative permittivity and ε_0 is the permittivity of vacuo (8.85 x 10^{-12} Fm^{-1}), the complex relative permmitivity (equation 2.17) can be written as the difference between the real relative permittivity (equation 2.18) and imaginary relative permittivity (equation 2.19).

$$\varepsilon^* = \varepsilon' - i\varepsilon'' \tag{2.17}$$

$$\varepsilon' = \frac{D_1}{\varepsilon_0 E_0} \tag{2.18}$$

$$\varepsilon'' = \frac{D_2}{\varepsilon_0 E_0} \tag{2.19}$$

A practical understanding of these parameters can be gained by considering alternating voltage applied to parallel RC circuit. At low frequencies, the alternating voltage **V**, will cause the dipoles within the system to orientate according to the frequency of the polarising field. As the frequency of the field increases, there will be a delay in the reorientation of dipoles as they fail to realign within the timescale of the field which leads to dielectric loss. The complex current **I**, in equation 2.20, can therefore be written in relation to the capacitive and resistive components of the system, I_C and I_R respectfully (equation 2.21 and equation 2.22),

$$\mathbf{I} = i\omega\varepsilon^* C_0\mathbf{V} = i\omega(\varepsilon'' + i\varepsilon')C_0\mathbf{V} \tag{2.20}$$

$$I_C = i\omega C_0\varepsilon'\mathbf{V} \tag{2.21}$$

$$I_R = i\omega C_0\varepsilon''\mathbf{V} \tag{2.22}$$

I_C leads the applied voltage by 90° and gives rise to energy storage, the latter component I_R is in phase with the applied voltage and gives rise to energy loss. The dissipation factor, tan δ, can now be calculated as a ratio of the energy lost to the energy that is stored,

$$\tan\delta = \frac{\varepsilon''}{\varepsilon'} \tag{2.23}$$

Dielectric spectra are often displayed as a function of frequency, where the real part, ε', is presented differently to the imaginary part, ε''. In the case of relaxation phenomena, this is characterised by a stepped decrease in ε' with increasing frequency and a peak in ε''. Whilst the dielectric strength, $\Delta\varepsilon$, of the system can be derived from the step in ε' (Figure 2.8), the relaxation time of the molecule(s), τ, is inversely proportional to the position of maximal loss ω_{max} (equation 2.24).

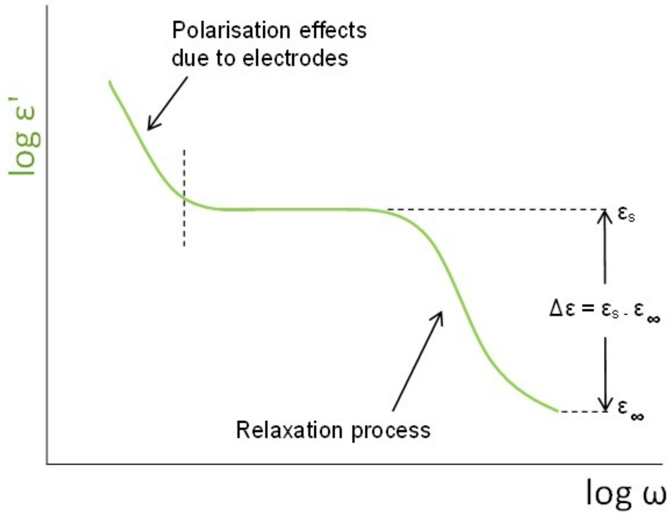

FIGURE 2.8: Real relative permittivity (log) as a function of frequency.

The shape of the peak will determine the distribution of relaxation times.

$$\tau = \frac{1}{\omega_{max}} \tag{2.24}$$

$$\Delta\varepsilon = \varepsilon_s - \varepsilon_\infty \tag{2.25}$$

For conduction phenomena, the type of conduction will dictate the behaviours seen in the spectra; purely ohmic conduction will cause ε'' to increase steeply with decreasing frequency (where dc conductivity is represented by $\frac{dlog\varepsilon''}{dlog(\omega)} = -1$), whilst ε' is completely independent of frequency. Non-ohmic conduction arises when charges collect at filler-matrix interfaces or electrode interfaces, this is represented by a sharp increase in ε' with respect to decreasing frequency. ε'' will still possess an increase in magnitude (with decreasing frequency), however the gradient will change such that $\frac{dlog\varepsilon''}{dlog(\omega)} > -1$.

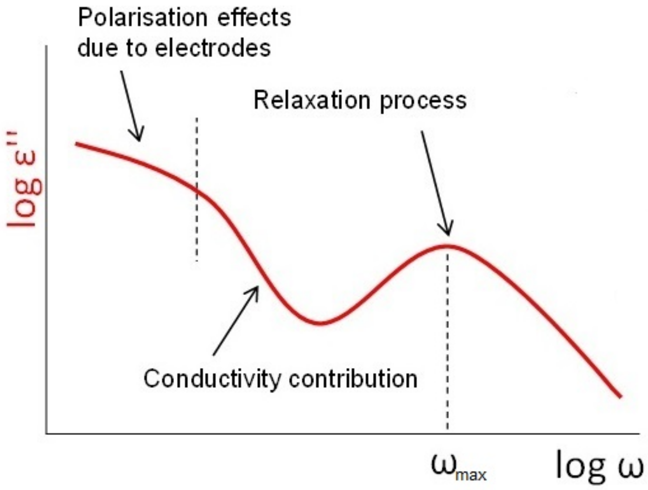

FIGURE 2.9: Imaginary relative permittivity (log) as a function of frequency.

2.7.1 The analysis of dielectric spectra

There are a number of model functions which are used to analyse the dielectric relaxation phenomena. One of the most well-known is the Debye function, which produces a symmetric peak as a function of frequency, however as Debye-like relaxation behaviour is rarely observed in real dielectrics, a number of non-Debye functions have been developed to provide a more suitable fit for asymmetric peak broadening. Based upon the Debye function (equation 2.26), the Cole-Cole (equation 2.27) and Fuoss-Kirkwood (equation 2.28) functions have been established [93],

- The Debye function, where the symmetric loss peak possesses a half width of 1.14 decades.

$$\varepsilon_D^* = \varepsilon_\infty + \frac{\Delta\varepsilon}{1 + i\omega\tau_D} \tag{2.26}$$

  here $\varepsilon_\infty = \lim_{\omega\tau\gg1} \varepsilon'(\omega)$, $\varepsilon_s = \lim_{\omega\tau\ll1} \varepsilon'(\omega)$ and the Debye relaxation time is inversely proportional to the position of maximal loss, $\omega_{max} = \frac{1}{\tau_D}$.

- The Cole-Cole function, was developed to account for a symmetrical broadening of the dielectric function.

$$\varepsilon^*_{CC} = \varepsilon_\infty + \frac{\Delta\varepsilon}{1 + (i\omega\tau_{CC})^{\beta'}} \tag{2.27}$$

where $0 < \beta' \leq 1$ gives rise to peak broadening and $\omega_{max} = \frac{1}{\tau_{CC}}$. In the case where $\beta' = 1$, the Debye function is achieved.

- The Fuoss-Kirkwood function, accounts for an asymmetry in the peak broadening.

$$\varepsilon^*_{FK} = \varepsilon_\infty + \frac{\Delta\varepsilon}{(1 + i\omega\tau_{FK})^{\gamma}} \tag{2.28}$$

where $\gamma (0 < \gamma \leq 1)$ gives rise to asymmetrical broadening in the relaxation function when $\omega > \frac{1}{\tau_{FK}}$. When $\gamma = 1$, the Debye function is obtained.

- However, the most widely used model function when dealing with solid dielectrics is the Havriliak and Negami function. This combines equations 2.27 and 2.28 to produce a more general function,

$$\varepsilon^*_{HN} = \varepsilon_\infty + \frac{\Delta\varepsilon}{(1 + (i\omega\tau_{HN})^{\beta'})^{\gamma}} \tag{2.29}$$

The Havriliak-Negami function must follow a set of bounds to hold true, $0 < \beta', \beta'\gamma \leq 1$. Parameters β' and γ are of such a nature due to the limiting characteristics of the complex dielectric function, where the plotted peaks of log ε'' vs log ω possess different gradients at low or high frequencies; for $\omega \ll \frac{1}{\tau_{HN}}$, $\varepsilon_s - \varepsilon'(\omega) \sim \omega^m$ and $\varepsilon''(\omega) \sim \omega^m$, where $m = \beta$, and for $\omega \gg \frac{1}{\tau_{HN}}$, $\varepsilon_s - \varepsilon'(\omega) \sim \omega^{-p}$ and $\varepsilon''(\omega) \sim \omega^{-p}$, where $p = \gamma\beta$. The values of m and p dictate the gradient (and therefore the shape) of imaginary relative permittivity peaks at low and high frequencies [93]. In the case of asymmetrical model functions, the characteristic relaxation time observed in spectra is not related to the position at which one would find the position of maximal loss.

2.8 AC breakdown testing

Regardless of the care taken in manufacturing insulating systems, the formation of imperfections is inevitable. These sites lead to the dielectric breakdown of the system, where the failure results in mechanical damage and/or electrical conduction. Although there are a number of theories surrounding the electrical breakdown of dielectrics, the most commonly used theory used to describe electrical breakdown is the avalanche theory [8]. Under a high electrical stress, the mobile charges within the system gain enough energy to be accelerated along the mean free path; in the case where the charges collide with an electron, there is the possibility that it is forced to exit its orbital surrounding molecule nuclei. This process is amplified as the initial process results in electron-hole pair and causes conduction within the system. Other breakdown theories have been summarised by Reading [8, 95].

The dielectric breakdown strength is an important factor to consider in high voltage applications as AC and DC breakdown analyses provide information about the maximum voltage a dielectric can withstand. By incrementally increasing the amplitude of the applied voltage across a dielectric, data can be obtained about the system which allows industry to preserve their operating systems and maintain safety. In addition to material flaws, attention should be directed at other factors which have an effect on breakdown strength, this includes the type of electrode used, the surface condition of the sample and the immersion medium. In the case of the thin film epoxy nanodielectrics being studied here, 6.3 mm spherical ball bearings were used and the breakdown strength per site was calculated by dividing the breakdown voltage by the local thickness of the insulator. As it is impossible to predict the exact voltage at which a system will breakdown, statistical analyses have been developed to estimate the probability of failure.

2.8.1 Two parameter Weibull analysis

A number of statistical methods are used to analyse electrical breakdown data, these include the two and three parameter Weibull distribution methods, both are commonly used for characterising the time to breakdown in solid insulation [96, 97]. In the case of the latter, the three parameter Weibull distribution includes the location parameter, τ_l, which serves to displace the distribution along the abscissa. There have been many comparisons between these two distributions [96, 98], most of which have concluded that the three-parameter Weibull distribution performs to provide a greater certainty for estimating parameters. However the simpler, two-parameter Weibull distribution can still be used to plot breakdown data that will reside within 90% confidence limits and this approach will be employed in this study [96].

Consider a sample of identical insulating systems which are subjected an electrical stress in the same environment with identical voltage conditions, regardless of the level of control over the conditions, the breakdown voltage of each sample will be different. It is not possible to determine the exact breakdown voltage of each system, but it is possible to calculate the probability that failure will occur within certain bounds,

$$P(x') = 1 - \exp\left[\left(\frac{V}{\alpha}\right)^{\beta}\right] \tag{2.30}$$

here x$'$ is the time to breakdown, V is the breakdown voltage, α is known as the scale parameter (or 'characteristic time to breakdown') that relates to the time at which $P(\alpha) = 1 - \frac{1}{e} = 0.6321$ and is analogous to the mean of a Gaussian distribution. The scale parameter acts to elongate the function along the abscissa. The β value is known as the shape parameter and determines the profile of the distribution. High values of β depict a narrow distribution of breakdown voltages, such that they are found to be within a similar range. Weibull data are frequently represented by rearranging equation 2.30 for equation 2.31 and plotting as a function of the log of the breakdown voltage, $\log_{10}(V)$.

$$\log_{10}\left\{-\ln\left[1 - P_w(x')\right]\right\} = \beta\left[\log_{10}(V) - \log_{10}(\alpha)\right] \tag{2.31}$$

Each data point is assigned a value of $P_w(x')$ which is calculated by Bernard's equation (equation 2.32), where i is the rank of the observation and N is the number of sites tested.

$$P_w(x')_{i,N} = \frac{(i - 0.3)}{(N + 0.4)} \tag{2.32}$$

The values of α and β values for this study are calculated via the 'maximum likelihood method' in Reliasoft Weibull++ software. The software takes partial derivatives of the likelihood function (with respect to parameters α and β) and sets the equation to zero. The estimated values for these parameters can be derived by solving for the unknowns simultaneously. The software is also able to calculate the confidence bands relate to the linear line plot. A mathematical description of the maximum likelihood method is described in Appendix A.

Within this study, the use of all above microscopic and spectroscopic techniques are used to probe the chemical and electrical properties of differently functionalised nanosilica and the nanodielectric systems prepared after their dispersion into epoxy. By doing so, it is hoped that methods can be perfected in the preparation of nanodielectric systems and further knowledge can be gained about the mechanisms at the interface which dictate nanodielectric traits.

2.9 Materials and preliminary investigations

The epoxy selected for this investigation is a two part system made from combining D.E.R 332 epoxy resin (Sigma Aldrich) with Jeffamine D-230 (Huntsman). Filled systems were prepared by functionalising amorphous nanosilicas (quoted particle size of 10 to 20 nm in diameter by Sigma-Aldrich) with various quantities of Silane z-6040 before introducing treated and untreated nanofillers into an epoxy matrix (at a 2 wt.% loading). As the preparation and production of nanocomposites is a far from trivial matter, preliminary studies were necessary to identify any difficulties which may be encountered.

2.9.1 Material quantities

The process for functionalising nanosilica was based upon the standard methods described by a number of authors [99, 100, 101, 102, 103]. In general, the nanofillers are functionalised in a solvent with the addition of a coupling agent; for example, Wang *et al* dispersed 5 g of nanosilica into 100 ml of ethanol solution containing 5% water (to aid hydrolysis) and acetic acid. The acid was added to control the rate at which the coupling agent condenses with itself, and to adjust the zeta potential to improve the stability of the colloidal system. To this solution, Wang *et al* added 50 ml of organosilane to functionalise the filler, which was left for 48 hours to allow surface modification to occur. The silica was washed thoroughly with fresh solvent before drying [99]. Following this method, preliminary studies were carried out using 200 mg of nanosilica in 5 ml of methanol. This solvent was chosen over ethanol as the boiling temperature is lower, therefore allowing the solvent to be removed more readily from the system (ethanol T_b = 78.4 °C, methanol T_b = 64.7 °C). The solution was ultrasonicated in a waterbath for 15 min to break up existing agglomerates and adjust the surface energy of the nanofiller [101]. As the degree of surface modification was the variable factor in this study, the optimum amount of coupling agent was first estimated in order to define the range of quantities explored in the functionalisation process.

The optimum quantity of coupling agent is often derived for surface modification to prevent sol-gel reactions, where an excess of organosilane can result in self-condensation and may prove disadvantageous if introduced into a polymer matrix system [101]. Conversely, if too little organosilane is added, the interactions at the nanofiller-matrix interface may not be at an optimum and weaker matrix bonding may result. Methods for estimating the optimum quantity of coupling agent has been published by a number of groups [61, 101, 104], however in this study the optimum amount of Silane z-6040 was calculated based on the particle size, density of the coupling agent and filler, and the length of the silane chains. Given the following ideal assumptions as factors,

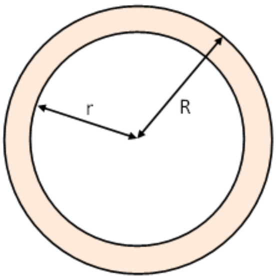

Nanoparticle radius, $r_{np} = 7.5 \text{ x } 10^{-9}$ m

Volume of nanoparticle, $V_{np} = \frac{4}{3}\pi r_{np}^3$

Density of nanoparticles, $\rho_{np} = 2.4 \text{ x } 10^6$ gm^{-3}

Length of Silane z-6040 chain, $l = 1.012 \text{ x } 10^{-9}$ m

Density of Silane z-6040, $\rho_{sz} = 1.07 \text{ x } 10^6$ gm^{-3}

Volume of silane layer around nanoparticle, $V_{sz} = \frac{4}{3}\pi(R_t^3 - r_{np}^3)$

Mass of Silane z-6040 needed to coat one nanoparticle, $m_s = (\rho_{sz})(V_{np})$

Number of nanoparticles in X g of nanosilica, $N_{np} = \frac{Xg}{(V_{np})(\rho_{np})}$

Mass of silane needed to coat X g of nanosilica, $M_s = \frac{(\rho_{sz})(V_{np})Xg}{(V_{np})(\rho_{np})}$.

The quantity of Silane z-6040 required for an optimal surface modification of 200 mg of nanosilica with average particle size 15 nm is calculated as 41 mg, this is *provided that* all nanoparticle agglomerations are dispersed before the functionalisation process occurs; i.e.; this calculated quantity of organosilane is for 200 mg of *isolated* nanosilica particles. Realistically, due to nanoparticle aggregation, one would expect this value to be much less.

The preliminary studies concluded that a number of changes needed to be made to the quantities of materials used. As the modification process involved leaving the solution for 48 h, the solvent had evaporated over this time; in samples containing an excess of coupling agent, the formation of a gel-like substance occured, which dried to form a solid layer of precipitate on top of settled nanosilica. This observation prompted two changes; firstly the nanoparticle solution should be kept in motion to keep the nanofiller in suspension to optimise the modification process, and secondly, washing is a vital part of the functionlisation process that must be carried out to remove any excess coupling agent. It was also found that the washing process saw significant filler mass losses, where the nanosilica was poured away as the solvent was decanted; it was decided that the mass of the nanosilica and coupling agent should be quadrupled such that 800 mg of nanosilica and 164 mg of Silane z-6040 were used per sample. All other chemical components would be scaled accordingly and a centrifuge would be employed to separate the solids from solvent to limit the amount of nanosilica lost.

2.9.2 The mixing method

The epoxy nanocomposite systems were prepared using methods developed by Reading *et al*, where factors such as the stoichiometry, curing temperature and curing time were determined [105, 106]. Their studies investigated a number of different mixing methods, which led to various effects on the filler dispersion; they concluded that, although mechanical mixing and ultrasonication were suitable for micro-based composites, the electrostatic forces associated with nanosized particulates proved to compete with standard mixing methods and therefore were not as successful in providing reasonable level of dispersion. In the preliminary studies, nanosilica was dispersed in D.E.R 332 resin via three mixing methods, magnetic mixing, ultrasonication in a waterbath and sonication via a probe. The mixtures were processed for 80 min and monitored every 10 min to observe the dispersion state of the filler. After 80 min of processing, samples processed via magnetic mixing and water bath ultrasonication still possessed visible agglomerates of filler and were therefore discarded. The specimen processed with the sonication probe was seen to be characterised by a noticeable improvement in its dispersion state after 30 min, however, there was an evident colour change seen in the resin.

To address the colour change in the resin, unfilled epoxy samples were sonicated for 80 minutes and observed at 10 minute intervals. Some authors have expressed caution when using probe sonicators as the energy focused at the tip of the probe has the potential to generate temperatures up to 100 °C [50], therefore an initial suggestion for the 'yellowing' of the epoxy resin was attributed to thermal degradation. Several resin samples of equal quantity were heated in an oven at 150 °C to induce resin colouring, the specimens were checked every 10 minutes for 80 minutes but no colour changes occured. A second suggestion was that the colour change is a product of conjugate bonds, where enough energy may be transferred from the probe into the resin system and break existing bonds to form alternating single and double bonds. The separation between ground states and excited states is smaller for conjugated bonds, therefore light of a shorter wavelength is absorbed and reflected from the sample; the colour observed by the viewer is dependent upon the number of conjugated bonds in the system [107]. The third possible expla-

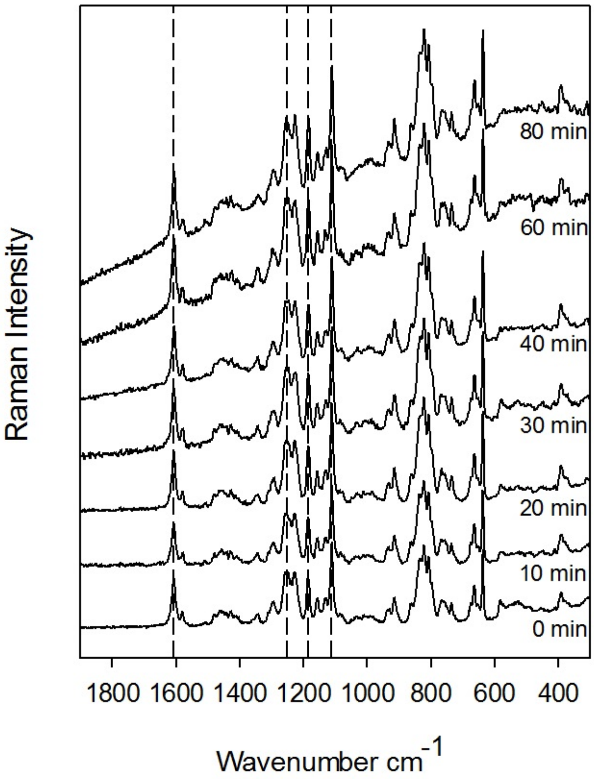

Figure 2.10: Raman spectra from epoxy resin sonicated for different durations.

nation for the discolouration was that the epoxy resin was oxidised via sonication. The instantaneous cavitation of the system caused by the probe disrupts the oxygen in the resin, or may react with oxygen from the surrounding environment which leads to the colour change. To test these concepts the sonicated samples were subjected to Raman spectroscopy; upon analysing the Raman data, there were no observable peaks that would indicate additional double carbon bonds in the system, or any spectral changes in relation to oxygen. However fluorescence was clearly observed in samples sonicated for over 40 minutes. The presence of fluorescence is a result of ageing in samples where there is the production of chromophores with increasing sonication time, this is most likely to be a product of both thermal ageing and oxidation.

2.9.3 Sonication time

The sonication time was decided from scanning electron microscopy images of cured sample systems where the filler had been sonicated for 30, 40 and 60 minutes, as seen in Figure 2.11. The brighter ‘spots’ in each image represent the nanofiller; the topographic contrast is dependent upon the yield of secondary electrons from the sample. The geometry of raised surfaces allow for a greater secondary electron emission as the distance from the interaction volume to the sample surface are generally less, increasing the likelihood for secondary electrons to escape. Unfilled regions are represented by darker, grey areas which are seen to be smooth and with few fractography features. The preliminary studies showed that the filled epoxy systems contained regions which were more densely filled than others, regardless of the sonication time. The red circles highlight the region in which nanofiller cannot be observed. Although the dispersion of the filler seems reasonable at a low magnification, at high magnifications, it becomes more apparent that the filler has aggregated to form agglomerates greater than 100 nm in size. The aggregates in the sample sonicated for 30 min are on order of 300 to 400 nm, where 10 min of further sonication reduces the average agglomerate size to 180 to 315 nm. After 60 min of sonication, the particle agglomerations are seen to measure on order of 200 to 330 nm, whilst the dispersion state is seen to be more homogeneous than the samples which had been sonicated for 30 or 40 min.

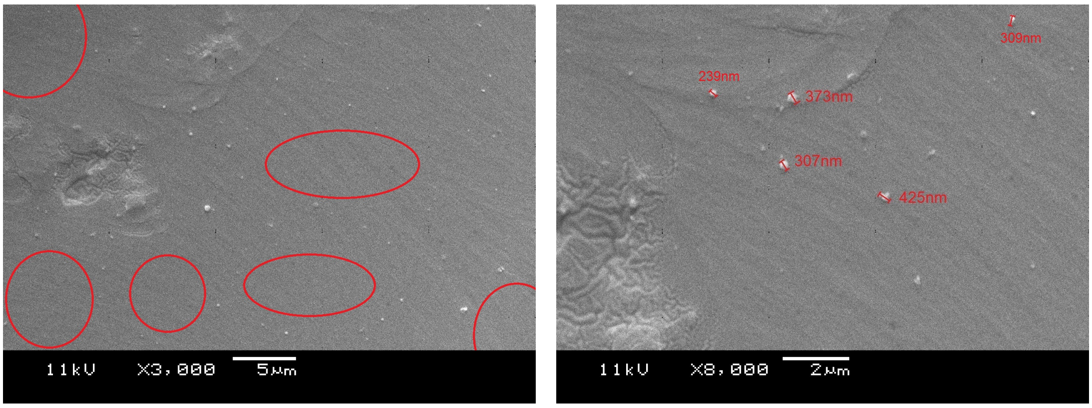

(a) Epoxy containing nanosilica after 30 min of sonication, low magnification.

(b) Nanosilica dispersion in epoxy after 30 min of sonication, high magnification.

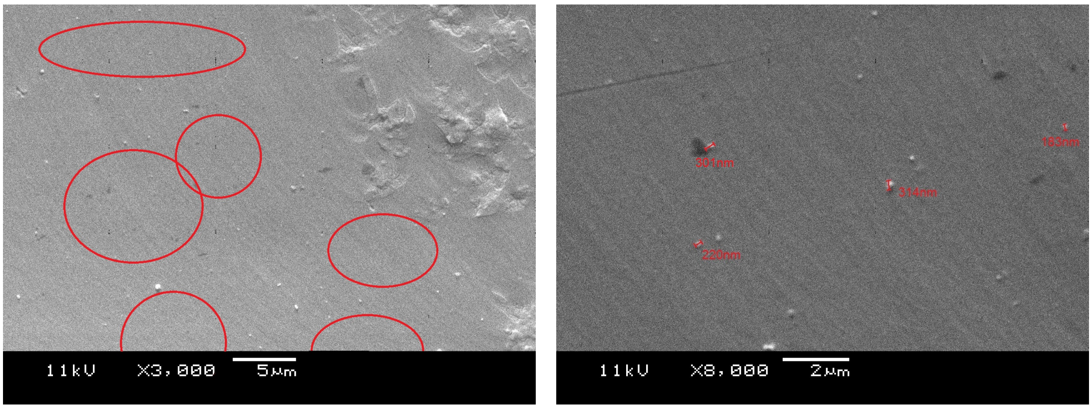

(c) Nanosilica dispersion in epoxy after 40 min of sonication, low magnification.

(d) Degree of nanosilica dispersion in epoxy after 40 min of sonication, high magnification.

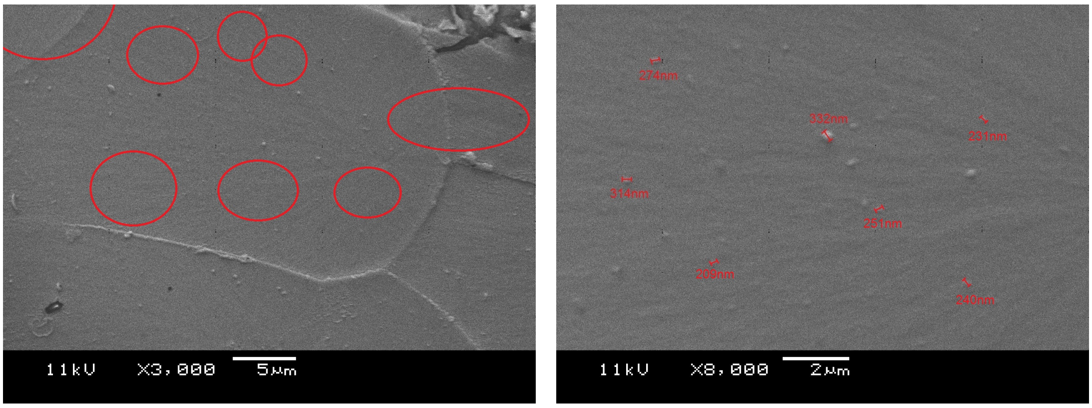

(e) Nanosilica dispersion in epoxy after 60 min of sonication, low magnification.

(f) Degree of nanosilica dispersion in epoxy after 60 min of sonication, high magnification.

Figure 2.11: Scanning electron micrographs of nanosilica sonicated into epoxy for 30, 40 and 60 minutes to analyse dispersion.

Figure 2.12(a) is a typical representation from the sample containing nanosilica sonicated for 40 minutes. The area in the bottom left of the image contains no observable filling phases, although there are regions within the bulk which show a dense population of nanofiller; confirming the inhomogeneity of the system. The images show how the agglomerates contribute to mechanical weakening and cause the films to fracture differently at these sites (yellow arrows). The black arrow shows an impurity that has cured in the resin. Further images for cured samples where the resin and nanoparticles were sonicated for 30, 40 and 60 minutes are available in Appendix B.

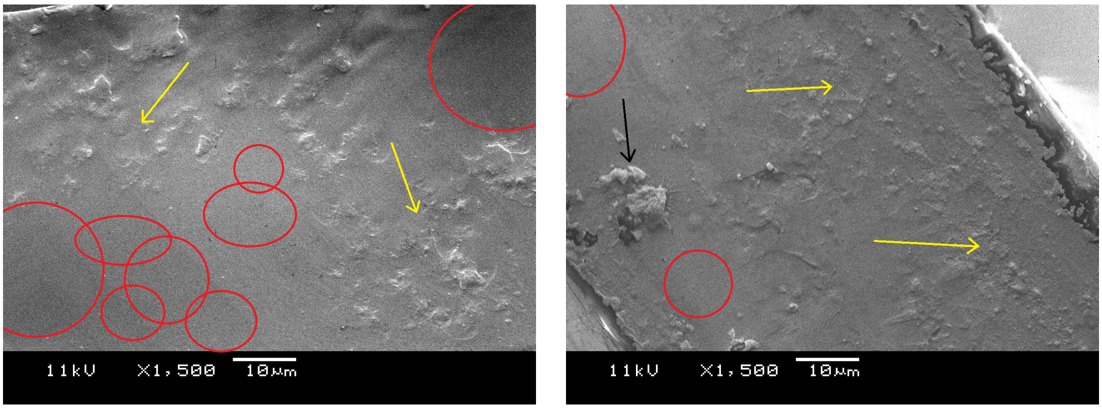

(a) Nanosilica dispersion (40 min of sonication). (b) Nanosilica dispersion (60 min of sonication).

Figure 2.12: SEM images of epoxy samples after 40 and 60 min of sonication representing fracture features in agglomerated regions.

2.9.4 The use of solvents in the sonication process

To prevent the degradation of the resin, some groups pre-disperse their functionalised nanofiller in solvent before dispersing the whole solvent system into the epoxy resin; this acts to stabilse the system temperature and decreases viscosity to promotes nanofiller dispersion [108, 109]. The epoxy resin (5.58 g) was combined with three solvents, methanol, acetone and diethyl ether (5 ml). The latter two solvents were seen to readily dissolve the epoxy resin, however there was a clear separation of components between the resin and methanol despite rigorous stirring and was therefore discarded. The remaining two epoxy samples were sonicated for 60 minutes. The solvent was expected to evaporate from the system, however FTIR spectra obtained from these systems show otherwise.

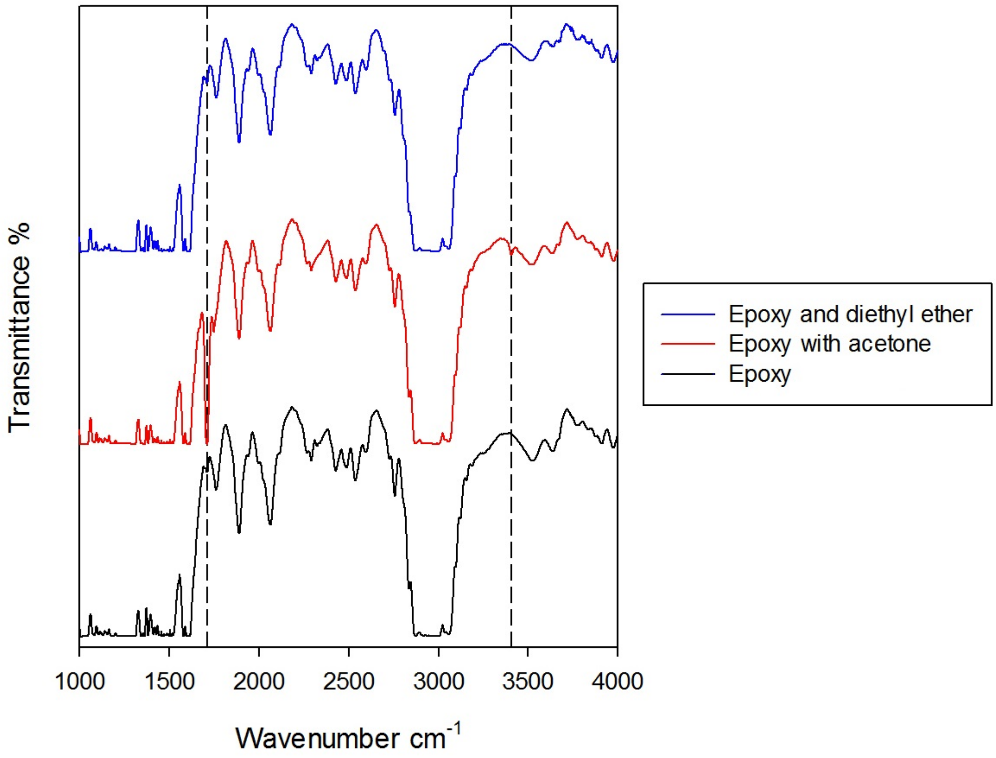

Figure 2.13: FTIR spectra obtained from epoxy resins mixed with and without solvent.

Figure 2.13 compares the spectra acquired from epoxy that had been sonicated for 60 min with diethyl ether, acetone and without solvent. Additional peaks in the epoxy resin-acetone sample is observed, markedly the peak at 1711 cm^{-1} which is a characteristic of C=O stretching bonds present in ketones [110] and is a clear indication that solvent remains in the system. Similarly, Figure 2.14 shows a small addition to the epoxy resin-diethyl ether spectra at 1110 cm^{-1}, which results from the C-O-C ether linkage in the solvent [110].

2.9.5 Preliminary studies summary

The preliminary studies completed in this section were vital for the successful preparation of nanocomposite samples; from them, the quantities of materials originally used have been increased by four-fold. Whilst mechanical mixing and sonication via a water-bath were considered unsuitable for the dispersion of nanofiller into an epoxy matrix, it was decided that 60 min of probe ultrasonication was the most efficient option for nanofiller dispersion. Although the aggregation sizes here were observed to be greater in size than 40 min of sonication, the dispersion state was seen to be more homogeneous. In addition to this, a decision was made that no solvent should be used to aid nanofiller mixing as the solvent could not be fully removed from the system, as shown by FTIR studies.

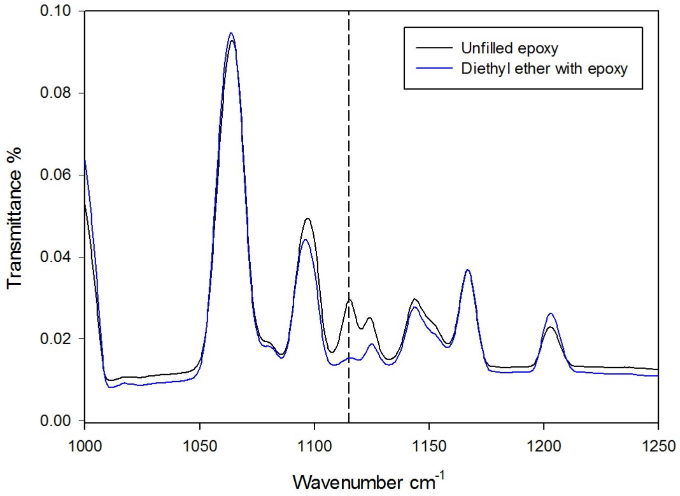

Figure 2.14: FTIR spectra obtained from pure epoxy resin and epoxy resin mixed with diethyl ether.

Chapter 3

Silica-epoxy nanodielectrics

Epoxy based materials have become a staple in the electrical insulation industry. The last 50 years has seen extensive research in developing epoxy-based composites which contain fillers of various types and sizes, the increased interest in nanocomposite materials has meant that a new generation of epoxy composites have become available for use. As discussed in previous chapters, a homogeneous dispersion of nanofiller in a polymer matrix is of great importance; for this reason, a number of groups have invested time and capital in investigating the use of coupling agents to promote bonding between the two phases, which is believed to increase material efficiency. Many authors typically calculate an optimum quantity of coupling agent required to functionalise a specific mass of filler, however there are few detailed studies which systematically vary this critical element in dielectric systems [111]. This chapter uses a range of spectroscopic techniques to quantitatively characterise the functionalised interface and study its effects on the chemical and electrical properties after dispersion into epoxy systems.

3.1 Functionalisation of nanosilica (using methanol)

The process of functionalisation is a common procedure in which an organofunctional surface reactant is used to functionalise the surface of a mineral substrate, the surface modification results in a greater adhesion to organic polymer matrices and promotes filler dispersion in the matrix [112].

Equation 3.1 represents the chemical formula for a typical organosilane.

$$R'_n \ \mathrm{SiY}_{(n-1)} \tag{3.1}$$

where, Y is a hydrolysable group (e.g. an alkoxy, chlorine or amine) which is involved in reactions with the inorganic substrate. The R' functional group is a non-hydrolysable organic moiety that allows a coupling agent to react with organic groups within the matrix.

In the case of this study, Silane z-6040 is the chosen coupling agent; the R' moiety represents $(CH_2)_3OCH_2CH(O)CH_2$, whilst the Y functional group represents a methoxy group OCH_3. This organosilane was chosen for the epoxide group at the end of R' because of its compatibility and reactivity with the amine hardener, Jeffamine D-230. Although the surface chemistry of nanofillers can be modified with the use of an anhydrous solvent (discussed later in Chapter 4), this Chapter will focus on the use of hydrous solvents in the chemical process. Hydrous functionalisation reactions involving organosilanes occur in the four stages as described below, these images are redrawn from Gelest Inc [112];

- **Hydrolysis** - The moisture in the system, either present on the surface of the substrate or available within the system, lends itself to the hydrolysis of the methoxy groups of the organosilane. This forms monomers with reactive silanol groups that react in the next stage of the process. The degree of hydrolysis can be controlled by the amount of water in the system and therefore some studies add water to their organosilane solutions to accelerate this part of the process [101].

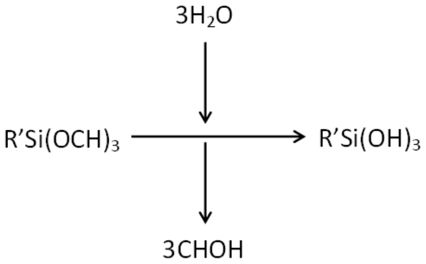

FIGURE 3.1: Hydrolysis of OCH_3 with moisture obtained from the evnironment (or added in).

- **Condensation reactions** - The resultant monomers undergo condensation reactions to form chains of oligomers. As this process is sensitive to the pH of the system, some studies adjust the pH of the solution with the use of an acid to control condensation reactions within the system [104, 99]. The water by-products formed in this process will contribute to the hydrolysis stage of the functionalisation process.

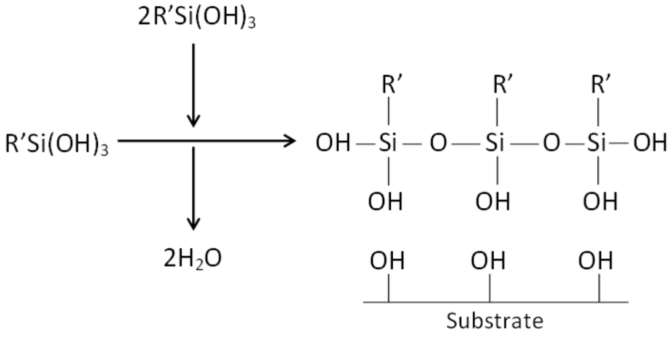

Figure 3.2: Condensation of $RSi(OH)_3$ monomers.

- **Hydrogen bonding** - Hydrogen bonding takes place between the hydroxyl groups on the substrate surface and organosilane. These bonds are weaker than covalent bonds and therefore drying is required.

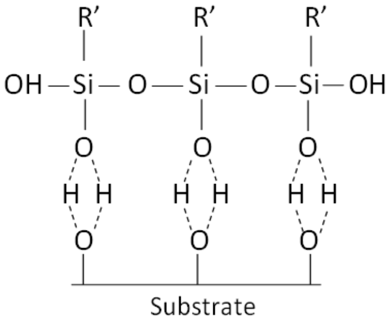

Figure 3.3: Hydrogen bonding between the organosilane oligomers and the substrate surface.

It is important to note that although the condensation of the organosilane monomers are often depicted as a linear structures [113, 112], it is possible for these chains to form with different configurations, where the trifunctionality of the organosilane may result in branched networks of coupling agent. This will act to change the thickness of the organosilane layer and may affect the overall nanocomposite properties.

- **Bond formation** - Finally, the solution is dried and covalent bonds form as moisture is removed from the system. The coupling agent bonds directly to the substrate via covalent bonding; typically one silicon atom in the organosilane will bond with one oxygen on the surface, this leaves the remaining silanol moieties to either bond other silanol groups or continue in free-form [112].

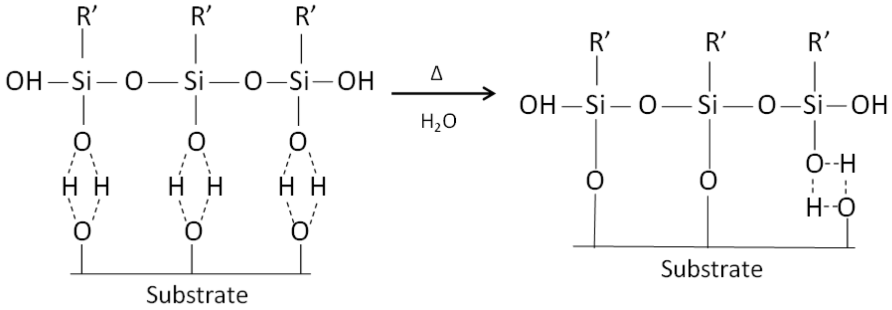

FIGURE 3.4: Drying, evaporating the solvent results in covalent bonds between organosilane and substrate surface.

This investigation studies epoxy composite systems which contain differently functionalised nanosilicas (Sigma Aldrich, quoted particle size of 10 to 20 nm). To prepare the samples, eight 800 mg nanosilica specimens were ultrasonicated in a 25 ml solution of methanol and acetic acid to break up existing agglomerates. The acid was added to the solvent to lower the pH of the system to 4 [99], this adjusted the zeta potential to promote stability within the colloidal system [101, 103] and control the condensation reactions that occur in the functionalisation process. For 800 mg of nanosilica, the optimum quantity of Silane z-6040 was calculated to be 164 mg; therefore the coupling agent was added in various quantities of 0 mg, 100 mg, 200 mg, 400 mg, 800 mg, 1600 mg and 2000 mg, which are quantities above and below the optimum amount. The samples were shaken vigorously for 46 h to ensure the nanosilica did not precipitate and allow the coupling agent to bind to the silica. Following this, the suspension was centrifuged and washed five times with methanol to remove any excess coupling agent. The samples were dried in an oven under vacuum at 40 °C for 10 days [45, 114].

3.2 Preparation of nanosilica-epoxy systems

Epoxy systems with 2 wt.% filler loading were produced by dispersing 150 mg of dried, functionalised nanosilica into 5.58 g of D.E.R 332 epoxy resin by the means of probe sonication. The probe was set to pulse at 0.7 s for an hour, where the pulsing was chosen to reduce the degradation that occurs due to the high energy from the probe. Furthermore the system was kept in a water bath which was renewed with cold water every 15 min to keep the system cool. The stoichiometry for these particular epoxy systems were earlier determined by Reading *et al* [115, 116, 117], where the optimal stoichiometric ratio was found to be 1000 parts resin to 344 parts hardener. This parameter is an important factor as a balance between the two parts is required to provide the most efficient performance [89]. For a stoichiometric ratio of 1000:344, 1.92 g of Jeffamine D-230 hardener (Huntsman) was added to the resin mixture and magnetically mixed into the system for 15 min before 15 min of degassing. The epoxy was poured into a pre-made mould, seen in Figure 3.5, with a 70 µm Melinex spacer and cured at 100 °C for 4 h. The resultant samples were air free epoxy films that measured 70 µm ± 10 µm in thickness. To ensure the epoxy could be removed easily, QZ-13 release agent (Resins-Online) was used to coat the moulds (wiped on and wiped off) before the mixture was poured in. The epoxy was made in accordance with studies completed by Reading *et al* [105, 115].

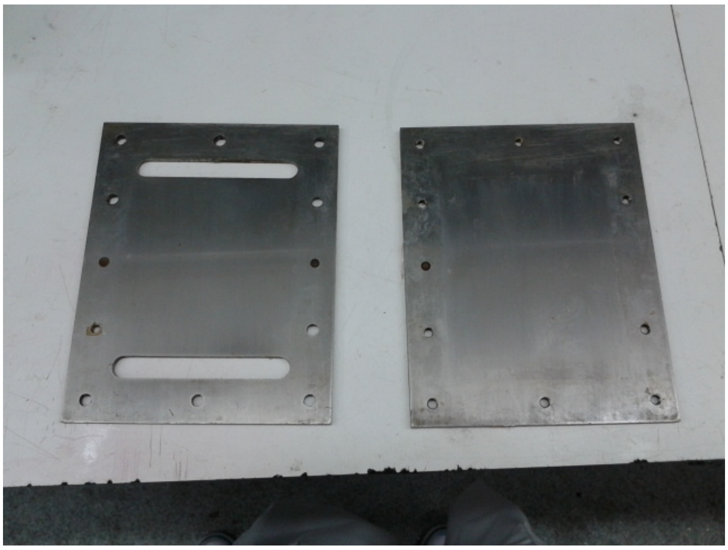

FIGURE 3.5: Gauge steel mould plates used for nanocomposite curing.

The functionalised nanosilica powders and the silica-epoxy nanocomposites prepared via the above methods have been designated the following names for use in the remainder of this thesis.

Sample	Silane (mg/800 mg silica)	Epoxy nanocomposite sample
M0	0.0	EM0
M1	100.0	EM1
M2	200.0	EM2
M4	400.0	EM4
M8	800.0	EM8
M16	1600.0	EM16
M20	2000.0	EM20

Table 3.1: Sample codes for nanosilica and nanocomposite systems with different degrees of functionalisation.

3.3 Methodology

3.3.1 Raman spectroscopy

Raman analysis of nanosilica powders were carried out using a Renishaw Raman RM1000 spectrometer. The system is coupled with a Leica microscope and a 785 nm continuous-wave diode laser light source, with maximum operating power of 25 mW. The spectrometer houses a holographic grating of 1800 mm^{-1} and a holographic (notch) filter to prevent the backscattered Rayleigh radiation from reaching the system's Peltier-cooled CCD detector. The spectrometer was set up in line with Renishaw recommendations for the non-confocal operation of the instrument. The system was adjusted to have a slit width of 50 µm and a CCD area of 20 pixels (image height) x 574 pixels (spectrometer range). Spectra were collected from the nanosilica samples which prepared by cold-pressing dry nanopowders in a Graseby Specac press at 5 tons. Spectra from each compacted disc-shaped sample were generated by integrating one hundred 10 s accumulations.

3.3.2 Fourier transform infrared spectroscopy

Infrared spectroscopy is often employed to detect changes in surface chemistry after functionalisation [118, 119, 120]. Typically, infrared spectrometers obtain data from their sample(s) by analysing light that is transmitted through the sample, however for thicker or opaque specimens, attenuated total internal reflectance infrared spectroscopy (ATR-FTIR) may be used. In this technique, the infrared beam is directed into a parallel sided crystal (usually germanium or diamond) that is in contact with the sample. The crystal must have a relatively high refractive index, one which is greater than the specimen to allow for total internal reflection; this results in an evanescent wave which penetrates small parts of the sample that is in direct contact with the crystal. The reflected light is collected by a detector, where the data are output as infrared spectra.

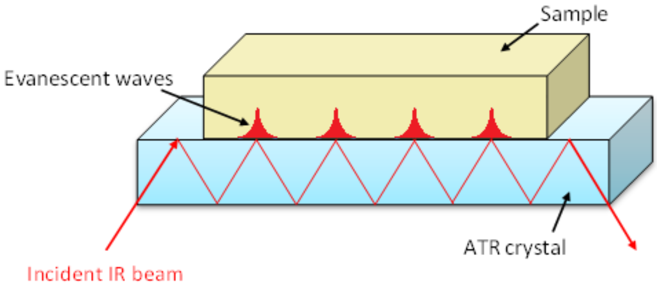

FIGURE 3.6: Schematic of the internal process within an ATR attachment.

ATR-FTIR spectroscopy may be a preferred technique in collecting infrared data as methods involving oils (such as a Nujol mull) may act to mask the spectrum of the nanopowder. ATR-FTIR also has the benefit of the powder being held in good contact with the crystal, the pressure applied helps improve the signal-to-noise ratio as air is removed [121, 122]. This investigation used a Thermo Nicolet 380 FTIR spectrometer combined with a Golden Gate single reflection diamond attenuated total reflectance attachment. Spectral data were acquired from the functionalised nanosilica powders for wavenumbers ranging from 4000 to 400 cm^{-1} over 32 scans at 4 cm^{-1} resolution. A background scan with no sample in the spectrometer was acquired before sample scans for calibration purposes. The spectrometer was operated in reflectance mode.

3.3.3 Scanning electron microscopy

Scanning electron microscopy was used to observe the degree to which the nanosilica was dispersed in the epoxy matrix. Specimens were prepared via a cryo-fracturing method, where the epoxy systems were cooled in liquid nitrogen for 15 minutes before they were fractured. This method is often used to reveal the characteristics of the specimen within the bulk, cooling the sample causes the films to become brittle and allow the sample to be broken cleanly. Without this step, the flexibility of the films would cause stresses in the bulk that causes it to tear in an undesirable manner and affect the way in which the nanofiller would be observed. The samples were gold coated with an Emitech K550X sputter coater to improve the conductivity of the sample and examined using a JEOL JSM 5910 scanning electron microscope with an accelerating voltage of 15 to 18 kV.

3.3.4 Differential scanning calorimetry

Differential scanning calorimetry measurements were obtained using a Perkin Elmer DSC 7, controlled by Perkin Elmer Pyris analysis software. An analyser unit regulates the main instrument temperature whilst an adjoining chilling system keeps the DSC head at a stable background temperature of 20 °C. The instrument was calibrated before use using indium (of known $T_m = 156.6$ °C [89]). The starting temperature for calibration was set to 140 °C and rose at 10 °C min^{-1} to 170 °C.

Approximately 5 mg of each nanocomposite was weighed, placed into aluminium cans of similar weight and sealed with an aluminium lid. Cans (and lids) were chosen such that their total weights were similar to a reference to allow for a baseline subtraction after the sample data were acquired. The specimens were heated from 50 to 120 °C at a rate of 10 °C min^{-1} before being cooled rapidly to 30 °C. The data obtained from the first acquisition of epoxies were discarded to remove the thermal history of the polymer [89]; a second acquisition was obtained at the same heating and cooling rates. The data from the DSC of two empty cans (sealed and of similar weight ± 0.05 mg) were subtracted from the sample data to remove the instrumental baseline.

3.3.5 AC electrical breakdown

The epoxy films were subjected to AC breakdown testing, where the thickness of twenty random sites on the film were recorded. Each of these sites was positioned between two 6.3 mm spherical ball bearing electrodes held by a purpose built cell (Figure 3.7) that fulfills the ASTM D149 standard [123]. The samples were submerged in silicone oil to prevent surface flashover and the oil was filtered every two days to avoid dust and dirt contaminating the system. The sites were subjected to an AC voltage which increased linearly at a ramp rate of 50 Vs^{-1} until system failure. The ball bearings were replaced with new ones every eight tests to ensure they remained unpitted; pitting of the ball bearings results in a change of geometry of the electrodes and alters the local electric field. This method closely follows the technique executed by Reading and Mills [8, 124].

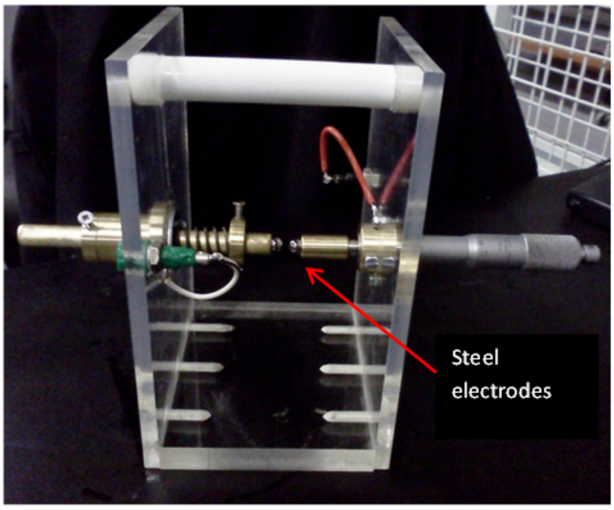

Figure 3.7: Electrical breakdown test cell built in line with the ASTM D149 standard, for use with AC voltage.

The AC breakdown voltage for each site was recorded and used to calculate the associated breakdown field. Reliasoft Weibull ++ software was used to apply mathematical operations on these values (Appendix A). The α and β values for the two parameter Weibull distribution were found for each nanocomposite system, along with 90% confidence bands for the data set.

3.3.6 Dielectric spectroscopy

Dielectric spectra were obtained used a Solatron 1296 dielectric interface coupled with a Schlumberger SI 1260 impedance/phase gain analyser; the system was controlled by Impedance software provided by Solatron Analytical. Samples were dried under vacuum at 40°C for 14 days before the dielectric films were placed in a custom made cell, complete with heating element to raise the temperature of the environment and sample. The cell shields the sample from external electrical noise in the range 10^{-2} to 10^{6} Hz [124]. However as data below 10^{-1} Hz took a long time to collect, and the data above 10^{5} Hz proved to possess a poor signal-to-noise ratio, a sinusoidal voltage of 1 V (RMS amplitude) was applied across the sample at frequencies ranging from 10^{-1} to 10^{5} Hz. Data were integrated over 10 cycles at 8 points per decade [8]. The process was completed for the following temperatures, 20 °C, 40 °C, 60 °C, 80 °C and 100 °C to investigate the molecular mobility of the system with increasing thermal energy. The cell and sample were held at each temperature for approximately 20 minutes before data were obtained, this was done to reduce the temperature fluctuations in the sample environment by allowing it to stabilise.

3.4 Quantifying the functionalisation state of nanosilica

The analysis of Raman and Fourier transform infrared spectra are often used to confirm the presence of coupling agents on the surface of nanofillers, where surface modification results in the addition of, or an increased intensity, of spectral peaks [33, 125, 126, 127, 128]. Figure 3.8 shows Raman spectra collected from unfunctionalised and functionalised nanosilica. The data here have been normalised with respect to the feature at 530 cm^{-1} which corresponds to Si-O bending [129, 130]. Raman systems have a sensitivity that allows the equipment to detect chemical groups which make up as little as 0.1% of the total sample; as Silane z-6040 contains epoxide groups and SiO_3 bonds, spectral peaks at 910 cm^{-1}, 1250 cm^{-1} and 635 cm^{-1} (corresponding to asymmetric ring deformation, C-O stretching and SiO_3 [131, 132, 133]) were expected to appear with increasing surface functionalisation. However, the spectra from Figure 3.8 clearly shows no evidence of these peaks; as other groups have been able to identify the surface modification of nanosilica using organosilanes, the data presented here is an indication that there is an insufficient organosilane in the system for detection. This could be a product of two things; firstly, the existence of nanosilica aggregates in functionalising solution would provide a smaller surface area for the organosilane to graft onto (therefore less organosilane exists in the system), and secondly, even if a certain degree of dispersion in the solvent may be reached (via ultrasonication), the centrifuging and drying processes will cause the silica to agglomerate (there may be coupling agent inaccessible for the Raman spectrometer to detect).

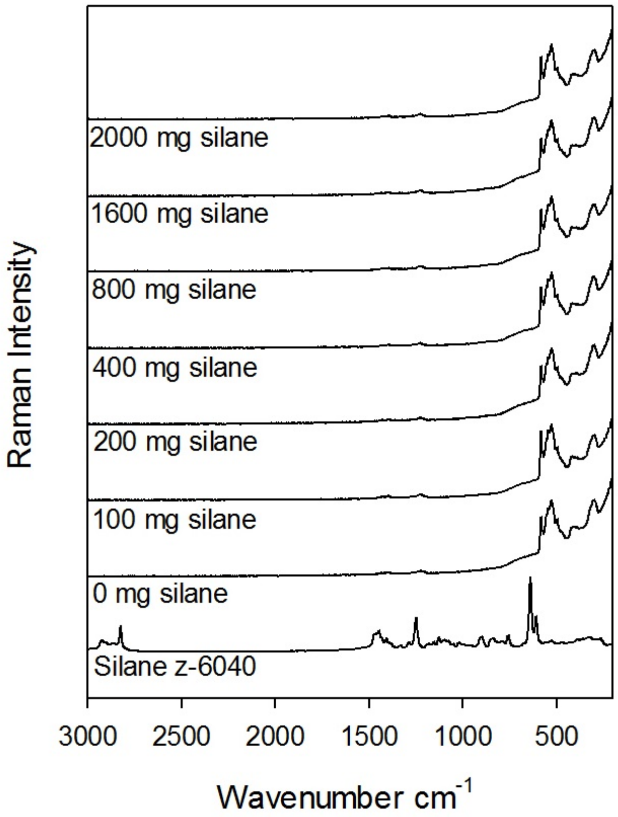

Figure 3.8: Raman spectra of nanopowders functionalised to different degrees with Silane z-6040.

The Raman spectra from the nanosilica is also non-comparable to other amorphous nanosilicas published in the literature [125], therefore the chemical composition of the filler was examined using energy dispersive X-ray spectroscopy (EDX), Figure 3.9, which confirmed the sample was primarily composed of silicon and oxygen. The product from

Sigma Aldrich is quoted to be of an amorphous nature, however as few systems are purely amorphous, the obtained spectra are assumed to be a product of various silica crystallinities that may exist in the system. The general rise in intensity from 800 cm^{-1} to 600 cm^{-1} resembles the beginning of a broad peak seen in amorphous silica [134], whilst peaks at 580 cm^{-1} and 450 to 550 cm^{-1} correspond to the bending of Si-O and vibration of Si-O-Si in crystalline forms of silica (respectively) [129, 135].

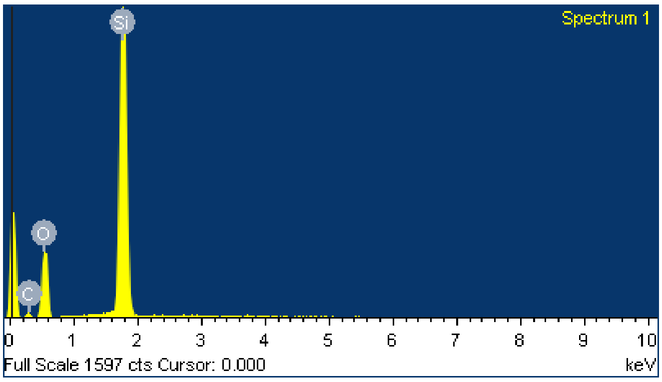

Figure 3.9: EDX analysis for untreated amorphous nanosilica obtained from Sigma-Aldrich.

As Raman spectra were unable to confirm the surface modification of the nanosilica with Silane z-6040, Fourier transform infrared spectroscopy was employed. This method of spectroscopy has been used by many groups to confirm the surface modification of their nanofillers after a functionalisation process [33, 43, 126, 127, 128, 136]. Specifically, Chen *et al* and Sideridou *et al* show how the stretching vibration of C=O can be observed in FTIR spectra from methacryloxypropltrimethoxysilane (MAPTS) on nanosilica particles [120, 137]. The infrared data shown in Figure 3.10 were collected from untreated and treated nanosilica samples, the characteristic peaks at 1200 to 1000 cm^{-1}, 805 cm^{-1} and 471 cm^{-1} represent asymmetric Si-O-Si stretching, SiO_4 tetrahedron ring and O-Si-O deformation respectively [120]. As the main component of each sample is composed of Si-O bonds, the spectra were normalised with respect to the peak around 1100 cm^{-1} as any changes are considered negligible. Although published research has shown that glycidoxypropyltrimethoxysilane (GPTS) can be successfully detected via this method, the infrared spectra in Figure 3.10 shows no addition of spectral peaks that are representative of epoxide rings at 1250 cm^{-1} [110, 131, 133] or CH_2 bonds between 2850 to 3000

cm^{-1} which are associated with the organosilane backbone [138, 139]. This supports the fact that despite sonication and functionalisation, agglomerates will still exist during the functionalisation and from drying processes which leads to smaller quantities of coupling agent present (or accessible) for detection on the nanosilica systems. A study by Lau *et al* who use a similar functionalisation processes also show present comparable data, where epoxide groups or CH_2 bonds are not present in FTIR data [140].

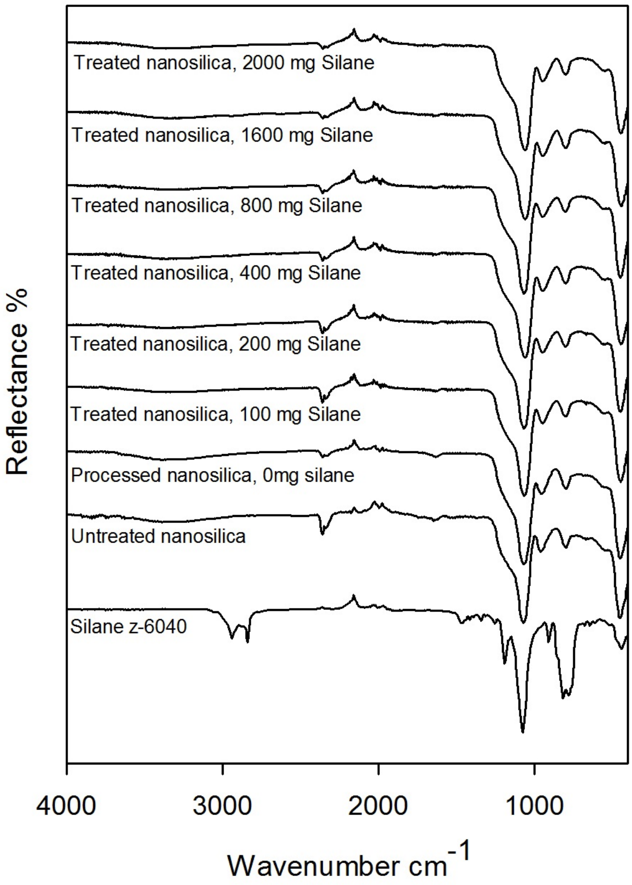

FIGURE 3.10: IR spectra obtained from nanosilica samples.

Despite this, there are differences in the hydroxyl peak at 3000 to 3700 cm^{-1} between samples which have and have not been processed. This feature is seen to possess a decreased intensity for samples which have been modified with the use of organosilane. Integrating the peak area shows a 44% decrease between M0 and M1, and a 63% decrease between M0 and M2 which indirectly confirms that the hydroxyl groups on the nanosilica surface have been replaced by Silane z-6040 chains. However, for samples modified with an excess quantity of Silane z-6040 (from samples M4), the decrease in the peak intensity falls to 30 to 50% which suggests that condensed organosilane networks may be geometrically unfavourable and 'block' the organosilane chains from bonding directly to the hydroxyl groups on the nanofiller surface. The peak is not completely eliminated from the spectra, regardless of the quantity of coupling agent used in the modification process which indicates that there may still be hydroxyl sites on the silica surface, as seen in Figure 3.11.

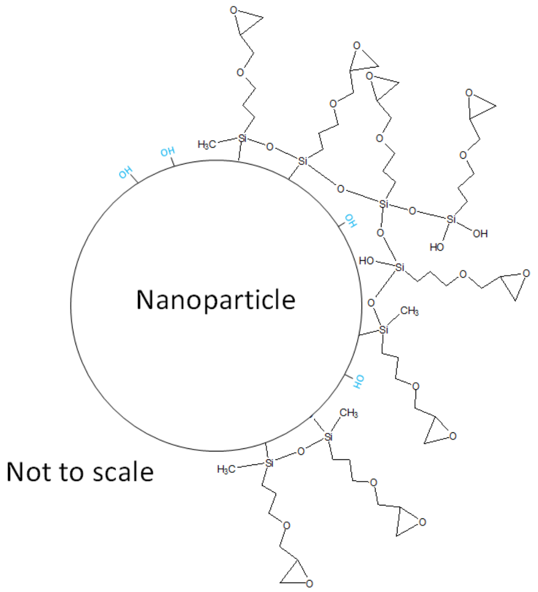

FIGURE 3.11: Condensation reactions on nanosilica.

As the coupling agent was not directly detected via either of the two spectroscopic techniques above, a range of samples were sent to Medac Ltd for combustion analysis. Combustion analysis determines the elemental fractions of carbon and hydrogen in the sample systems. For the nanosilica sample that was processed in solvent but without coupling agent (M0), the quantities of carbon and hydrogen show a negligible difference to that which was obtained directly from the supplier (untreated). This is to be expected, as no surface modification has taken place on the nanosilica of M0. The percentage content of carbon was, however, seen to increase for samples M4 and M20; as carbon is present in the backbone chain of Silane z-6040 an increase was expected with respect to the quantity of coupling agent used to modify the nanofiller. As each carbon atom in the organosilane backbone will be bonded to at least two hydrogen atoms, it is reasonable to assume the hydrogen content will always be higher. In samples which have been unfunctionalised, there will be additional hydrogen atoms from the hydroxyl groups contributing to the percentage content as they have not been replaced at the silica surface.

For samples which have been processed with an excess of coupling agent, the organosilane is expected to condense into networks which increase the quantity of carbon detected.

Medac Ltd state there is a ±0.3% uncertainty in their combustion analysis tests and therefore the carbon data from M4 and M20 fall within this uncertainty and supports the fact that the networks of organosilanes will have an effect on the carbon-hydrogen ratio within the system (as seen in Figure 4.3). This increased detection of carbon also suggests that although agglomerates exist pre-functionalisation, the use of an untrasonicator disperses the aggregates sufficiently for a degree of surface modification to occur; however, this is not at optimum and is still below the quantity required for Raman and FTIR detection.

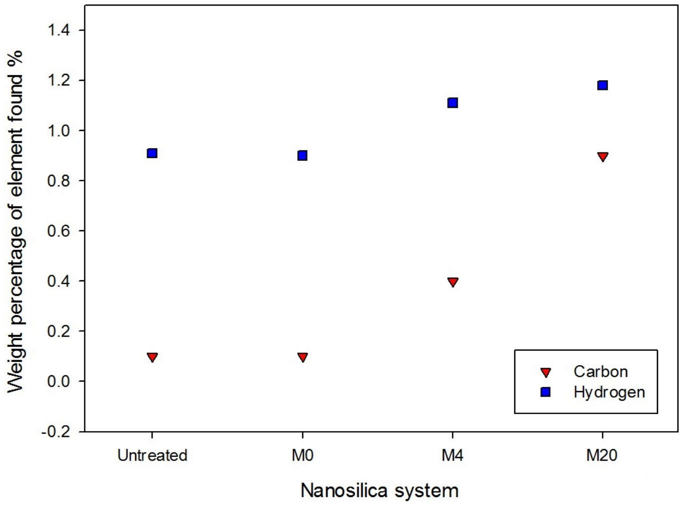

FIGURE 3.12: Data obtained from combustion analysis of functionalised nanosilicas.

3.5 Quantifying the degree of nanosilica dispersion in epoxy

The dispersion states of the nanofiller in the various nanocomposite systems were analysed by scanning electron microscopy. The section of this thesis on the preliminary studies for samples preparation included SEM images obtained with the JEOL JSM-5910 system (described in Section 3.3.3); although these images were successful in showing fractography features (Figure 2.11), this instrument was unable to obtain images of high resolution as required for this study. Field emission gun scanning electron microscopy (FEG-SEM) was therefore employed as an alternative. The resolution of such systems is far greater than typical scanning electron microscopes, due to the characteristics of the different emission sources. SEM systems such as the JEOL JSM-5910 house a tungsten

(W) filament that produces electrons via thermionic emission, the images obtained are of a lower resolution than FEG-SEM systems as the heat causes thermal drifting of the electrons. FEG-SEMs house cold cathode emitters where electrons are emitted from a sharpened tungsten tip with the application of electrical potential (on order of 100 nm in size). The geometry of this tip results in an electron beam of a smaller diameter which makes it possible to obtain images with a greater resolution [141]. The fractography in epoxies has been well established, where numerous papers have discussed the fracture features in different epoxy nanocomposite materials [142, 143, 144]. The following SEM images were obtained using a JEOL FEG-SEM 6500F system, where Figure 3.13 shows how the texture of virgin epoxy is smooth with accordance to its amorphous structure. The blue arrow represents the direction propagational force that was used to fracture the film, this is also highlighted by the direction of the grain in the fractography.

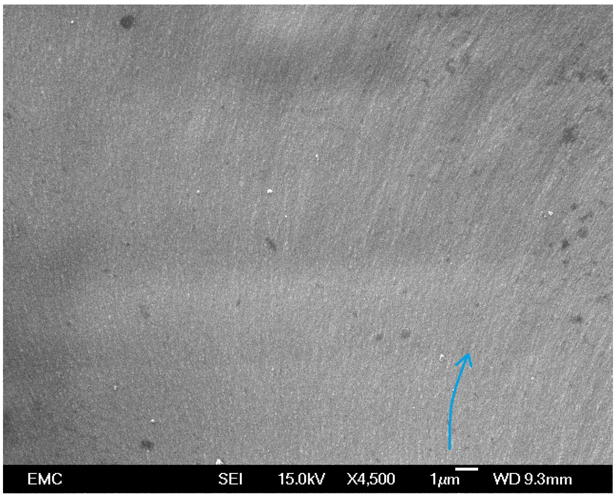

FIGURE 3.13: An unfilled epoxy specimen. The blue arrow represents the direction of force which fractured the specimen.

The images shown in Figure 3.14 were obtained from EM0; they demonstrate how some areas in the bulk are more densely filled than others, where the lighter coloured agglomerations measured over 2 μm in size and the grey areas (circled in red) represent unfilled areas of the bulk. Figure 3.14(c) shows a high magnification image of nanofiller agglomerates; although there are isolated particles (green circles), the aggregate is clearly over 100 nm in size. The light coloured feature in Figure 3.14(b) is representative of dust on the surface.

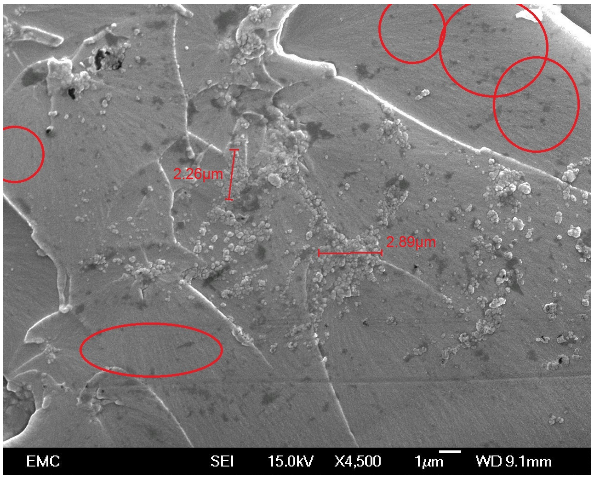

(a) Agglomerations of nanosilica causes fracture features to occur.

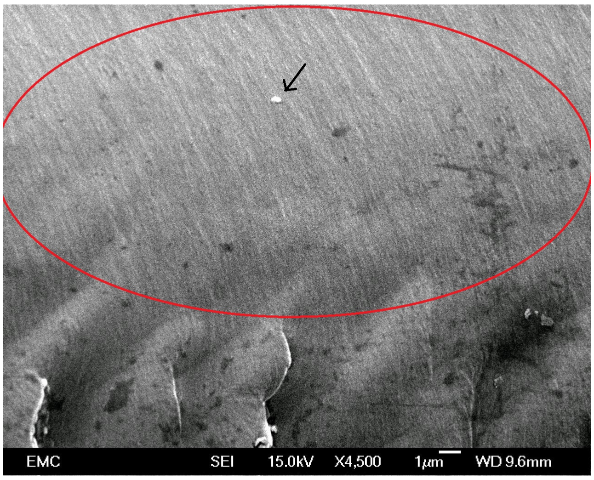

(b) The red circles represent unfilled regions of the epoxy.

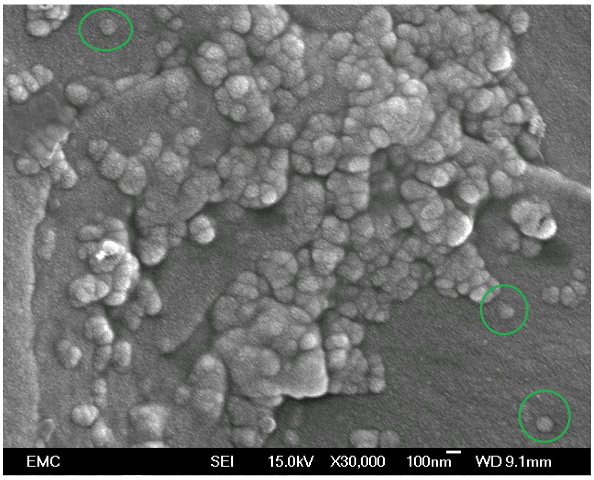

(c) Silica agglomerates in EM0 measure >600 nm in size.

FIGURE 3.14: FEG-SEM images obtained from EM0 of various magnifications, where the unfilled regions indicate the inhomogeneity of the composite.

Comparitively, samples EM1 and EM4 (represented by figures 3.15(a) and 3.15(b) respectively) show how a greater degree of surface modification has a positive effect on the dispersion of nanofiller in a nanocomposite system; the agglomeration size in EM1 is on order of 2 to 3 µm, whilst those in EM4 measure 1 to 2 µm. The size of the aggregates are seen to decrease to further to an average of 1.5 µm for epoxy systems containing M16 in Figure 3.16, where the high magnification images of EM16 show a greater number of isolated particles present in the system (green circles).

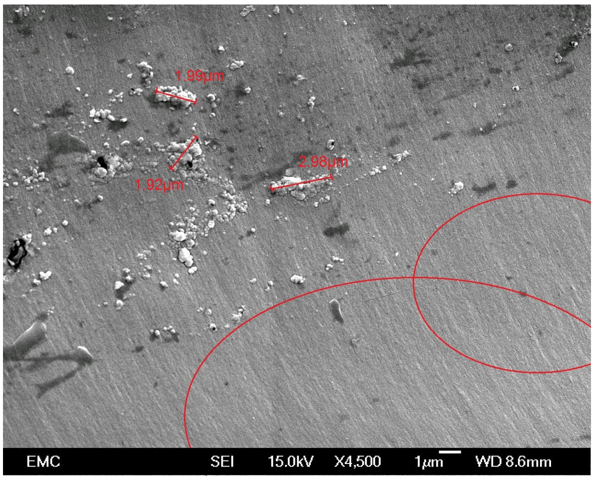

(a) Filled EM1 system at low magnification. Aggregate sizes are on order of 2 to 3 µm.

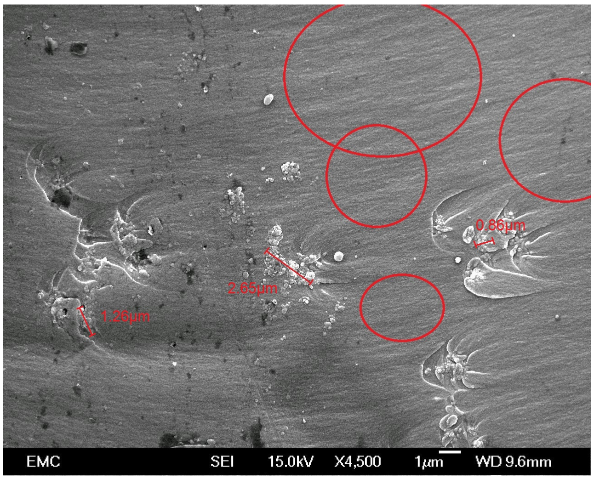

(b) EM4 sample with aggregate sizes of 1 to 2 µm.

FIGURE 3.15: Images obtained from different silica-epoxy nanocomposite systems.

This suggests that despite the existence of agglomerates in the solvent during functionalisation, the achieved dispersion allows for a degree of modification for solutions containing a greater quantity of organosilane and the aggregates (formed from drying) will re-disperse with the aid of chemical bonding between the coupling agent and matrix. The artefact in Figure 3.16(b) is not part of the epoxy nanocomposite system and is identified as dust that may have settled on the surface of the sample whilst in transition.

However, there are significant regions within bulk that appear unfilled must not be overlooked (circled in red); although the agglomerations appear to reduce in size with increasing surface modification, the existence of nanoparticle clusters will result in inhomogeneity or unfilled regions. For the most efficient dispersion and functionalisation of nanofiller, a pre-disperser (such as a chemical dispersing agent) should be used before the addition of coupling agent. The images from this study were compared to other nanodielectric systems by Lau *et al* who showed SEM images for polyethylene systems loaded with 2 wt.% and 5 wt.% nanosilica, their nanocomposite materials showed a decrease in agglomeration size with the treatment of the filler. Similar effects are seen in a number of other studies where the agglomeration size decreases with the use of a coupling agent [145, 146].

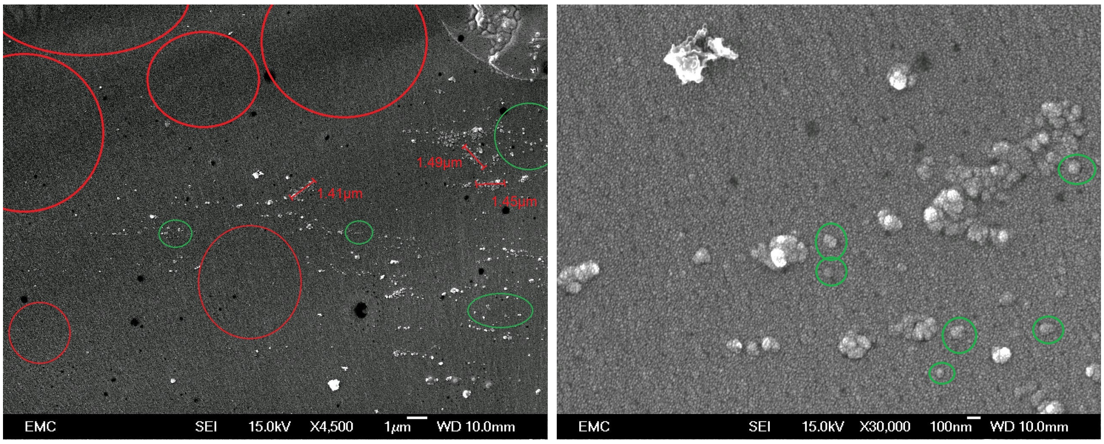

(a) Nanofiller dispersion appears to be greater in ET16. (b) Isolated nanoparticles measure on order of 100 nm.

FIGURE 3.16: FEG-SEM images obtained from EM16 showing a greater number of isolated particles.

It is important to note how Figure 3.16(b) is also of great significance as the image presents isolated nanoparticles that measure on order of 100 nm. This is contrary to the measurements stated by Sigma-Aldrich which will unquestionably change the ‘optimum' quantity of organosilane required for 'optimum' functionalisation. This is further discussed in the summary. Further FEG-SEM images are available in Appendix B.2.

3.6 Electrical properties of nanosilica-epoxy dielectrics

3.6.1 AC electrical breakdown analysis

The main influences of electronic breakdown are believed to be intrinsic or due to defects and/or impurities. In the case of the former, the dielectric strength of a polymer is dependent upon the material itself, where breakdown occurs due to the material being unable to stabilise the energy distribution from free electron collisions within the bulk (electron movement is induced by an applied field); whereas in the case of the latter, microcavities or contaminants are assumed to act as concentration centres for localised enhancement of the electric field that will initiate breakdown. The electrical breakdown strength of the nanocomposite films were investigated using AC breakdown studies. Figure 3.17 represents the data obtained from the epoxy systems presented in the form of two parameter Weibull probability distribution. When comparing data obtained from the unfilled epoxy (UE) and epoxy containing nanosilica directly from the supplier (EN), there is evidence that the addition of nanofiller marginally reduces the breakdown strength of the virgin polymer matrix. However the Weibull distribution shows that the data are within the 90% confidence bounds of each other and therefore the data can be considered statistically similar.

It was assumed that data obtained from EN and EM0 would be alike as neither of the nanosilica within the epoxy had been treated, however the Weibull plot shows that this is not the case. This difference in AC breakdown strengths for these two samples is thought to be a result of moisture on the surface of the nanosilica in EN, the filler in this system was dispersed into the epoxy matrix directly from the supplier container; whereas M0 underwent the functionalisation process (without coupling agent) that involved drying. The removal of moisture on the surface of the filler due to drying or functionalisation has a significant impact on the AC breakdown strength of the dielectric as it reduces the formation of percolation or sub-percolation paths within the bulk of the nanocomposite

[1, 58, 147]. These percolation paths around filler agglomerates within the bulk will contribute to failure as charges accumulate in these areas and provide charge transport links between one water shell to another [148]. The data obtained from AC breakdown studies in this investigation are similar to those by Talaka *et al* and Huang *et al*, who both saw an increase in AC breakdown strength of their dried treated nanofiller systems (compared to their virgin polymeric systems) [35, 149].

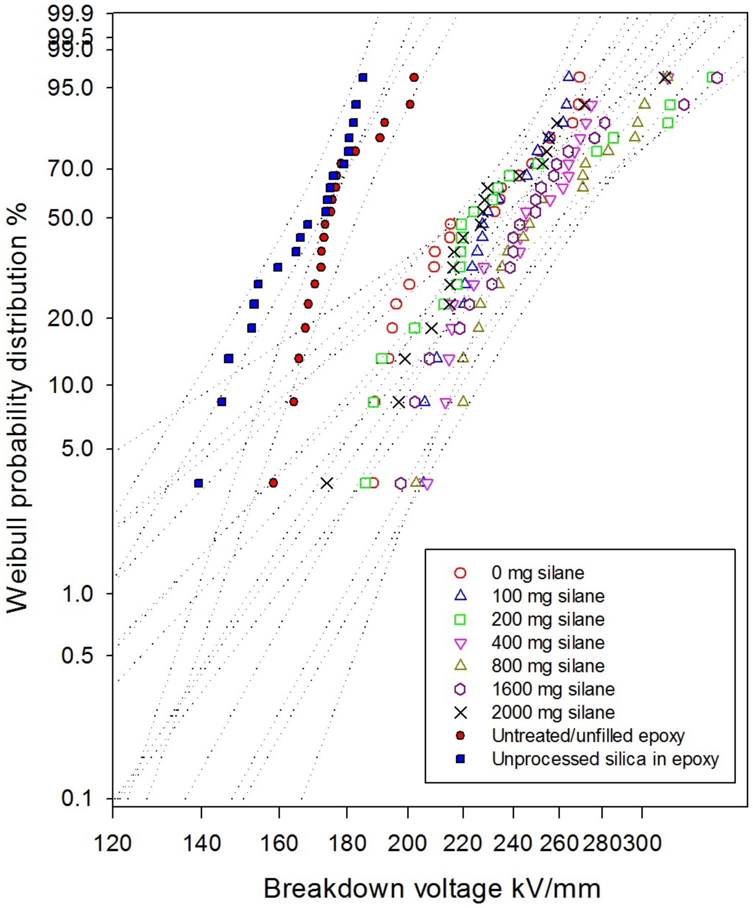

Figure 3.17: Two parameter Weibull distribution for AC breakdown data obtained from epoxy films containing differently functionalised nanosilicas.

The data from all systems containing functionalised silicas support this concept as there is a clear separation in α values from samples containing unprocessed and processed silicas; there is at least a 38% increase in α when comparing EN with the epoxy systems dispersed with dried nanosilicas. Furthermore, the overall increase in α-values (for EM0 to EM20 in comparison to EN) are attributed to an increased nanofiller dispersion for all treated silicas. The FEG-SEM images reveal that the dispersion state of the system improves with an increased use of coupling agent and this is assumed to have a positive effect on the AC breakdown strength. Studies have shown how the agglomeration of micron-sized fillers induces a negative effect on the breakdown strength of polymer composites by forming a defect centre in which the local electric field is distorted and enhanced [95, 150]. Huang *et al* comments on how the agglomeration of nanofiller may act as defect centers (voids within crevices [56]) to enhance the local electric field which results in a lower breakdown strength for the system [149]. Although a hundredth the size of conventional fillers, the distortion effects induced by nanosized fillers will still have an effect on a polymer composite. For well dispersed systems, the greater inter-particle spacing will contribute to higher breakdown strengths as conduction channels are less likely to form. An increased homogeneity has seen to limit the enhancement of electric fields that lead to breakdown [34, 149].

When comparing the AC breakdown data from individual functionalised systems, the initial increase in α is an indication of an increasing bond strength between filler and matrix with the increased functionalisation of nanosilica. The largest α-values are seen for samples EM4 and EM8 which is thought to indicate that the nanosilicas have been modified to an optimum. The α-value shows a decreasing trend for samples containing nanosilica functionalised to a greater degree (EM16 and EM20), this may be due to a number of reasons; firstly, the geometry of the condensed networks of organosilanes may have had a negative effect on epoxy chains bonding with the filler, and secondly, the additional free space caused by the organosilane networks may act to trap moisture and contribute negative effects. This second theory is supported by IR data, which shows there is a greater amount of moisture present in systems containing silicas functionalised with an excess of coupling agent.

Despite a noticeable increase in α for these functionalised systems, the β values for the nanocomposites are comparitively low which typically implies a low level of homogeneity. This is contrary to the information provided by FEG-SEM, and it is therefore reasonable to assume that the changes in stoichiometry (with the addition of epoxide groups from the organosilane) may have lead to the formation of an inhomogenous structure due to variations in the degree of cross-linking throughout the bulk. The data are presented in Table 3.2 and Figure 3.18, where the uncertainties for the alpha value are based upon 90% confidence bounds as calculated by the Reliasoft Weibull ++ software.

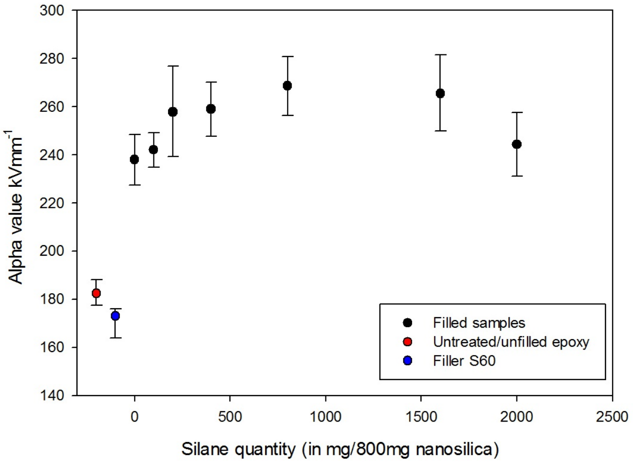

FIGURE 3.18: α values for epoxy systems.

Sample	α value (kVmm^{-1})	β value
UE	182 ± 5	14 ± 4
EN	173 ± 6	13 ± 5
EM0	238 ± 10	9 ± 3
EM1	242 ± 7	13 ± 4
EM2	257 ± 19	5 ± 1
EM4	258 ± 11	9 ± 2
EM8	268 ± 12	8 ± 2
EM16	265 ± 16	6 ± 2
EM2K	244 ± 13	7 ± 4

TABLE 3.2: Two parameter Weibull values for AC breakdown data.

3.6.2 Differential scanning calorimetry

As a decrease in filler size leads to an increased volume fraction of interphase in the total composite system, the glass transition temperature, T_g , is a significant parameter to consider when studying nanocomposites. However, the addition of nanofillers to polymer matrices has been reported to lead to a number of different effects and therefore the behaviour of this particular property remains poorly understood. Many authors associate the glass transition temperature with the degree of bonding between the particle surface and polymer molecules; whilst some groups have shown a decrease in T_g due to weak interactions between filler and matrix [100, 151], others have shown an increase in T_g which is attributed to the restriction of polymer chains at the nanofiller surface [1, 152]. There have also been reports that show how the glass transition temperature of nanocomposite systems vary with an increase or decrease of filler loading [32, 153]. Irwin *et al* describe these behaviours as a product of two competing mechanisms; typically a decrease in T_g may occur due to additional free volume created within the interphase which may allow for large scale mobility of the polymer chains; however, this effect may be counteracted by the formation of strong bonds between the polymer chains and the filler surface [154].

Differential scanning calorimetry is a technique that is used to determine the melting, crystallisation and glass transition temperature of a material and was therefore used to determine the glass transition temperatures of the nanosilica-epoxy systems. Figure 3.19 shows typical differential scanning calorimetry data. This particular sample represents the heat flow in a virgin epoxy system, where the increase in heat flow around 80 °C is indicative of the T_g. The mid-point of each step-change was taken to determine the T_g of each sample and the resulting values of T_g are given in Figure 3.20 and Table 3.3 [89].

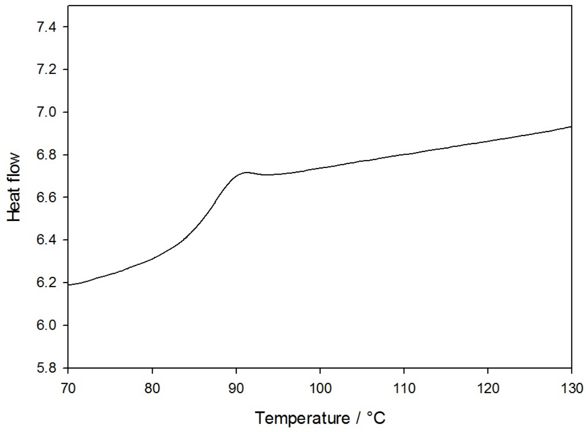

Figure 3.19: Typical data obtained from differential scanning calorimetry when investigating the glass transition temperature, T_g.

The unfilled epoxy systems in this study had an optimum stoichiometric ratio of 1000 parts epoxy resin to 334 parts curing agent. Each resin molecule has two epoxide groups, one at either end of the molecule; similarly, the molecules in the curing agent possess an amine group at each end. The components react such that all the curing agent is consumed in the cross-linking process (where there was neither a deficiency nor an excess of the hardener upon completion of curing). For systems containing unmodified nanosilicas, some of the epoxy molecules would bond directly to the filler such that one epoxide group would bond to the hydroxyl groups on filler surface, this leaves only one epoxide group available for cross-linking with curing agent. This changes the overall stoichiometry, where the excess of amine groups is expected to decrease the T_g of the filled system due to a lower degree of cross-linking (less energy is needed to break a decrease in bonds). Although the expected decrease in T_g was not obtained, the data for unfilled epoxy and EM0 are within experimental uncertainty of one another. In addition, a small increase in T_g between the two samples is not unusual as Reading *et al* observed the same behaviour upon the addition of untreated silica into the same epoxy system [155].

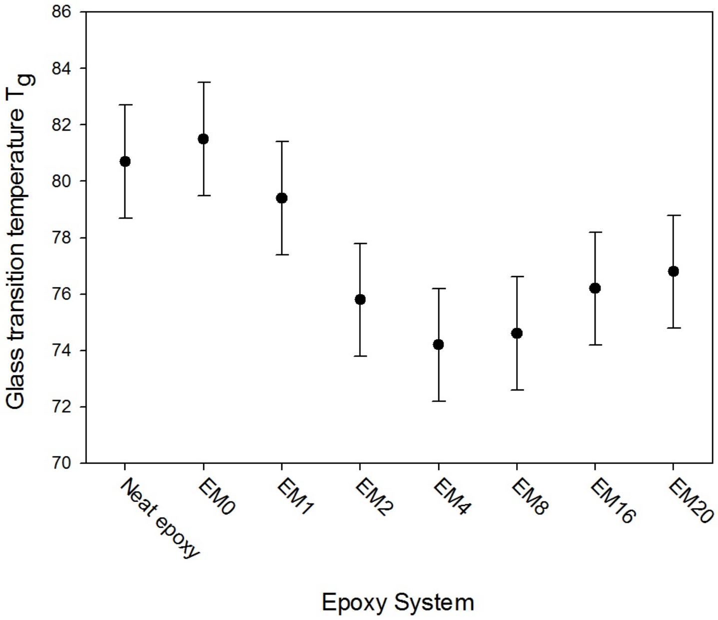

FIGURE 3.20: T_g for epoxy nanocomposites containing differently modified nanosilicas.

Sample	T_g ±2°C
UE	80.7
EM0	81.5
EM1	79.4
EM2	75.8
EM4	74.2
EM8	74.6
EM16	76.2
EM20	76.8

TABLE 3.3: T_g values.

However, when functionalised nanosilicas are introduced into the system, the stoichiometry will change according to the bonding process between the organosilane and the rest of the system. The addition of modified nanosilicas will see an increased number of epoxide groups in the system from the organosilane molecules, where the organosilane epoxide groups bond with an amine group on the end of a hardener molecule and the amine group at the opposite end will bond with an epoxide group from a resin molecule. In this case, all the amine groups would be consumed before all the epoxide groups have reacted and this is expected to have a significant effect on the T_g, where an excess quantity of resin has been seen to decrease the T_g of the system by a number of groups [89, 156, 157]. This is is attributed to an increased amount of free space available in the system due to a change in the polymer architecture and a decrease in the bond strength between the epoxy and hardener components of the system. However, when functionalised nanosilicas are introduced into the system, the stoichiometry will change according to the bonding process between the organosilane and the rest of the system.

The addition of modified nanosilicas will see an increased number of epoxide groups in the system from the organosilane molecules, where the organosilane epoxide groups bond with an amine group on the end of a hardener molecule and the amine group at the opposite end will bond with an epoxide group from a resin molecule. In this case, all the amine groups would be consumed before all the epoxide groups have reacted and this is expected to have a significant effect on the T_g, where an excess quantity of resin has been seen to decrease the T_g of the system by a number of groups [89, 156, 157]. This is is attributed to an increased amount of free space available in the system due to a change in the polymer architecture and a decrease in the bond strength between the epoxy and hardener components of the system.

Although an excess quantity of epoxide groups in the system is explained by considering the filler-organosilane-amine chain configuration, other configurations must also be considered; as the modified nanosilicas are first dispersed into the epoxy resin with the use of a sonicator, it is possible that the application of heat from the probe acts to open some oxirane rings on the organosilane or resin molecules which facilitates a reaction. This can result in two possible reactions, one where the open ring of the organosilane reacts with the hydroxyl group that branches from the molecule backbone. This implies that both the epoxide groups on the resin are still available for reaction with the hardener, as seen in Figure 3.21. However the geometry of the resin to the organosilane is unfavourable for resin molecules to bond to other organosilanes bonded to the filler surface and/or curing agent molecules. Again, extra free space is created in the interphase which leads to a reduction in T_g.

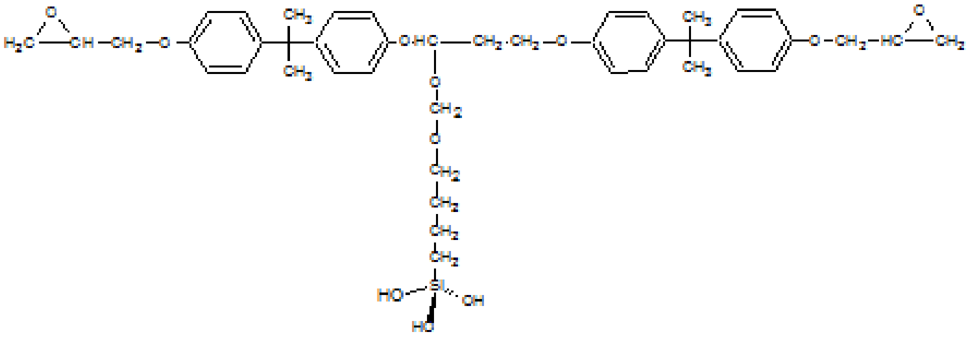

FIGURE 3.21: Organosilane epoxide groups bonded with the hydroxyl group of the epoxy resin.

Alternatively, the epoxide rings from both the organosilane and epoxy resin may react with each other (with the application of a heat catalyst) [104]. Similar to systems containing untreated nanosilicas, this would result in an excess of amine groups in the system.

The data collected via differential scanning calorimetry all point towards the fact that a change in stoichiometry have significant effects. In addition, the change in the stoichiometric ratio will have an influence the secondary processes which may occur in the curing process, where etherification may have a greater influence on the overall architecture of the system. The stoichiometry ratio may affect the AC breakdown strength, where weak or defective regions may form within the bulk that lead to breakdown phenomena, as seen by Nguyen *et al* [89, 158].

3.6.3 Dielectric spectroscopy

Dielectric spectra showing the temperature dependence of the complex permittivity, ε^* (as a function of frequency) for an unfilled epoxy system is shown in Figure 3.22; the spectra show typical characteristics which are expected with varying frequency [101, 104]. A local maximum in the real part of the relative permittivity, ε', is seen to appear from temperatures at (and above) T_g (80 °C), this is attributed to an α-relaxation in the system by Andritch in a diepoxide-bisphenol-A based epoxy system [101]. This maximum shifts to higher frequencies with increasing temperature and can be seen as a stepped feature in ε' and a broad peak in the imaginary data, ε'' (from T_g and higher). At frequencies above 10^5 Hz, there is evidence of the formation for a stepped feature in ε', this is representative of a β-relaxation which is also seen to shift to higher frequencies with increasing temperature. The β-relaxation in these nanocomposite specimens are associated with rotation of the hydroxyether group [$CH_2CH(OH)CH_2O$] in the backbone, which results from the bonding between the epoxide groups in the epoxy resin and amine groups from the hardener [159, 160]. This relaxation characteristic can also be seen in the corresponding ε'' data, where the development of a relaxation peak is beginning to form. At 100°C, the steep increase in ε'' between 10 to 0.2 Hz is indicative of conductivity contributions, with gradient of $\frac{dlog\varepsilon''}{dlog(\omega)}$ = -1. This must not be mistaken for spectra representing Maxwell-Wagner-Silliars effect at frequencies below 0.2 Hz, where low frequency dispersions arise from the limited freedom of charge carriers within the specimen. The charges collect at interfacial regions which result in polarisation layers the electrode interfaces [1, 93, 161, 162]. In this case, $\frac{dlog\varepsilon''}{dlog(\omega)} > -1$. This non-ohmic behaviour is also observed in ε' at 100°C, where there is a small increase at low frequencies [93].

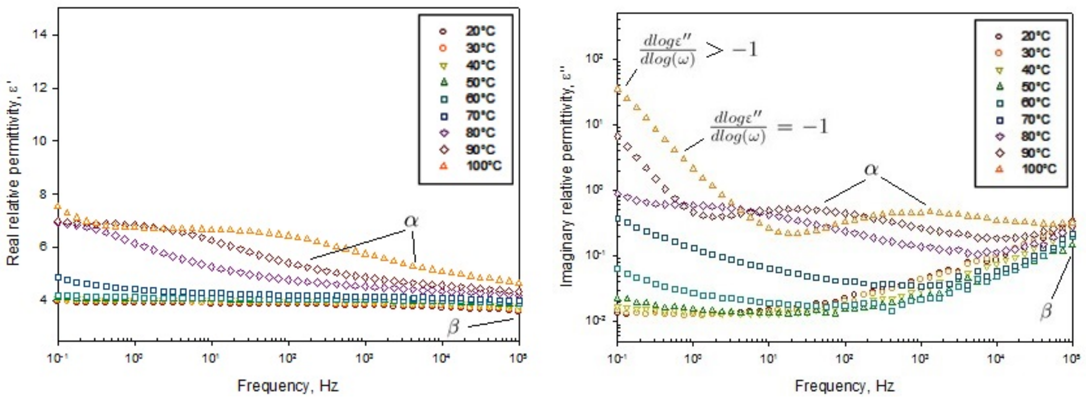

(a) ε' vs frequency for UE.

(b) ε'' vs frequency for UE.

FIGURE 3.22: Real permittivity data from unfilled, untreated epoxy.

The introduction of 2 wt.% nanofiller has two effects on the relative permittivity of the system. The first observation is contrary to original expectations, as the permittivities for both filler and matrix are similar ($\varepsilon'_{nanosilica} \approx 3.9$ [163] and $\varepsilon'_{epoxy} \approx 4$ [33, 99, 164]), the overall effects of mixing the two was expected to result in negligible change in ε'. However, it can be clearly seen from the data (Figure 3.23) that the addition of dried untreated nanofillers increases the relative permittivity of the system and is a likely effect of the excess amine groups due to the change in stoichiometric ratio; conversely, this will be a product of excess epoxide groups for the systems containing functionalised filler, where the unreacted groups contribute to a higher relative permittivity. Similar behaviour has also been observed in other studies where ε' has shown an increase with the addition of 0.5 wt.%, 2 wt.% and 5 wt.% of nanosilica [104, 165, 166, 167].

Polarisation effects are more pronounced with the addition of nanofillers as charges collect at the filler-matrix interface. At temperatures above T_g, ε' sees a steep rise at frequencies below 10 Hz, this is mirrored by characteristics in ε'', where $\frac{dlog\varepsilon''}{dlog(\omega)}$ >-1. This indicates a build-up of charge at the filler interface which results in the Maxwell-Wagners-Silliars effect. For frequencies between 10 to 100 Hz (at 100 °C), $\frac{dlog\varepsilon''}{dlog(\omega)}$ = -1; similar to Figure C.1(b), this is representative of ohmic conductivity contributions.

In addition, these (filled) systems possess a relaxation feature in ε'' (at 20 °C, 30 °C and 40 °C), which is thought to be a feature of the filler-matrix interface and is attributed to a α'-relaxation by Couderc *et al* [106].

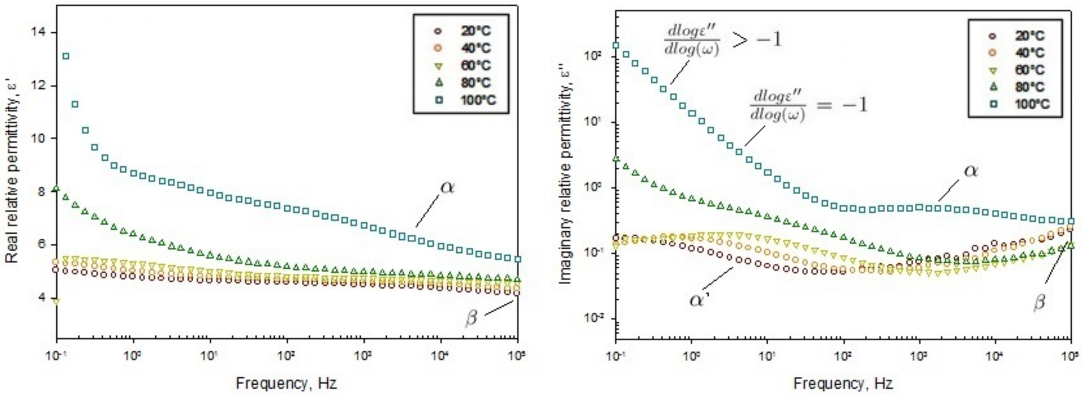

(a) ε' vs frequency for EM0.

(b) ε'' vs frequency for EM0.

FIGURE 3.23: Dielectric spectra obtained from EM0 as a function of frequency, with respect to increasing temperature.

The dielectric spectroscopy data obtained from the functionalised epoxy nanocomposite systems show an initial decrease in the ε' with increasing functionalisation and is indicative of restricted chain mobility at the interface. The spectra obtained from EM2 (figures 3.24(a) and 3.24(b)) displays a broad α-relaxation that indicates the bonding strength between filler and matrix is strongest here as energy is stored in the system over a greater range of frequencies and stands to reason as the silica in the epoxy has been modified with the optimal quantity of coupling agent. Samples EM8 to EM20 contain nanosilicas which have been functionalised with an excess quantity of coupling agent; the general increase in ε' suggests that the excess results in the condensation of the organosilane chains that forms a thicker layer of Silane z-6040 around the nanoparticle and contributes a greater free volume for polymer chain movement [101]. Dielectric spectra for EM1, EM8 and EM20 are available in Appendix C.

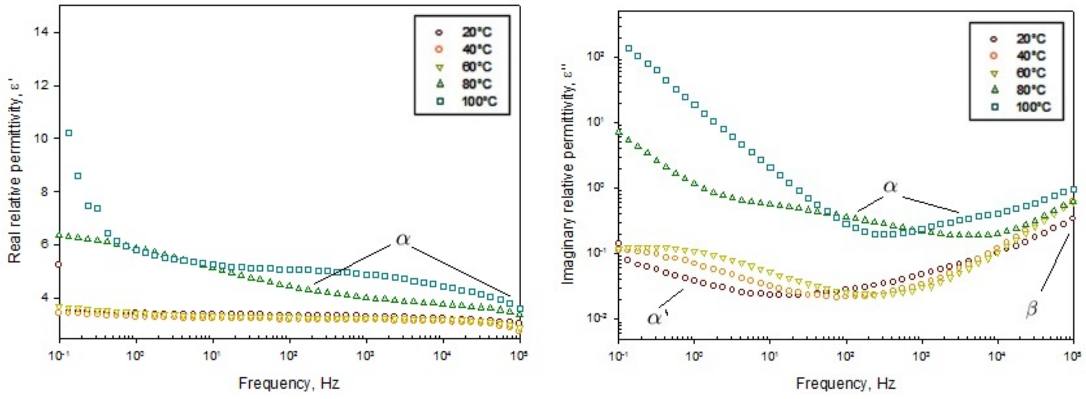

(a) ε′ vs frequency for EM2. (b) ε′′ vs frequency for EM2.

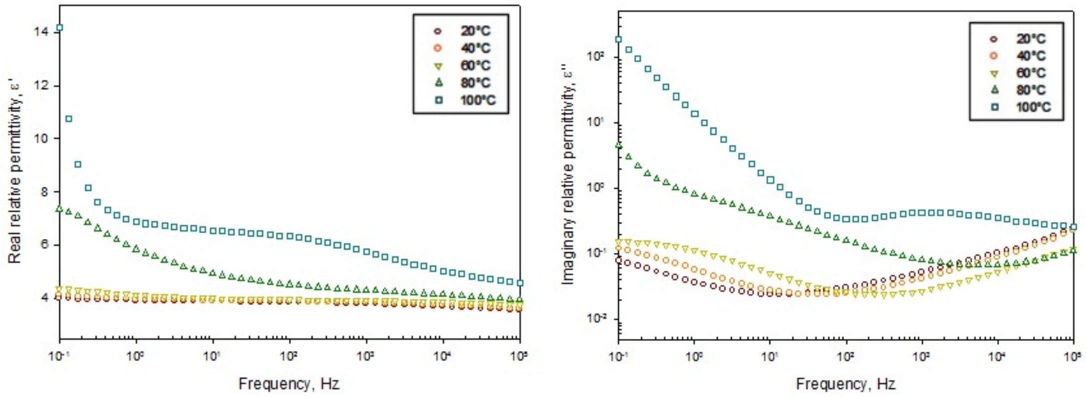

(c) ε′ vs frequency for EM4. (d) ε′′ vs frequency for ET4.

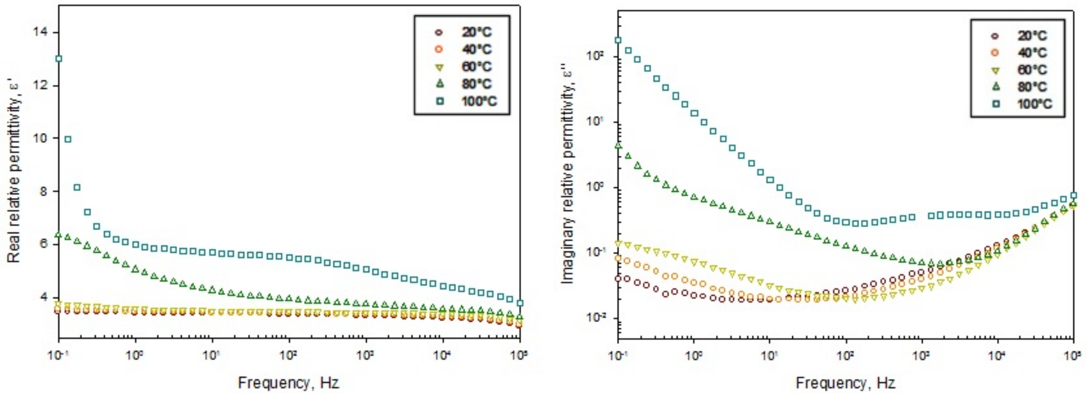

(e) ε′ vs frequency for EM16. (f) ε′′ vs frequency for EM16.

FIGURE 3.24: Dielectric spectra of nanocomposite systems EM0, EM4 and EM16 as a function of frequency, with respect to increasing temperature.

3.7 Chapter summary

The results presented in this chapter have shown that the electrical properties of nanocomposite systems strongly depend on the degree of functionalisation of the nanofiller. The study has thus far been able to modify the surface chemistry of nanosilica using an organosilane coupling agent, Silane z-6040. Although the epoxide groups or CH_2 bonds from the coupling agent could not be detected via Raman or infrared spectroscopy, the decrease in the hydroxyl peak in the latter spectra suggests that the functionalisation process has been successful. Furthermore, combustion analysis has confirmed a significant increase in the elemental fractions of carbon in functionalised systems which confirms that organosilane has been grafted onto the surface.

One of the initial premises of functionalising nanosilica was to induce a more homogeneous dispersion and optimise the filler-matrix interface. A number of groups have previously described how the use of coupling agent acts to increase dispersion [24, 46, 69] and reduces the agglomeration size in the system. This has typically produced a positive effect on the electrical insulating properties of the polymer; despite this, few groups have considered the degree of functionalisation as a variable parameter in their studies where the effects remained to be verified. The scanning electron microscope provides images which show how the dispersion state of nanosilica appears to increase with increasing surface modification. Nevertheless, there are still regions of epoxy where the aggregates are clearly seen although the clusters reduce in size with increasing surface modification; in some cases isolated nanoparticles can be observed within the aggregated regions and supports how the use of coupling agent strongly influences the dispersion state of the system. However, findings from scanning electron microscopy are contradicted by the β-values obtained in the AC breakdown tests which suggests that dispersion is not as homogenous as seen in FEG-SEM topography, or that the unbalanced stoichiometry of the system increases the uncertainty in the data. Calculations have shown that for 800 mg of isolated nanoparticles (average 15 nm in diameter) 164 mg of Silane z-6040 should be used for optimum surface modification. However, as the FEG-SEM images clearly shows that agglomerates exist in the system, and without the use of a dispersing agent pre-modification, it would be reasonable to assume that less than 164 mg of coupling agent would be required to functionalise the exposed surface area of the agglomerates. Furthermore, upon close inspection of the FEG-SEM images, the isolated particles were seen to measure on order of 100 nm, if this is the case, then the optimum organosilane quantity for 800 mg of 100 nm diameter nanosilica is 22.09 mg of nanosilica, which is much less than the 165 mg used in processing. However, it is found that the optimum electrical properties typically occur for samples which contain nanosilica (800 mg) functionalised with 200 mg of organosilane; this suggests that the condensation stage of the functionalisation process is much more complex than assumed in the literature; most papers follow a procedure believing the coupling agent condenses before attaching itself to the surface of the filler, however the parameters that govern this reaction are particularly sensitive (i.e. processing acidity and processing temperature) and controlling these types of sol-gel reactions is not as simple as adjusting the pH or silane concentration. In the case of this investigation, there is reason to believe that the condensation of the organosilane occurs (even at low concentrations of coupling agent) and therefore is needed in excess before an optimum graft is achieved.

The various spectroscopic techniques have confirmed that the degree of surface modification on nanofillers will have an effect on the dielectric properties of an epoxy system. In addition to the findings above, DSC studies and dielectric spectroscopy have led to a further understanding of what may occur at the interface. For samples that contain nanosilica with an increasing level of modification, the stoichiometry of the system changes such that there is a greater quantity of epoxide groups in the system (than amine groups) which leads to a decrease in T_g [89]. Despite this, the bonds between the filler and polymer strengthen to produce a decrease in the relative permittivity which is indicative of restricted chain mobility in the epoxy. For a system that contains a filler that has been modified with an excess of coupling agent, the interfacial region around the filler is suspected to form condensed organosilane networks that may be geometrically unfavourable for polymer bonding. This will produce a greater amount of free volume such that the polymer chains can move more freely and lead to changes in the relative permittivity.

Chapter 4

Silica-epoxy nanodielectrics - An anhydrous method

Many groups studying nanodielectrics employ methods of functionalisation that use hydrous solvents (or add water) to allow for a hydrolysis stage in the process. Despite the use of acids to stabilise the behaviour of the colloid and regulate the extent of condensation reactions, the previous chapter has shown that these precautions are insufficient in controlling the variable parameters when modifying the surface of the nanofiller. This chapter describes the next steps in functionalising nanosilica in a more controlled manner. Tetrahydrofuran (THF) is an anhydrous solvent whereby there are no hydroxyl groups in the system. The use of this solvent in place of methanol will result in a higher degree of control over condensation reactions where the condensation process can be restricted [112]; this chapter sets out to investigate the effects of using an anhydrous solvent in the functionalisation process.

4.1 Functionalisation of nanosilica (using THF)

This method of functionalising nanosilica involves no hydrolysis or condensation of coupling agent, instead, two possible subsitution mechanisms are described in literature that explains the manner in which organosilane bonds to the nanosilica.

S$_N$2 - The electronegativity of the methoxy groups on the organosilane provide a positive region along the backbone (Si$^{\delta+}$). The hydroxyl groups on the surface of the nanosilica contain nucleophilic oxygen atoms that attack the positively charged site on the organosilane, forcing the methoxy group to depart. This process happens simultaneously, where the oxygen nucleophile forms a bond with the organosilane as the methoxy group leaves. The remaining positive hydrogen (H$^+$) bonds with the leaving group to form methanol and provides stability in the system [168, 169].

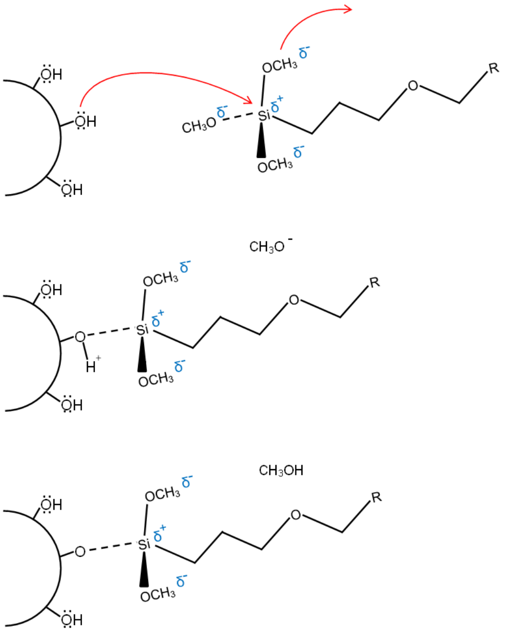

FIGURE 4.1: S$_N$2 mechanism.

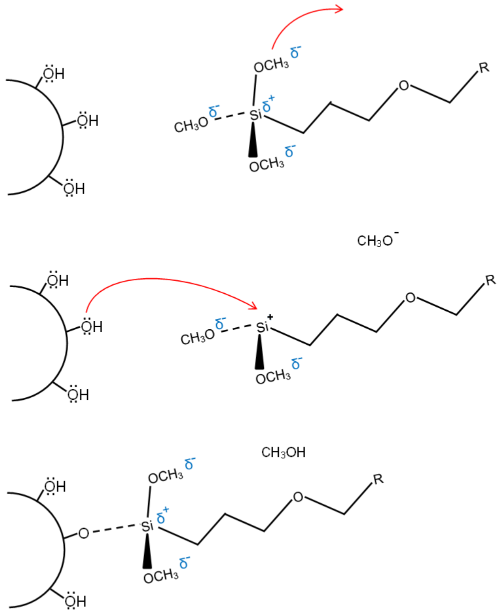

FIGURE 4.2: S$_N$1 mechanism.

S$_N$1 - This alternative substitution is a two-step process. The formation of a methoxy ion (CH_3O^-) results in a silicon cation on the organosilane chain. This region of positive charge is attracted to the oxygen nucleophile on the surface of the nanoparticle substrate, where the nucleophile lends its negative charge to form covalent bonds with the silicon cation. Again, the remaining hydrogen atom on the substrate bonds with the methoxy groups to form methanol as a by-product and completes the functionalisation process [168, 169].

Eight 800 mg samples of nanosilica from Sigma Aldrich (quoted particle size 10 to 20 nm) were ultrasonicated in 25 ml of fresh distilled tetrahydrofuran (THF) for 15 min in order to obtain a homogeneous suspension. To compare the effects of using an anhydrous solvent in the functionalisation process of the nanosilica, the quantities of materials used in these experiments were kept constant with those used in the hydrous method of functionalisation. The coupling agent was introduced in quantities of 0 mg, 100 mg, 200 mg, 400 mg, 800 mg, 1600 mg and 2000 mg, before the suspension was shaken vigorously for 46 h at room temperature. All suspensions were spun on a centrifuge at 3500 rpm for 10 min and the supernatant was decanted off. The remaining solid was washed three times with dry THF and twice with fresh diethyl ether. This second solvent is also anhydrous in nature with a boiling point of 34.6 °C and is more easily removed than THF which has a boiling point of 66.0 °C. The silica was shaken during each of the washing processes to ensure excess organosilane was removed efficiently. All samples were dried under high vacuum at 40 °C for 10 days [45]. The surface modification of nanosilica in this chapter is based on studies by Brown *et al* [114].

4.2 Nanocomposite preparation

Epoxy nanocomposite films with a 2 wt.% filler loading were formed by adding 150.0 mg of dried, functionalised nanosilica into 5.58 g of D.E.R. 332 epoxy resin (Sigma Aldrich). The filler was dispersed into the resin with the use of a probe sonicator for 60 min, which was set to pulse in 0.7 s intervals and placed in a cold water bath to inhibit the degradation of the resin. A stoichiometric ratio of 1000:344 (resin to hardener) was achieved by magnetically mixing 1.92 g of Jeffamine D-320 hardener (Huntsman) into the resin mixture for 15 min and degassed in a vacuum oven for 15 min to remove trapped air in the system [115]. The epoxy was then poured into moulds (with a 70 µm melinex spacer) which were pre-coated in release agent and cured in an oven at 100 °C for 4 h. The release agent QZ-13 (from Resinsonline) is a low-viscosity solution which is ideal for use when demoulding epoxy specimens. The product was chosen for its ability to withstand temperatures up to 150 °C, has no chemical effect on epoxy systems and is non-corrosive towards the gauge-steel mould plates [115].

The samples prepared via the use of an anhydrous solvent are designated names with the following code;

Nanosilica powder name	Slane (mg/800mg silica)	Epoxy nanocomposite name
T0	0.0	ET0
T1	100.0	ET1
T2	200.0	ET2
T4	400.0	ET4
T8	800.0	ET8
T16	1600.0	ET16
T20	2000.0	ET20

Table 4.1: Sample name designations.

4.3 Characterisation of nanosilica and surface modification

Raman spectroscopy and Fourier transform infrared spectroscopy were used to confirm and quantify the chemical changes on the surface of nanosilica after the modification process. Whilst the functionalised nanofiller was examined in powder form in the ATR-IR, the samples for Raman analysis were formed in a Graseby Specac press, where the powders were shaped into discs by applying a pressure of 5 tonnes. Figure 4.3 represents the data acquired via Raman spectroscopy, where each spectra were integrated from one hundred 10 s accumulations with a Renishaw Raman RM1000 spectrometer as described in the previous chapter. The system was set to non-confocal mode in line with Renishaw's recommendations for non-confocal operation, with a slit width of 50 µm and a CCD area of 20 x 574 pixels.

The spectra presented here are similar to those obtained from the samples of hydrously functionalised nanosilicas in Chapter 3. The data have been normalised with respect to the Si-O bending peak at 530 cm^{-1} [129, 130] as any changes in this feature are consider negligible. The functionalised nanosilica powders possess Raman peaks at 975 cm^{-1} and 830 cm^{-1} which correspond to the rocking and bending of Si-O-Si [170]. However, there is no visible change in the spectra between differently modified fillers; epoxide groups possess Raman peaks at 910 cm^{-1} and 1250 cm^{-1}, neither of which are observed in the spectra. The lack of spectra features representing alkyl groups (at 1450 cm^{-1} [110]) support that fact that, like the functionalised filler in Chapter 3, the agglomeration of nanoparticles pre-modification decreases the amount of organosilane on the silica. In addition, the drying of the filler causes agglomerations which acts may prevent Raman spectroscopy from accessing the chemical changes at the interface.

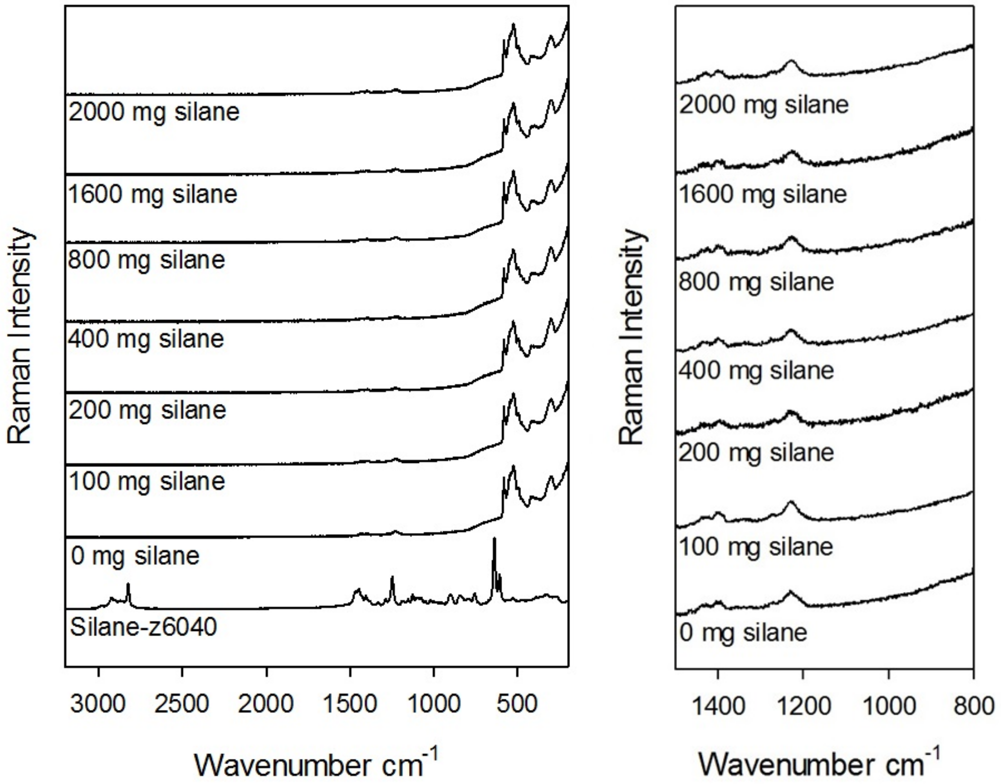

FIGURE 4.3: Raman spectra obtained from differently functionalised nanosilica using THF solvent.

The powder functionalised nanosilica was also subjected to ATR-FTIR spectroscopy. Infrared spectra were obtained using a Thermo Nicolet 380 FTIR spectrometer with an ATR diamond attachment. Figure 4.4 represents the data obtained from untreated and treated nanosilica powders acquired over 32 scans at 4 cm^{-1} resolution in reflectance mode. The prominent peak feature seen at 1000 cm^{-1} is representative of asymmetric Si-O-Si stretching; again, as this is the main component of the system, changes to this peak are considered negligible and the spectra were normalised with respect to this peak.

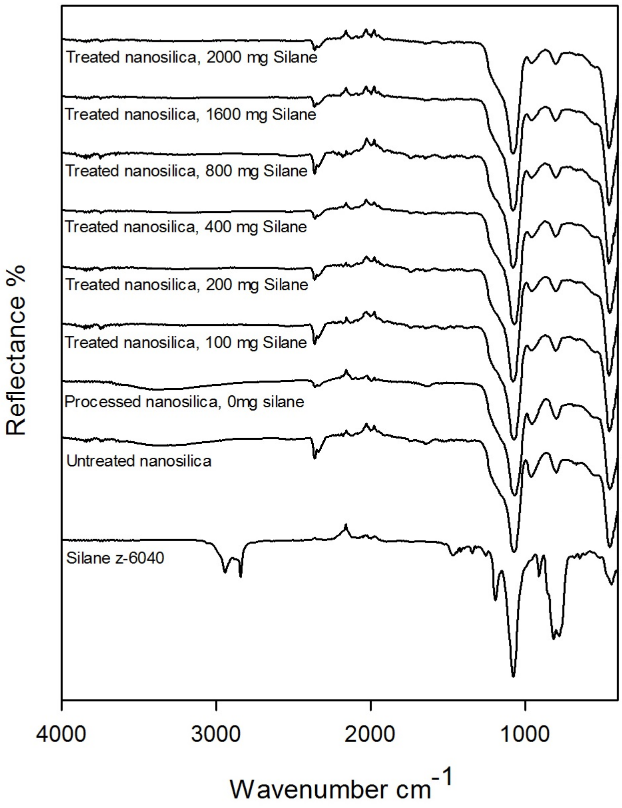

Figure 4.4: ATR-FTIR spectra obtained from differently functionalised nanosilica.

Infrared spectroscopies have similar sensitivities to Raman spectroscopies (0.1% composition detection), it was therefore no surprise that epoxide peaks or CH bonds could not be detected using ATR-FTIR (discussed in detail in Chapter 3). However, there are observable changes in the broad peak seen between 3000 and 3700 cm^{-1} which is attributed to Si-OH bonding. The signal obtained from the Si-OH bonding is reduced as a greater quantity of coupling agent is used and is indicative a greater degree of surface functionalisation. The peak is seen to show a marked decrease in intensity in comparison to T0 as the hydroxyl groups have been removed and replaced with organosilane chains; by integrating over the area of the hydroxyl peak it is found that the intensity decreases by ∼77% for T1 and T2, and ∼74% for the remaining samples. Like Chapter 3, it is assumed that after optimum Silane z-6040 graft has been achieved, the excess coupling agent bonded to the surface of the filler may act to trap moisture or be geometrically unfavourable for strong bonds to form. Features between 2000 to 2500 cm^{-1} are artefacts of the measurement system, where the presence of carbon dioxide leads additional features in the spectra [171]. Lau *et al* have also published the same findings using the same materials and functionalization process, using a Perkin Elmer Spectrum GX fourier transform infrared system [140].

Combustion analysis completed by MEDAC Ltd. demonstrates the chemical changes between the functionalised and unfunctionalised samples. Elemental fractions of carbon and hydrogen were expected to be the equivalent for the untreated silica and T0 as neither had been modified with coupling agent. However this is not the case, both carbon and hydrogen contents are higher for the processed nanosilica which may be due to minor contamination in the functionalisation process. Nevertheless, an increase in the carbon content can be detected for samples which have been functionalised, this indicates the organosilane has successfully been grafted onto the nanosilica surface. The hydrogen atoms on the surface also increase with increasing functionalisation; this should be the case as there are at least ten hydrogen atoms attached to the carbon backbone of Silane z-6040. For this reason, the greater percentage content of hydrogen to carbon in T20 was not expected, the result is considered as an anomalous data point. Lau *et al* have also used combustion analysis to detect elemental changes in their functionalised nanofiller specimens. They saw a 0.36% and 0.18% increase in carbon and hydrogen (respectively) after modifying amorphous nanosilica with trimethoxy(propyl)silane [140].

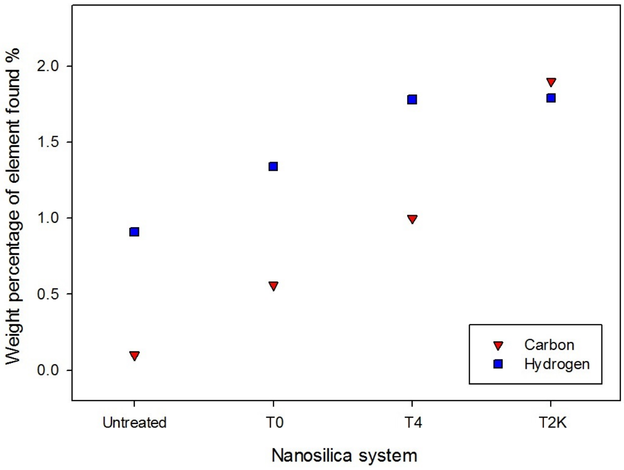

FIGURE 4.5: Combustion analysis data obtained from nanosilica systems. There is an increased carbon and hydrogen fraction with increasing silica treatment.

4.4 Nanosilica dispersion in an epoxy matrix

Scanning electron microscopy was employed to investigate the dispersion state of the filler within the epoxy. The thin epoxy films were prepared by cooling the thin film in liquid nitrogen for 15 min before being fractured. This process resulted in clean breaks as the flexible films become hard and brittle, reducing the amount of 'tearing features' observed. Each sample was mounted on a scanning electron microscopy stub and sputter coated to improve conductivity for use in the SEM. As the JEOL JSM-5910 system described in Section 3.3.3 did not provide the resolution desired for this study, the JEOL FEG-SEM 6500F system was used to image the surface cryofractured samples.

Figure 4.6 represents the same unfilled epoxy system in Chapter 3 (for reference). At low magnification, the bulk of the sample appears smooth, where fractography features can be seen at the edges of the specimen. At high magnifications the ability of the FEG-SEM system is apparent, where the gold sputter coating on the sample can be identified as the granular texture on the surface.

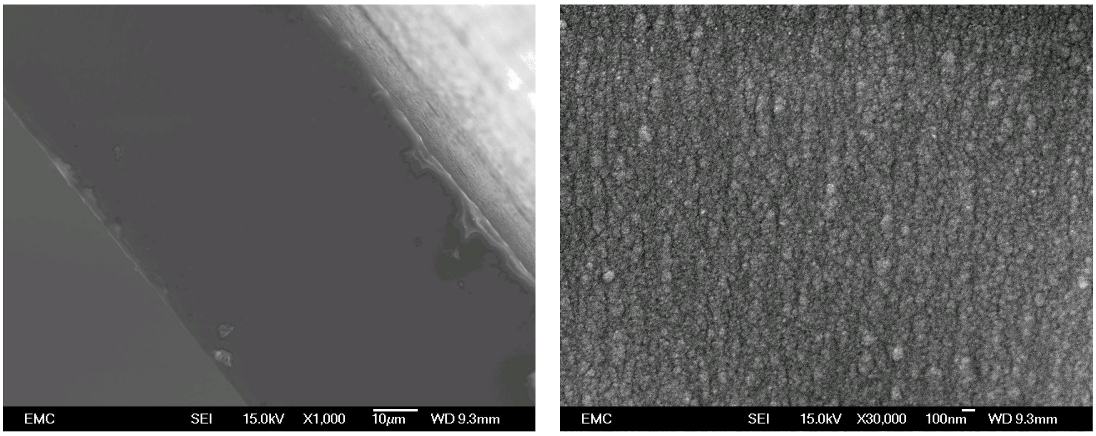

FIGURE 4.6: Low and high magnifications of an unfilled epoxy sample.

The images obtained from filled specimens are shown in Figures 4.7 to 4.11. Without the use of coupling agent, the nanoparticles are seen to agglomerate in regions in varying degrees. Figures 4.7(a) and 4.7(b) were obtained from different regions in ET0 and represent regions where there are nanofiller agglomerations and areas where the epoxy remains unfilled. The circled regions in Figure 4.7(b) highlight the unfilled areas of the image, whilst the nanofiller can be clearly seen as the lighter, clustered features in the image. Specifically, these two images draw attention to how mechanical weaknesses arise from nanofiller aggregation. Lange *et al* proposed a mechanism called 'crack pinning' in microcomposites which describes how particles force a propagating crack to fracture around the filler. This forms bow-like features or tails which may generate secondary cracks to help disperse physical stresses applied to the material [172, 173]. These types of pinning have been suggested to be indicative of the bond strength between filler and matrix, where the greater the bond, the greater the pinning effect [174]. The fracture features as seen in Figures 4.7(a) and 4.7(b) indicate the direction of the propagating force which fractured the sample (blue arrow) and are similar to those observed by Lange *et al*, where the cracks in the epoxy are deflected around the filler aggregations (some shown by yellow arrows). The dark specs result from the lack of gold coating on the sample, where there may have been dust present on the surface whilst in the coater.

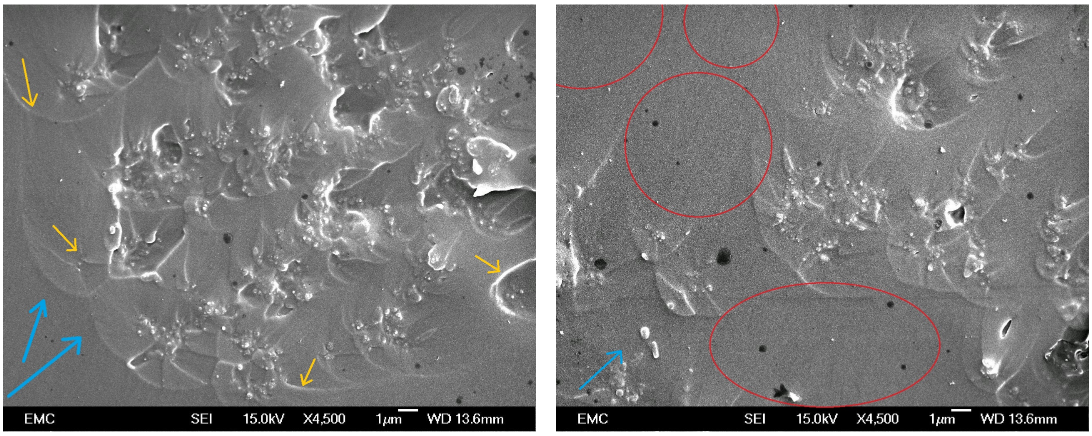

FIGURE 4.7: Low magnification images obtained from ET0 highlighting fracture features.

Figure 4.8 to 4.11 present a collection of FEG-SEM images that represent a range of samples from ET1 to ET16. The darker grey areas are representative of unfilled regions, whereas the bright areas arises from a greater emission of secondary electrons from the filler. In general, the dispersion state of the nanofiller is seen to improve with the use of a coupling agent, although agglomerations of nanoparticles still exist within the bulk. For example, at low levels of surface modification (ET1), there are regions which are sparsely filled (red circles) whilst others contain volumes of clustering (Figure 4.8(a)). The pinning effects of the agglomerated filler is evident in the densely populated regions and are highlighted by the yellow arrows. Figure 4.8(b) is typical of a densely populated region, where the nanofiller is seen to agglomerate in sizes of the order of 3 µm. Similarly, the images obtained from ET4 (Figure 4.9) show large unfilled regions (red circles), where the filled areas of bulk contain agglomerates that measure on order of 1.5 to 3 µm. This finding is significant when comparing these images with ET8 (Figure 4.10), where the agglomeration sizes are seen to range from approximately 0.47 to 1.53 µm. The aggregate sizes decrease even further in ET16, where the clusters range from 0.18 to 0.45 µm. With an increasing degree of functionalisation, an increased number of isolated particles are observed (green circles); as the agglomeration sizes are seen to decrease with a greater nanoparticle surface modification, it stands to reason that the particles from the agglomerates are dispersed elsewhere as single particles. This shows that the coupling agent is successful in promoting the homogeneity of the filler within the matrix. The images obtained from ET16 support this argument as there is a significant improvement in the dispersion of the nanosilica and a greater number of isolated particles (as seen from FEG-SEM images, Figure 4.11). Furthermore, it is interesting that any 'pinning' phenomena is more pronounced with increasing surface modification of the nanosilica as seen in Figures 4.9(a) and 4.10(a) which is indicative of a greater bond strength between the nanofiller and the epoxy matrix [172, 173], where stronger bonds at the interface lead to greater pinning effects and prominent fracture features.

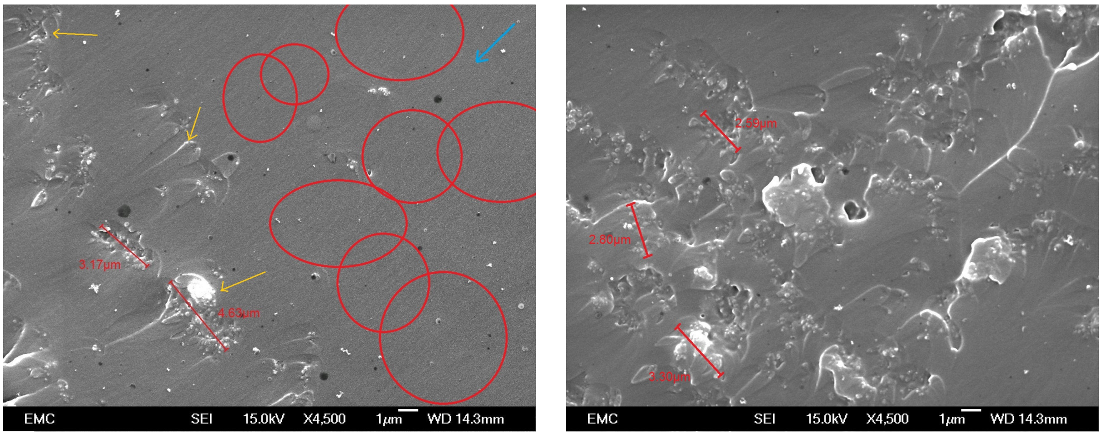

(a) Pinning effects occur around the nanofiller.

(b) Filler agglomerations average 3 µm in ET1.

Figure 4.8: FEG-SEM images obtained from ET1 with filler aggregates measuring on order of 3 µm.

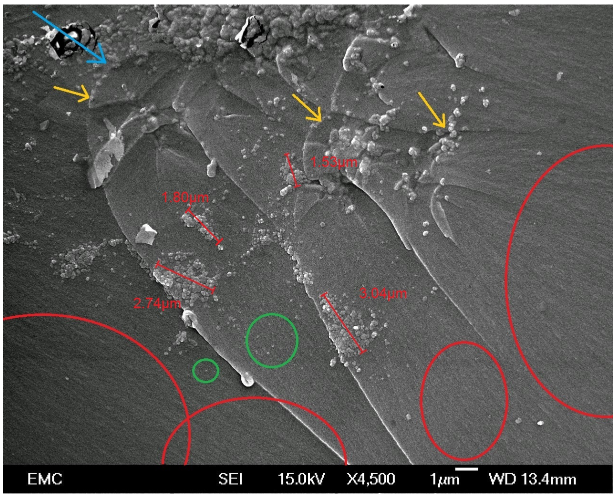

(a) Pinning effects appear more pronouced in ET4.

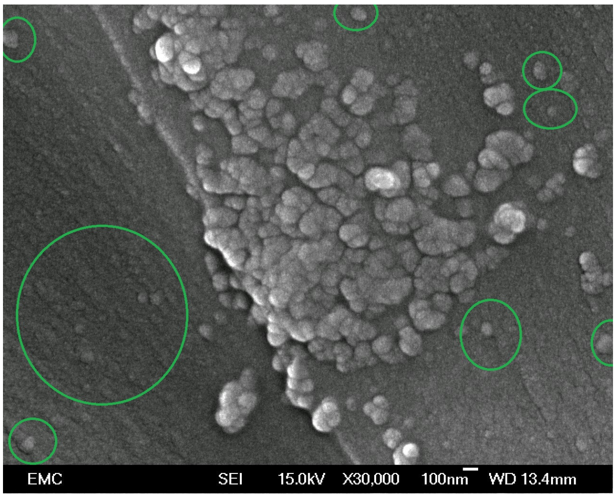

(b) High magnification of larger agglomerates in ET4.

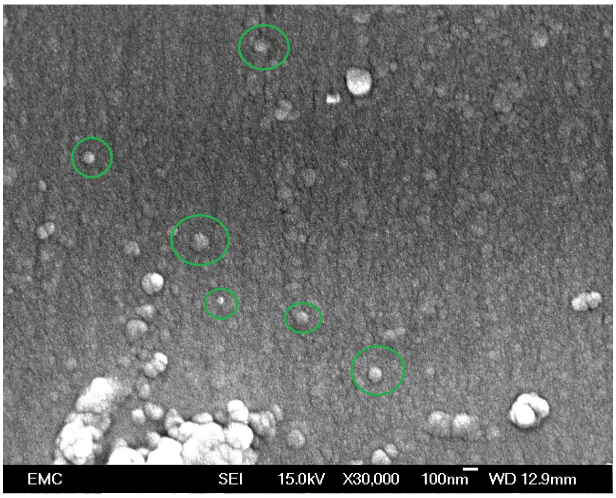

(c) Examples of isolated nanosilica particles in ET4.

Figure 4.9: FEG-SEM images obtained from sample ET4 at different sites.

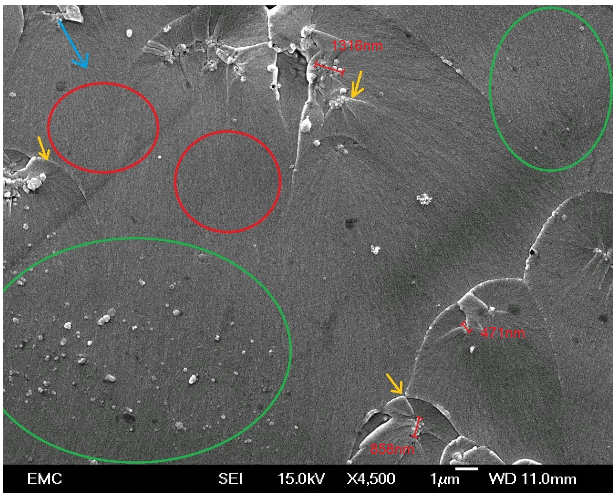

(a) Low magnification of epoxy system ET8.

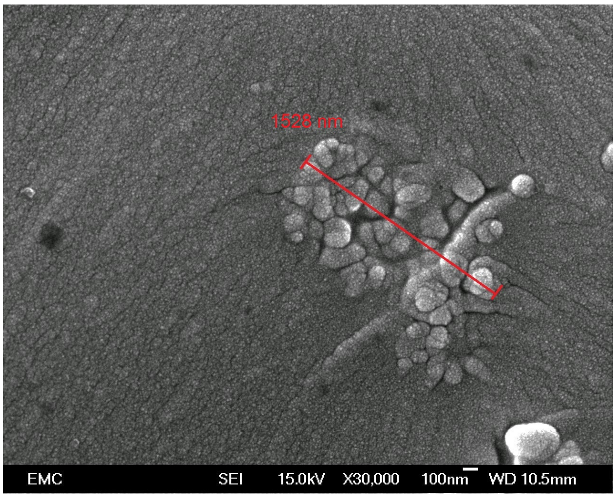

(b) The aggregates in ET8 appear to be reducing in size.

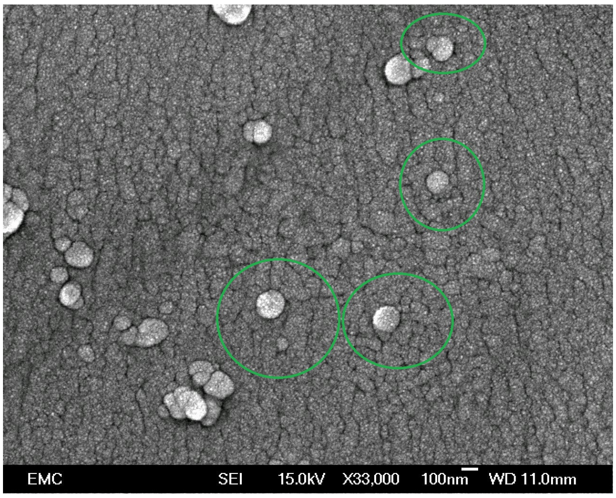

(c) Isolated nanoparticles are clearly observed in ET8.

FIGURE 4.10: FEG-SEM images from ET8 showing a higher degree of homogeneity than samples ET0 to ET4.

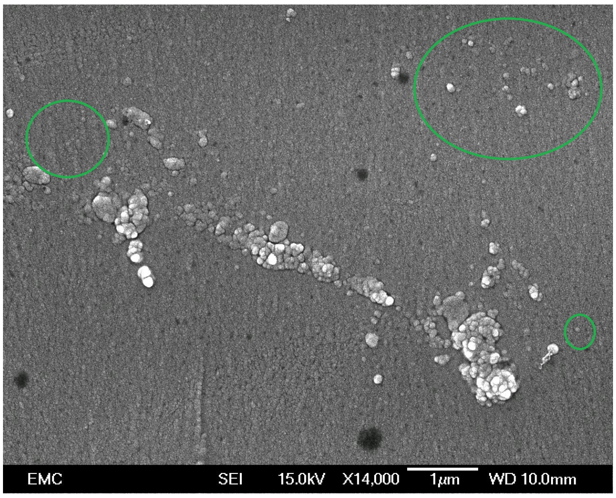

(a) Nanofiller dispersion appears to be greater in ET16.

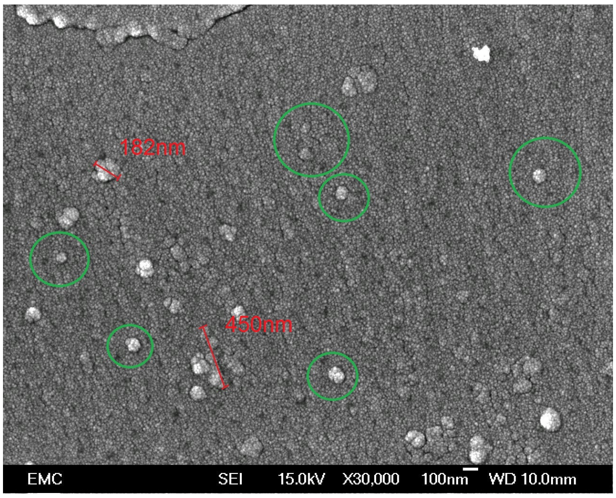

(b) Isolated nanoparticles are clearly observed in ET16.

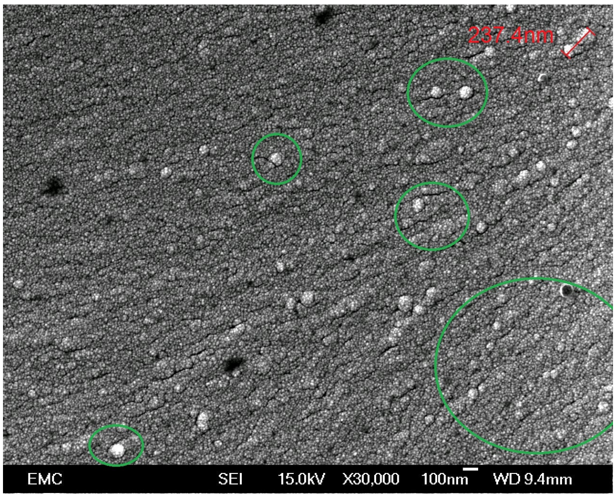

(c) Image of epoxy system ET16, at high magnification.

FIGURE 4.11: FEG-SEM images obtained from different sites of ET16, the dispersion is seen to increase significantly with an increased use of coupling agent.

4.5 Electrical properties of nanocomposite samples

4.5.1 AC electrical breakdown analysis

AC breakdown tests were carried out on the nanosilica-epoxy systems to study the electrical consequences of functionalising the nanosilica before dispersion into the resin. Figure 4.12 compares the two parameter Weibull distribution for the AC breakdown data obtained from twenty sites on an unfilled system (UE) represented by circles, and those which contain unfunctionalised nanosilica; the filled squares are data obtained from a composite system containing nanosilica directly from the supplier (EN), whereas the red and black empty circles present data obtained from M0 and T0 respectively. In the latter two of these samples, the nanosilica was washed with solvent but no coupling agent was included in the process. All parameters corresponding to Figure 4.12 were generated using Weibull++ software and are printed in Table 4.2.

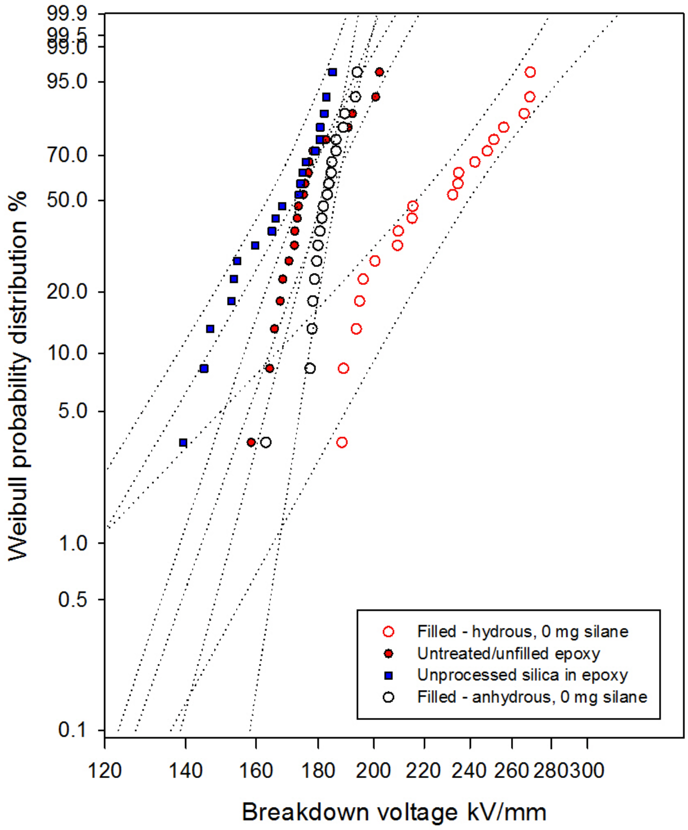

FIGURE 4.12: The two parameter Weibull probability distribution for unfilled and untreated samples.

As none of the fillers in these systems have been functionalised, similar results were expected from all systems, however it is evident that the AC breakdown strength is lowest in EN than all other samples. As described in Section 3.6.1, this is due to the moisture adsorbed onto the substrate surface and is reported to donate charge carriers into the system that are accelerated through conduction channels formed by the moisture [1, 58]. Samples EM0 and ET0 contain nanosilicas which have been dried and are seen to possess a higher breakdown strength than that seen in EN. Despite this, there is a distinct difference between EM0 and ET0 which suggests the two systems are not equivalent. As all materials used to prepared these two composites were constant, with the exception of the solvent, it stands to reason that the differences in the α- and β- parameters stem from the use of hydrous or anhydrous solvents in the functionalisation process. Although rigorous washing methods are in place, acid residue may still remain on the filler system which will alter the breakdown strength by changing the balance of charge at the interface. The significant difference in the α-values for EM0 (238 kVmm^{-1}) and ET0 (185 kVmm^{-1}) gives rise to speculations that the charge at the filler interface of EM0 has been altered due to the use of acid in the preparation of nanosilica. This causes the mobile charges within the system to be attracted to the filler and result in energy being dissipated into the filler itself and reduce the likelihood of breakdown. Similarly there is a considerable difference in the β-value of these two systems, where the β-value of EM0 is substantially lower than that of ET0. This indicates a greater spread in the AC breakdown data and implies a greater degree of inhomogeneity, as M0 was prepared with a hydrous solvent, it stands to reason that any remnant moisture on the filler could hinder particle dispersion, increasing the β-value [58, 147]. When reviewing the FEG-SEM images obtained from EM0 and ET0, smaller agglomerates are observed in ET0, this implies a greater degree of homogeneity as they filler may be dispersed as isolated particles (most likely smaller aggregates) elsewhere.

Sample	α value (kVmm^{-1})	β value
Unfilled	182	14
EN	173	13
EM0	238	9
ET0	185	32

TABLE 4.2: Two parameter Weibull values.

In Chapter 3, the electrical properties of the system were thought to improve for samples containing nanosilica with a higher degree of functionalisation; for samples containing highly modified nanosilica, it is assumed that the condensation reactions in the hydrous solvent created a network of organosilane chains which resulted in a greater likelihood of system failure. As the work described here (in Chapter 4) involves modifying silica using an anhydrous solvent, condensation reactions are restricted. Once an optimum graft of coupling agent is achieved, no more reactions are thought to take place and therefore the electrical properties of the nanocomposite systems were expected to improve (with respect to the degree of modification on the nanosilica), reach a maximum (in the case of an optimum graft) and plateau for all other samples containing silica functionalised with excess organosilane. However, the Weibull plots show that this is not the case. The AC breakdown data acquired from the epoxy systems containing a 2 wt.% filler loading of differently functionalised nanosilica is represented as a two parameter Weibull plot in Figure 4.13.

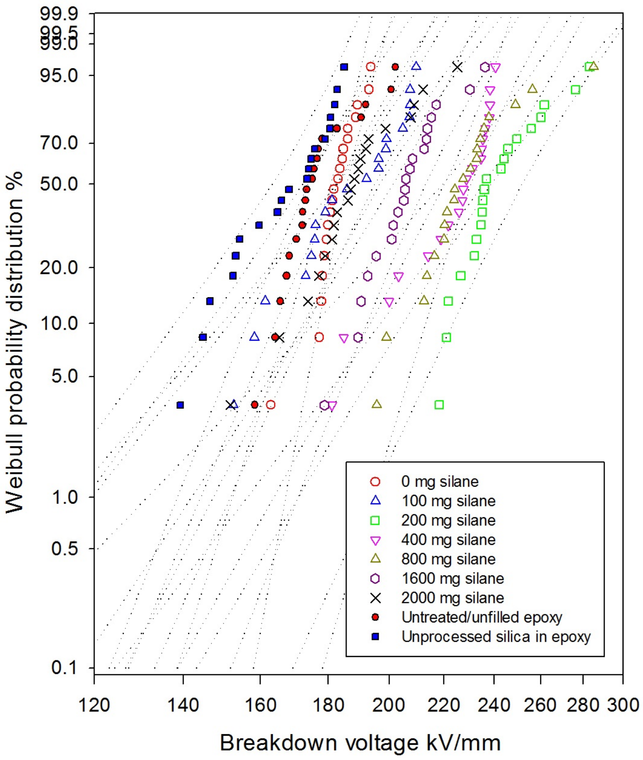

FIGURE 4.13: Weibull probability distribution of AC breakdown data obtained from nanosilicas treated anhydrously.

Systems containing treated nanosilica possess a higher AC breakdown strength which increases with a greater dispersion (as seen in FEG-SEM images) due to a greater degree of surface modification [175]. The α-values are seen to increase to a maximum for ET2, before decreasing thereafter; although this suggests that this indicates the strongest bonding between filler and matrix, it is arguable that the α-value for ET8 is within the experimental uncertainty (as shown by error bars). The β-value obtained for ET8 is lower than that calculated for ET2 which indicates the latter has a smaller degree of uncertainty in its breakdown values; however, as the β-values for each of these samples are within their own uncertainties, and the FEG-SEM images show a greater degree of dispersion, the conclusion is that ET8 has a better degree dispersion. This can also be said for ET4 which possesses the narrowest spread in breakdown data, its β-value and corresponding uncertainty falls within the uncertainty (in β) of ET2 and ET8.

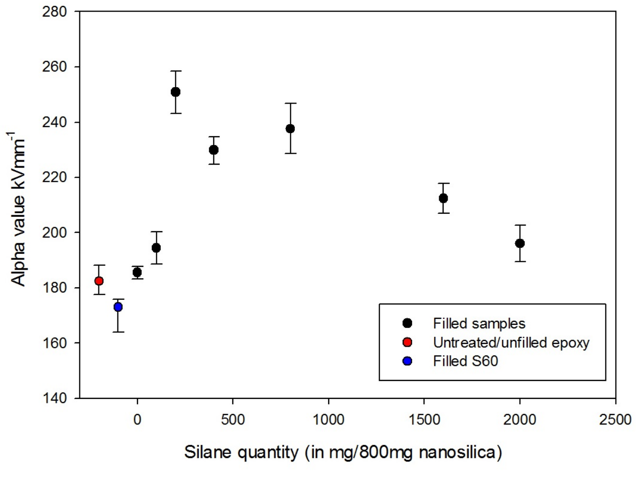

FIGURE 4.14: α-values for epoxy systems.

Sample	α value kVmm^{-1}	β value
UE	182 ± 5	14 ± 4
NE	173 ± 6	13 ± 5
ET0	185 ± 2.	32 ± 9
ET1	194 ± 6	13 ± 4
ET2	250 ± 8	13 ± 3
ET4	229 ± 5	19 ± 6
ET8	237 ± 3	10 ± 3
ET16	212 ± 5	15 ± 4
ET2K	196 ± 7	11 ± 3

TABLE 4.3: Weibull values for AC breakdown data.

The α-values are seen to decrease for functionalised systems ET16 and ET20, suggesting that although the dispersion state in these samples have improved (as seen from the FEG-SEM images), the restriction of the condensation reactions are not as controlled as once thought. The AC breakdown behaviour of these (overly modified) systems may also be a product of a change in stoichiometry as there is an excess quantity of epoxide groups (as explained in Section 3.6.2 [89, 158]). There may be defective regions in which weaker bonding exists between the constituent parts of the epoxy which increases the likelihood of breakdown phenomena.

4.5.2 Differential scanning calorimetry

All epoxy systems containing functionalised nanosilica were subjected to testing in the differential scanning calorimeter to determine the glass transition temperature of the nanocomposite. A Perkin Elmer DSC 7 system was calibrated using a reference sample of indium before the sample temperature was raised from 50 to 120 °C at a rate of 10 °C min^{-1} before reducing the temperature of the system to 30 °C. The experiment was run twice for each sample, only the second sets of data were considered in this investigation as the first was required to remove any thermal history in the polymer. The data obtained produced typical graphs as seen in Figure 3.19 (Chapter 3). As in the case of the DSC data in Chapter 3, the baseline data from an empty can was subtracted and the glass transition temperature was taken as the mid-point of the step-change in the heat flow data for each system.

The T_g is a parameter that is related to the molecular mobility and reflects the structure of the epoxy system. A decreasing particle size is seen to increase the total interfacial volume that occupies the total composite volume [57], differential scanning calorimetry can be used to analyse the interfacial region that is created with the introduction and modification of nanofiller. A higher T_g is associated with restricted mobility of polymer chains at the filler interface, whereas a low T_g is typically indicative of weak interactions between the matrix and phase(s) that lead to greater chain mobility. The uncertainty in the glass transition temperature was calculated via the standard error.

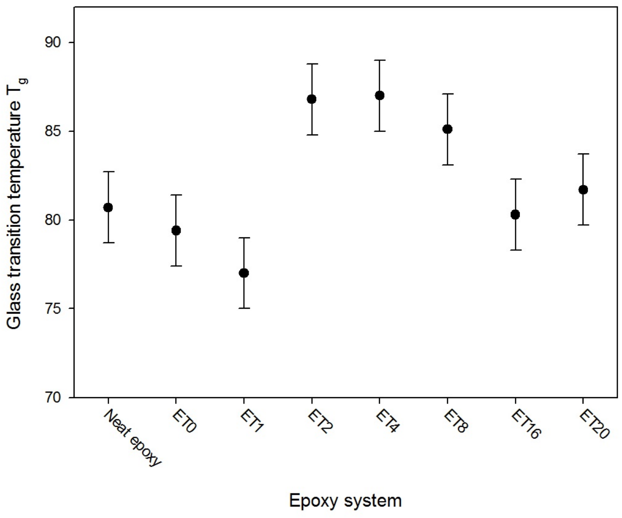

FIGURE 4.15: Glass transition temperature for epoxy nanocomposite systems.

Sample	$T_g \pm 2$ °C
UE	80.7
ET0	79.4
ET1	77.0
ET2	86.8
ET4	87.0
ET8	85.1
ET16	80.3
ET20	81.7

TABLE 4.4: T_g values.

The differential scanning calorimetric data obtained from the epoxy systems in this study are shown in Figure 4.15, and are very different to those obtained from nanocomposite containing hydrously functionalised nanosilicas. This difference highlights the fact that there are a number of mechanisms at work which affect the T_g of the system. Previously in Chapter 3 the glass transition behaviour is described purely as a product of changing stoichiometry, this chapter suggests that this may not be the dominant factor as once assumed and that the bond strength between filler and matrix will compete against the effects of stoichiometry to alter the T_g further. It is clear that the samples containing T2 and T4 possess the highest T_g value and is an indication that there is the greatest restriction of the polymer chains in the interphase (than other samples). As the strength of the bonds between the filler and matrix increase, the T_g will increase accordingly and this will act against the mechanisms that lower the T_g due to changes in the overall stoichiometry. For composites ET0 and ET1, the decrease in T_g from neat epoxy suggests that weaker bonding exists within the system. In this case of ET1, there may be an insufficient quantity of coupling agent on the surface, where the bonded organosilane chains form a geometrically unfavourable surface such that bonding between nanofiller surface and epoxy are hindered. This will provide a greater amount of free space which will allow for further chain mobility. The decrease T_g for these may also be a product of a change in the stoichiometry, where the introduction of additional epoxide groups (from the organosilane) will see a decrease in the T_g as seen by Nguyen *et al* and Ishida *et al* [158, 157]. Similarly, an excess of epoxide groups will explain the decrease in T_g for samples ET8 to ET20.

4.5.3 Dielectric spectroscopy

Dielectric spectroscopy was used to investigate and analyse the effects of applying an external AC field to each nanosilica-epoxy system. Many groups use this method of spectroscopy to investigate the interactions at the polymer-filler interface such that molecular behaviour can be deduced [1, 16, 176]. Dielectric spectra were obtained from every nanosilica-epoxy system (dried prior to the study, under vacuum at 40 °C over 14 days) using a Solartron 1296 dielectric interface paired with a Schlumberger SI 1260 Impedance/phase gain analyser.

Figures 4.16(a) and 4.16(b) represent a virgin epoxy system, the data here are the same as in Chapter 3, which are reprinted to aid comparison. The dielectric spectra show typical behaviours for epoxy systems as the temperature is increased [177, 178, 179], an increasing temperature increases both the real part, ε', and imaginary part, ε'', of the relative permittivity as there is more energy in the system for molecular mobility. As described in Chapter 3, an α-relaxation can be observed in ε' when the system is heated to T_g (80 °C) and above. This is seen to shift from the lower frequencies at 80 °C to approximately 10^2 Hz and 10^3 Hz for 90 °C and 100 °C respectively. A β-relaxation associated with the rotation of the hydroxyether group [$CH_2CH(OH)CH_2O$] in the backbone of the epoxy is observed in ε'' data, which is also seen to shift to higher frequencies with increasing temperature [159, 160]. The steep increase in ε'' from 10^1 to 0.2 Hz (at 100 °C) is representative of ohmic conduction contributions where $\frac{dlog\varepsilon''}{dlog(\omega)} = -1$ [93], whereas the gradient change below 0.2 Hz is indicative of polarisation at the filler-matrix interface ($\frac{dlog\varepsilon''}{dlog(\omega)} > -1$).

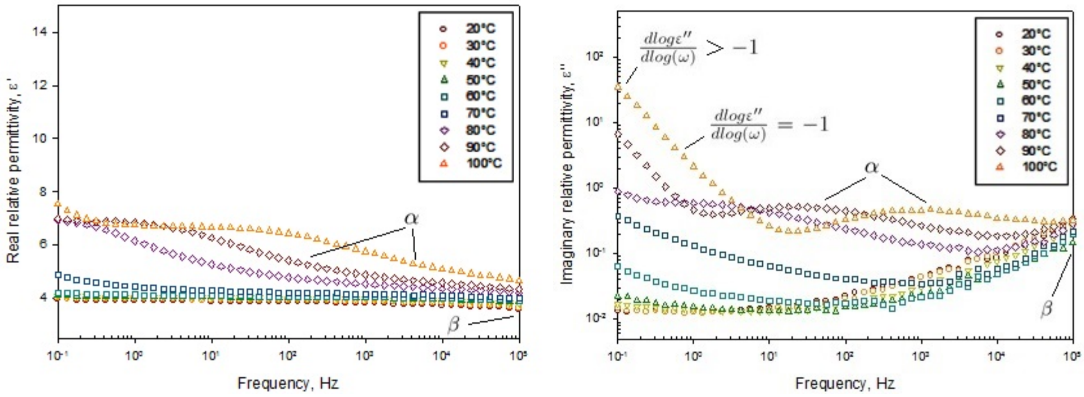

(a) ε′ vs. frequency for an unfilled system.

(b) ε″ vs. frequency for an unfilled system.

FIGURE 4.16: Dielectric spectra from an unfilled system.

The introduction of untreated nanosilica into the system shows a general increase in the relative permitivitty. The behaviour has also been observed by Plesa *et al* who sees an increase in the ε′ and attributes this phenomenon to the introduction of new dipoles that lead to interfacial polarisation at the nanofiller surface [167]. However, with the dispersion of treated nanosilicas, ε′ is expected to decrease as the strongly dipolar hydroxyl groups have been removed from the surface of the filler and replaced with organosilane chains which restrict polymer chain mobility at close proximity to the particle surface [104]. This is represented in ε′ data at T_g (Figures 4.17 to 4.18) which were obtained from ET0 to ET16.

For systems which contain fillers functionalised with a low quantity of organosilane (i.e. ET1), there may be an overall weaker bonding within the system and the tails from organosilane molecules may act to ‘block’ unreacted epoxy chains from bonding directly to the surface of the filler. This implies there may be a greater amount of free volume around each nanoparticle, where the unanchored end of the polymer has a greater freedom and allows it to resonate at higher frequencies [106]. This is supported by behaviour observed in Figures 4.17(a) and 4.17(c) where there is a shift in the α-relaxation at low frequencies (for ε′). The same α-relaxation (most obvious at 100 °C) is seen to move to lower frequencies in samples ET2 to ET8, where an increasing surface modification of the nanosilica results in enhanced interactions leading to reduced molecular mobility. In the case of ET16 and ET20, the α-relaxation is seen to shift slightly to higher frequencies, implying there is a small increase in polymer chain mobility, perhaps due to a thicker coupling agent graft which gives rise to an overall available movement. There are also spectral behaviours in ε' at temperatures above T_g that are specific to ET0, ET1 and ET20 (ET20 is in Appendix C). These indicate non-ohmic conduction at low frequencies where low frequency dispersion [161] or quasi-DC behaviour [180] causes ε' to increase with decreasing frequency. This behaviour supports the concept that an uneven organosilane graft (in the case of ET1) or a thick organosilane layer (due to condensation reactions in ET16 and ET20) exist for some samples, where mobile charges may be trapped in the increased free volume.

Furthermore, the introduction of nanosilica also leads to the emergence of a relaxation peak in ε'' at frequencies between 10^{-1} to 10^2 Hz, this feature has been noted in silica-epoxy nanocomposites by Couderc *et al* who attribute the additional peak to an α'-relaxation. They describe two possible reasons for the phenomena [106]; firstly, the relaxation may have occured as a result of moisture that may be on present in the interfacial layer between the nanofiller and the polymer matrix which will introduce a Maxwell-Wagner-Silliars effect; and secondly the α'-peak may be associated with the glass transition temperature of the interface itself, as seen by Fragiadakis *et al* [181, 182]. Similar to the data shown in Figures 4.17 and 4.18, the α'-peak observed by Couderc *et al* occurs at a higher frequency than that published by Fragiadakis *et al*, they suggest that this is due to weaker bonding between filler and matrix, and therefore a greater mobility of the interface in their samples. This may explain why the α'-peak becomes increasingly prominent for samples ET0 to ET2, where the effect of an increasing silica modification increases the bond strength between the filler and the matrix until an optimum graft of coupling agent is used; from ET4 this relaxation feature remains as prominent and indicates the nanosilica cannot be functionalised further. This is also reflected in the general shift of the α'-relaxation that moves to lower frequencies for samples which contain nanosilica that have been functionalised to a greater degree and is most obvious in data collected at 60 °C. The β-relaxation observed at high frequencies in ε'' is seen to increase with the degree of modification on the nanosilica, this represents a greater loss and implies that [$CH_2CH(OH)CH_2O$] possesses restricted chain mobility as there is a greater bonding strength to the nanofiller surface.

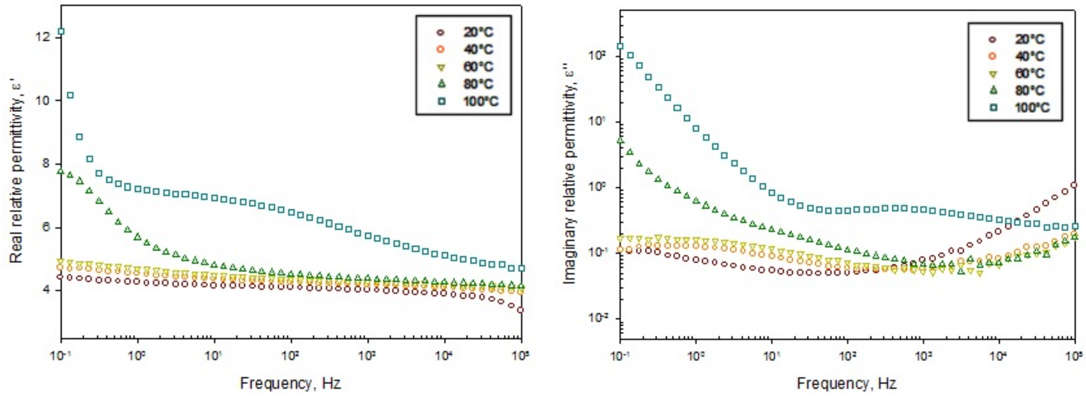

(a) ε′ vs frequency for ET0. (b) ε′′ vs frequency for EM0.

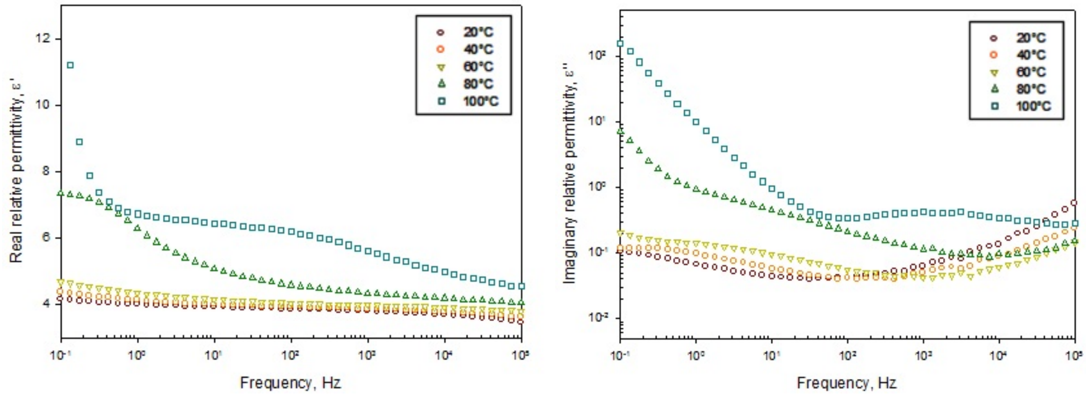

(c) ε′ vs frequency for ET1. (d) ε′′ vs frequency for ET1.

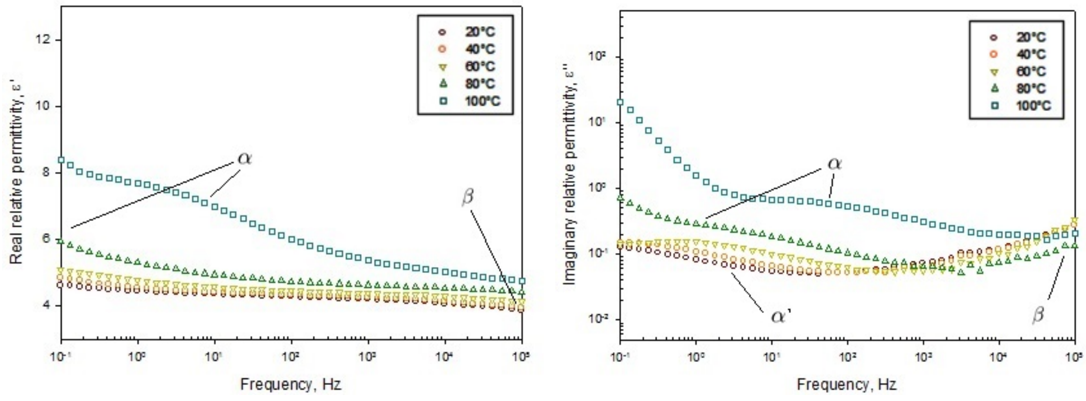

(e) ε′ vs frequency for ET2. (f) ε′′ vs frequency for ET2.

FIGURE 4.17: Dielectric spectra of nanocomposite systems ET0, ET1 and ET2 as a function of frequency, with respect to increasing temperature.

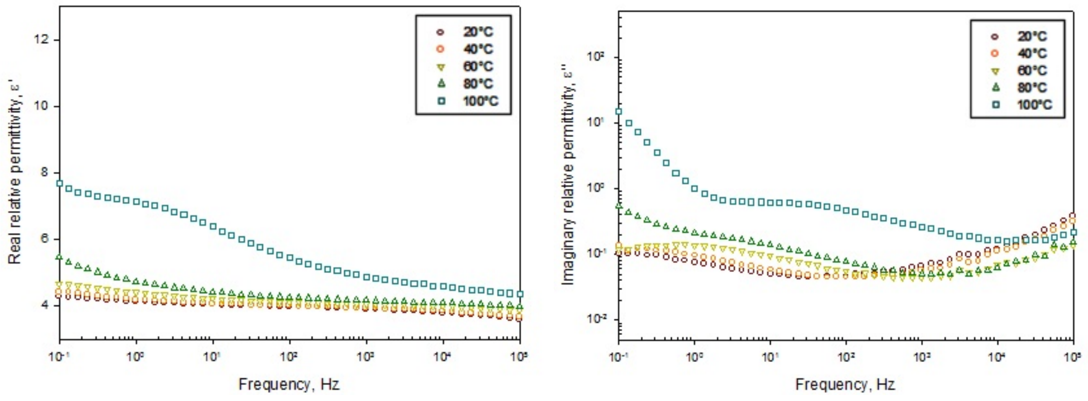

(a) ε′ vs frequency for ET4.

(b) ε′′ vs frequency for ET4.

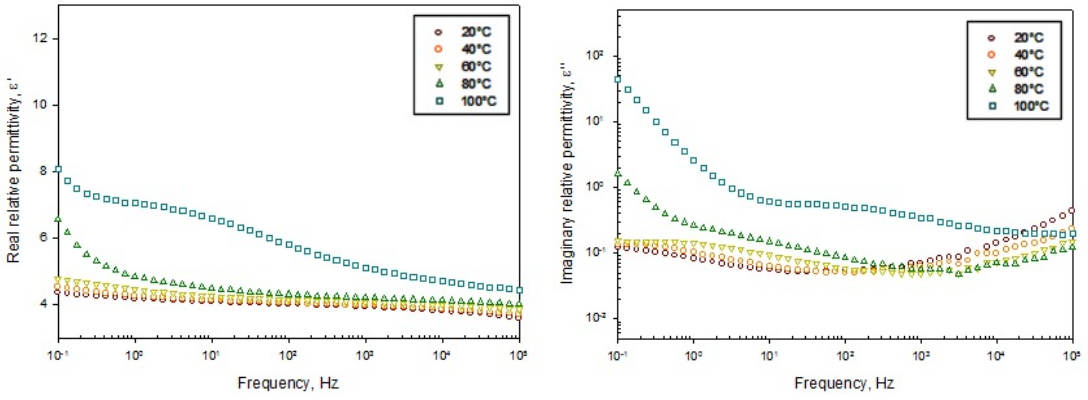

(c) ε′ vs frequency for ET16.

(d) ε′′ vs frequency for ET16.

FIGURE 4.18: Dielectric spectra for nanocomposite systems ET4 and ET16 as a function of frequency, with respect to increasing temperature

4.6 Chapter summary

The use of an anhydrous solvent in the modification process was sought to retard condensation reactions between organosilanes which occur due to the hydrolysis of the coupling agent in the presence of water. Spectroscopic techniques such as Raman spectroscopy and ATR-FTIR spectroscopy were used to confirm the surface modification of the filler. Although the former method did not provide any conclusive data, the infrared spectra showed a decrease of Si-OH bonds in the system which is an indirect measure of surface modification, as the hydroxyl groups are consumed by reactions with the coupling agent.

Combustion analysis confirms that there is an increased elemental fraction of carbon in the system that also indicates a successful organosilane graft on the nanofiller.

Scanning electron microscopy was used to analyse the dispersion state of the nanosilica-epoxy systems. It is seen that, for systems containing nanosilicas that have been functionalised with a higher concentration of Silane z-6040, there are fewer regions in which clusters of nanofiller can be observed and the aggregate size is seen to decrease. Although the systems do not reach the state where the filler is uniformly distributed throughout the system, the reduction in aggregation size is an indicator that the homogeneity of the nanocomposite is increasing, where isolated particles can be observed within the bulk. This means the interfacial region will increase in volume and occupy a greater fraction within the composite, this has an evident effect on the dielectric properties of the system.

For nanosilica samples which were modified with small amounts of organosilane, it was is assumed that the filler would possess non-uniform Silane z-6040 coverage that would result in poor dielectric properties of a nanocomposite system. Nanosilica functionalised with the optimum coupling agent quantity was expected to produce the best results, as the most efficient degree of modification would have taken place. As an anhydrous solvent was used in the functionalisation process, the restrictions on condensation reactions was assumed to prevent further surface modification for silicas that had been functionalised with an excess of Silane z-6040 and the unreacted surplus of coupling agent would be removed from the system via rigorous washing. The electrical investigations have shown that this is clearly not the case. The AC breakdown of the nanocomposite systems is seen to increase with the increasing functionalisation of nanosilicas; until now, it stood to reason that after reaching a maximum, the AC breakdown would remain of the same order for increasingly functionalised systems (as the degree of functionalisation had already reached a maximum). However the breakdown strength reaches a maximum (for the sample containing optimally functionalised nanosilica) and continues to decrease. Similarly, the trend in the differential calorimetric data and dielectric spectra show an increase in the glass transition temperature and relative permittivity (real and imaginary) until the system reaches a maximum, and decreases thereafter for epoxies that contain excessively functionalised filler within the system. Although it would be simple to assume that these behaviours are purely a product of the surface modification, the fluctuations in T_g behaviour imply there is a significant effect on the stoichiometry of the system, which acts to complete with the positive effects of filler funtionalisation.

As the mechanisms at the interface are yet to be fully understood, suggestion(s) are put forward as to why these types of behaviours are observed, even when anhydrous materials are used in the modification process.

- Firstly, the assumptions made in this chapter were that the use of an anhydrous solvent in the functionalisation process would restrict the condensation of the coupling agent, such that surface modification would reach an maximum and stop after an optimum Silane z-6040 graft was formed; despite this, there will be moisture in the environment (on containers or introduced into the system when being agitated in the sonication or shaking process) that will act to hydrolise the organosilane and promote the condensation of the coupling agent.

- Secondly, it is also worth consider the following, in the case where the system is completely anhydrous (remove moisture on the surface of containers, in the coupling agent, in the atmosphere etc...) the substitution mechanisms in the modification process would change for an increasing degree of Silane z-6040 concentration in the functionalisation solvent. The substitutions describe the attraction between an oxygen nucleophile on the substrate surface and a silicon cation in the backbone chain of the Silane z-6040. As glycidoxypropyltrimethoxysilane has three methoxy groups at the end of every chain, in the case of an optimum modification, it may be assumed that nearly every one of the three methoxy groups are attached to the surface of the silica.

  Now consider two neighbouring silane chains (A and B) that are in suspension about a number hydroxyl groups on the substrate surface. Figure 4.19(a). In the case where excess Silane z-6040 is used, the first chain (A) to react with the surface will possess a silicon with a lower positive charge (blue δ^+) than its unbonded neighbour (B). There will be competition for bonding with the remaining hydroxyl groups on the surface, however as the oxygen nucleophiles in the system will have an affinity to bond with the cations with the highest positive charge (red δ^{+}), the reaction is most likely to occur with unreacted methoxy groups, i.e. silane chain B.

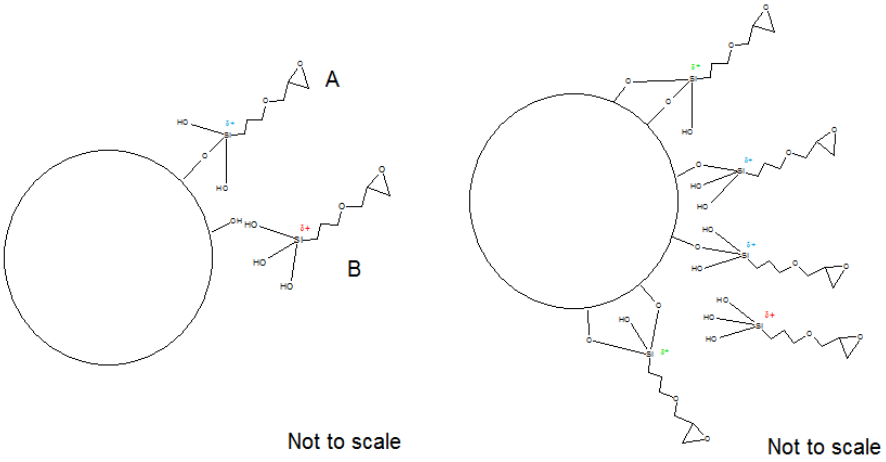

(a) One organosilane chain bonded, another attacking.

(b) Bonded organosilane chains to surface.

FIGURE 4.19: Suggested mechanism for behaviour at the filler surface.

This overall process where a number of silane chains is in competition with each other may result in some methoxy groups being still attached to the organosilane chain. If there is a high concentration of coupling agent, it may be the case a uniform layer of organosilane exists but could be much denser than once thought, 4.19(b). This theory is in contrast to the conventional understanding of surface modification as described in Section 4.1; it would explain the changes in glass transition temperature and dielectric spectra due to the free volume and/or chain mobility of the silane/methoxy groups, and alter the stoichiometry of the system. This study highlights the significant role of this last factor, which changes the overall behaviour of the composite and should be studied further.

Chapter 5

Confocal Raman Spectroscopy

Raman spectroscopy is an invaluable method used to identify the chemical groups within a specimen. Although some studies only require analyses from the sample surface, it is often the case that detail is needed from the within bulk. Confocal Raman spectroscopy is a technique that utilises a confocal microscope to allow a specimen to be scanned in three dimensions, its non-destructive nature provides versatility and makes this technique suitable for use in a range of fields ranging from from biology to art, and pharmacy to polymer science [183, 184, 185, 186]. This chapter examines confocal Raman spectroscopy as a tool in analysing dielectric films, specifically the photon scattering model proposed by MacDonald *et al* is scrutinised and developed. The model has been then applied to the nanosilica composites prepared in Chapters 3 and 4 such that any optical effects of introducing differently functionalised nanosilicas could be investigated.

5.1 A brief history into confocal Raman spectroscopy

It was long believed that confocal Raman spectroscopy had a resolution of 1 μm^3 when optically sectioning specimens [187]. However, the last two decades have seen a number of publications questioning the accuracy of confocal Raman spectroscopy and this has led to the reconsideration of how Raman data should be interpreted whilst using confocal Raman optics [184, 188, 189, 190, 191, 192]. Although the degree of resolution and precise form of confocal Raman depth profiles have routinely been described and modelled through the application of ray optics, the shortcomings in this approach have not been overlooked. Tabaksblat *et al* were amongst the first to address the distinct benefits and limitations of confocal Raman spectroscopy, where their early model simplifies issues by ignoring the effects of refraction at the air-sample interface, and scattering and absorption within the bulk [187]. They tested the ability of a confocal Raman system to differentiate spectra from layered samples, where their findings suggested that the optical properties of the microscope objective had a significant impact on the theoretical performance of a confocal Raman spectrometer and therefore influenced collected data. This research was fundamental in recognising how the resolution in confocal Raman spectroscopy was not as spatially accurate as once thought. In 2001, Michielsen described the degradation of axial resolution due to refractive index mismatches between the examined specimen and its environment [188]. The focal point was found to spread as the paraxial and marginal rays were no longer focused together in the desired sample plane. This publication also drew attention to the typical shape of a confocal Raman depth profile of a thin film; the intensity of the Raman response sees a gradual rise to a maximum at ∼20 µm below the sample surface as the focal point penetrates the top surface and focuses into the bulk, a monotonic decrease is observed as the stage is raised further and a steep decrease occurs as the focal point passes out of the film. Subsequently, a number of groups focused their research on laminated polymer systems in an attempt to explain the effects of refraction, understanding the observable 'mixed' spectra from two laminates when nearing film-film interfaces and model the nature of the Raman response from *and* around the focal point when using confocal optics. The loss in axial resolution has been discussed by many authors [184, 189, 193, 194, 195, 196]; Everall used geometric ray tracing methods to calculate the true point of focus, z_t, with respect to the apparent focal point below the sample surface, Δ_z, and the depth of focus, d.o.f. These can be calculated using equations 5.1 and 5.2 [193].

$$z_t = \Delta_z \left[m_R^2 \frac{NA^2\left(\tilde{n}^2 - 1\right)}{\left(1 - NA^2\right)} + \tilde{n}^2 \right]^{\frac{1}{2}} \tag{5.1}$$

$$\text{d.o.f} = \Delta_z \left[\left[\frac{NA^2\left(\tilde{n}^2 - 1\right)}{\left(1 - NA^2\right)} + \tilde{n}^2 \right]^{\frac{1}{2}} - \tilde{n} \right] \tag{5.2}$$

where m_R is the nominal radius and $\tilde{n} = (\frac{n_1}{n_2})$. From these equations, Everall showed that for a polymer system ($n_2 = 1.5$) studied with a NA of 0.95, the focal point of the system is elongated by a factor of 2.2. In the case where the microscope is focused 5 µm below the surface, the depth of focus is extended from 7.5 µm to 18.5 µm; this significant finding contradicts past publications which state the axial resolution is of the order of 2 µm [187]. The elongation of the focal region explained the collection of 'mixed' spectra at laminate interfaces which were a result of a combinations of spectrums from each laminate system. Everall concluded that great care should be taken when analysing data obtained with metallurgical objectives, and how the effects of refraction could be minimised with the use of an immersion medium and immersion objective [193].

As the use of oil immersion objectives were recommended to remove distortions due to refraction [191, 196, 197], many groups reported how the use of immersion oils allowed stage movements of the microscope to be directly related to the point of focus. This also provided an increase in spectral intensities due to the reduction of scattering at the surface and a lower refractive index mismatch between the lens system and specimen [194, 198]. These studies also highlighted the importance of choosing the correct immersion oil when using confocal Raman spectroscopy. Firstly, the refractive index of the oil should closely match that of the specimen to improve the image resolution and reduce the amount of refraction that occurs at the sample interface. Secondly, for convenience, the oil should be chosen such that the spectral characteristics are very different to those of the sample; this will make it easier to separate the spectra from different materials. Finally, spectral distortions can arise from an immersion medium that possess high fluorescence properties, so low fluorescing oils were advised [191].

Despite precautions to limit refraction, evidence of spectral contributions from out-of-focus planes were still observed whilst the microscope was focused within close proximity to laminate interfaces; in addition, there were no explanations for the presence of a characteristic maximum in intensity when focused ~20 µm below the sample surface. A turning point in confocal Raman spectroscopy occurred in 2003 when MacDonald *et al* published a study on semi-crystalline polymers [199]. This paper highlighted the importance of scattering, both at the sample surface and within the bulk, it demonstrated how transparent polymers with similar refractive indices produced notably different depth profiles and attributed this to the difference in bulk material characteristics [200]. They found that the turbidity of a material will have an impact on confocal Raman data, where an increase in turbidity contributes to an increasing loss of Raman signal with increasing focal depth due to a greater degree of scattering from the bulk [199, 201]. This is contrary to beliefs that spherical aberrations and refraction were solely responsible for Raman signal losses. A further in-depth discussion regarding confocal Raman resolution is available in Appendix D.1.

5.2 The photon scattering approach

In 2007, MacDonald *et al* proposed a novel concept which was based on the scattering process of Raman photons [202], this model has so far been able to address the unexplainable characteristics of confocal Raman depth profiles and describes the confocal Raman process entirely via physical processes; it accepts the notion that Raman photons may be generated from locations well away from the focal point, which is contrary to previous conceptions of the process.

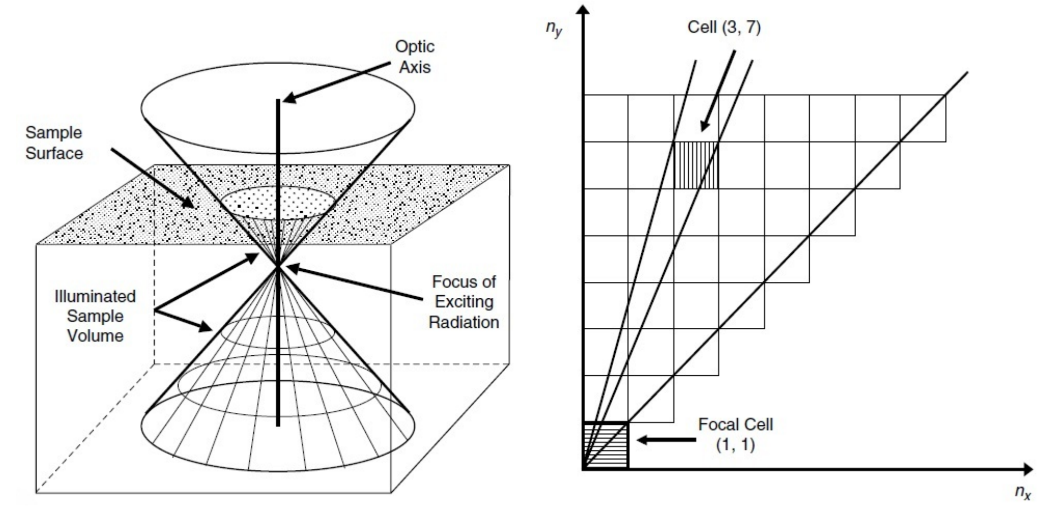

(a) (b)

FIGURE 5.1: a) Schematic diagram of extended volume from which Raman photons can be generated, b) Two dimensional view of cells. Reprinted from [202].

The numerical simulation derived from this approach incorporates parameters that relate to the particular optical properties of the irradiated material; these include the attenuation of photons within the bulk due to scattering and absorption processes, the efficiency with which Raman photons can be generated with the material *and* can be detected by the optical system. The probability of a Raman photon emerging from a trajectory such that it can be detected is dependent upon the point of generation within the illuminated volume, this is demonstrated by Figure 5.1 which shows how the illuminated volume extends along the optical axis of the system, n_z. The focal point is taken to be at $(1,1)$, where the shape of the illuminated volume is reflected in the mirror plane below this point [191].

Using cylindrical polar coordinates, the probability that Raman photons are detected from a general annular cell (n_r, n_z) is given as,

$$P_{r,z} = \frac{1}{2}\left\{\cos\left[\tan^{-1}\left(\frac{n_r - 1}{n_z}\right)\right] - \cos\left[\tan^{-1}\left(\frac{n_r}{n_z}\right)\right]\right\} \tag{5.3}$$

The contributing signal from each annular cell will be a result of the local intensity of the exciting radiation. Assuming for simplicity that the intensity of the beam is constant across its diameter, the probability that Raman photons are produced and detected becomes,

$$P_{r,z} = \frac{1}{2}K_e\frac{\Phi_p}{n_z^2}\left\{\cos\left[\tan^{-1}\left(\frac{n_r - 1}{n_z}\right)\right] - \cos\left[\tan^{-1}\left(\frac{n_r}{n_z}\right)\right]\right\} \tag{5.4}$$

where Φ_p is the total exciting photon flux and K_e is a constant.

The effects of scattering and absorption within the sample will reduce the intensity of the beam and serve to reduce the probability that Raman photons are detected. These factors are assumed to vary exponentially with respect to the depth below the sample surface,

$$P_{r,z} = \frac{1}{2}\left\{\cos\left[\tan^{-1}\left(\frac{n_r - 1}{n_z}\right)\right] - \cos\left[\tan^{-1}\left(\frac{n_r}{n_z}\right)\right]\right\}\left\{K_e\frac{\Phi_p}{n_z^2}\exp(-k_e)\Delta_z\right\}.\exp(-k_R)\Delta_z \tag{5.5}$$

where Δ_z is the depth of the cell below the sample surface and k_e and k_R are constants which characterise the rate of attenuation for incident photons and Raman photons within the material respectively.

Finally, on the assumption that the difference in the attenuation rate of incident photons and Raman photons is negligible ($\exp(-k_e) \approx \exp(-k_R)$), the production of Raman photons from each cell is calculated as,

$$R_{r,z} = A \left\{ \cos \left[\tan^{-1} \left(\frac{n_r - 1}{n_z} \right) \right] - \cos \left[\tan^{-1} \left(\frac{n_r}{n_z} \right) \right] \right\} \left\{ \frac{1}{n_z^2} \exp - 2k_e \Delta_z \right\} \tag{5.6}$$

where A is a constant.

The photon scattering model generated data which were in good agreement with the experimental data obtained from thin polymer films and produced profiles that closely matched semi-crystalline polymers with nominally equivalent refractive indices but different optical clarities [202]. A publication by Freebody *et al* demonstrates how the model can successfully predict the difference in the form of Raman depth profiles when using oil immersion objectives compared with dry objectives, and shows its compatibility with the reality of surface refraction [191]. However, depth profiles in this publication were generated using variable parameters chosen by the user where the attenuation coefficient k_e, was determined by visually observing the best fit to empirical data; this chapter sets out to develop a more rigorous method of finding the optimum parameters for the photon scattering model when fitting simulated data to Raman depth profiles. Three polymer systems will be studied, where the observed results will be compared to simulated data derived from an attenuation coefficient found via alternative experimental methods.

5.3 Materials and methodolgy

For comparison with studies published by MacDonald *et al* and Freebody *et al*, two polymers were used in this study [202, 191]. The first was a binary polyethylene blend containing 20% high density polyethylene (HDPE) and 80% low density polyethylene (LDPE). Both polymers were supplied by Dow Chemicals, where the former polyethylene is marketed as HDPE 35060E and the latter was a non-commercialised polymer used as a base resin for cable grade products [191]. The second polymer studied was Novolen 3200MC, this propylene/ethylene copolymer contains ∼0.3% dibenzylidene sorbitol (DBS) to improve its optical clarity [203]. These two semi-crystalline polymers are characterised by refractive index values of 1.54 [204] and 1.53 [191] (respectively), which are considered to be equivalent in this study [202].

Polymer film specimens were produced using a Graseby Specac hydraulic press equipped with heated thin-film attachment; the required polymer was heated past its melting point and pressed with a load of five tonnes. The thickness of each sample was varied by using spacers and adjusting the amount of polymer placed in the press. To vary the crystallinity within the system, the molten polymers were processed differently after pressing. Of the two polymers under investigation, three polymer systems were produced. Both Novolen 3200MC and the polyethylene blend were quenched directly from the melt to hinder the formation of lamellar structures. The third polymer system was prepared from polyethylene where the molten polymer was placed in an oil bath at 115 °C to allow HDPE spherulites to form via isothermal crystallisation, this was then quenched in water. This produced a system with HDPE-rich crystals amongst regions of crystalline LDPE [200]. Polarising optical microscopy images showing the different crystallinities of each polymer system are available in Appendix D.2.2. The notation PEQ, PEX and NQ will be used throughout the rest of this thesis to represent quenched polyethylene, isothermally crystallised polyethylene and quenched Novolen 3200MC respectively.

Two immersion oils were used in this investigation; firstly, poly(dimethylsiloxane) is a colourless, odourless liquid that is often used as a lubricant and insulating medium in high voltage systems due to its non-flammable nature. Obtained from Dow Corning, silicone oil has a stated refractive index of 1.41 and, in the case of this study, has a viscosity of 20 cSt [205]. The second immersion oil is formulated by Cargille Laboratories, a company that specialises in producing optical microscopy immersion oils to provide high resolution and improved brightness. Designated Oil A, the organic immersion oil possesses low fluorescence properties and therefore easily lends itself to use under the microscope. In contrast to silicone oil, Oil A has a viscosity of 150 cSt and a refractive index of 1.52 [204]. These materials were used in studies completed by Freebody *et al* [191].

5.3.1 Ultraviolet-visible spectroscopy

To establish an attenuation coefficient for each material, ultraviolet-visible spectroscopy was employed. Optical transmittance data were determined from polymer films of different thickness using a Perkin Elmer Lambda 35 dual beam UV-visible spectrometer. The system houses both deuterium and tungsten light sources, which are automatically selected to provide ultraviolet and visible light respectively. Data were collected for wavelengths in the range of 700 to 300 nm at intervals of 0.5 nm. The instrument was first calibrated for 100% transmission (with nothing in either the sample or reference beam paths) before the specimen of interest was mounted orthogonally to the beam axis and data were acquired. Transmittance data were first obtained with the samples in air to study the effects of refraction; this process was repeated for samples in an empty polymethyl methacrylate (PMMA) cuvette, a PMMA cuvette containing silicone oil, and a PMMA cuvette containing Oil A. Thus, a set of data was obtained for samples studied in 'air conditions' and another for those studied in 'oil conditions'. The derived transmittance data values were plotted as a function of sample thickness; the data analysis is discussed in Section 5.4.

5.3.2 Confocal Raman spectroscopy

The Raman response from various depths below a sample surface were obtained using the same Renishaw system described in Chapter 3. The spectrometer was set up in line with Renishaw recommendations for the confocal operation of the instrument and had a slit width of 15 µm and a CCD area of 4 pixels (image height) x 574 pixels (spectrometer range) which performed as a virtual pinhole in the back focal plane [191, 206]. A Leica x50 air objective (NA 0.75) and a Leica x50 immersion objective (NA 0.90) were used to obtain spectra with the laser focused at various positions above, within and below each specimen. At each position, spectra integrated from twenty 10 s accumulations recorded using Wire 3.2 software and processed with Sigmaplot 11.0.

5.3.3 Simulating the photon scattering approach

Prior to this study, Microsoft Excel was used to calculate the Raman response of various polymer systems in order to produce confocal Raman depth profiles [191, 202, 200]. This method required the user to firstly input parameters such as the total exciting photon flux, Φ_p, a constant, K_e and the attenuation coefficient, k_e, then manually adjust the stage position such that the simulation could sum the total Raman signal from each illuminated cell in the system. The value of the attenuation used to simulate the Raman response was the one which gave the best visual fit, as found via trial and error. However this process was labourious and time intensive, the process was optimised to increase efficiency by coding the mathematics into Matlab ®, where the optimum attenuation coefficient used to simulate depth profiles for every thickness of each polymer was obtained via a least mean squares method. The code calculates the Raman intensity at given points within a depth profile using a range of attenuation coefficient values, each calculated intensity value is compared with the experimental intensity value for the corresponding depths; as thicker films have a greater number of experimental data points that thin films, the absolute error for each profile is divided by the number of data points in each profile, these error values are summed for all thicknesses on that polymer system. The derived value for the attenuation coefficient for each polymer was that with the least mean error over all sample thicknesses and was used to print the simulated depth profiles as seen with experimental data in Section 5.4.3. The work completed in Matlab ® is available in Appendix D.7.

5.4 Results and discussion

5.4.1 Ultraviolet-visible spectroscopy

Figure 5.2 shows optical transmission data obtained from isothermally crystallised films of the polyethylene blend; here samples in air, in an unfilled cuvette, immersed in silicone oil and immersed in Oil A are represented by filled circles, filled triangles, unfilled squares and unfilled diamonds respectively. In deriving this figure, the data obtained under the four sets of experimental conditions described above were separately fitted to equation 2.6 [84, 85]. It is important to note that this equation is only valid in cases where the intensity of the transmitted beam is far greater than that of the beam which is scattered in the forward direction [86].

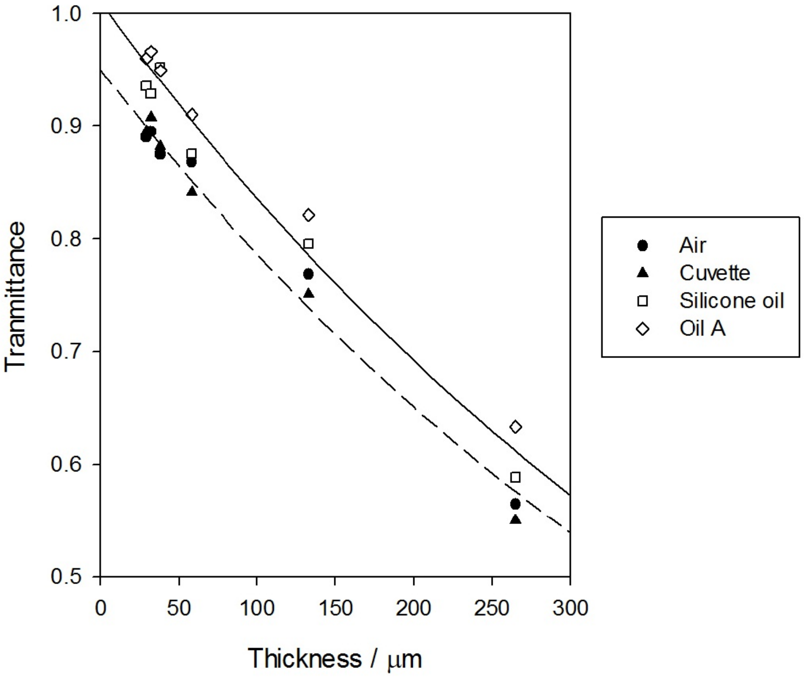

FIGURE 5.2: Optical transmission data obtained from PEX samples in air and oil (shapes) with Beer-Lambert Law fit (lines).

Examination of the derived *a* values indicate that the variability in these was not statistically significant as the values fell within the 90% confidence bounds of each other; the mean of the four values was therefore determined as being representative of bulk scattering in PEX, irrespective of experimental arrangement. This value for *a* was used to generate the best fit lines in Figure 5.2, where the solid line represents the best fit to all the points obtained with the specimens in an immersion oil. The dashed line represents all measurements made with the specimens in air. The process was repeated for the three systems considered and the resulting data are listed in Table 5.1. The corresponding figures for PEQ and NQ are in Appendix D.3, where the *a* values are significantly smaller than that of PEX. The *a* value obtained from NQ is the smallest which is to be expected as there is an induced optical clarity from the DBS agent [203]. Unfortunately, due to the high viscosity of Oil A, problems associated with air bubbles were often encountered when using this immersion medium (even with the application of vacuum pumping); results obtained from NQ films in Oil A were neglected due to poor conformity to equation 2.6. From Table 5.1, it is evident that conducting transmission experiments with the samples in air significantly reduces C in equation 2.6.

According to the Fresnel equations in Section 2.4, the beam intensity is attenuated by a factor Φ_s on entering and on leaving a parallel sided slab of material of refractive index n_s, where Φ_s is given as [86],

$$\Phi_s = \frac{4 n_s n_i}{(n_s + n_i)^2} \tag{5.7}$$

Thus for the materials considered here, which have refractive indices ~1.54, interfacial effects at an ideal air specimen interface would be expected to reduce the measured transmitted intensity by ~9%, compared with the case of oil immersion. This is in reasonable agreement with the data shown in Table 5.1.

Material	C (air)	C (oil)	a / µ m^{-1}
PEX	0.95 ± 0.01	1.01 ± 0.01	(1.89 ± 0.19) ×10^{-3}
PEQ	0.93 ± 0.005	1.06 ± 0.01	(6.74 ± 0.63) ×10^{-4}
NQ	0.919 ± 0.002	0.983 ± 0.001	(9.9 ± 1.7) ×10^{-5}

Table 5.1: A summary of the optical transmission coefficients obtained from UV-visible transmission data at a wavelength of 785 nm.

5.4.2 Confocal Raman spectra

The Raman spectra from each material studied were obtained at the beginning of the investigation, Figure 5.3 represents those from the two polymers and the two immersion oils considered. It was important to locate the spectral peaks within the spectra to avoid spectral interference when using an immersion medium. Comparing the spectra from both immersion oils, it is clear that in contrast to Oil A, silicone oil possesses few spectral characteristics which may interfere with those from polyethylene and Novolen 3200MC. There are two prominent features in PE which occur at 1288 cm^{-1} and 1123 cm^{-1}, these represent CH_2 twisting [207] and C-C skeletal stretching of carbon atoms [208] respectively; the most prominent peak for Novolen 3200MC is at 805 cm^{-1} which relates to C-C rocking [209]. The spectral contributions from Oil A fall in the same region as the spectra from the polymers in study and therefore silicone oil was chosen as the immersion medium as its main features are seen below 750 cm^{-1} with less pronouced peaks at 1400 cm^{-1}, 1250 cm^{-1}, 850 cm^{-1}, and 785 cm^{-1}, that would not complicate the overall spectra. Depth profiles for PE and NQ were obtained from spectral peaks at 1123 cm^{-1} and 805 cm^{-1} respectively as there were no overlapping of spectra from the immersion oil. The maximum intensity of the chosen Raman peak was plotted as a function of stage position for both dry and oil immersion objectives in order to generate depth profiles.

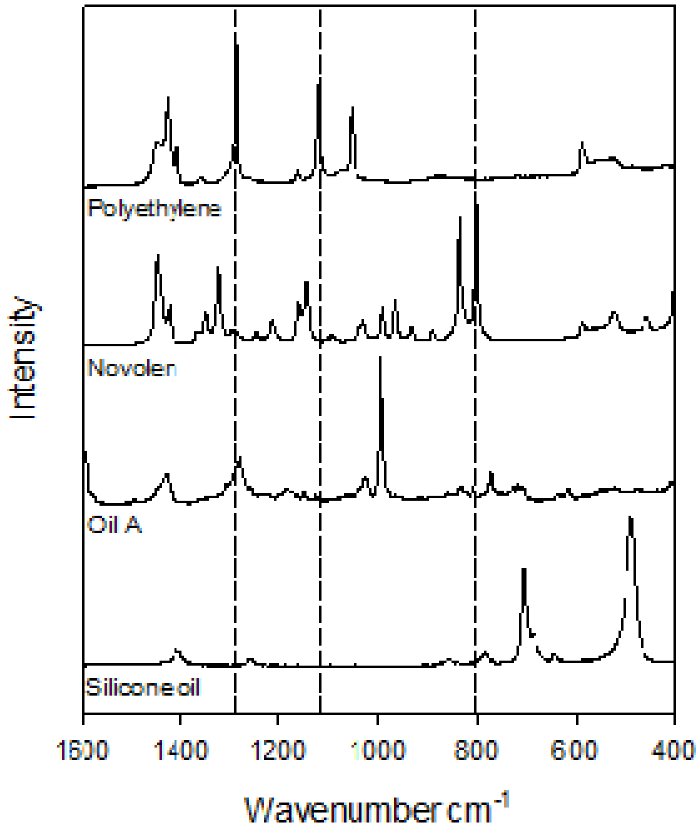

FIGURE 5.3: Raman spectra obtained from the polyethylene, Novolen 3200MC, silicone oil and Oil A.

5.4.3 Confocal Raman depth profiles

For depth profiles presented in this thesis, data obtained with the laser focused at the top sample surface were plotted at zero on the abscissa. Positive stage positions correspond to data obtained with the nominal laser focus below the sample surface and negative values of stage position relate to the data obtained from focal distances above the top sample surface. Each plot includes dashed and continuous lines which represent data derived via the numerical simulation based upon equation 5.6, in which A and k_e were treated as adjustable parameters. The dashed lines were produced using the attenuation coefficient obtained via the least mean errors method (k_e) discussed in Section 5.3.3, and the continuous lines were generated using values of attenuation coefficient derived from the UV-visible data (k_{ea}) in Section 5.4.1. For the remainder of this thesis, the values of attenuation coefficient found by the iterative method will be written as k_{ei}, whilst those calculated from UV-visible spectroscopy will be written as k_{ea}. As A is effectively determined by the exciting laser intensity, which varies somewhat from day-to-day, it was necessary to optimise this for each of the data sets shown.

Figure 5.4 shows a selection of Raman depth profiles acquired from three polymer systems with thickness 110 ± 5µm to 130 ± 5µm, whilst plots in Figure 5.5 compare the depth profiles for three different thicknesses for the same polymer (PEX). All profiles were obtained using a dry objective lens (x50, NA 0.75). For the thinner films, it was generally necessary to displace the depth profile predicted by the simulation by a small amount along the abscissa to optimise correspondence with the experimental data. This is an issue that has been highlighted previously [191] and is associated with the finite resolution inherent in the simulation. Although it is possible to increase the resolution numerically, the impact of the explicit omission of factors such as diffraction and spherical aberrations from the simulation become increasingly apparent.

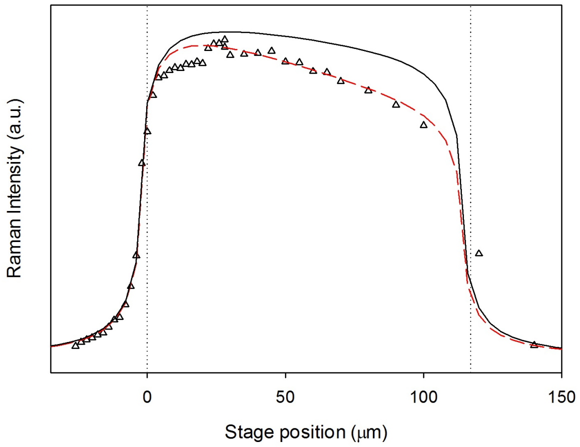

(a) PEQ film of thickness 117 μm.

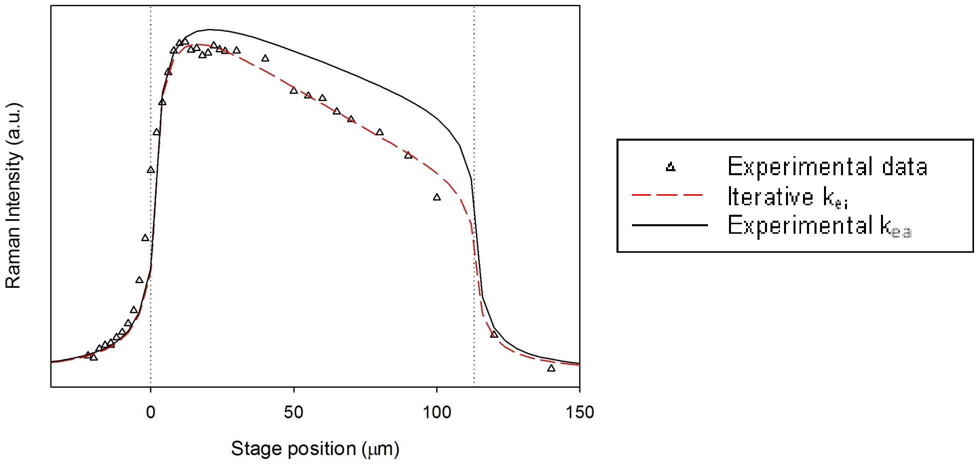

(b) PEX film of thickness 113 μm.

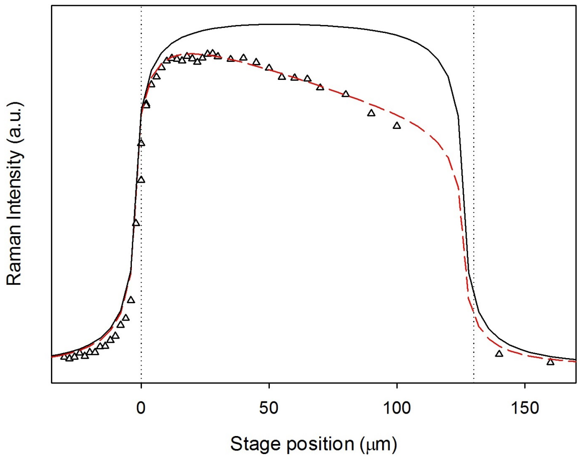

(c) NQ film of thickness 130 μm.

FIGURE 5.4: Profiles for different polymer films, (110 to 130) ± 5 μm in thickness.

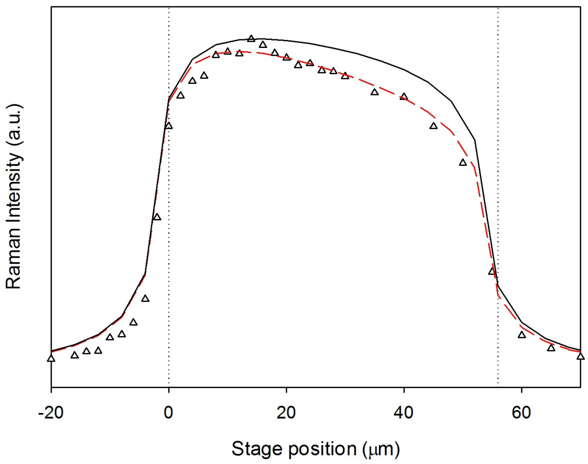

(a) PEX of film thickness 56 μm.

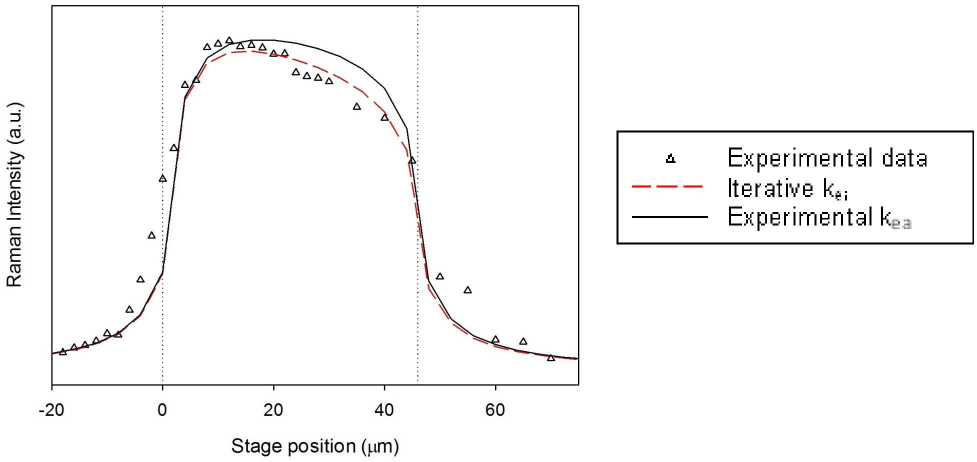

(b) PEX of film thickness 46 μm.

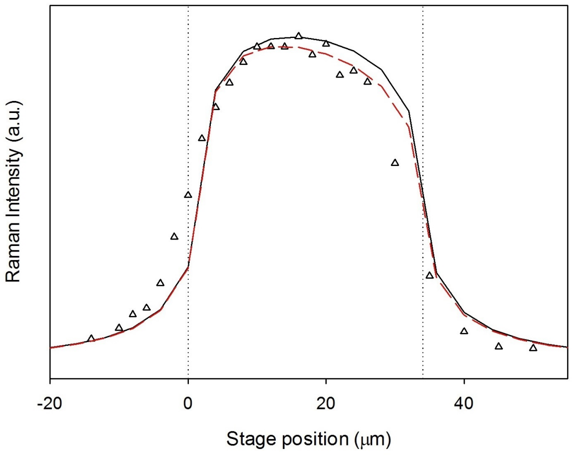

(c) PEX of film thickness 34 μm.

FIGURE 5.5: Depth profiles for PEX of different thicknesses in air (± 5 μm).

These figures demonstrate the capability of the photon scattering model; the simulation is able to account for the extent to which light is scattered in each morphologically different system, whilst using an attenuation coefficient derived via the iterative method, k_{ei}. The values of k_{ei} (calculated by the simulation) are listed in Table 5.2 and show a marked increase with the increasing scattering characteristics of the system. The remainder of the depth profiles for all polymer systems are available in Appendix D.4.

Material	k_{ei} / µm^{-1}	k_{ea} / µm^{-1}
PEX	$(10.50 \pm 0.01) \times 10^{-3}$	$(1.89 \pm 0.19) \times 10^{-3}$
PEQ	$(6.90 \pm 0.01) \times 10^{-3}$	$(6.74 \pm 0.63) \times 10^{-4}$
N32	$(6.20 \pm 0.01) \times 10^{-3}$	$(9.9 \pm 1.7) \times 10^{-5}$

Table 5.2: The attenuation coefficients used to simulate the dashed and continuous lines in depth profiles.

Despite being associated with the same physical processes, it is clear that the simulated data generated using k_{ea} (derived from UV-visible spectroscopy) has a poor correspondence to k_{ei} and the experimental data from each polymer system; this was thought to be due to a number of reasons. Firstly, with an air objective, significant additional scattering can occur at the air/specimen interface and can affect the form of the Raman depth profile obtained [191]. Secondly, refraction at both the upper and lower air/specimen interface causes the optical thickness of the specimen, t_o, to differ from the actual thickness of the specimen by a factor related to the refractive index of the sample material, n_2. Finally, if the stage is positioned such that the upper surface of the sample is imaged, then raising the stage a distance Δ_z, will cause the the paraxial and marginal rays to be focused at different planes within the specimen. The focal point is found to be elongated along the optic axis, such that the depth of focus (d.o.f) is given as [188],

$$\text{d.o.f} = \Delta_z \frac{n_2}{n_1} \left| 1 - \frac{\cos\left[\sin^{-1}\left(\frac{NA}{n_2}\right)\right]}{\cos\left[\sin^{-1}\left(\frac{NA}{n_1}\right)\right]} \right| \tag{5.8}$$

where n_1 is the refractive index of the immersion medium (air in this case) and NA is the numerical aperture of the objective lens [188]. Consider the consequences of refraction for a polyethylene film of thickness 200 µm in air, refraction at the upper surface will lead to an optical specimen thickness of ∼130 µm. If the nominal focal point were focused 100 µm below the upper surface, the paraxial ray would be focused at a depth of 154 µm, whilst the marginal ray would be focused at a depth of 202 µm (according to equation 5.8), such that it is 2 µm below the lower sample surface. However, if the stage were raised by 131 µm, then the paraxial ray would be focussed at the lower surface such that between stage positions of 100 µm and 130 µm, the focal spread would progressively emerge from the sample's lower surface. The consequences of all the effects described above make it increasingly difficult to compare the k_{ea} obtained by UV-visible spectroscopy and the Raman depth profile data obtained in air.

5.4.4 Oil immersion and the refractive index mismatch

Past publications have employed immersion oils to dramatically alleviate issues associated with surface scattering and refraction effects [191, 194, 197, 198] and therefore the use of an immersion oil proved to be the next step forward in the study of polymer films. In the case of silicone oil, the minimal interference between this immersion spectrum and polyolefin spectra has meant that the separation of these spectra are more convenient to use over Oil A. However, silicone oil ($n = 1.41$) is not a perfect match to the refractive index of the two polymers used ($n \sim 1.54$), and while it has been shown that this is not a problem as far as the elimination of surface scattering effects is concerned [202], it is necessary to consider how influential this may be with respect to surface refraction effects. Figure 5.6 shows plots of film thickness, t_R, measured using a micrometer, against the optical thickness for the same film (using the microscope), t_o. The series of data are for PEQ, PEX and NQ, and are represented by circles, squares and triangles respectively. The unfilled symbols are for data obtained in air, whereas the filled symbols are those immersed in silicone oil. In each case, the PE and NQ data sets overlap, as would be expected based upon their refractive indices; all data for each immersion medium have therefore been combined in generating the best fit relationship between thickness and optical thickness, assuming that these two quantities are related by:

$$t_R = \Psi t_o \tag{5.9}$$

where Ψ is a constant of proportionality that stems from refraction at the specimen surface in oil.

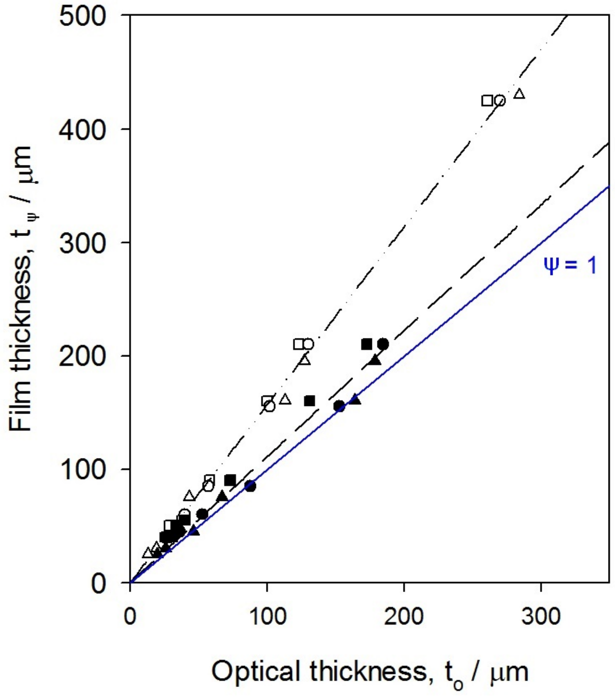

FIGURE 5.6: Film thickness t_R vs optical thickness t_o.

Table 5.3 lists the derived Ψ values and compares these with the relevant refractive index contrast values.

Immersion medium	Ψ	n_s/n_i for PE	n_s/n_i for NQ
Air	1.568± 0.015	1.54	1.53
Silicone oil	1.111± 0.025	1.092	1.085

TABLE 5.3: Values of the constant of proportionality and refactive index contrast between the n_s and n_i.

Although it has been previously implied that the refractive index of the immersion oil has very little effect on the refraction effects at the surface of the system (i.e. $n_{siliconeoil}$ and n_{OilA} are equivalent) [202], the data from Table 5.3 show $\Psi \neq 1$ for silicone oil. Therefore the stage movements needed to be corrected to provide reliable values of focal depth whilst depth profiling using silicone oil as an immersion medium, this is not required for profiles obtained for systems in Oil A as $\Psi = 1$ within certainties.

To examine the effect of focal blurring on the experimental response, confocal Raman depth profiles were acquired from a 82 µm thick polyethylene film whilst immersed in silicone oil and Oil A. Raw depth profile data obtained from a PEX sample immersed in Oil A (triangles) are presented together with (corrected) data obtained in silicone oil (squares) in Figure 5.7, the data sets have been normalised with respect to intensity. In this figure, zero on the abscissa again corresponds to the top of the film, while the vertical dashed line indicates the position of the lower surface, as determined by the micrometer.

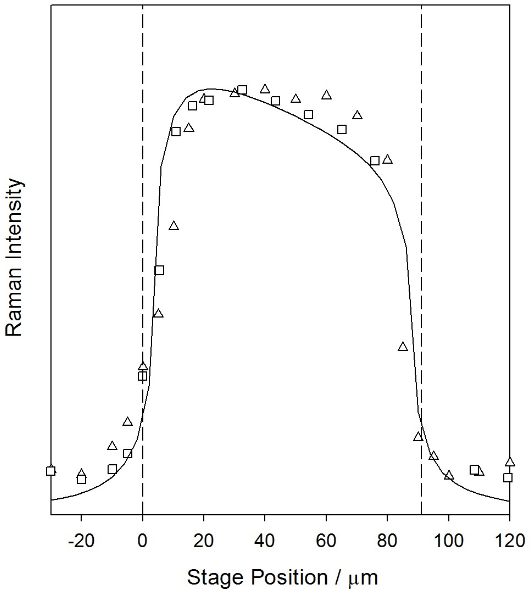

FIGURE 5.7: Example of a depth profile from a film of PEX immersed in Oil A and silicone oil, thickness 82 ± 5 µm.

The Raman profile data agree with the physical limits of the film when immersed in Oil A, which is to be expected as the refractive index mismatch is kept to a minimum. For the same PEX system immersed in silicone oil, it is found that the empirical data agrees with the physical limits of the film provided the abscissa is re-scaled (using the appropriate correction factor in Table 5.3) to account for the displacement of the nominal focal point whilst the microscope is focused within the sample. Similar adjustments were also made for conditions when microscope was focused below the lower surface of the specimen, when the light would be refracted a second time and another shift in the focal point would occur. The true point of focus, z_t, when focused below the second sample surface is obtained by equation 5.10;

$$z_t = t_R + \Delta_z - t_R \frac{n_3}{n_s} \tag{5.10}$$

where t_R is the film thickness, Δ_z is the apparent focal point and n_3 is the refractive index of the third medium. In this investigation, $n_3 = n_i$ as silicone oil was above and below the sample. With these changes to the abscissa, the form of the decay within the bulk of the sample is equivalent (within experimental error) when the system is immersed in both silicone oil and Oil A. This indicates that under these experimental conditions, focal blurring does not have a major effect on the data.

5.4.5 Confocal Raman depth profiles - Oil immersion

With the correct adjustment of the abscissa, the refractive index mismatch between sample and immersion media are considered negligible, for this reason it was justifiable to use silicone oil as an immersion medium as its spectral peaks were less likely to interfere with those of the polymer systems. Figures 5.8 to 5.9 represent a small sample of Raman depth profiles obtained from thin polymer films of comparable thickness, whilst immersed in silicone oil. For all obtained whilst the sample is immersed in oil, the background signal was removed from the spectra by subtracting the average magnitude of the background noise. The empirical data show the typical rise in intensity as the focal point passes through the top surface of the film and lowers ∼20 µm into the bulk. The attenuating effects of the material then become apparent as the decline in Raman intensity is observed. As the focal point nears the lower sample interface, the Raman intensity drops significantly and continues to decrease at a slower rate when the focal point is focused below the second surface. Figures 5.9(a) and 5.9(b) show unusual characteristics between 0 µm and 20 µm, where the intensity is not seen to rise to a maximum as the other profiles do. This may be due to an unlevelled region of the polymer film which is seen to distort the generic Raman depth profile form. Although the surface for all the polymer systems here are smooth, it has been seen that abraded samples provide a different Raman response; Freebody found that the greater the surface abrasion, the greater the attenuation of the Raman response within the bulk of the sample [210]. Further confocal Raman depth profiles obtained from polymer systems of different thicknesses are available in Appendix D.6.

Simulated Raman depth profiles were obtained using the attenuation coefficients k_{ei} (dashed line) and k$_{ea}$ (solid line), the values are shown in Table 5.4. The iterative values of k_{ei} derived from samples immersed in oil resembles k_{ea} more closely than the k_{ei} values derived from samples in air. This supports the fact that the use of an immersion oil mitigates the effects of refraction and scattering at the surface. Despite this, there is still a significant difference between the simulated results using the different values of attenuation coefficient. Specifically, the use of k_{ea} (a physically measured value via UV-visible spectroscopy) in the model gives a greater attenuation than would be anticipated. This implies that the scattering and attenuation seen in the UV-visible spectrometer and confocal Raman spectroscopy are not equivalent, or else the physics included in the simulation is fundamentally deficient.

Material	k_{ei} / µm^{-1}	k_{ea} / µm^{-1}
PEX	$(1.0 \pm 0.01) \times 10^{-3}$	$(1.89 \pm 0.19) \times 10^{-3}$
PEQ	$(2.0 \pm 0.1) \times 10^{-4}$	$(6.74 \pm 0.63) \times 10^{-4}$
NQ	$(2.0 \pm 0.1) \times 10^{-4}$	$(9.9 \pm 1.7) \times 10^{-5}$

TABLE 5.4: The attenuation coefficients used to simulate the dashed and continuous data using k_{ei} for samples in oil and k_{ea} respectively.

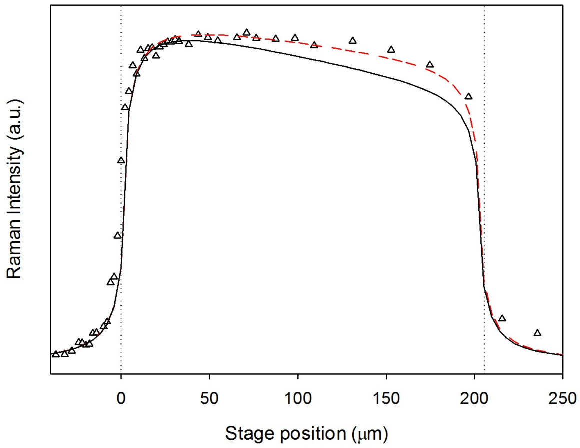

(a) PEQ film of thickness 185 μm.

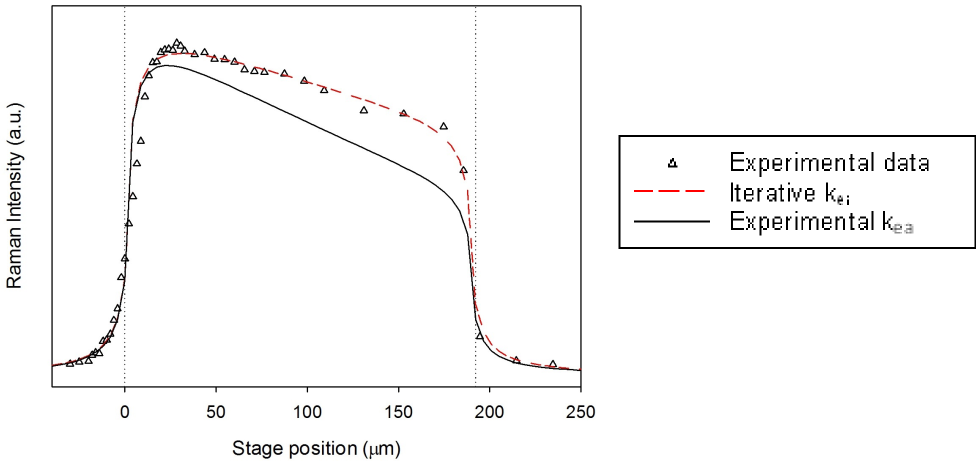

(b) PEX film of thickness 173 μm.

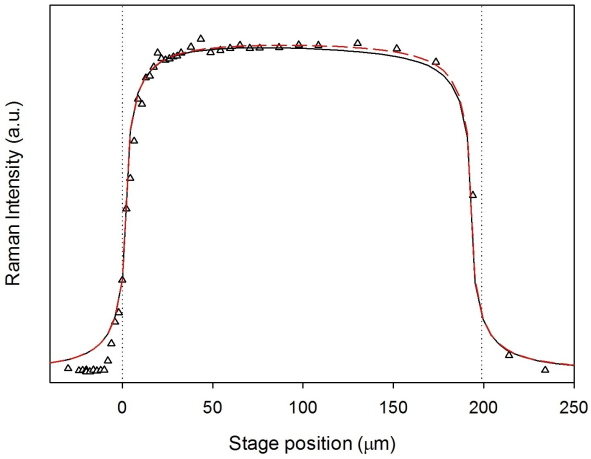

(c) NQ film of thickness 179 μm.

FIGURE 5.8: Profiles for different polymer systems (175 to 185) ± 5 μm in thickness.

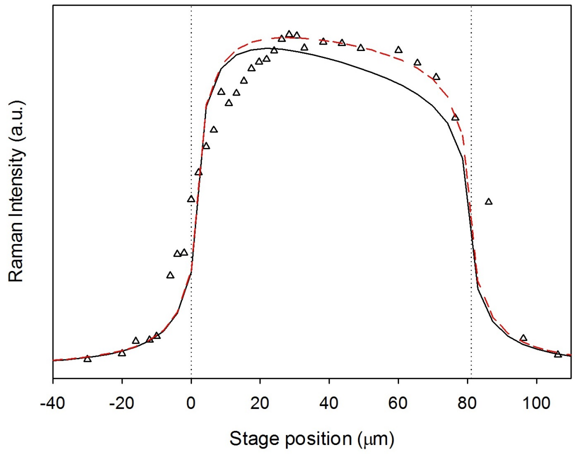

(a) PEX of film thickness 73 μm.

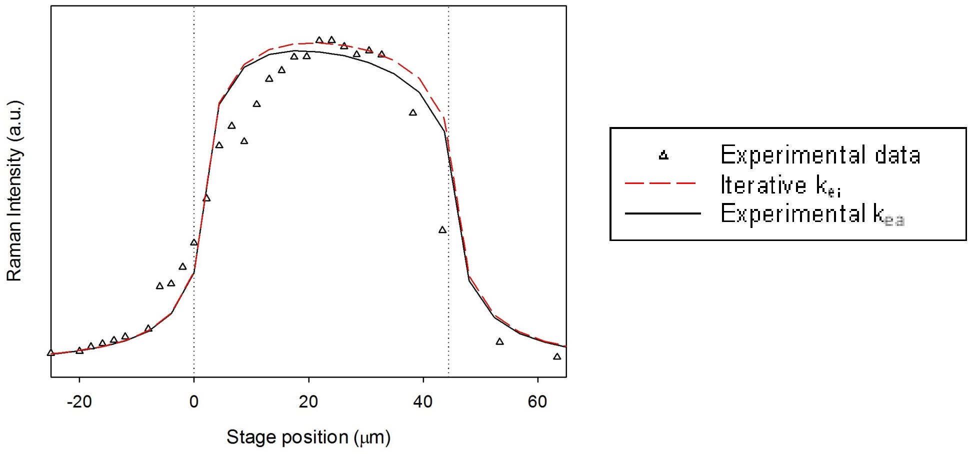

(b) PEX of film thickness 40 μm.

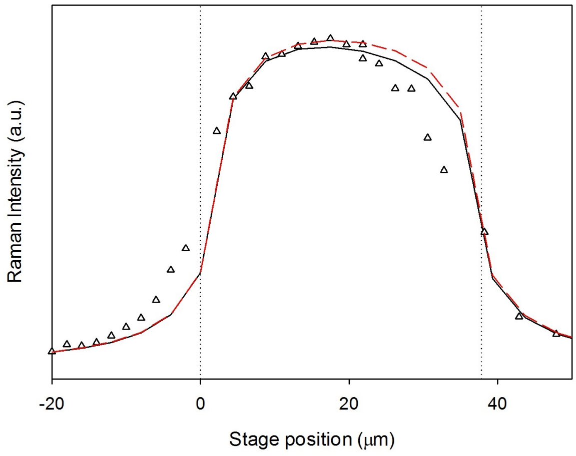

(c) PEX of film thickness 34 μm.

FIGURE 5.9: Depth profiles for PEX of various thicknesses in silicone oil (± 5 μm).

5.5 The photon scattering approach: The revised model

Regardless of the capability of the photon scattering approach to simulate model data which closely matches the experimental Raman depth profiles, the attenuation coefficients (k_{ei}) required to simulate these Raman depth profiles are significantly lower than those values obtained via UV-visible spectroscopy (k_{ea}). That is to say, the simulated profile data using k_{ea} provides poor correspondence to empirical data, where the samples show a lower rate of attenuation than what has been derived from UV-visible data. One of the initial premises of the photon scattering model was that the photon flux was soley dependent on an extinction rate based on the forward transmission of photons within the system, the original equation 5.6 includes two scattering terms which are represented mathematically as signal attenuation,

$$\exp(-k_e \Delta_z) \tag{5.11}$$

$$\exp(-k_R \Delta_z) \tag{5.12}$$

The former relates to the attention of the incoming photon flux into the sample whilst the latter relates to the attenuation of the excited Raman photons as they exit the sample. Equation 5.6 assumes that these two different processes are physically and mathematically equivalent. However, from this study we acknowledge that the Raman scattering process is a complex one; it is evident from experimental data (shown in Figures 5.8 and 5.9) that incident photons within the Raman process are attenuated to a lesser degree than predictions from optical transmission data. Evidently, alternative processes are at work which have yet to be considered. To account for an increased Raman photon count in the simulation, the following factors were taken into consideration;

1. Any incident photon may generate a Raman photon anywhere within the illuminated volume.
2. Regardless of where the Raman photon is generated, if that Raman photon possesses a trajectory which is co-linear to another Raman photon that is able to be detected, it will contribute to the Raman spectrum.

3. Incident photons which are scattered prior to Raman photon generation, may still have the capacity to elastically interact with the sample and generate a Raman photon providing their trajectory remains within the illuminated volume. This implies that not all scattered photons will be lost to the system.

Within the scope of this study, the model has been revised such that the exciting beam is attenuated less significantly than would be anticipated by the original model; within an illuminated confocal Raman system, any photons that scattered from one cell into another cell, that is also within the illuminated volume are still available to induce excitation and may contribute to the total Raman intensity. Figure 5.10 shows how an incident photon may interact to generate a Raman photon; in case a), the incident photon (blue arrows) is scattered out the illuminated volume such that it is not detected by the CCD (red arrows) b) represents a generated photon that adopts a trajectory that allows detection by the CCD and c) shows how an incident photon may be scattered to another position in the illuminated volume before interacting and producing a Raman photon.

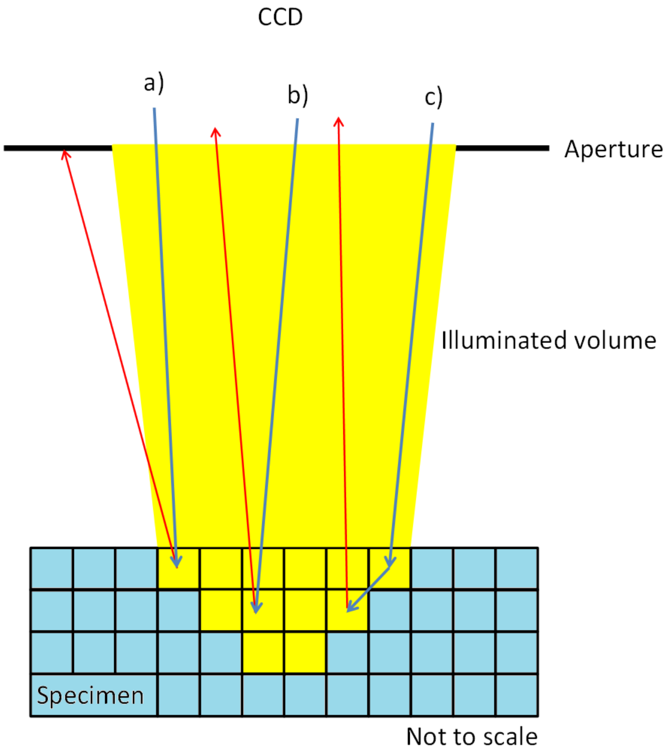

FIGURE 5.10: Incident photons generating secondary and Raman photons which are collected by the detector.

Consider an illuminated volume within a sample, where the focal point is focused at a plane j. If each plane is a slice in which the photon flux changes (due to scattering and attenuation), the photon flux that enters slice j, Φ_{pj}, is written as a product of the photon flux that has entered the previous slice $(j+1)$, $\Phi_{p(j+1)}$, and an attenuation factor, $\exp(-k_e)$,

$$\Phi_{pj} = \Phi_{p(j+1)}\exp(-k_e) \tag{5.13}$$

Such that the change in flux, $\Delta\Phi_p$, can therefore be written as;

$$\Delta\Phi_{pj} = \Phi_{p(j+1)}\left[\exp(-k_e) - 1\right] \tag{5.14}$$

$$\Delta\Phi_{pj} \propto \left[\exp(-k_e) - 1\right] \tag{5.15}$$

Mathematically, a straightforward method to reduce this loss in flux would be to divide $\Delta\Phi_p$ by an arbitrary quantity greater than unity. However, this is seen to be physically unrealistic as there is a low probability that a scattered photon will enter an adjacent layer, interact to excite a Raman photon and reaches the detector. Therefore the change in flux is chosen to be modified as below,

$$\Delta\Phi_p \propto \frac{\left[\exp(-k_e) - 1\right]}{n_z^{l_e}} \tag{5.16}$$

where l_e is a constant that is not material dependent. Evidently, there is no justification per se for adopting this particular approach other than it provides a convenient mathematical way to test the veracity of the concept that is represented schematically in Figure 5.10.

Figures 5.11 and 5.12 present the data obtained using the revised model simulated using the attenuation coefficient k_{ea} such that it can be compared with empirical data. The revised model shows a significant improvement in modelling the confocal Raman response when depth profiling thin polymer films. The original photon scattering approach generated depth profiles with a greater attenuation rate than the experimental Raman response when implementing a physical value of attenuation (k_{ea}). The revised model adjusts the change in flux through a layer by a factor of n_z^{le} and reduces the overall amount of attenuation through the bulk of the sample to provide a closer fit to the experimental data. The value of l_e used in *all* simulations for the revised model was set at 0.5; there is no obvious reason for choosing this value, other than it provides depth profiles which closely resemble experimental data for all polymer types over all thicknesses. However, it does imply that there is underlying physics which still need to be considered, such as the changes in beam intensity as a function of distance from the optical axis. This is a reasonable assumption as other authors have shown that this factor plays a significant role in the intensity of the Raman response [189, 190, 193, 197]. Depth profiles and simulated data for a range of polymer films are available in Appendix B.

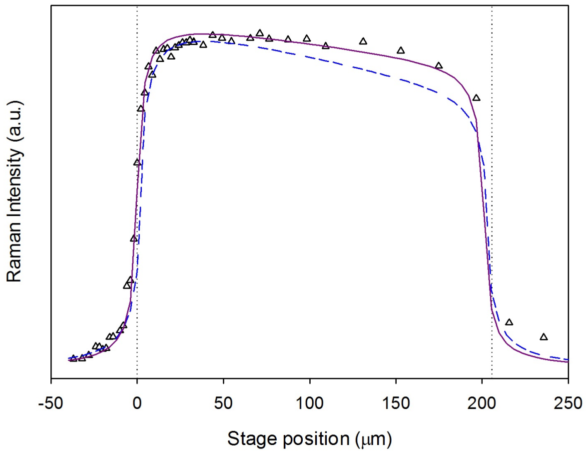

(a) PEQ film of thickness 185 µm.

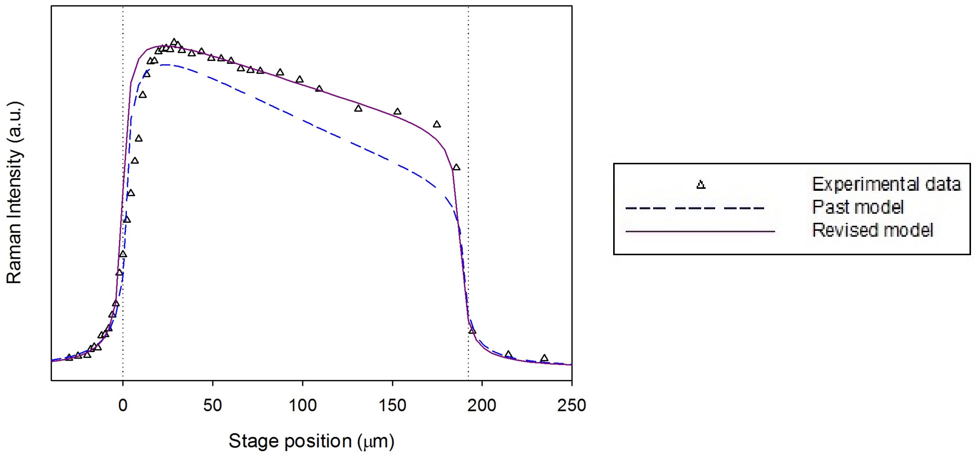

(b) PEX film of thickness 173 µm.

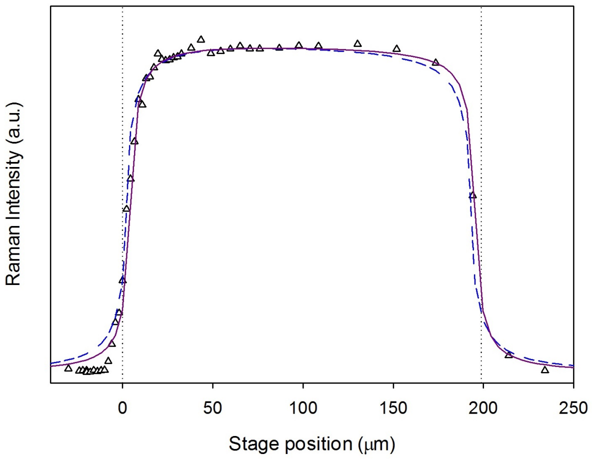

(c) NQ film of thickness 179 µm.

Figure 5.11: Profiles comparing different polymer systems (175 to 185)± 5µm in thickness.

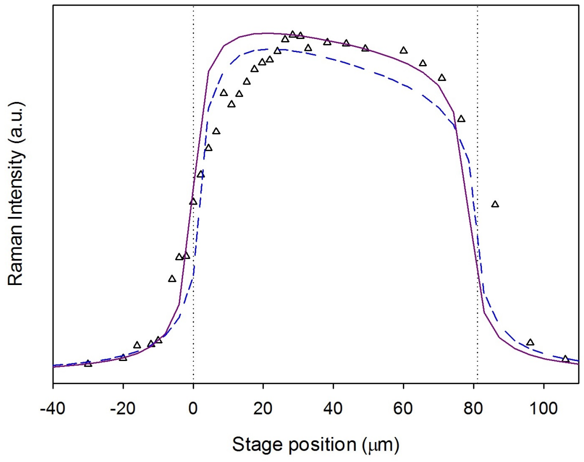

(a) PEQ of film thickness 73 μm.

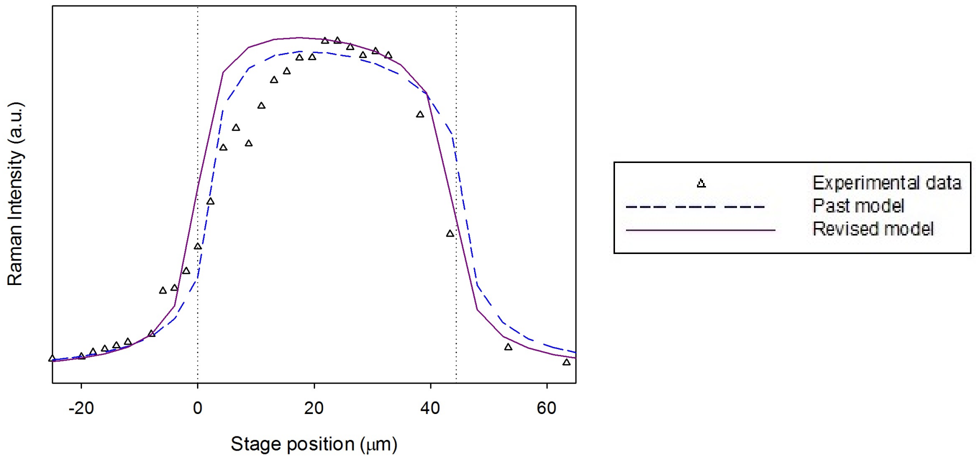

(b) PEQ of film thickness 40 μm.

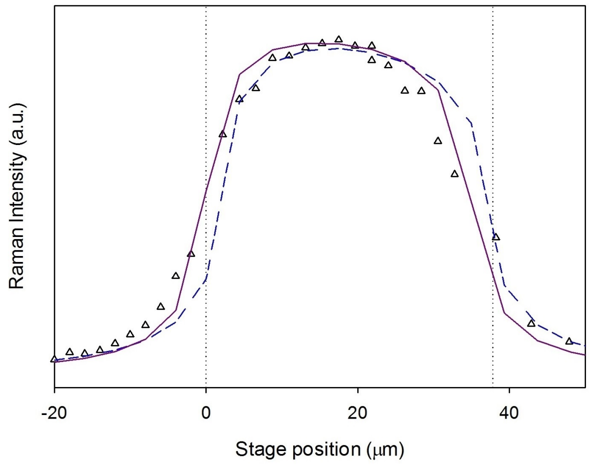

(c) PEQ of film thickness 34 μm.

FIGURE 5.12: Depth profiles for PEX of different thicknesses in silicone oil (± 5μm).

5.6 Confocal Raman spectroscopy and nanodielectric films

The studies into confocal Raman spectroscopy was extended to the nanodielectric films prepared in Chapters 3 and 4. As the resolution of this technique is on the scale of microns, it was not the intention to use this method to probe the interface directly, but to investigate the optical effects of introducing nanofillers into an epoxy matrix, and analyse the influence of varying the interface. Depth profiles were obtained from five epoxy systems; the Raman response of each focal position within the sample were taken with respect to the peak at 1609 cm^{-1} (associated with the stretching of the phenyl ring) [110]. The data obtained from unfilled epoxy is represented in Figure 5.13 which shows the typical form from a thin film. There is increase to maximum as the stage is raised by ~20 µm and monotonically decreases until the focal point nears the second oil-sample interface. The intensity drops significantly until the point of focus is moved out of the sample, where the Raman signal decreases at a slower rate.

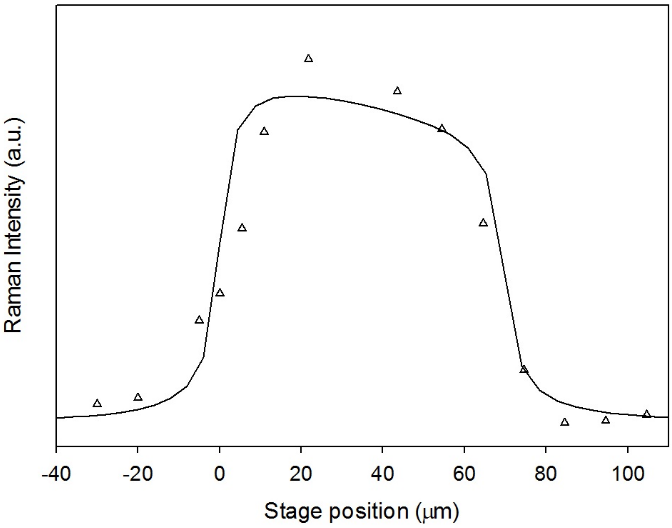

FIGURE 5.13: Unfilled system film of thickness 65 µm.

Figures 5.14 and 5.15 represent the confocal Raman depth profiles obtained from filled epoxy films (EM2, EM16, ET2 and ET16). With the addition of nanofiller, the rate of attenuation was expected to decrease as the nanoparticles introduce a degree of turbidity. However, it is clear from these data that introduction of 2 wt.% functionalised nanosilica has no effect on the optical properties of the epoxy system, this may be due to the inhomogeneity of the nanocomposite, where there is no guarantee that the focal point of the confocal Raman system will intersect nanofiller as it passes through the film.

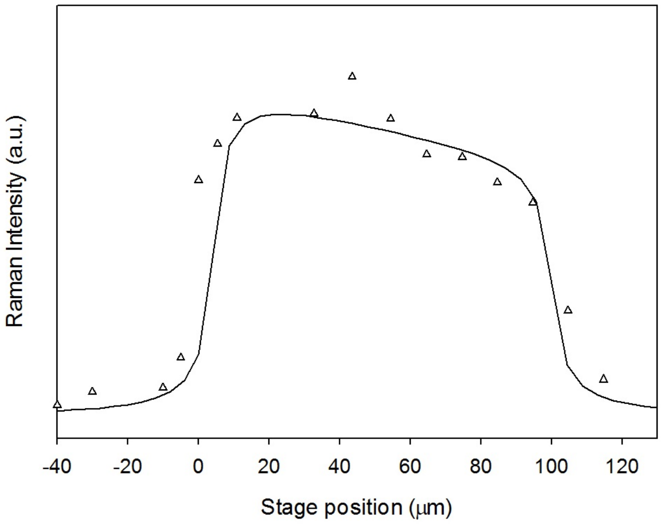

(a) EM2 film of thickness 88 μm.

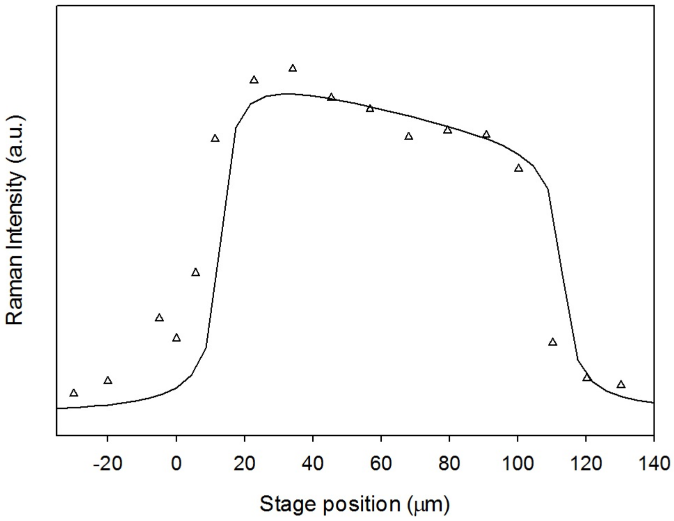

(b) EM16 film of thickness 93 μm.

FIGURE 5.14: Raman response for nanocomposites containing hydrously functionalised nanosilica.

Despite this, the revised photon scattering approach is able to predict the Raman response of the nanodielectric films containing 2 wt.% of nanosilica. The solid line shows generated data from the photon scattering simulation; the value of attenuation coefficient, k_{ea}, used to fit these lines were obtained via UV-visible studies, where transmittance data (at 785 nm) was fitted to the Beer-Lambert law. The k_{ea} was measured to be (2.43 ± 1.51) x 10^{-3}µm.

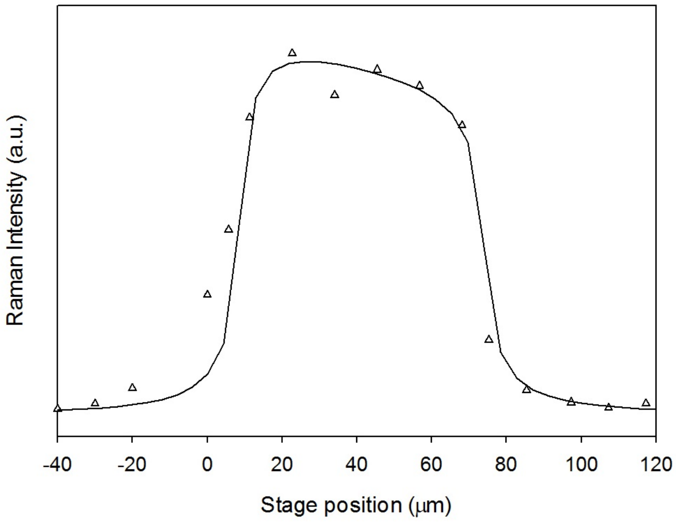

(a) ET2 film of thickness 63 µm.

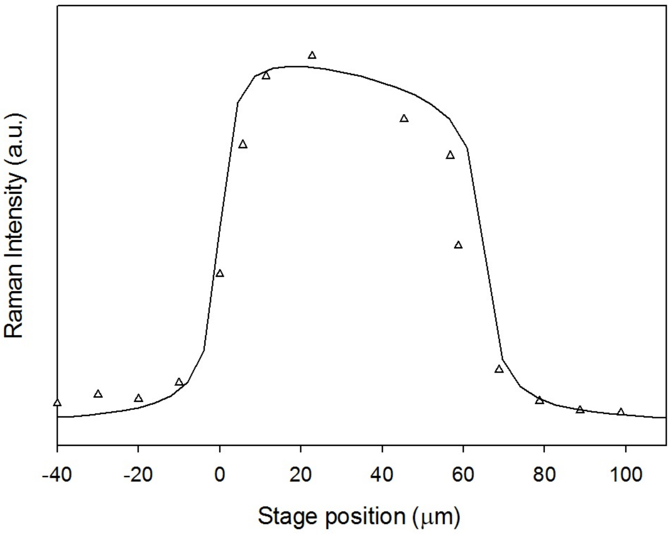

(b) ET16 film of thickness 61 µm.

FIGURE 5.15: Raman depth profiles from epoxy films containing anhydrously functionalised nanosilica.

5.7 Chapter summary

This chapter investigates confocal Raman spectroscopy as a method to examine thin dielectric films. Whilst past models were based on ray tracing geometry to include the effects of refraction or diffraction [184, 188, 189, 190], these failed to predict the form of a depth profile successfully when depth profiling thin polymer films. This investigation focuses on the novel photon scattering approach proposed by Macdonald *et al*, where confocal Raman depth profiles were completed on three polymer systems in both air and using oil immersion, such that the simulation could be applied and tested against the empirical data. The values for the attenuating factor were calculated by finding an attenuation coefficient with the least mean error; these values of attenuation coefficient (k_{ei}) were able to produce depth profile curves that closely matched the experimental profiles whilst the samples were in air and immersed in oil. The study investigated the use of a mismatched immersion medium and its practical effects on the system, where the focal point was elongated along the z-axis. This issue was easily resolved by adjusting the abscissa appropriately. However, it was found that simulated results using an attenuation coefficient, k_{ea} (derived from physical experiments), implied the attenuation coefficient was significantly greater than that obtained via the confocal Raman spectrometer.

The original simulation was revised such that it takes into account Raman photons which may be generated from scattered incident photons and detected by the CCD. By including this mathematical process in equation 5.6 reduced the amount of flux lost within the system was reduced. Although there are no explanations as to why $\Delta\Phi_p \propto \frac{[exp(-k_e)-1]}{n_z^{l_e}}$ (where $l_e = 0.5$), the concept that the system does not rely on purely forward scattering processes is reasonable. It proves interesting that the photon scattering approach is able to generate profiles in good form with experimental data whilst the value of l_e is kept constant and would be a good basis to further understand the underlying physics. The refined numerical model successfully showed that the photon scattering approach was able to predict the Raman response for thick polymeric samples and for thin polymer films with various degrees of crystallinity. It has shown that the scattering of incident photons does not necessarily result in their loss to the system and the simple concept of attenuation cannot be applied uniformly to both incident and Raman scattered photons.

Significantly, physical parameters obtained through experimental methods have been incorporated directly into the model which indicates a closer representation of the physical processes within the material and accounts for a range of materials with different optical characteristics; this includes the application of the revised model to nanodielectric films prepared in this study. The data from this study have shown that, regardless of the method of functionalisation (via a hydrous or anhydrous solvents) this has no observable influence on the Raman response of nanodielectric films with this specific filler loading and these degrees of functionalisation. However, if a degree of homogeneity is obtained in the functionalisation process (therefore a uniform modification of organosilane on each), the Raman response may be influenced in an entirely different manner, adjustments to the revised photon scattering approach may have to be made and further study would be required.

Chapter 6

Conclusion

This investigation used a range of spectroscopic techniques to chemically and electrically analyse a range of polymer systems. Nanosilica samples were modified via silane chemistry to varying degrees with the use of both hydrous and anhydrous solvents. The mechanisms behind hydrous functionalisation involves the condensation of the organosilane and has the potential to form condensed networks of coupling agent; in contrast, the anhydrous route of functionalising nanosilica was expected to limit the formation of condensed organosilane chains, providing a greater degree of uniformity around the nanofiller particles. The aim of the study was to examine the effects of the differently functionalised nanosilicas and compare data obtained from nanocomposites containing the hydrous and anhydrously modified nanofillers.

Nanocomposite samples were produced by introducing functionalised nanosilica into an epoxy matrix by the means of probe sonication and thermally cured with the addition of an amine hardener. The afore mentioned nanofillers were modified to various degrees with the addition Silane z-6040. Two batches of nanosilica samples were prepared to investigate the influence of hydrous and anhydrous solvents, whilst one was processed with the use of methanol and acetic acid (hydrous solvent), the other was functionalised in tetrahydrofuran (anhydrous solvent).

Raman spectroscopy and ATR-FTIR spectroscopy were employed to quantify the degree of surface modification on the nanosilica samples. It was shown that these methods were unable to detect the presence of the coupling agent from epoxide rings, SiO_3 bonds or CH bonds, this has been attributed to pre-existing agglomerates in the functionalisation process which block access to the complete nanosilica surface area and reduce the amount of organosilane in the system. In addition, the compression of the nanopowders for testing would have decreased the amount of surface area accessible to the Raman or infrared techniques, which would also have a negative effect on organosilane detection.

Although Raman and ATR-FTIR spectroscopy were unable to detect the surface modification directly, the latter method showed a decrease intensity of the hydroxyl peak which indicated that organosilane had replaced these groups on the filler surface. This was confirmed by the completion of combustion analyses, where the existence of additional carbon in the samples signified a successful organosilane graft. The increased weight percentage of carbon (with respect to quantity of coupling agent used in the modification process) indirectly suggests that the silica had also been successfully functionalised to a greater degree. In the ideal case where nanosilica agglomerations did not exist in the functionalisation process, the calculated quantity of Silane z-6040 was 164 mg for 800 mg of nanosilica (averaging 15 nm in diameter). However, due to pre-existing aggregates this value was to be considered as a guideline for gauging how much coupling agent should be used. Despite this, the electrical properties of the system reflect that those composites containing nanosilicas functionalised with 200 mg of organosilane produce samples that possess the most promising electrical results. It is therefore arguable that, although the agglomerations of nanoparticles *do* exist in the functionalisation solvent, the ultrasonicator does provide a degree of dispersion to allow for a reasonable degree of surface modification. This concept is supported by the FEG-SEM images, where the increased use of coupling agent is assumed to increases the ease in which the aggregates disperse into epoxy, thereby producing smaller agglomerations and a greater number of isolated particles. However it is of importance to recognise how the washing and drying phase of nanosilica preparation will partly undo the benefits of using a coupling agent, as the filler will flocculate during centrifuging and the effects may be irreversible upon drying. This will explain the larger clusters of nanofiller observed in the epoxy matrix, along with the pre-existing agglomerates before the modification process. In future work, the use of a nanofiller dispersing agent is strongly advised before functionalisation. Other groups have overcome this issue with the use of sol-gel processing which involves the synthesis and functionalisation of monoparticles whilst in solution before dispersion into the appropriate matrix [211, 212, 213]. This allows for an optimum surface modification such that agglomerates are less likely to form in the composite system.

The nanofiller functionalised with a hydrous solvent were expected to undergo a greater degree of organosilane condensation than those functionalised via the anhydrous route, especially in the case where there is an excess of coupling agent. As seen in FEG-SEM images, the average particle agglomerations in nanocomposites composed of hydrously functionalised nanosilicas are larger than those measured in samples containing anhydrously functionalised fillers (for each equivalent degree of functionalisation). It is assumed that thicker, more continuous, networks of Silane z-6040 form during the hydrous modification process which may act to hold the agglomerates together and/or interact with adjacent condensations and contribute to an increased aggregation of nanofiller. These condensation reactions have a significant impact on the nanocomposite properties as they reduce the positive effects of modifying the surface of the nanofiller by introducing a greater amount of impurities, defects and a greater imbalance in the stoichiometry. For silicas that were modified with an insufficient quantity of organosilane, it is assumed that some of the filler surface area remains unfunctionalised and leads to an overall weaker bonding between filler and matrix when introduced into a polymer system; whereas an excess use of coupling agent would lead to a thicker, non-uniform interphase resulting in a decrease in polymer properties. This is reflected in the results obtained from electrical studies.

In both Chapters 3 and 4, similar AC breakdown behaviours are observed; an increasing degree of nanosilica modification sees an initial rise in the AC breakdown strength of nanosilica-epoxy systems before the dielectric strength is seen to decrease. The breakdown characteristics are thought to be a product of a number of mechanisms; as previously mentioned (Chapter 3), agglomerations act as defect centres to enhance the local electric field and initiate breakdown, it therefore stands to reason that the decrease in aggregate size (as seen in FEG-SEM images) will decrease the likelihood of breakdown and increase the bond strength between filler and matrix. Furthermore, it is worth noting how anhydrously prepared nanocomposites possess a higher β-value in comparison to the samples blended with hydrously modified fillers, this is attributed to a greater degree of homogeneity in the systems containing anhydrously treated nanofillers.

However, as the AC breakdown strength tends to decrease after reaching a maximum (at samples EM2 and ET8 for Chapters 3 and 4 respectively), there is reason to believe that there are competing mechanisms. It may be the case that the level of dispersion becomes a less dominant factor in dictating the dielectric strength whilst the thickness of the coupling agent gains a greater influence; for example, consider the organosilane interphase as a layer that acts to 'hold' charge around a nanoparticle, any excess energy may be dispersed into the particle itself which reduces the likelihood of breakdown. However, for a greater degree of functionalisation (with a thicker interfacial region), there will be a greater number of charges 'held' about the filler and the rate at which the energy is dissipated may not be sufficient, leading the material to fail. In addition, it is thought that the thicker organosilane grafts form percolation channels for mobile charges to accelerate and travel, which contributes to a lower breakdown strength. This percolation concept stands to reason when comparing the nanocomposites containing hydrously and anhydrously functionalised nanosilica; if thicker networks of coupling agent exist around silicas modified hydrously, a greater amount of charge will be stored in the interface, this will lead to a higher values of α and is reflected in the experimental data. The percolation effects also extend to the presence of moisture in the system; as described by Zou's Water-shell Model, hydroxyl groups from the hydrous solvent will provide channels for charges to traverse through the bulk and result in breakdown.

As an addition to these parameters, differential scanning calorimetery has revealed that the stoichiometry of the system plays a significant role in the glass transition temperature and will therefore have an inherent effect on the dielectric spectra. The stoichiometric balance is altered with the introduction of fillers; by dispersing untreated nanosilica into the system the epoxide groups on the ends of the resin chains will react with the hydroxyl groups on the surface. This will result in fewer epoxide groups to cross-link with the hardener amine groups, leading to an overall change in the epoxy structure due to excess hardener. Conversely, the addition of modified fillers in an epoxy matrix will increase the number of epoxide groups in the system, which will result in a greater free volume and change the polymer architecture. Both these types of stoichiometric imbalances will result in a lower T_g, that is seen to have an effect on the electrical properties of the system.

The differential scanning calorimetric data obtained from nanocomposites with anhydrously functionalised nanosilica is considerably different from that obtained from the composites containing hydrously treated nanofillers. The imbalance in the stoichiometry in nanocomposites composed of hydrously modified nanofillers is seen to decrease the T_g of the system with increasing surface functionalisation. However, with the samples that have been prepared using an anhydrous method, the data are first seen to exhibit a maximum T_g value for samples containing nanosilica functionalised with 200 mg and 400 mg of Silane z-6040. This suggests that, although the stoichiometry has an significant effect, the bond strength between filler and matrix has a greater influence on the T_g of the system when functionalised with these specific quantities of of coupling agent. These effects are less evident in the epoxies containing hydrously functionalised nanosilicas as the condensed networks of organosilane grafts may have caused the overall bond strength between the two phases to decrease.

The two preparation methods in functionalising the nanofiller is seen to have a marked effect when comparing the data from dielectric spectroscopy; in general, both cases see an increase in the relative permittivity with the introduction of nanofiller, this is most likely due to bound moisture present on the surface. Spectra in Chapter 3 confirms this, as the use of hydrous solvent in the modification process shows a greater increase in the relative permittivity than those seen in Chapter 4 which used an anhydrous solvent in the modification process. Based on the concept that condensation reactions are limited for those samples prepared with anhydrously functionalised nanosilicas, a number of different features can be observed when comparing the two sets of systems. Firstly the α-relaxation in ε' moves to lower frequencies in anhydrous samples (for samples containing silicas processed with excess organosilane) and is indicative of restricted movement due to the bonding at the filler-matrix interface. This relaxation is seen to move to a higher frequency (with increasing modification) in samples containing the hydrously modified nanosilica and implies there is a greater amount of free space for polymer chain movement. Furthermore, there is a distinct broadening of the α-peak for the hydrous system containing functionalised with 200 mg of organosilane and indicates that energy is stored over a greater range of frequencies, this suggests for the most efficient functionalised nanocomposite; the calculation of the quantity of coupling agent is therefore vital, where insufficient or excess silane will act to reduce the positive effects of modifying the filler. For samples prepared hydrously, the shift of the β-relaxation to lower frequencies in ε'' implies that there is a greater restriction of the rotation of the hydroxyether group [$CH_2CH(OH)CH_2O$] which suggests that although the overall movement has been increased, there may be a limited mobility of the backbone once a condensed network is formed.

When comparing the two sets of systems at 100 °C, those prepared hydrously possess a considerable increase in ε' which is representative non-ohmic conduction due to interfacial or electrode polarisation. This supports to the theory that charges may be stored within the interphase around the nanofiller due to an increased volume of free space, or that they may be trapped in condensed chains/networks of organosilane. The characteristic is also seen in the anhydrously functionalised samples; however only in those which contain silica with low degrees of functionalisation (from the increased free volume) and that which had been modified to the greatest excess (charges trapped in condensed organosilane layer). The dielectric spectra has brought to light concepts that are similar to Tanaka's Multicore Model, whereby there are at least two layers that may exist around the filler. The first closely bound layer is an indication of the overall bonding between the filler and coupling agent, where there is less mobility directly at the filler surface due to the covalent bonds. The second outer layer may have more mobility due to the condensation of organosilane which will give rise to additional free space for the epoxy chains to move, this contributes to the shifts in relaxation features to lower and higher frequencies.

These studies have highlighted the sensitivity of nanocomposite systems as a whole. The importance of dispersion via mechanical or chemical methods should be considered throughout the sample preparation process, whether it be during the functionalisation process or whilst the filler is being introduced into the matrix. The investigations into modifying nanosilicas with organosilane chemistries has show how a complete dispersion of aggregates prior to surface modification is paramount to reduce the uncertainty in data, furthermore this will allow one to calculate the optimum stoichiometric ratio required for optimum cross-linking with the appropriate degree of surface functionalisation. Although the dielectric strength for samples containing hydrously functionalised nanosilicas is typically higher, those containing anhydrously functionalised nanosilicas have provided data which suggest that they possess a greater degree of dispersion, this is assumed to have increased the bond strength between filler and matrix, where the maximum T_g for all samples have been observed in the anhydrously prepared nanodielectric films. The dielectric spectra also show a higher range of frequencies for the α-relaxation in the epoxies containing hydrously functionalised nanofiller, this increases imples there is a greater degree of chain movement within the interphase which increases the general relative permittivity of these systems. All data point towards the use of anhydrous methods of functionalising nanosilica as the condensation reactions are limited and also reduces the moisture in the system that leads to undesirable results.

The final chapter in this thesis sets out to set out to understand underlying issues within the field of confocal Raman spectroscopy and investigate its performance whilst depth profiling a range of thin polymer films. The studies from Chapter 5 focuses on the proposed photon scattering approach by Macdonald *et al* and supports concept that the confocal Raman response should be based upon the detection of signal collected from an illuminated volume, as opposed to the intensity that is obtained from a focal point.

Confocal Raman depth profiles were obtained from three differently prepared polymer systems of different thicknesses. To test the ability of the photon scattering approach, simulated depth profiles for each polymer film were compared to the experimental data. The confocal Raman response was simulated using the photon scattering approach, where the model assumes that Raman photons can only contribute to confocal Raman spectra if they are generated within the illuminated volume *and* traverse a trajectory that allows them to be detected by the CCD. This study saw the original model (developed by Macdonald *et al*) optimised and improved such that simulations could be directly related to the physical parameters obtained through experimental methods; whilst the original photon scattering approach was able to predict the behaviour of the confocal Raman response using an attenuation value derived from the best visual fit to experimental data, this study used iterative mathematics to find an attenuation coefficient with the least mean error over all thicknesses for each polymer system and was successful in providing a more accurate fit for all systems. However, when using an attenuation coefficient derived from UV-visible spectroscopy, this ‘physical’ value indicated the attenuation coefficient was considerably higher than that observed with the Raman spectrometer. Initially thought to be a product of refraction and spherical aberration, immersion media were introduced to reduce the negative effects of such phenomena. A comparison was completed on the same polymer film immersed in two oils (silicone oil and Oil A) to investigate the effects of a refractive index mismatch, it was concluded that adjustments could be made for a realistic representation of the film thickness and stage movements with the use of a constant of proportionality, Ψ. Despite this, there was still a marked difference between the attenuation coefficient obtained via the iterative method and that derived from UV-visible spectra. By reconsidering the scattering mechanisms within the bulk, such that $\exp(-k_e\Delta_z) \neq \exp(-k_R\Delta_z)$, the photon scattering approach was modified to take into account any scattered incident photons which may give rise to Raman photons that also possessed a trajectory which enabled its detection, and contribute to the spectra. This allowed the simulation to generate confocal Raman depth profiles with values of attenuation coefficient obtained via UV-visible studies, which closely matches profiles obtained through experimental methods. Although various other factors are in need of investigation, such as the value of l_e, the modified photon scattering approach was able to replicate the confocal Raman response of a thin polymer film more closely than other currently proposed models. This approach was applied to the nanocomposite films developed in Chapters 3 and 4. The revised model was able to successfully predict the Raman response of the nanodielectric films as the point of focus was lowered into the sample and out the second surface. The experimental data obtained from depth profiling the nanodielectric films shows no visible change from typical vertical depth profiles, however it may be the case that a low filler loading of 2 wt.% has a negligible effect on the turbidity of the entire system, where the total organosilane graft is insufficient to be detected by the sensitivity of the equipment (as discussed above).

6.1 Future Work

This investigation has used a range of spectroscopic techniques that have highlighted the fact that nanocomposite systems are extremely complex, where a number of parameters need to be strictly controlled to fully understand the mechanisms that occur at the filler-matrix interface and within the bulk. These do not just include the quantity of coupling agent used when modifying nanofillers with organosilane chemistry, but the changes in stoichiometry due to the degree of functionalisation which is altered due to the extent of condensation reactions within the system. Future work may therefore include the following;

- The existance of pre-existing nanofiller agglomerations in the functionalisation process meant that optimum surface modification may not have been achieved. By using a chemical pre-disperser, isolated particles can be obtained pre-treatment and decrease the uncertainty in the degree of surface modification.
- As the anhydrous method of functionalising nanosilica has seen to show more consistent results with a lower uncertainty, nanosilica should be functionalised to various degrees via this method and dispersed into epoxies with different stoichiometric ratios. The study should conclude if mathematical calculations for the 'optimum' quantity of coupling agent can be calculated simply on the size of the filler and density of coupling agent.
- Increase the filler loading of the nanocomposite systems to investigate how this effects the chemical and electrical effects of silica-epoxy composites. It is also assumed that the increase in filler loading will lead to the detection of organosilane coupling agent (via Raman and FTIR spectroscopy) as the total surface area of the nanofiller will occupy a greater volume of the system.

- Improve the photon scattering model by studying the different effects of changing the value of l_e in the simulation. If there can be an explanation for the optimal value, then this will give an insight into the underlying physics which will enable the simulation to be developed further.

- Cross polar optical microscopy can also be used to locate the nanoparticles within the matrix systems, the focal point of confocal Raman spectroscopy can then be adjusted to intercept the filler and examine the effects of the interface of the confocal Raman response.

Appendix A

The Maximum Likelihood Function

The maximum likelihood function finds the most likely values of the distribution values. In the case of this study, these parameters are α and β. Every population of samples undergone breakdown tests will have a probability density function, which estimates the number of samples that may breakdown between times $t = \mathrm{t}_1\mathrm{:t}_2$,

$$\text{Probability density function} = g(t; \phi_1, \phi_2 ... \phi_n) \tag{A.1}$$

where ϕ_n are the estimated parameters. in the case of (complete) breakdown data, one can describe the likelihood function as the product of all probability density functions; each data point in the set will have one element.

$$L = \prod_{k=1}^{n} g(t; \phi_1, \phi_2 ... \phi_n) \tag{A.2}$$

By taking the natural logarithm of L, we obtain

$$\Lambda = \ln L = \sum_{k=1}^{n} g(t; \phi_1, \phi_2 ... \phi_n) \tag{A.3}$$

To calculate the most likely value of a parameter, the partial derivative of this equation is set to zero for each parameter, leaving the unknowns to be solved simultaneously,

$$\frac{\partial \Lambda}{\partial \phi_n} = 0 \qquad \text{where } k = 1,\, 2 \ldots\ n. \tag{A.4}$$

Appendix B

Scanning electron microscopy

B.1 Images from preliminary studies

The preliminary SEM studies (using the JEOL JSM 5910) show that sizeable aggregates exist of order >100 nm. Although these tend to reduce in size with increasing sonication time, they do not reach dimensions small enough to allow the composite to qualify as a ‘nanocomposite’. Specifically, these images show how there will be filled and unfilled regions regardless of the sonication time. Crack pinning features, as described by Lange *et al* [172], are present in Figures B.1(e) and B.1(g).

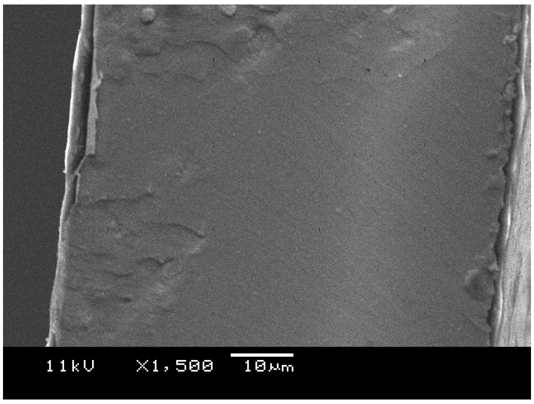

(a) Epoxy film with nanosilica sonicated into resin for 30 min.

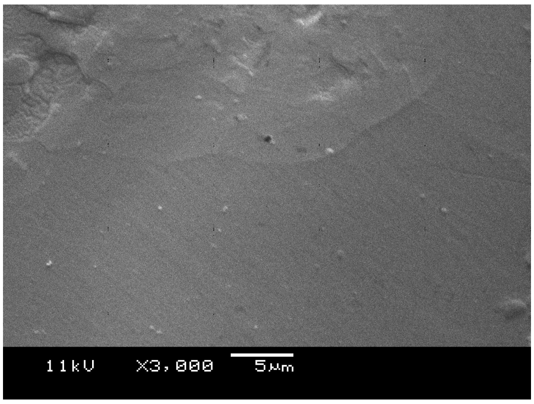

(b) Epoxy system with nanosilica sonicated into resin for 30 min.

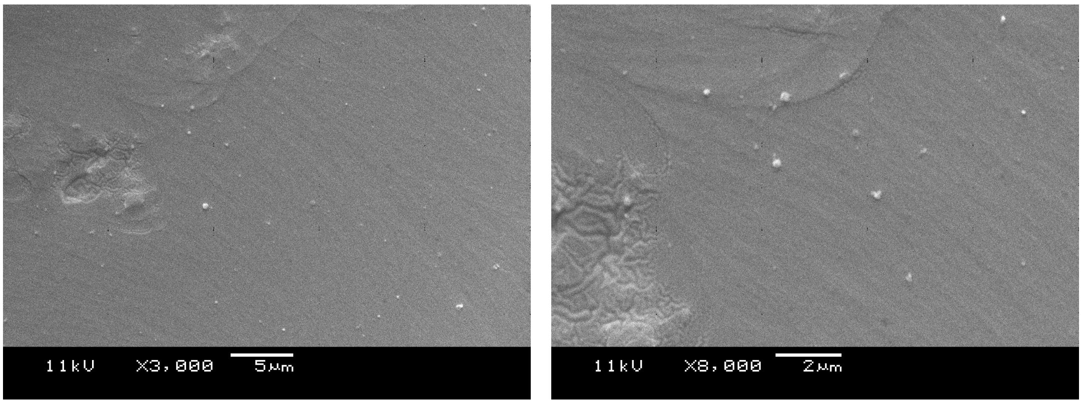

(c) Epoxy film with nanosilica sonicated into resin for 30 min.

(d) Nanodielectric film after 30 min of sonication.

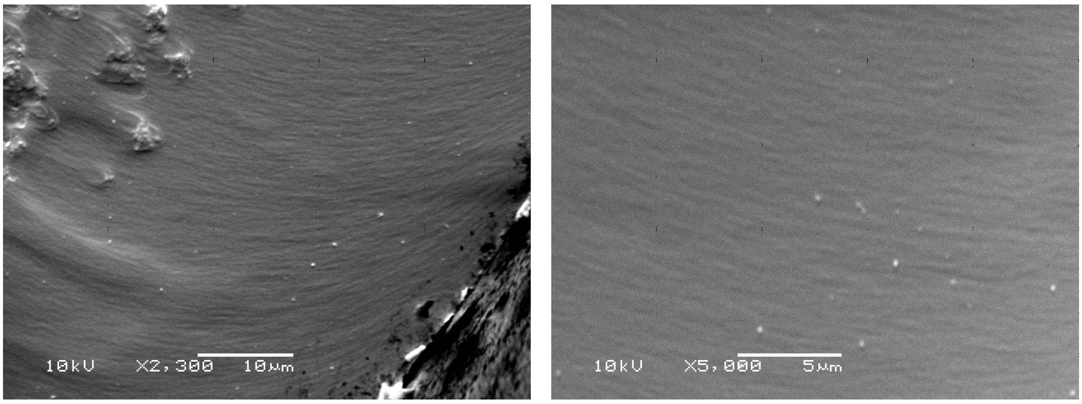

(e) Epoxy sample after 40 min sonication.

(f) Epoxy film after 40 min sonication.

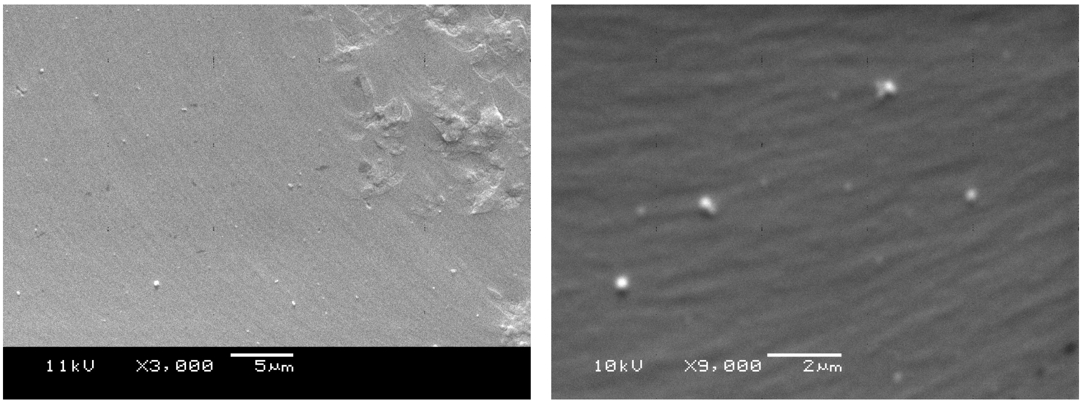

(g) Epoxy sample after 40 min sonication.

(h) Cured epoxy after 40 min of nanosilica sonication.

Figure B.1: SEM images of samples containing nanosilica sonicated for 30 and 40 min.

Although the aggregation size is seen to be of similar order for samples sonicated for 60 minutes (to 40 minutes), these appear to possess a greater degree homogeneity.

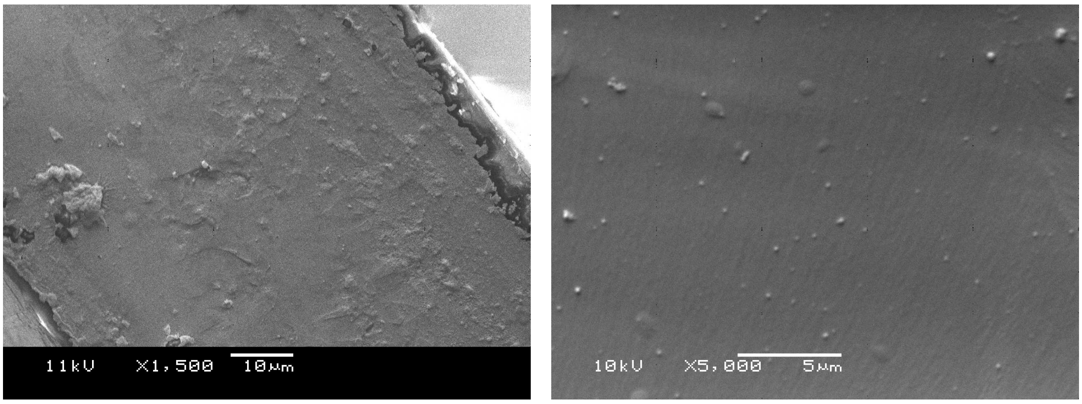

(a) Epoxy sample after 60 min sonication.

(b) Epoxy film after 60 min sonication.

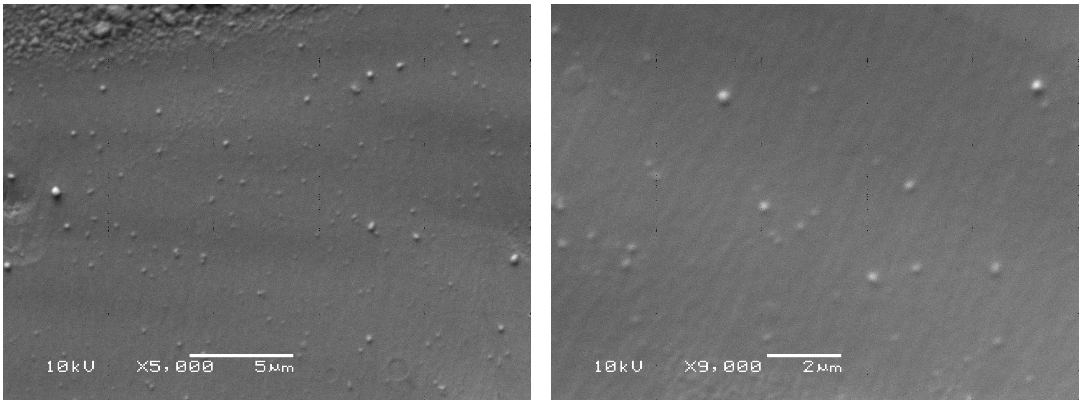

(c) Sample sonicated for 60 min.

(d) Sample sonicated for 60 min.

FIGURE B.2: SEM micrographs of epoxy after 60 min of sonication to analyse dispersion.

B.2 FEG-SEM micrographs

Micrographs obtained using the JEOL FEG-SEM 6500F show a marked improvement in the resolution of images. A selection of images are shown below, where the grey areas are representative of unfilled regions. Samples prepared with hydrously functionalised nanosilica is seen to possess aggregates that are of a similar size to those which are anhyrously functionalised, although a greater number of isolated particles have been observed in the latter. The FEG-SEM images highlight the effects of pinning in these nano-epoxy systems, where greater pinning effects are associated with stronger matrix bonding to the filler. These features are most pronounced in systems containing nanosilica which has been functionalised with an excess organosilane, particularly in the anhydrous systems.

B.2.1 Samples containing nanosilicas prepared in methanol

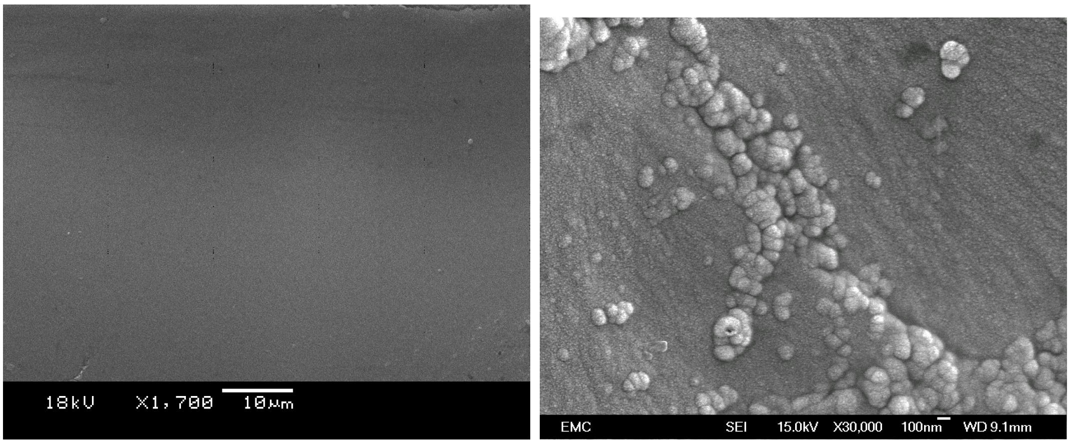

(a) Unfilled epoxy system at low magnification.

(b) EM0 system, clear agglomerates are visible.

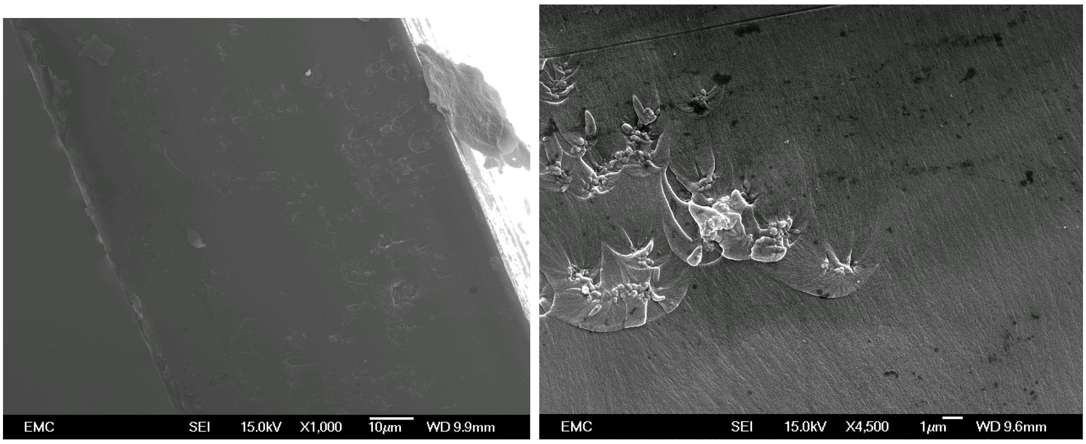

(c) EM1 epoxy system at low magnification.

(d) EM1 epoxy system at high magnification where pinning effects can be seen.

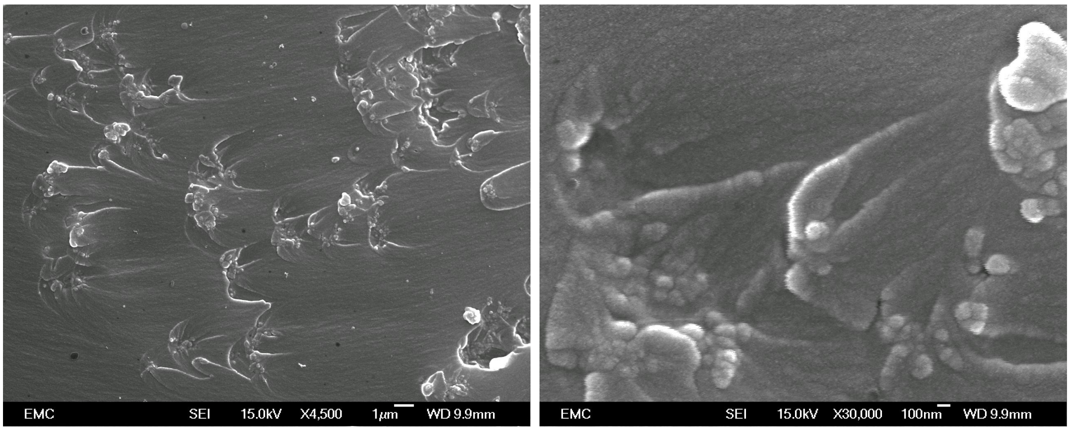

(e) EM4 epoxy system at low magnification.

(f) EM4 epoxy system at high magnification.

Figure B.3: SEM micrographs of nanodielectrics with different degrees of hydrous functionalisation.

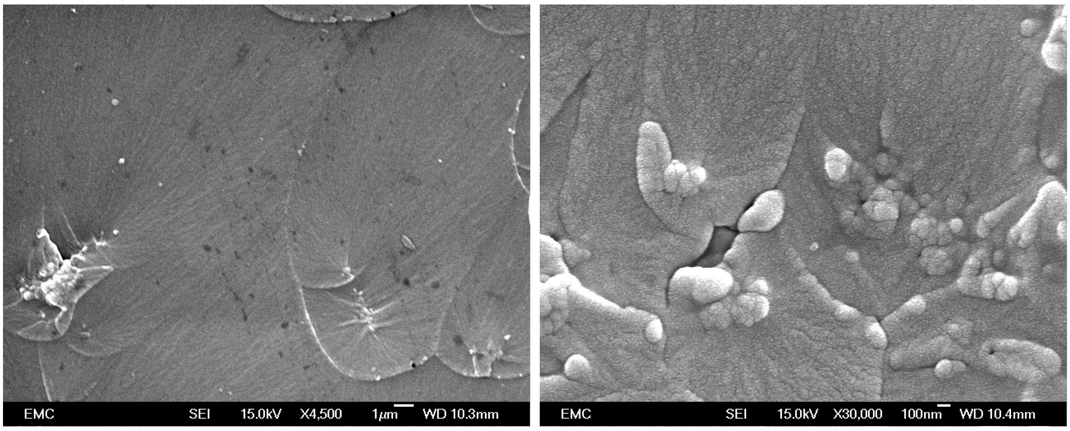

(a) EM8 epoxy system at low magnification.

(b) EM8 epoxy system at high magnification.

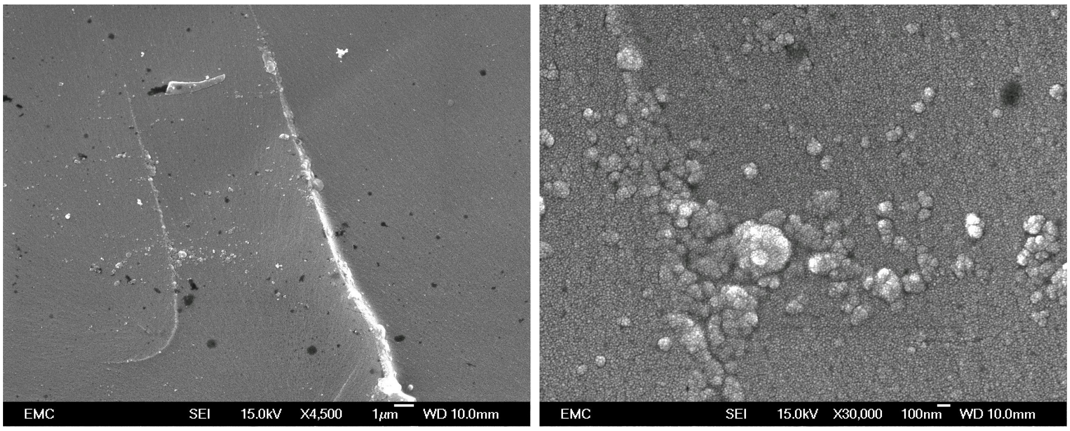

(c) EM16 epoxy system at low magnification, smaller aggregates are represented.

(d) EM16 epoxy system at high magnification, isolated particles are present.

Figure B.4: SEM images of nanosilica-epoxy samples.

B.2.2 Samples containing nanosilicas prepared in THF

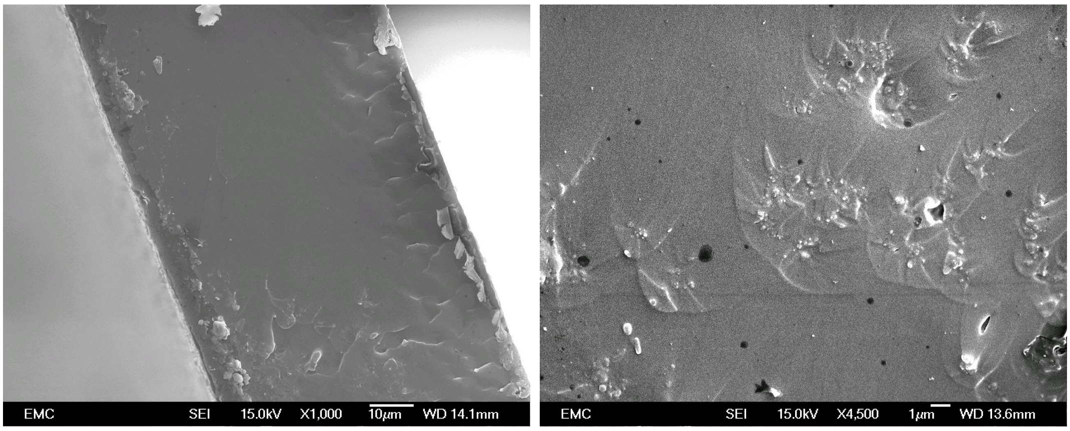

(a) ET0 epoxy system at low magnification.

(b) ET0 epoxy system at high magnification.

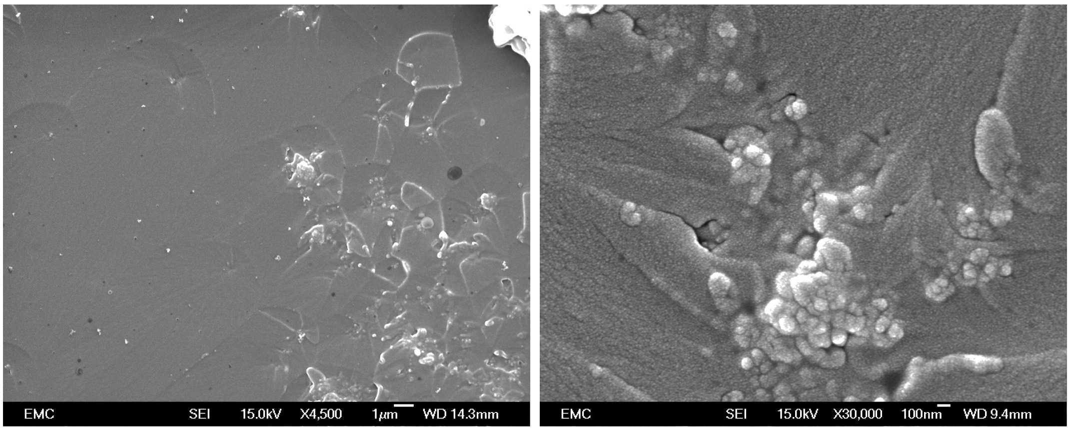

(c) ET1 epoxy system at low magnification.

(d) ET1 epoxy system where aggregation size is smaller than in ET0.

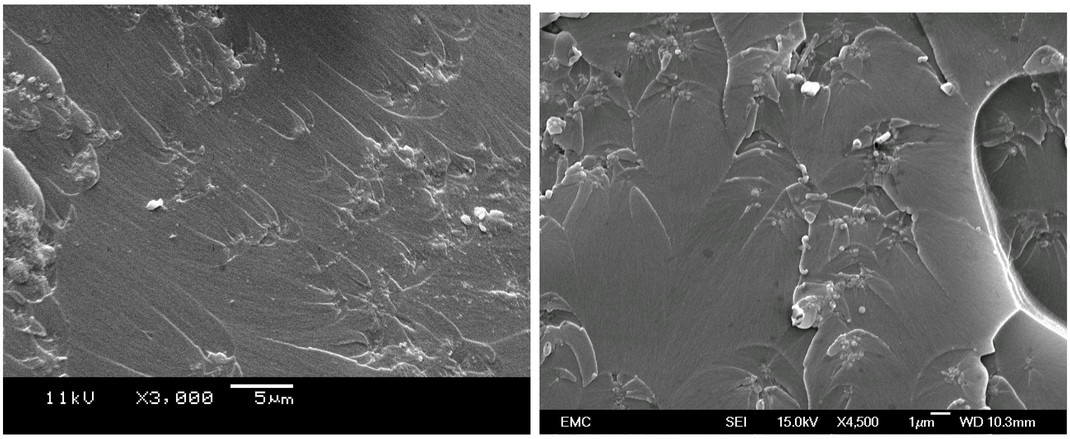

(e) ET4 epoxy system, pinning effects are more obvious than in ET1.

(f) ET8, high magnification.

Figure B.5: SEM micrographs of nanodielectrics with different degrees of anhydrous functionalisation.

Appendix C

Dielectric spectra

The following figures are dielectric spectra obtained from epoxy nanocomposites which contain 2 wt.% nanosilica. The first section represents dielectric spectra for samples EM1, EM8 and EM2000 which contain nanosilicas that have been functionalised with a hydrous solvent. The second section shows spectra acquired from ET8 and ET20 which is filled with nanosilica which have been prepared with an anhydrous solvent. All graphs represent the dielectric spectra obtained at a range of temperatures. Figure C.1 has been repeated again such that comparison can be made to an unfilled epoxy system.

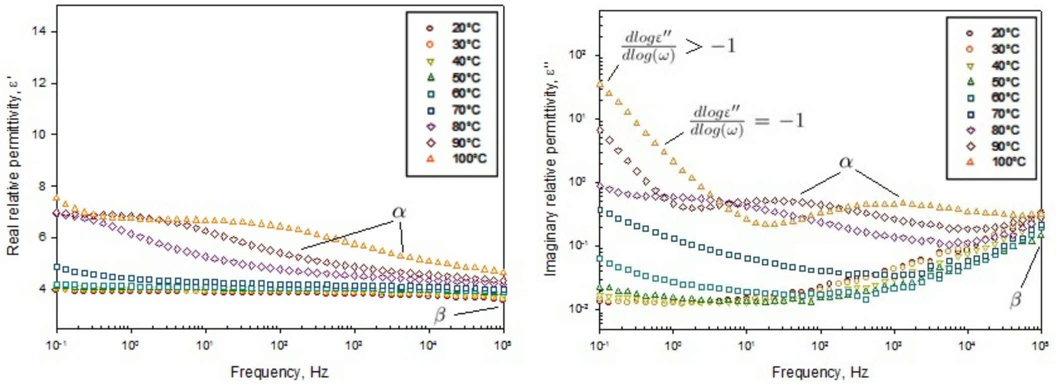

(a) Unfilled epoxy system, ε′ vs. frequency.

(b) Unfilled system, ε′ vs. frequency.

Figure C.1: Dielectric spectra from an unfilled epoxy system.

C.1 Nanocomposites containing hydrously modified filler

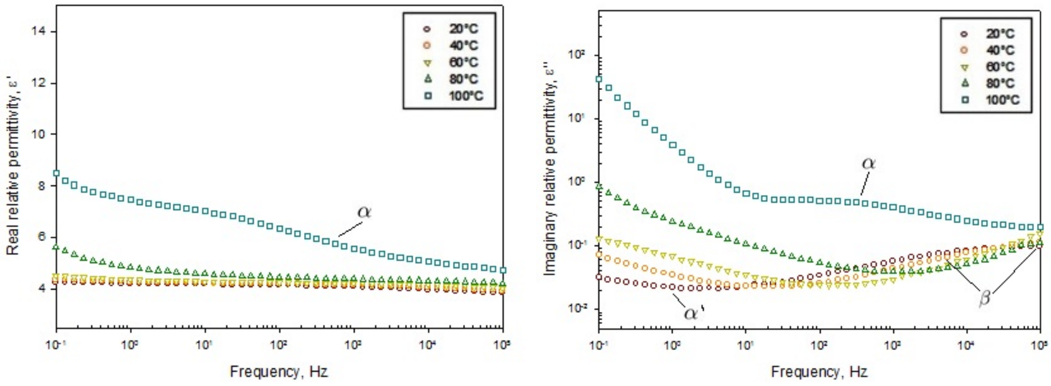

(a) EM1, ε′ vs. frequency.

(b) EM1, ε′′ vs. frequency.

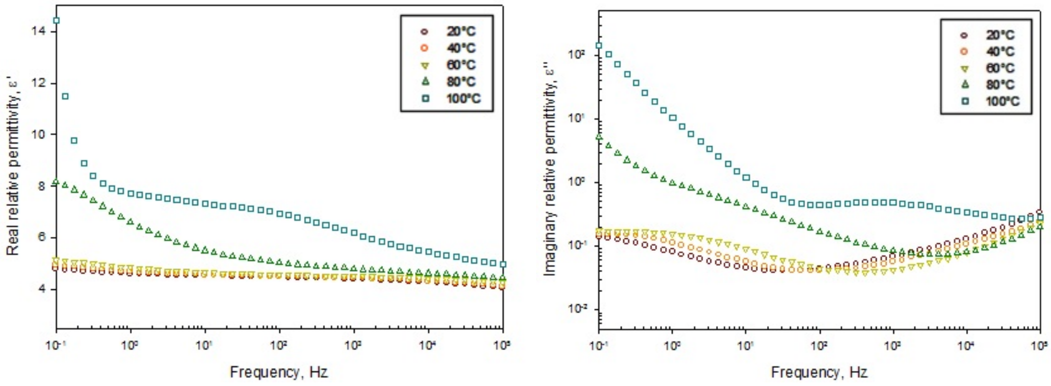

(c) EM8, ε′ vs. frequency.

(d) EM8, ε′′ vs. frequency.

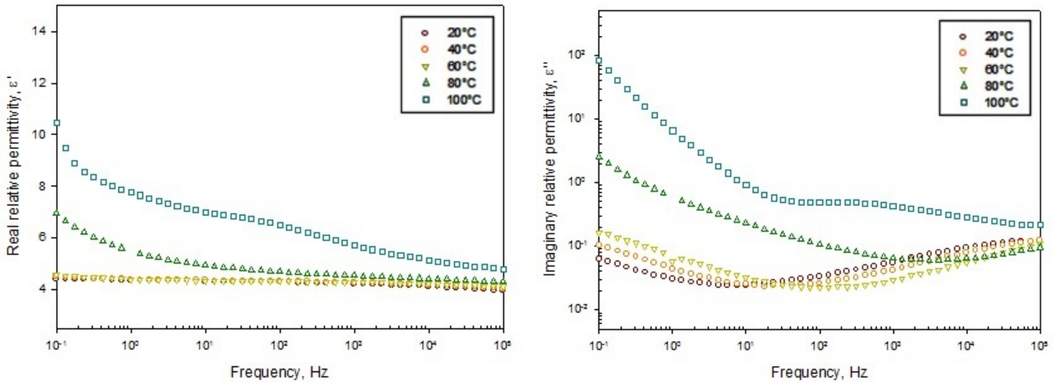

(e) EM20, ε′ vs. frequency.

(f) EM20, ε′′ vs. frequency.

FIGURE C.2: Dielectric spectra obtained from nanodielectrics containing hydrously functionalised nanosilicas.

C.2 Nanocomposites containing anhydrously modified filler

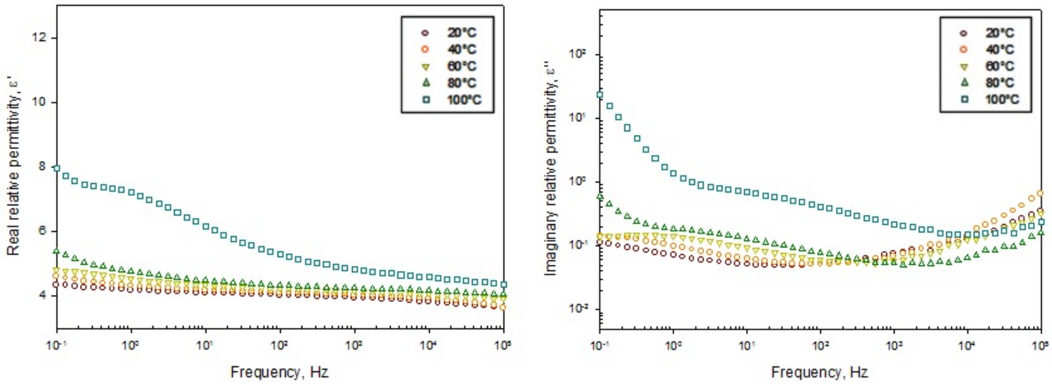

(a) ET8, ε′ vs. frequency. (b) ET8, ε′′ vs. frequency.

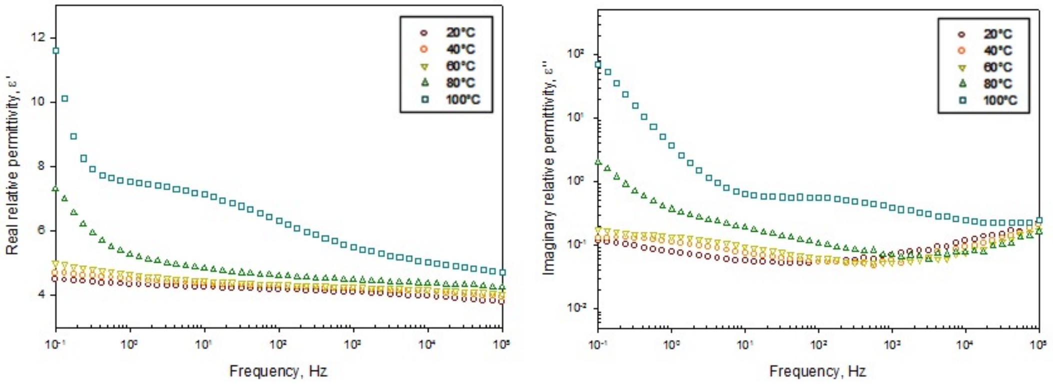

(c) ET20, ε′ vs. frequency. (d) ET20, ε′′ vs. frequency.

Figure C.3: Dielectric spectra obtained from nanodielectrics containing anhydrously functionalised nanosilicas.

Appendix D

Confocal Raman spectroscopy

D.1 Confocal Raman Spectroscopy, further discussion.

Confocal Raman spectroscopy involves combining Raman spectroscopy with a confocal microscope such that this can be achieved. Until the mid-1950s, optical microscopes were scientific instruments composed of one or more lenses; reflected light images were obtained by illuminating a selected field with light which is then scattered back via a number of lenses to create a magnified view at the eyepiece.

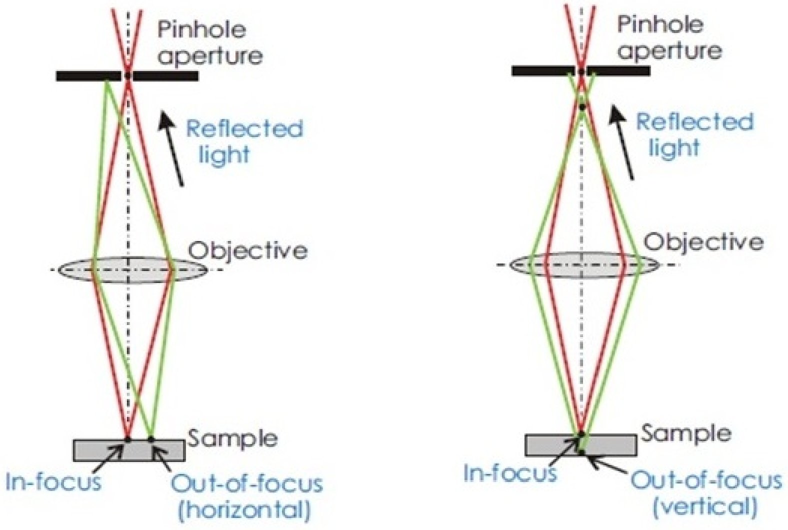

FIGURE D.1: Schematic diagram of a confocal microscope. Reprinted from [214].

However, the quality of these images were poor as the reflected light flooded the microscope from all angles. This issue was overcome by Minsky who designed and developed the first confocal microscope in 1955 [215]; the insertion of a simple pinhole aperture between the source and objective made it possible to focus light at a single point, and blocked scattered light from out-of-focus regions which made significant improvements to the final image.

A number of authors have published their research describing the accuracy of confocal Raman spectroscopy, where many have provided mathematical derivations to illustrate the manner in which the physical material properties *and* the system optical properties influence the Raman response. Tabaksblat *et al* research is considered amongst the first authors to recognise the shortcomings of confocal Raman spectroscopy; within their research they collected depth profile data using various combinations of objectives and pinhole apertures. Their studies predicted that for a 40 μm thick polymer block, at least 20% of the total scattered light collected through a 300 μm aperture arose from planes further than 5 μm from the focal plane (with a laser wavelength of 514 nm). These predictions were compared to empirical data obtained from a 40 μm polyethylene film, where only 10% of the total detected light was found to originate from regions 5 μm away from focus [187]. Tabaksblat *et al* concluded that the resolution of confocal Raman spectroscopy was on the order of ~1 μm laterally and ~2 μm vertically, where the discrepancies between experimental data and theoretical predictions were attributed to refraction effects at the interface. This was in addition to the research completed on laminated samples as described in Section 5.1. Shortly after Tabaksblat *et al's* publication, Hell *et al* reported

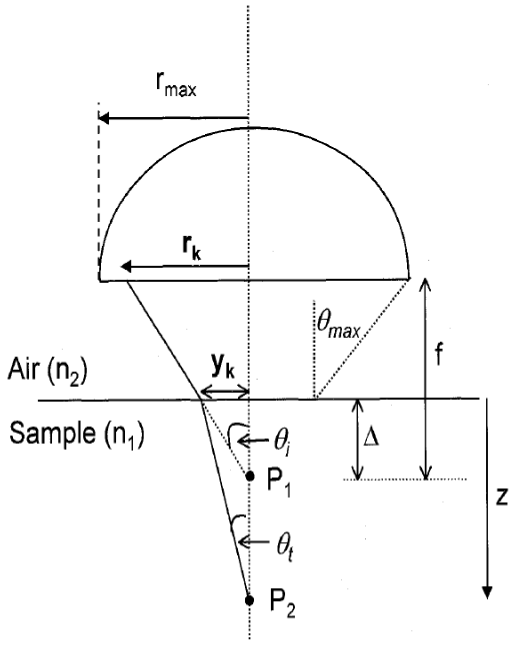

FIGURE D.2: Geometric ray tracing of refracted light. Reprinted from [193].

a decrease in the quality of confocal fluorescent images as the focal point was lowered into a specimen [216]; their study attributed the image degradation to a shift in the focal point due to refractive index mismatches between specimens and the environment. These concepts were extended to confocal Raman spectroscopy by Michielsen [188] and Everall who used ray tracing methods to calculate the true depth of focus, z_t, with respect to the apparent focal point, Δ_z, as shown in equation 5.1 (Chapter 5). In his 2000 publication, Everall also assessed the extent to which the focal point was elongated along the optical axis and showed how can be calculated using equation 5.2 (Chapter 5). Furthermore, Everall also details the relationship between the laser intensity distribution within the specimen, assuming that the laser source has a Gaussian intensity profile [196], the intensity distribution $I(m)$ is given as,

$$I(m) = I_0 \mathrm{exp}\left(\frac{-2m^2}{\phi_f^2}\right) \tag{D.1}$$

where $I(m)$ is Gaussian intensity distribution, I_0 is the incident axial intensity, and ϕ_f is the filling factor which describes the extent of the trunication of the Gaussian beam [196]. For an ideal system set-up, the entrance pupil of the objective should be filled such that the beam is apertured at $\frac{1}{e^2}$ its orginal intensity. For optimum filling, $\phi_f = 1$, however this may not always be achievable. In the case where $\phi_f > 1$, an overfilled objective is observed and serves to decrease the amount of energy transmitted as the beam distribution is cut off at high intensity values; conversely, if $\phi_f < 1$, the objective is then underfilled and the opposite will occur. Everall's publication confirmed the sensitivity of the transmitted intensity with respect to the fill factor, where large values of ϕ_f result in a broadening of the radial distribution $m.I(m)$ with respect to the normalised radius. When plotted as a function of true point of focus z_t, the laser intensity $m.I(m)$ broadens at a greater rate with increasing focal depth, Δ_z. It is seen that, in the case of $\Delta_z = 2$ µm, the depth of focus would be similar to that of the diffraction limit and therefore contribute a defocusing factor [193].

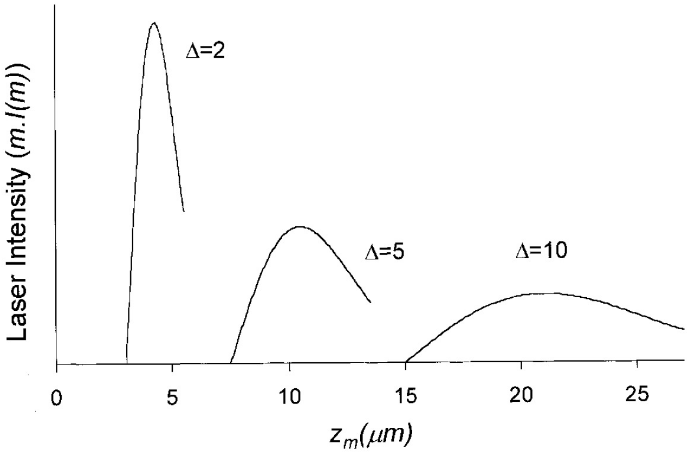

FIGURE D.3: Laser intensity vs point of focus. Reprinted from [193].

By taking into account the changes in radial distribution of the laser, Everall derived the Raman response, $R(z_t)$, based on the efficiency of the confocal aperture (with respect to m). Two weighting methods were described; one where the influence of the confocal aperture is overlooked and weights each point that produces detectable Raman photons with respect to the square of the numerical aperture, NA^2_{eff},

$$R(z_t) = mI(m)NA^2_{eff} \tag{D.2}$$

$$NA^2_{eff} = \frac{1}{n^2}\left[\frac{m^2NA^2}{1+m^2NA^2-NA^2}\right] \tag{D.3}$$

whilst the second approach assumes that a perfect confocal aperture is in use, such that chromatic aberration is negligible. Only photons scattered from the angle of incidence are able to pass back through the aperture. The weighting factor for the probability that a photon transversing exactly from this angle is m. The Raman response in this case is,

$$R(z_t) = m^2I(m) \tag{D.4}$$

In comparison, Baldwin *et al* discussed the efficiency of the confocal aperture when using confocal optics, their calculations reported a 'forbidden zone' in which Raman photons cannot be collected [189]; they make modifications to Everall's initial derivations [193] to include parameters such as the expected depth of focus, Δ_z, refractive index, n, numerical aperture, NA, and radius of the confocal aperture, ρ, resulting in equation D.5;

$$R(z_t) = mI(m)\Omega(\Delta_z, n, NA, \rho) \tag{D.5}$$

Modifications were made to this model by Bruneel *et al* who included off-axis intensity effects, which saw an improvement in predicting the behaviour of confocal Raman depth profiles [190]. Baia *et al* however, adapted Baldwin *et al*'s model to include diffraction [217]; their studies calculated the Raman response by integrating the intensity of concentric Airy rings at various depths within the focal volume. They claimed that the elongation of the focal point (with respect to depth) is less aparent when considering the diffraction effects than if one were only to consider refraction, particularly for experiments employing metalurgical objectives. A summary of confocal Raman theories was published by Tomba *et al* showing extensive comparisons with existing models and experimental data whilst using dry, metallurgical objectives [218]. The report concluded that models by Everall and Baldwin *et al* 'nicely captured' the features of the intensity profiles, although additional parameters such as the numerical aperture and refractive index were important to refine their models further, as seen by Bruneel *et al.*

With the recommendations that an immersion oil should be used in confocal Raman optics, further studies were completed with laminate samples immersed in an immersion media. This was seen to increase the intensity of the spectra as it reduced the amount of scattering at the interface and mediated the refractive index difference between air and the sample. Froud *et al* used confocal Raman spectroscopy to depth profile a laminated polystyrene/polymethyl methacrylate systems [198]; their study confirmed how the use of immersion media improved the overall accuracy of confocal Raman spectroscopy and reported how they were able to resolve eleven adjacent polymer layers from depths greater than 100 μm beneath the sample surface, with the use of an immersion oil. However, concerns were raised over the physical effects of an immersion media on a polymer specimen; Tomba *et al* discussed the manner in which small molecules from liquids (with low molecular weights) could penetrate the surface of glassy polymers and cause possible damage via swelling [219]. A simple solution was suggested, where a thin protective film could be inserted between oil and specimen to preserve the sample;

the system is subjected to vacuum before immersion and therefore the film is able to follow the contours of the sample to promote the physical contact and take into account physical imperfections [219]. This method can be used as an alternative arrangement developed by Vyörykk *et al*, where a cover glass placed between the objective and the sample, immersion fluids are used to decrease the refractive index mismatch between the solid layers [194].

D.2 Polarising optical microscopy and results

D.2.1 Sample preparation and microscopic method

Samples for optical microscopy were prepared via solution blending. Polymer pellets were added to preheated xylene at 130 °C and the solution was stirred vigorously until the polymer pellets were seen to dissolve. The quantities of material used were weighed to give a concentration of 1% w/v [203, 220] and fresh xylene was added frequently to maintain the solution concentration as it evaporated off. The hot polymer solution was then pipetted onto a glass slide and the solvent was removed with the use of a hot plate. The resulting sample was placed in a Mettler FP52 hotstage, where the temperature was controlled according to the crystallisation process (described in Section 5.3) to produce PEQ, PEX and NQ samples which were suitable for optical microscopy. Transmission optical micrographs were obtained using a Leica Aristomet microscope with the use of a cross polarised illumination.

D.2.2 Polarised optical images

As shown in Figure D.4(a), when the polyethylene system is quenched straight from the melt (PEQ), smaller spherulites are formed. In contrast, the polyethylene system crystallized isothermally at 115 °C (PEX) contains large banded spherulites, which crystallize through a distinct two phase process [220, 221].

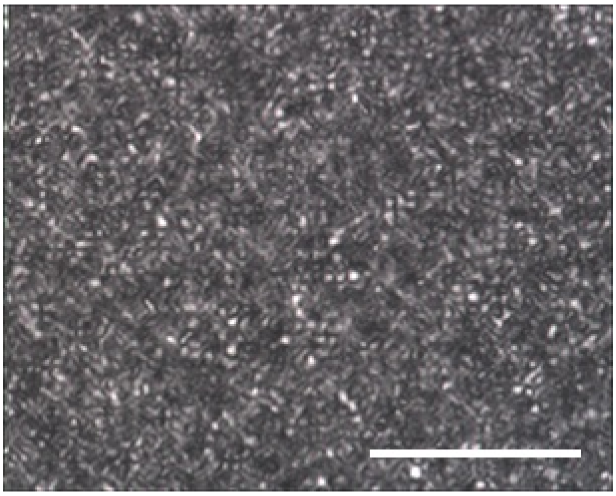

(a) Quenched polyethylene.

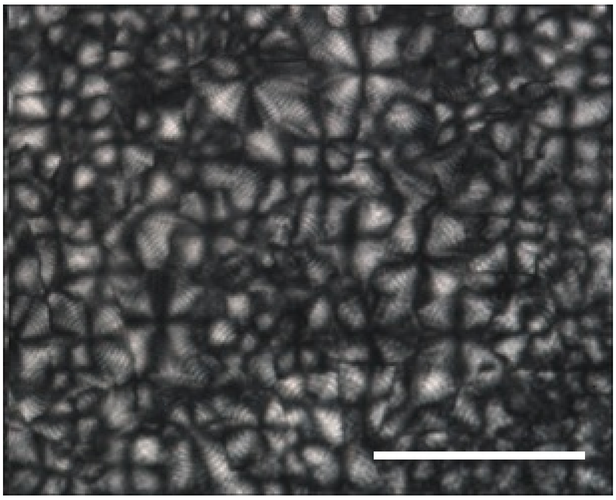

(b) Isothermally crystallised polyethylene.

(c) Quenched Novolen 3200MC.

FIGURE D.4: Optical images from the polymer systems. Scale bar represents 100 μm.

Initially, the HDPE crystallizes to form a framework of thick lamellae and are separated from one another by regions of LDPE that solidifies upon quenching; this molecular segregation occurs on the scale of some tens of nanometres. The difference in morphology manifests itself in significantly different light scattering behaviour [222]. The addition of DBS in NQ has meant that no visible structure at optical resolutions can be observed. DBS is a strong nucleating agent for polyolefins [223, 224, 225] and therefore the polymer is observed to be non-birefringent when viewed between crossed polars.

D.3 Optical Transmission Data

Optical transmission data were obtained from all polymer samples for a range of thicknesses. Figures D.5 and D.6 represent the data obtained from PEQ and NQ respectively. The filled shapes are data acquired from samples in air, whilst the unfilled shapes are data obtained from samples immersed in silicone oil and Oil A.

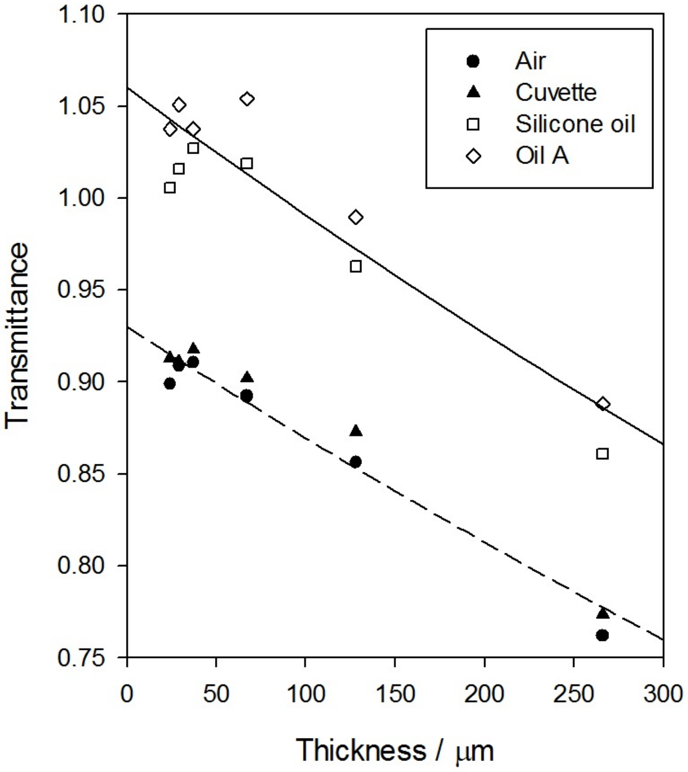

Figure D.5: Optical transmission data obtained from PEQ samples in air and oil (shapes) and Beer-Lambert Law fit (lines).

The lines of best fit were fitted to the Beer-Lambert Law (equation 2.6), where the dashed lines are representative of air data and solid lines show the best fit for oil data. All air data were considered as one system as the α values indicated that the variability for each system was not statistically significant (values fell within 90% confidence bounds of each other). This is also the case for data obtained for samples immersed in oil.

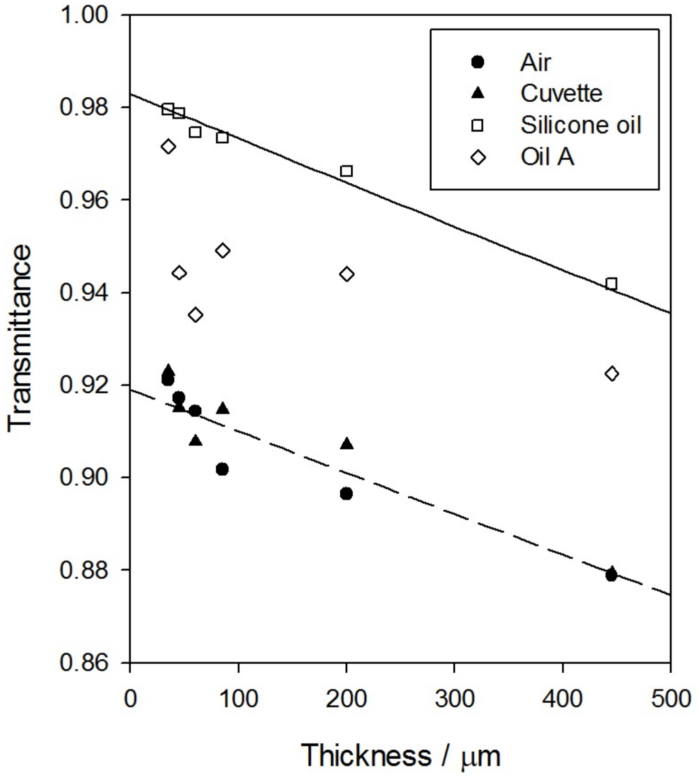

FIGURE D.6: Optical transmission data obtained from Novolen 3200MC samples in air and oil (shapes) and Beer-Lambert Law fit (lines).

D.4 Confocal Raman depth profiles - Films in air

For all profiles presented in the appendices, data obtained with the laser focused at the top sample surface were plotted at zero on the abscissa, whilst negative and positive stage positions relate to the nominal point of focus above and below the top surface respectively.

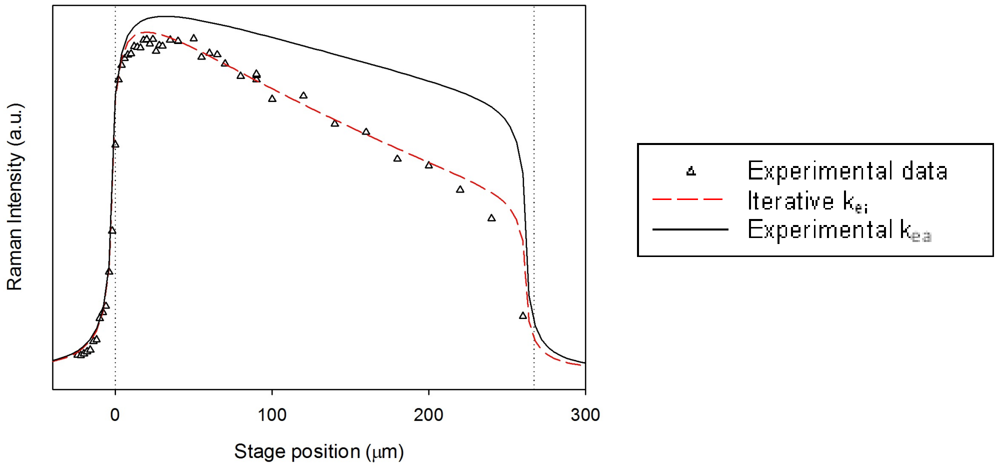

(a) PEQ film of thickness 267 μm.

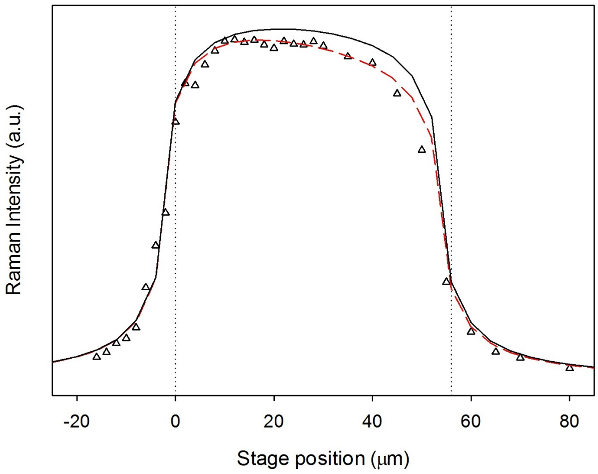

(b) PEQ film of thickness 56 μm.

FIGURE D.7: Depth profiles obtained from two thicknesses of PEQ films in air ± 5 μm, using the original model.

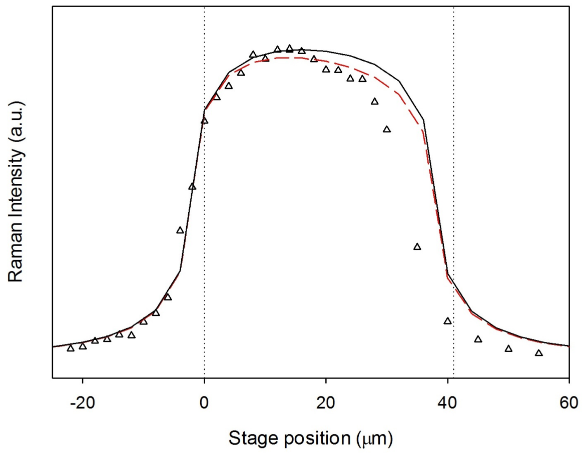

(a) PEQ film of thickness 41 μm.

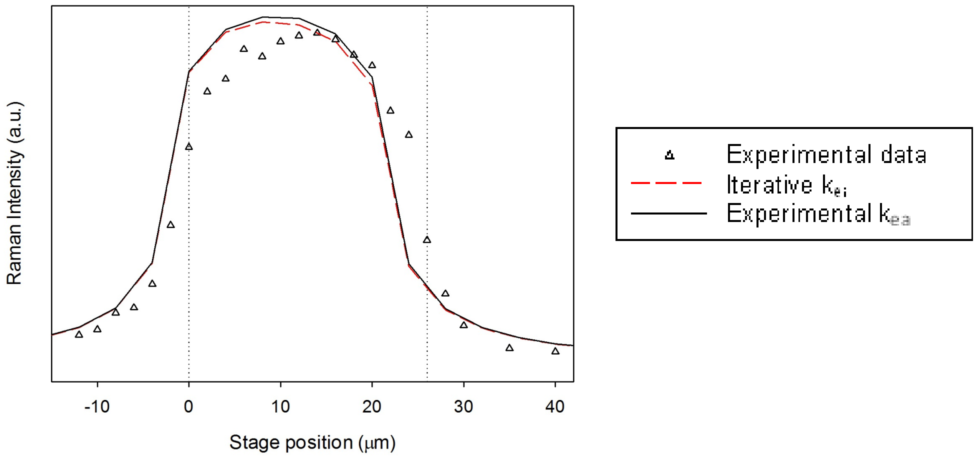

(b) PEQ film of thickness 26 μm.

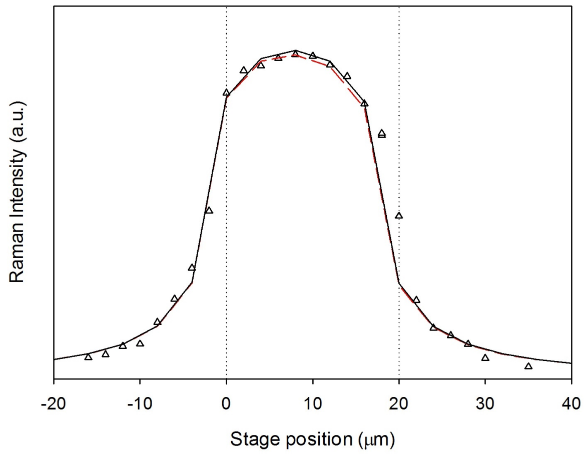

(c) PEQ film of thickness 20 μm.

Figure D.8: Raman depth profiles from PEQ ± 5 μm, using the original model.

In Section 5.4.3, it was stated that due to the finite resolution inherent in the simulation, it was sometimes necessary to displace the generated depth profile along the abscissa to optimise correspondence with the experimental data, particularly for thin films. Figure D.9(b) highlights why this may be so, where it can be seen how the dotted lines representing the top and bottom surface of the films do not align with the top and bottom surface of the film represented by experimental data.

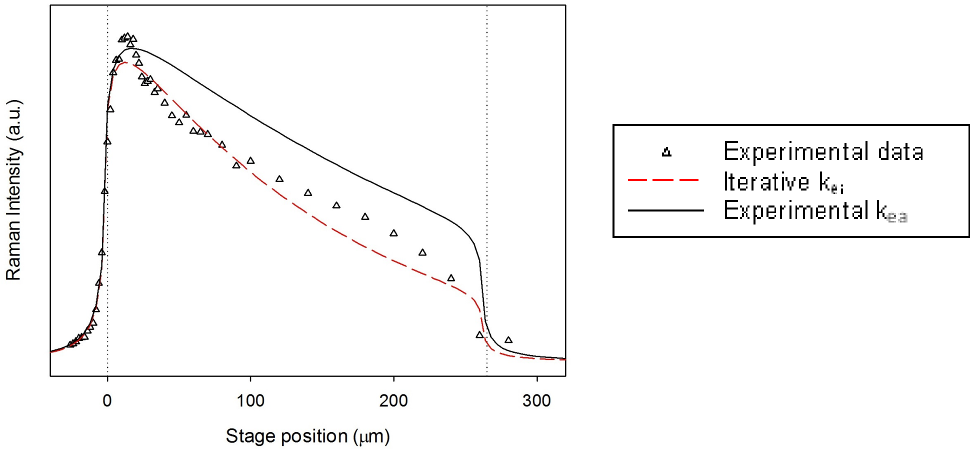

(a) PEX film of thickness 265 μm.

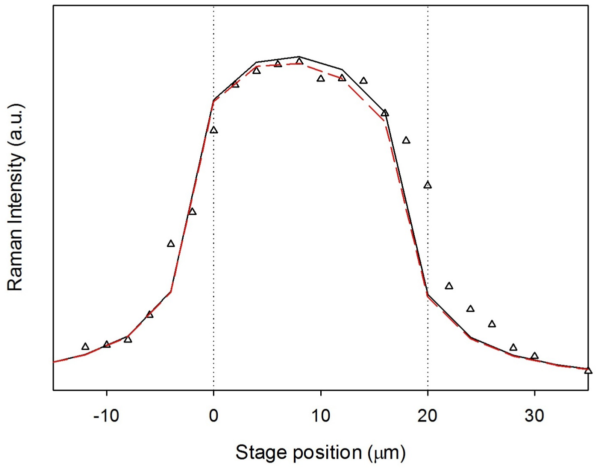

(b) PEX film of thickness 20 μm.

FIGURE D.9: Remainder of depth profiles obtained from PEX in air ± 5 μm. Generated using the orginal model.

From the depth profiles in this section, it is clear that there is poor correspondence between the generated Raman profiles using k_{ea} obtained via UV-visible data and experimental data. The discrepancies between these two sets of data were initially thought to be due to refraction effects at the sample surface, these were mitigated with the use of an immersion oil. The depth profiles obtained from samples immersed in oil are available in the next section.

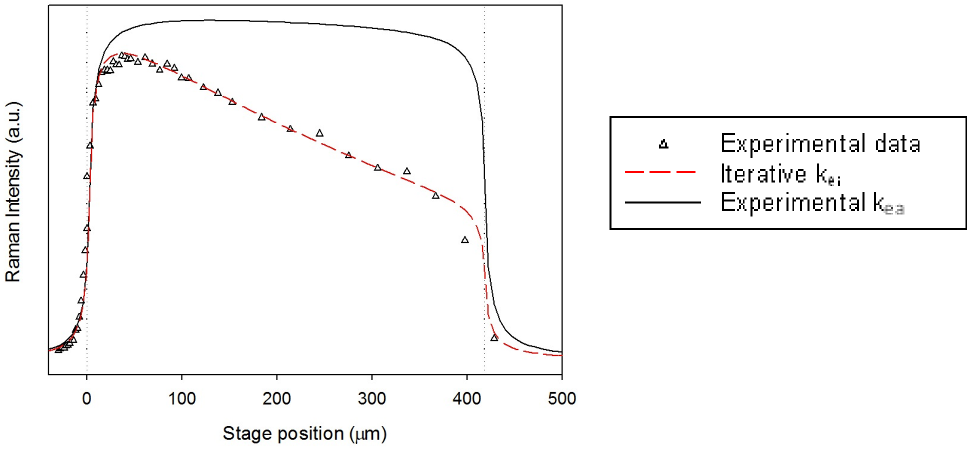

(a) NQ film of thickness 273 μm.

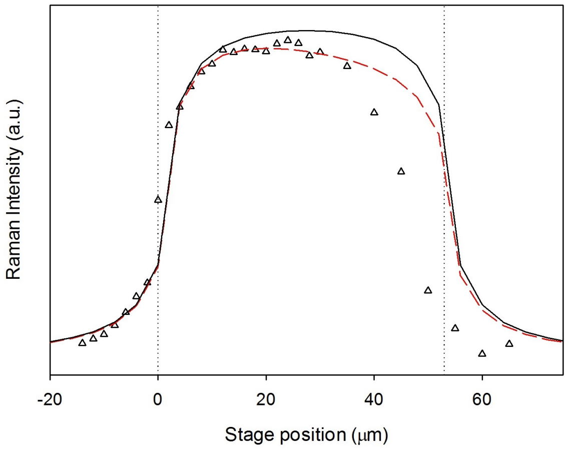

(b) NQ film of thickness 53 μm.

FIGURE D.10: Depth profiles obtained from NQ in air ± 5 μm. The lines are generated by the original model.

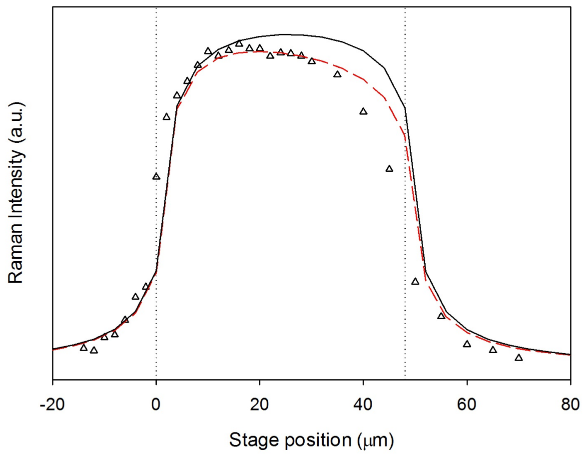

(a) NQ film of thickness 48 μm.

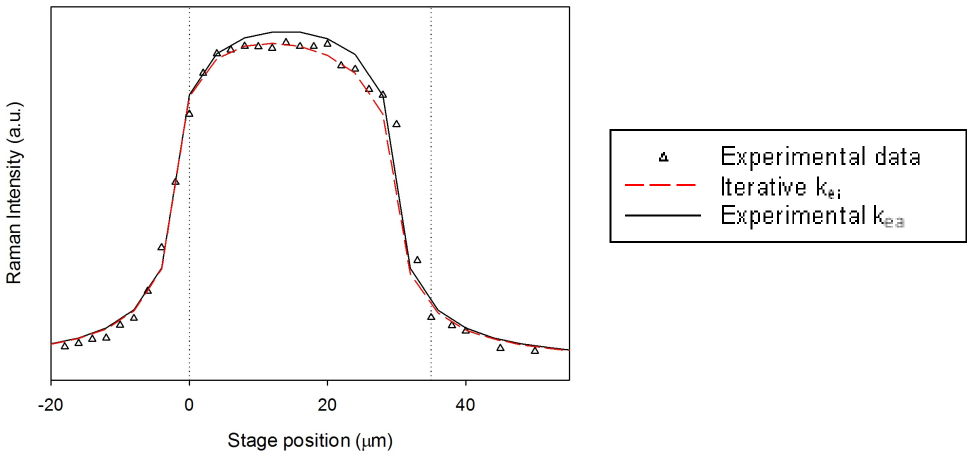

(b) NQ film of thickness 35 μm.

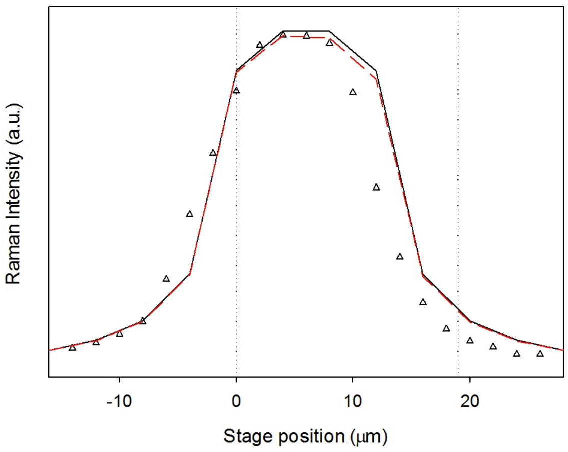

(c) NQ film of thickness 19 μm.

Figure D.11: NQ depth profiles ± 5 μm. Lines are generated from the original model.

D.5 Confocal Raman depth profiles - Films in oil

The following figures are representative of experimental depth profiles obtained from samples immersed in oil. Again, the dashed and solid lines represent the generated Raman depth profiles from the photon scattering model whilst using k_{ei} and k_{ea} respectively. As the refraction effects are alleviated by the use of an immersion oil, the bottom surface of the thickest sample from each polymer system cannot be observed due to the limitations of the objective.

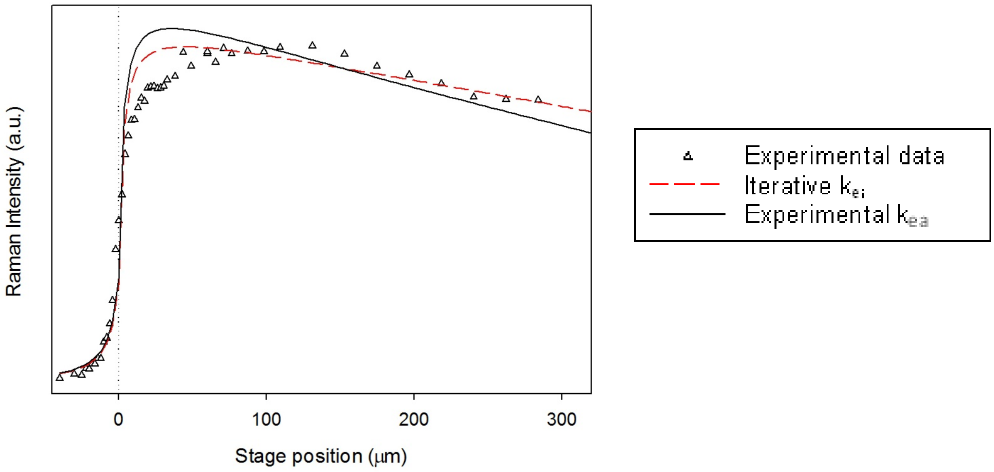

(a) PEQ film of thickness 411 μm.

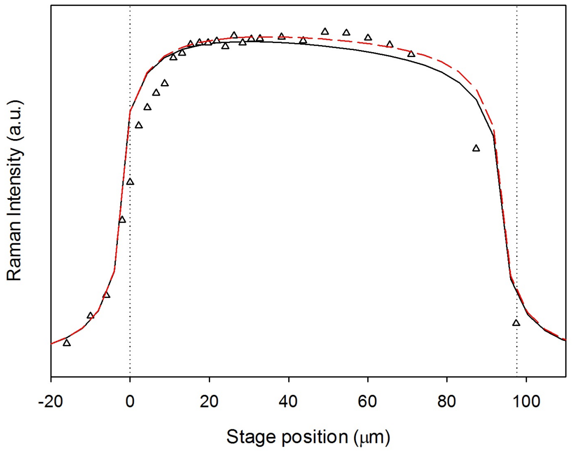

(c) PEQ film of thickness 88 μm.

FIGURE D.12: Profiles obtained from PEQ in oil ± 5 μm. Lines are generated by the original model.

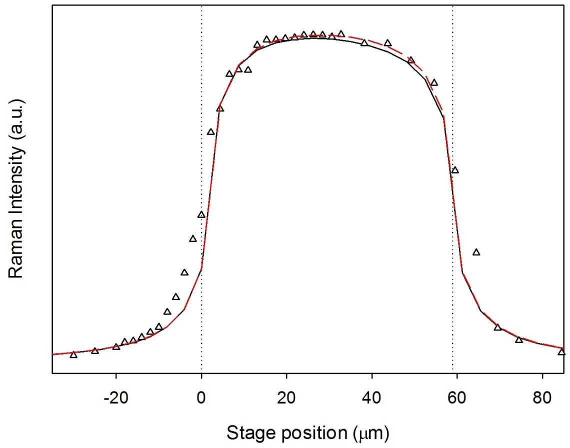

(a) PEQ film of thickness 53 μm.

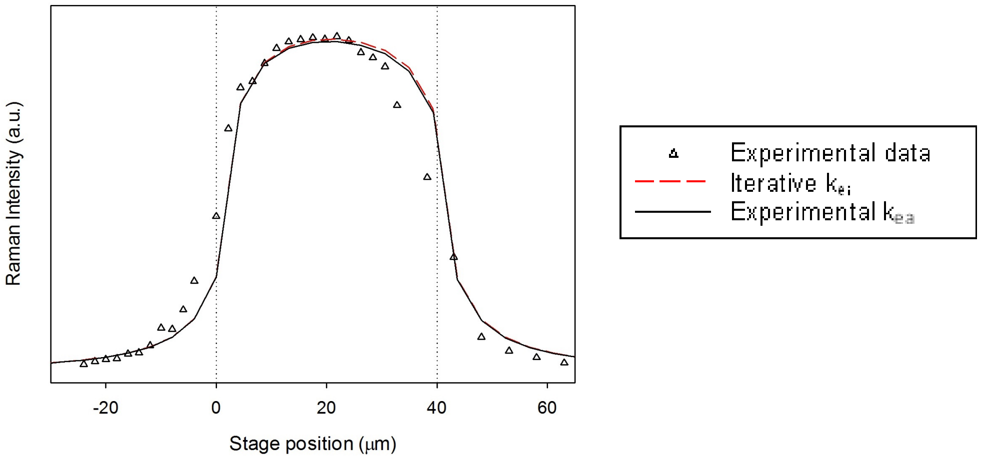

(b) PEQ film of thickness 36 μm.

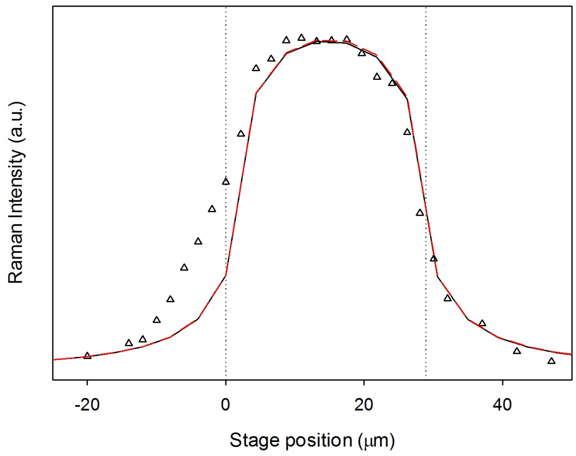

(d) PEQ film of thickness 26 μm.

FIGURE D.13: PEQ profiles in oil ± 5 μm. Lines are generated by the original model.

Figure D.13(d) from PEQ shows an unusual rise to maximum where the typical Raman depth profile shape is not observed when the focal point is focused -20 µm to 0 µm above the top sample surface. This is attributed to an unlevel surface in the area from which the data is acquired, as described in Section 5.4.5. In addition, the depth profiles obtained presented in this section (Figures D.12, D.13, D.14, D.15 and D.16) highlight how the effects of refraction have a significant impact on the Raman depth profile, in which the rate of attenuation is much higher for samples in air.

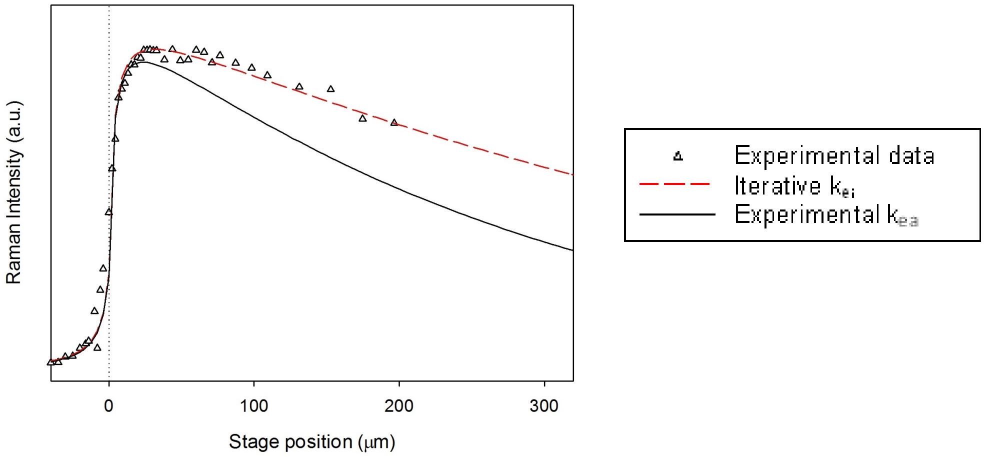

(a) PEX film of thickness 408 µm.

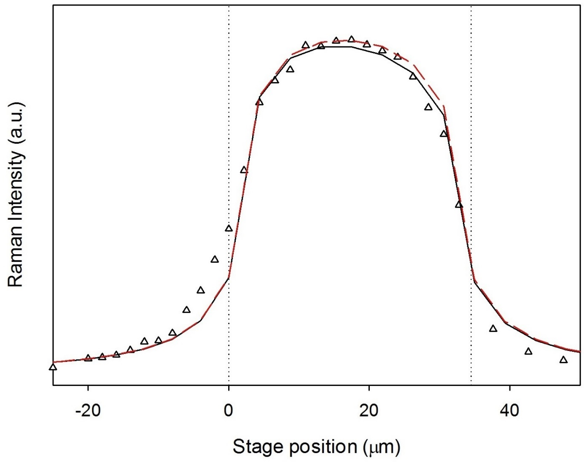

(c) PEX film of thickness 31 µm.

Figure D.14: Depth profiles obtained from PEX in silicone oil ± 5 µm. The lines are generated by the original photon scattering approach.

The attenuation coefficient for NQ was found to be the lowest and provides depth profiles with the lowest gradient as the focal point passes through the bulk of all samples. Much like the thinnest film for PEX, Figure D.16(d) shows how it is necessary to adjust the generated Raman depth profiles on the abscissa to correspond to the experimental data. The difference between the simulated profiles generated with k_{ei} and k_{ea} is minimal in comparison to those attenuation coefficients derived for PEQ and PEX.

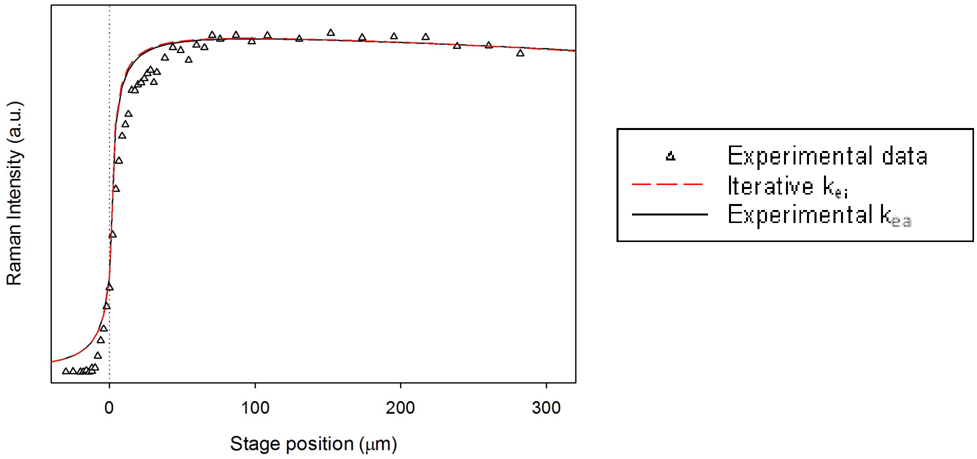

(a) NQ film of thickness 417 μm.

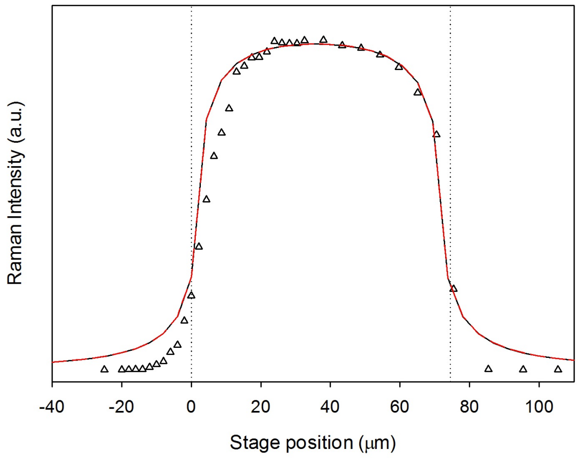

(c) NQ film of thickness 67 μm.

FIGURE D.15: Depth profiles obtained from NQ in silicone oil ± 5 μm. The lines are generated by the original photon scattering approach.

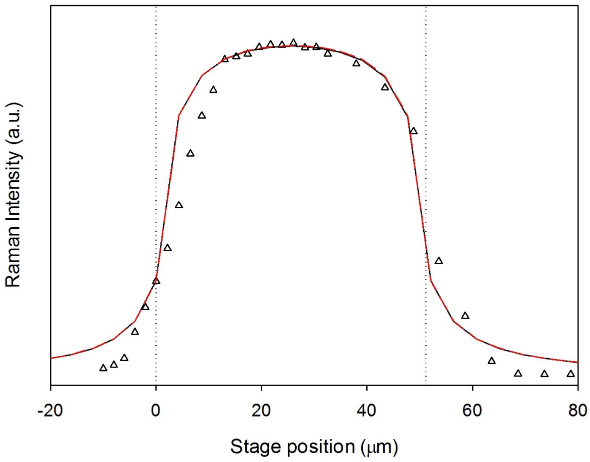

(a) NQ film of thickness 46 μm.

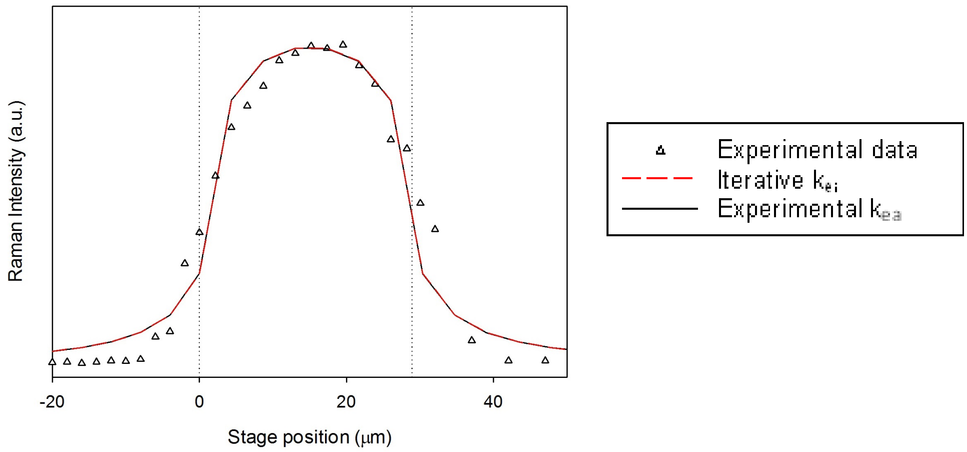

(b) NQ film of thickness 26 μm.

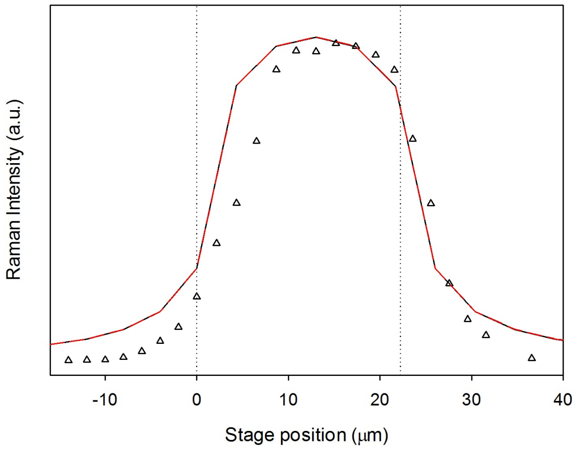

(d) NQ film of thickness 20 μm.

Figure D.16: NQ profiles in oil ± 5 μm. Lines are generated from the original model.

D.6 Depth profiles generated from the revised model

Figures D.17 and D.18 present the data obtained using the revised model simulated using the attenuation coefficient k_{ea} such that it can be compared with empirical data. The revised model shows a significant improvement in modelling the confocal Raman response when depth profiling thin polymer films, where a change in the photon flux (proportional to $n_z^{l_e}$) has been implemented. The dashed line represents the original model, whereas the solid line represents data generated from the revised model.

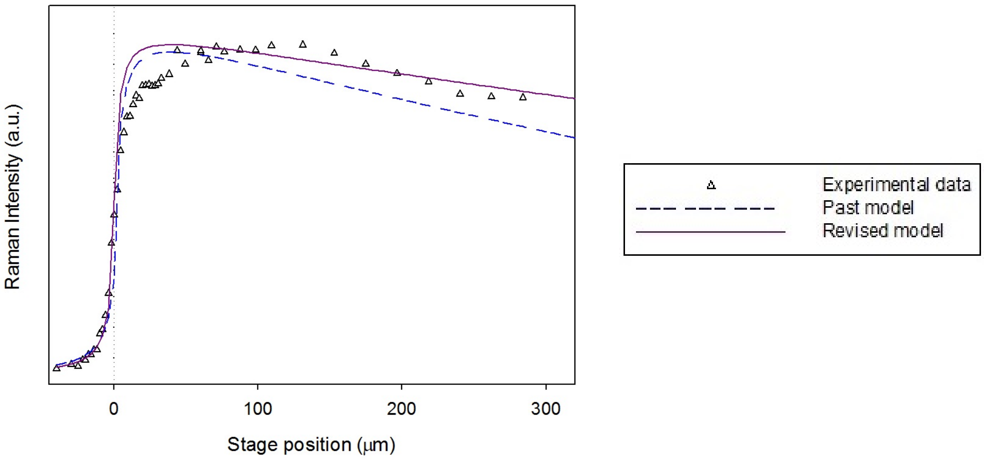

(a) PEQ film of thickness 411 μm.

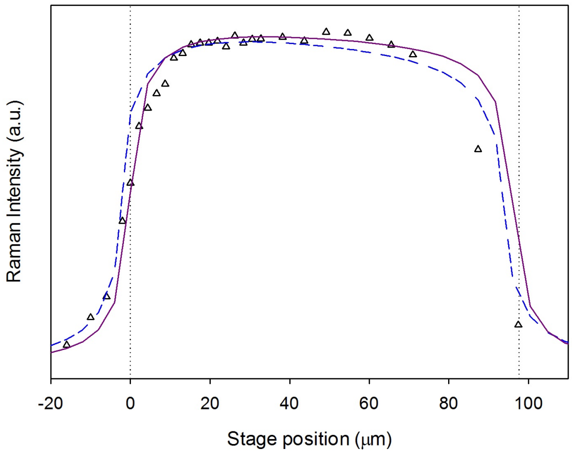

(c) PEQ film of thickness 88 μm.

FIGURE D.17: Depth profiles from PEQ in silicone oil ± 5 μm. The data were generated using $k_{e\alpha}$ using both the original and revised models.

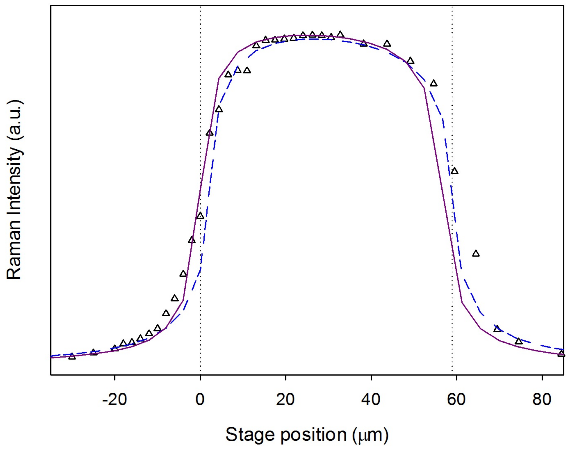

(a) PEQ film of thickness 53 μm.

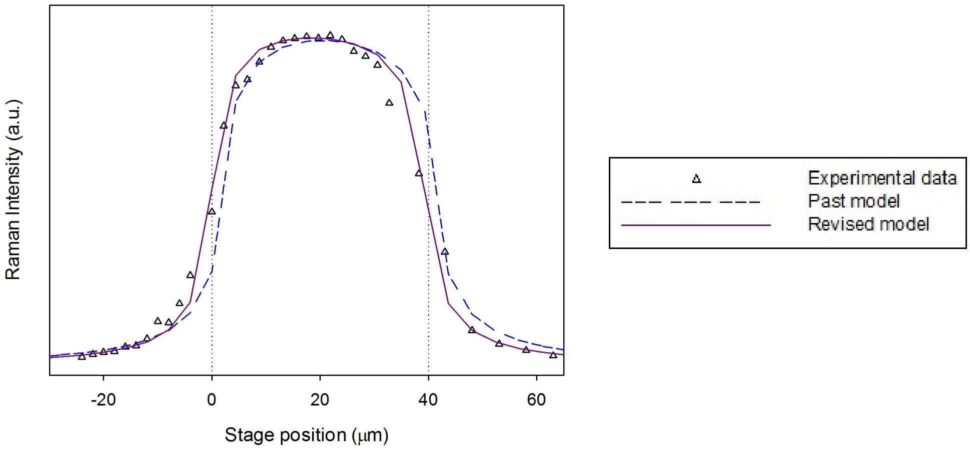

(b) PEQ film of thickness 36 μm.

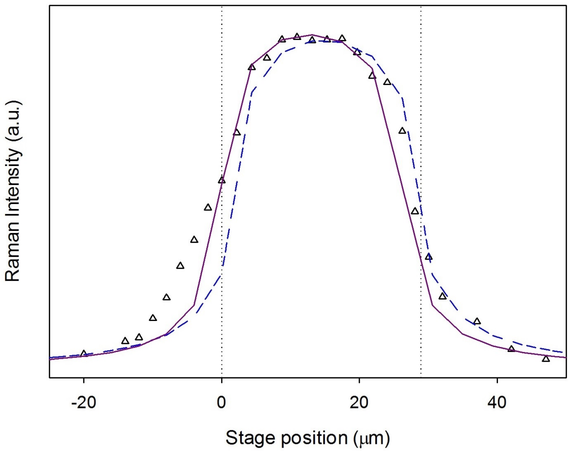

(d) PEQ film of thickness 26 μm.

FIGURE D.18: PEQ profiles in oil ± 5 μm. Lines show modelled data using k_{ea}.

From Figures D.17, D.18, D.19, D.20 and D.21, it is clear that the revised photon scattering model simulates confocal Raman depth profiles with a greater correspondence to empirical data when using a 'real' physical value of attenuation coefficient k_{ea} (than the original model), where the mathematics in the revised model acts to attenuate the incident light to a lesser degree. Different lateral adjustments (on the abscissa) may have been made to the two models for each sample which is why the simulated data may not necessarily align together.

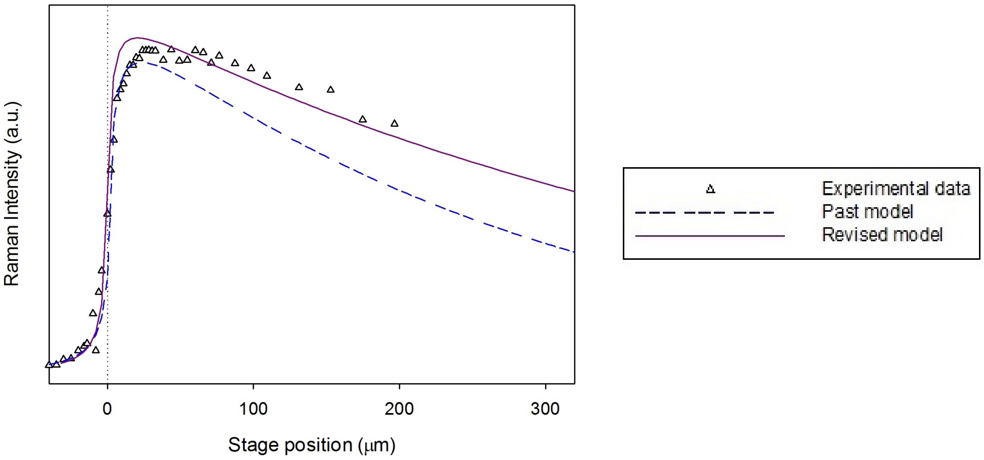

(a) PEX film of thickness 408 μm.

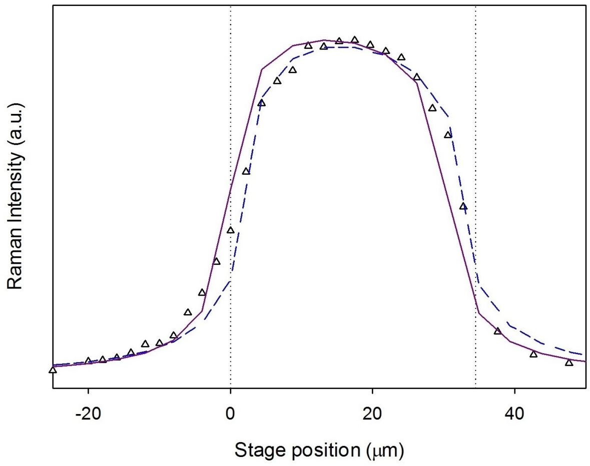

(c) PEX film of thickness 31 μm.

FIGURE D.19: Profiles obtained from PEX in oil ± 5 μm. Lines show modelled data using k_{ea}.

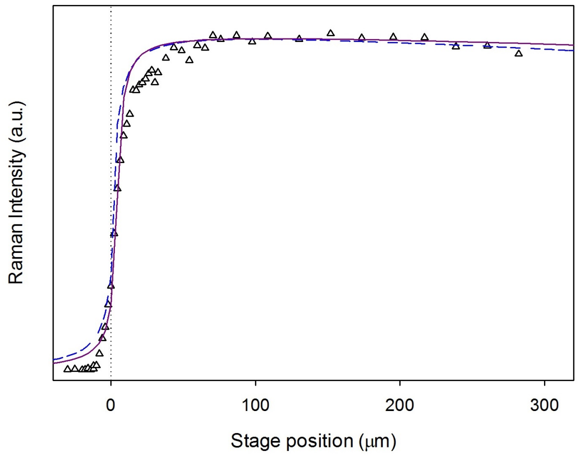

(a) NQ film of thickness 417 μm.

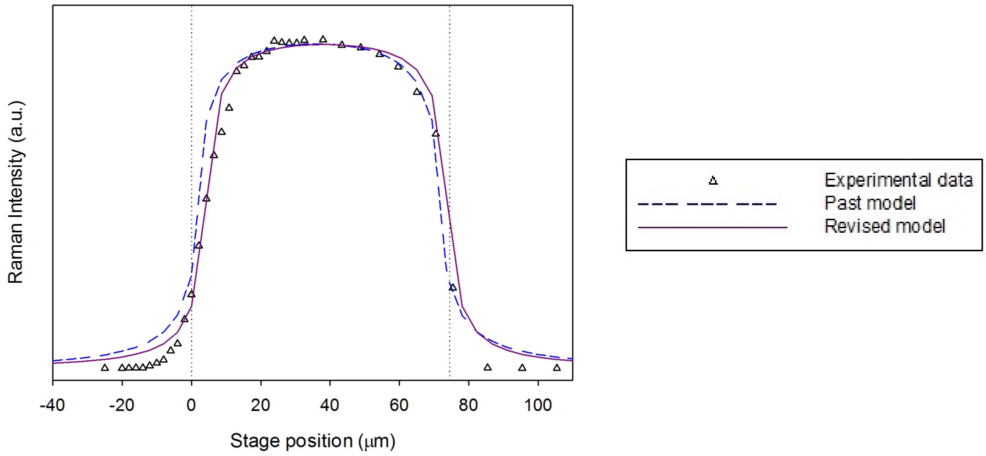

(b) NQ film of thickness 67 μm.

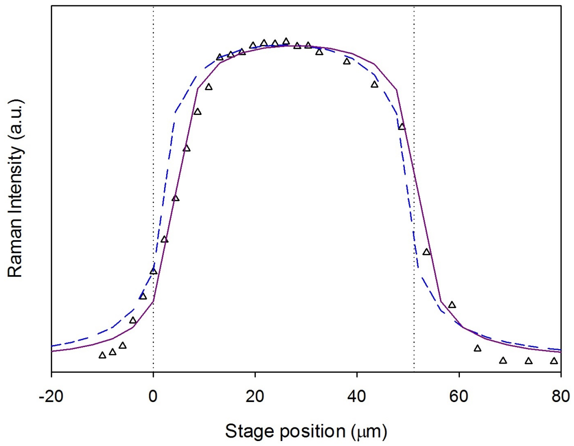

(d) NQ film of thickness 46 μm.

FIGURE D.20: NQ profiles in oil ± 5 μm. Lines show modelled data using k_{ea}.

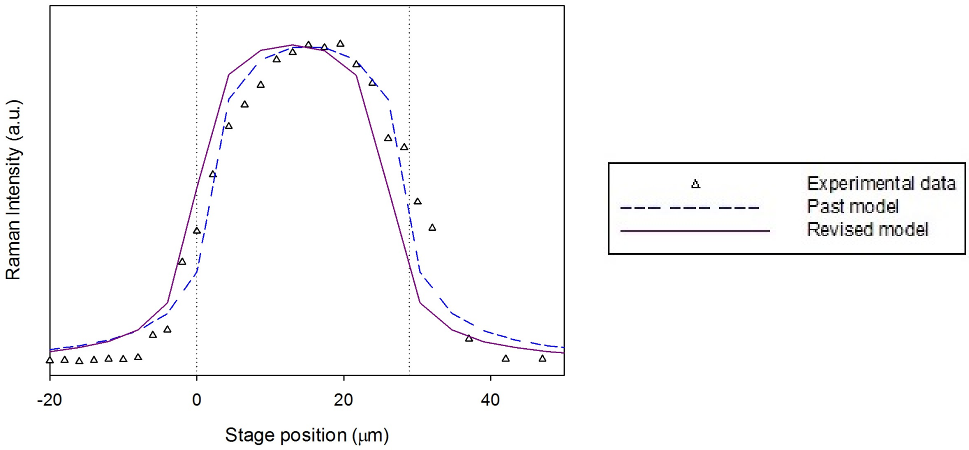

(a) NQ film of thickness 26 μm.

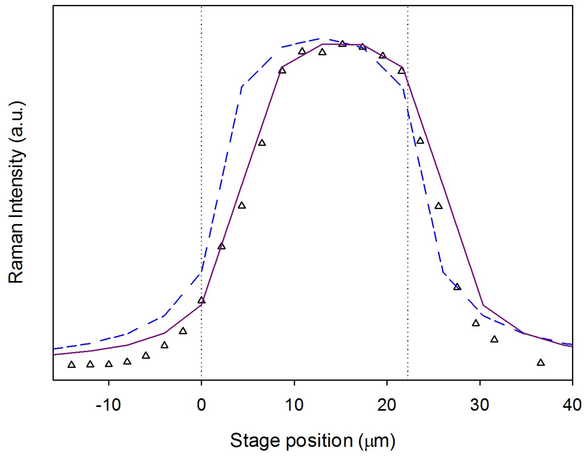

(c) NQ film of thickness 20 μm.

FIGURE D.21: Profiles from NQ in oil ± 5 μm. Lines show modelled data using k_{ea}.

D.7 Matlab code

```
%To get to output folder
current_time=clock;
outputfolder = sprintf('C:/Users/Cee/Documents/Sync/Matlabresultsmodel4/

Model4results-\%04i\%02i\%02i-\%02i\%02i\%02i',current_time(1), current_time(2),
current_time(3), current_time(4), current_time(5), current_time(6));
%stored the current time to be printed
mkdir(outputfolder);
printedheader = 0;

%***PARAMETERS***
Sample_thickness_values = Optical_thickness;% in microns
Height_values = HeightN;
Cell_size = 4; % in microns
Counter_sample_thickness = 0;
for Sample_thickness = Sample_thickness_values
Counter_sample_thickness = Counter_sample_thickness + 1;

Top_stage_pos_min = ((Sample_thickness*2)/-Cell_size)+2001;
Step_size = 1;
Max_stage_pos_min = ((Sample_thickness)/Cell_size)+2001;
Top_surface_values = Top_stage_pos_min:Step_size:Max_stage_pos_min;
%This runs it for all the #'s in the bracket
Ext_coef_ke = 0.00189*Cell_size;
%The bottom surface is kept lower in the code because "Top_surface" isn't defined yet
Loss_exp_le = 0.5;
Cone_waist = 1;
Total_flux = 10000;
Height = Height_values(Counter_sample_thickness);
    %***Start code***
    Acc_stage_position = zeros(1, length(Top_surface_values));
    AccN = zeros(1, length(Top_surface_values));
    AccO = zeros(1, length(Top_surface_values));
    %This stores ALL of the outputs for Raman_detected_new, Raman_detected_old
    %for each of the values in Top_surface_values.
    %The first parameter is rows and the second is columns. The zeros will
    %output a zero matrix with said ^ dimensions.
    %Top surface values will be the length of Top_surface_values, ie; if there
    %are 4 top_surf_values, we will have 4 columns.

    Top_surface_counter = 0; %counting the # of times
            we been through the top surface loop
```

```
for Top_surface = Top_surface_values
    Top_surface_counter = Top_surface_counter + 1;
    Bottom_surface = Top_surface+(Sample_thickness/Cell_size)-1 ;

    Index = 1:4000;
    Position_z = Index - 2001;
    Position_z(Position_z >=0) = Position_z(Position_z >=0)+1;
    Radius = abs(Position_z)+(Cone_waist-1);
    Area = Radius.^2;

    %***Values that are needed for the code before the loop***
    Counter = 0;
    Flux_in = Total_flux;
    Raman_acc_new = 0;
    Raman_acc_old = 0;

        for Current_position_z = Index
            Counter = Counter + 1;

            % Outside the sample we get
            Sample_bounds = 0;
            local_ke = 0;
            local_C = 1;

            % HOWEVER, inside the sample
                if (Current_position_z >= Top_surface &&
    Current_position_z <= Bottom_surface)
                    Sample_bounds = 1;
                    local_ke = Ext_coef_ke;
                    local_C = Radius(Counter).^Loss_exp_le;
                end

            Lost_flux = Flux_in*(1-exp(-1*local_ke))./local_C;
            Intensity= Flux_in/Area(Counter);
            Raman_generated = Intensity*Sample_bounds;
            Z_Re_surface = Index(Counter)-Top_surface;

            %***For the NEW MODEL***
            if Sample_bounds == 0
               Raman_detected_new = 0;
            else
               Raman_detected_new = Raman_generated*exp(-Ext_coef_ke*Z_Re_surface);
            end
```

```
                Raman_detected_new = Raman_detected_new + Raman_acc_new;
                Raman_acc_new = Raman_detected_new;

                %***For the OLD MODEL***
                Relative_to_surface = (Index(Counter)-Top_surface)*Sample_bounds;
                Raman_detected_old = (Total_flux)*
        exp(-2*Relative_to_surface*Ext_coef_ke)*Sample_bounds/Area(Counter);

                Raman_detected_old = Raman_detected_old + Raman_acc_old;
                Raman_acc_old = Raman_detected_old;

                Flux_in = Flux_in - Lost_flux;
            end

        Raman_detected_new = Raman_detected_new*Height;
        Raman_detected_old = Raman_detected_old*Height;
        Stage_position = (Top_surface-2001)*-Cell_size;

        Acc_stage_position(Top_surface_counter) = Stage_position;
        AccN(Top_surface_counter) = Raman_detected_new;
%use the top_srf_count cos it's to do with that loop not this
%current "counter" one within this loop
        AccO(Top_surface_counter) = Raman_detected_old;
    end
    figure %opens a new figure window so they don't overwrite
    plot(Acc_stage_position,AccN,'-b')%the dash means a solid line (blue)
    hold on %this holds the current graph such that the 2nd plot goes on top
    plot(Acc_stage_position,AccO, '--r') %dashed (--) line red
    hold off %turns hold off... Duh.

    title(sprintf('thickness = \%g', Sample_thickness));

    outputfilename = sprintf('\%s/Model4results.csv', outputfolder);
    outputfile = fopen(outputfilename, 'a');

    Printing_counter = 0;
    if printedheader == 0
       fprintf(outputfile, 'Acc_stage_position,AccN,AccO,Top_surface_values,
Sample_thickness,Cell_size,Ext_coef_ke,Loss_exp_le
,Cone_waist,Total_flux,Height\n');%This puts the headings
in for the top surface etc etc
       printedheader = 1;
    end
```

```
    for Stage_position = Acc_stage_position
        Printing_counter = Printing_counter +1;
fprintf(outputfile, '\%g,\%g,\%g,\%g,\%g,\%g,\%g,\%g,\%g,\%g,\%g\n',
                                Acc_stage_position(Printing_counter),
AccN(Printing_counter), AccO(Printing_counter),
                                Top_surface_values(Printing_counter),
Sample_thickness, Cell_size, Ext_coef_ke,
Loss_exp_le, Cone_waist, Total_flux, Height);
printf = "print formatted string"

    end

fclose(outputfile);
end

outputfilename_txt = sprintf('%s/Model4results.txt', outputfolder);
outputfile_txt = fopen(outputfilename_txt, 'a');%HERE 'a'
fprintf(outputfile_txt, 'Thickness\t%s\r\n', sprintf('%g, ', Sample_thickness_values));
fprintf(outputfile_txt, 'Ext_coef_ke\t%g\r\n', Ext_coef_ke);
fprintf(outputfile_txt, 'Loss_exp_le\t%g\r\n', Loss_exp_le);
fprintf(outputfile_txt, 'Cone_waist\t%g\r\n', Cone_waist);
fprintf(outputfile_txt, 'Total_flux\t%g\r\n', Total_flux);
fprintf(outputfile_txt, 'Height\t%s\r\n', sprintf('%g, ', Height_values));

fclose(outputfile_txt);
```

Bibliography

[1] J. K. Nelson, editor. *Dielectric Polymer Nanocomposites.* Springer, 2010.

[2] L. Fang. *Chinese Ceramics (Introductions to Chinese Culture).* Cambridge University Press, 3 edition, 2011.

[3] C.Green and A.Vaughan. Nanodielectrics - how much do we really understand? *IEEE Electrical Insulation Magazine*, 24(4):6–16, 2008.

[4] M. Reibold, P. Paufler, A. A. Levin, W. Kochmann, N. Ptzke, and D. C. Meyer. Materials: Carbon nanotubes in an ancient damascus sabre. *Nature*, 444:286, 2006.

[5] H. R. Dennis, D. L. Hunter, D. Chang, S. Kim, J. L. White, J. W. Cho, and D. R. Paul. Effect of melt processing conditions on the extent of exfoliation in organoclay-based nanocomposites. *Polymer*, 42(23):9513–9522, 2001.

[6] L. A Utracki. *Clay-Containing Polymeric Nanocomposites Volume 2.* Rapra Technology Ltd, 2004.

[7] J. Verhoeven and A. Pendray. The mystery of the damascus sword. *Scientific American*, pages 74–79, January 2001.

[8] M. Reading. *An Investigation into the Structure and Properties of Polyethylene Oxide Nanocomposites.* PhD thesis, School of Electronics and Computer Science, 2010.

[9] M. Sumita, H. Tsukihi, K. Miyasaka, and K. Ishikawa. Dynamic properties of polypropylene composites with ultrafine particles. *Journal of Applied Polymer*, 29(5):1523–1530, 1984.

[10] T. Agag, T. Koga, and T. Takeichi. Studies on thermal and mechanical properties of polyimide-clay nanocomposites. *Polymer*, 42:3399–3408, 2001.

[11] D. R. Johnston and M. Markovitz. Corona-resistant insulation, electrical conductors covered therewith and dynamoelectric machines and trasnformers incorporating components of such insulated conductors, 1988.

[12] P. O. Henk, T. W. Korsten, and T. Kvarts. Increasing the electrical discharge endurance of acid anhydride cured dgeba epoxy resin by dispersion of nanoparticle silica. *High Performance Polymers*, 11:281–296, 1999.

[13] M. Kozako, N. Fuse, Y. Ohki, T. Okamoto, and T. Tanaka. Surface degradation of polyamide nanocomposites caused by partial discharges using iec(b) electrodes. *IEEE Transactions on Dielectrics and Electrical Insulation*, 0:833–839, 2004.

[14] N. Fuse, M. Kozako, T. Tanaka, S. Murase, and Y. Ohki. Possible mechanisms and superior partial discharge resistance of polyamide nanocomposites. *Annual Report Conference on Electrical Insulation and Dielectric Phenomena.*, pages 161–169, 2004.

[15] T. Tanaka, A. Nose, Y. Ohki, and Y. Murata. Pd resistance evaluation of ldpe/mgo nanocomposite by a rod-to-plane electrode system. *IEEE International Conference on Properties and Applications of Dielectric Materials*, pages 319–322, 2006.

[16] J. K. Nelson and J. C. Fothergill. Internal charge behaviour of nanocomposites. *Nanotechnology*, 15(5):586–595, 2004.

[17] K. Y. Lau, A. S. Vaughan, G. Chen, and I. L. Hosier. Polyethylene nanodielectrics: The effect of nanosilica and its surface treatment on electrical breakdown strength. *Conference on Electrical Insulation and Dielectric Phenomena*, pages 21–24, 2012.

[18] S. Li, G. Yin, and J. Li. Breakdown performance of low density polyethylene nanocomposites. *International Conference on the Properties and Applications of Dielectric Materials*, pages 1–4, 2012.

[19] C. Chiang, C. M. Ma, F. Wang, and H. Kuan. Thermo-oxidative degradation

of novel epoxy containing silicon and phosphorous nanocomposites. *European Polymer Journal*, 39:825–830, 2003.

[20] A. Motori, F. Patuellil, A. Saccanil, G. C. Montanari, and R. Mulhaupt. Improving thermal endurance properties of polypropylene by nanostructuration. *2005 Annual Report Conference on Electrical Insulation and Dielectric Phenomena*, pages 195–198, 2005.

[21] T. Tanaka. Dielectric nanocomposites with insulating properties. *IEEE Transactions on Dielectrics and Electrical Insulation*, 12(5):914–928, 2005.

[22] A. K. Lau. *Multifunctional Polymer Nanocomposites.* CRC Press, 2010.

[23] P. C. Powell. *Enigineering with Polymers.* Chapman and Hall, 1983.

[24] I. Hamerton. *Recent Developments in Epoxy Resins.* Rapra Technology Ltd, 1996.

[25] F. Lapique and K. Redford. Curing effects on viscosity and mechanical properties of a commercial epoxy resin adhesive. *International Journal of Adhesion and Adhesives*, 22:337–346, 2002.

[26] Y. Cao and J. Cameron. The effects of curing conditions on the properties of silica modified glass fiber reinforced epoxy composite. *Journal of reinforced plastics and composites*, 26(1):41–50, 2007.

[27] X. Wang and J. K. Gillham. Analysis of crosslinking in amine-cured epoxy systems: The one-to-one relationship between tg and conversion. *Journal of Applied Polymer Science*, 45(12):2127–2143, 1992.

[28] H. Lee and K. Neville. *Epoxy Resins: Their Applications and Technology.* Literary Licensing, 2012.

[29] C. A. May and Y. Tanaka. *Epoxy Resins: Chemistry and Technology.* Marcel Dekker Inc, 1973.

[30] S. Pashaei, Siddaramaiah, and A. A. Syed. Investigation on thermal, mechanical and morphological behaviours of organ nanoclay incorporated epoxy nanocomposites. *Journal of Engineering and Applied Sciences*, 5:1292–1301, 2010.

[31] Rashmi, N. M. Renukappa, R. Chikkakuntappa, and N. Shivakumar Kunigal. Montmorillonite nanoclay filler effects on electrical conductivity, thermal and mechanical properties of epoxy-based nanocomposites. *Polymer Engineering*, 51:1827–1836, 2011.

[32] S. Singha and M. J. Thomas. Dielectric properities of epoxy nanocomposites. *IEEE Transactions on Dielectrics and Electrical Insulation*, 15(1):12–23, 2008.

[33] M. Roy, J. K. Nelson, R. K. MacCrone, L. S. Schadler, C. W. Reed, R. Keefe, and W. Zenger. Polymer nanocomposite dielectrics - the role of the interface. *IEEE Transactions on dielectrics and electrical institution*, 12:629–643, 2005.

[34] T. Imai, F. Sawa, T. Ozaki, T. Shimizu, R. Kido, M. Kozako, and T. Tanaka. Evaluation of insulation properties of epoxy resin with nano-scale silica particles. *Pcocecdings of 2005 International Symposium on Electrical Insulating Materials*, pages 239–242, 2005.

[35] M. Takala, H. Ranta, P. Nevalainen, P. Pakonen, J. Pelto, M. Karttunen, S. Virtanen, V. Koivu, M. Pettersson, B. Sonerud, and K. Ka. Dielectric properties and partial discharge endurance of polypropylene-silica nanocomposite. *IEEE Transactions on Dielectrics and Electrical Insulation*, 17:1259–1267, 2010.

[36] S. Pegel, P. Potschke, G. Petzold, I. Alig, S. M. Dudkin, and D. Lellinger. Dispersion, agglomeration, and network formation of multiwalled carbon nanotubes in polycarbonate melts. *Polymer*, 49:974 – 984, 2008.

[37] F. H. Gojny, J. Nastalczyk, Z. Roslaniec, and K. Schulte. Surface modified multi-walled carbon nanotubes in cnt/epoxy-composites. *Chemical Physics Letters*, 370:820 – 824, 2003.

[38] Y. Y. Huang and E. M. Terrentjev. Dispersion of carbon nanotubes: Mixing, sonication, stabilization and composite properties. *Polymers*, 4:275–295, 2012.

[39] T. R. Fromyr, F. K. Hansen, and T. Olsen. The optimum dispersion of carbon nanotubes for epoxy nanocomposites: Evolution of the particle size distribution by ultrasonic treatment. *Journal of Nanotechnology*, 2012:1–14, 2012.

[40] R. M. Reilly. Carbon nanotubes: Potential benefits and risks of nanotechnology in nuclear medicine. *The Journal of Nuclear Medicine*, 48:1039 – 1042, 2007.

[41] Q. Wang, G. Chen, and A. Alghamdi. Influence of nanofillers on electrical characteristics of epoxy resins insulation. *International Conference on Solid Dielectrics*, pages 263–266, 2010.

[42] M. Z. Rong, M. Q. Zhang, and W. H. Ruan. Surface modification of nanoscale filler for improving properties of polymer nanocomposites: a review. *Materials Science and Technology*, 22(7):787–796, 2006.

[43] Y. Guo, M. Wang, H. Zhang, G. Liu, L. Zhang, and X. Qu. The surface modification of nanosilica, preparation of nanosilica/acrylic core-shell composite latex, and its application in toughening pvc matrix. *Journal of Applied Polymer Science*, 107:2671–2680, 2008.

[44] J. K. Nelson, J. C. Fothergill, L. A. Dissado, and W. Peasgood. Towards and understanding of nanometric dielectrics. *IEEE Conference on Electrical Insulation and Dielectric Phenomena*, pages 295–298, 2002.

[45] C. Yeung and A. S. Vaughan. A study of how varying degrees of functionalised nanofiller have an effect on nanodielectrics. *2012 Conference on Electrical Insulation and Dielectric Phenomena*, 2012.

[46] I. Ramirez, E. Cherney, S. Jayaram, and M. Gauthier. Nanofilled silicone dielectrics prepared with surfactant for outdoor insulation applications. *IEEE Transactions on Dielectrics and Electrical Insulation*, 15(1):228–235, 2008.

[47] Y. H. Lee, C. B. Park, M. Sain, M. Kontopoulou, and W. Zheng. Effects of clay dispersion and content on the rheological, mechanical properties and flame retardance of hdpe/clay nanocomposites. *Journal of Applied Polymer Science*, 104:1993–1999, 2003.

[48] M. Reading, Z. Xu, A. S. Vaughan, and P. L. Lewin. On sample preparation and dielectric breakdown in nanostructured epoxy resins. *Journal of Phyiscs: Conference Series*, 310:1–7, 2011.

[49] D. Misra, D. Bauza, Z. Chen, T. Chikyow, H. Iwai, and Y. Oben, editors. *Dielectrics for Nanosystems 4: Materials Science, Processing, Reliability, and Manufacturing*, volume 28. 2010.

[50] Hielscher Ultrasonics. *UP200S/UP400S Instruction Manual, Ultrasonic processors for laboratories.*, 2006.

[51] Famas-Technology. Filler treatment with famasil silanes and titanates information sheet.

[52] Myer Kutz. *Applied Plastics Engineering Handbook: Processing and Materials.* William Andrew, 2011.

[53] C. A. Harper and E. M. Petrie. *Plastics Materials and Processes: A Concise Encyclopedia.* Wiley-Blackwell, 2003.

[54] C. W. Reed. Functionalisation of nanocomposite dielectrics. *IEEE International Symposium on Electrical Insulation (ISEI)*, pages 1–4, 2010.

[55] T. J. Lewis. Nanometric dielectrics. *IEEE Transactions on Dielectrics and Electrical Insulation*, 1(5):812–825, 1994.

[56] M. Roy, J. K. Nelson, R. K. MacCrone, and L. S. Schadler. Candidate mechanisms controlling the electrical characteristics of silica/xlpe nanodielectrics. *Journal of Material Science*, pages 3789–3799, 2006.

[57] T. J. Lewis. Interfaces and nanodielectrics are synonymous. *IEEE International Conference On Solid Dielectrics*, pages 792–795, 2004.

[58] C. Zou, J. C. Fothergill, and S. W. Rowe. A "water shell" model for the dielectric proeprties of hydrated silica-filled epoxy nano-composites. *IEEE Transactions on Dielectrics and Electrical Insulation*, 15:389–392, 2008.

[59] D. Fabiani, G. C. Montanari, and L. Testa. Effect of mechanical stress on fast pulse-like conduction in xlpe based materials. *IEEE Transactions on Dielectrics and Electrical Insulation*, 15:1–4, 2010.

[60] S. Retzke and J. Kindersberger. Role of the interface on the resistance to high voltage arcing, on tracking and erosion of silicon/sio2 nanocomposites. *IEEE Transactions on Dielectrics and Electrical Insulation*, 17(2):607–614, 2010.

[61] D. Ciprari, K. Jacob, and R. Tannenbaum. Characterisation of polymer nanocomposite interphase and its impact on mechanical properties. *Macromolecule*, 39:6565–6573, 2006.

[62] G. Tsagaropolous and A. Eisenberg. Dynamic mechanical study of the factors affecting the two glass transition behaviour of filled polymers. similaries and differences with ramdom ionomers. *Macromolecule*, 28:6067–6077, 1995.

[63] D. Pitsa and M. G. Danikas. Interfaces features in polymer nanocomposites: A review of proposed models. *NANO: Brief Reports and Reviews*, 6:497–508, 2011.

[64] E. Chabert, M. Bornet, E. Bourgeat-Lami, J. Y. Cavaill, R. Dendievel, C. Gauthier, J. L. Putaux, and A. Zaoui. Filler-filler interactions and viscoelastic behavior of polymer nanocomposites. *Materials Science and Engineering*, 381:320–330, 2004.

[65] J. Y. Li, L. Zhang, and S. Durcharme. Electric energy density of dielectric nanocomposites. *Applied Physics Letters*, 90:1–3, 2007.

[66] H. J. Sue and K. T. Gam. Epoxy nanocomposites based on the synthetic a-zirconium phosphate layer structure. *Chemistry of Materials*, 16:242–249, 2004.

[67] M. I. Sarwar, S. Zulfiqar, and Z. Ahmad. Preparation and properties of polymamide-titania nanocomposites. *Journal of Sol-Gel Science and Technology*, 44:41–46, 2007.

[68] F.Beari, M Brand, P. Jenkner, R. Lehnert, H. J. Metternich, J. Monkiewicz, and H.W. Siesler. Organofunctional alkoxysilanes in dilute aqueous solution: new accounts on the dynamic structural mutability. *Journal of Organometallic Chemistry*, 265:208216, 2001.

[69] F. Bauer, H.J. Glsel, U. Decker, H. Ernst, A. Freyer, E. Hartmann, and V. Sauerland nad R. Mehnert. Trialkoxysilane grafting onto nanoparticles for the prepara-

tion of clear coat polyacrylate systems with excellent scratch performance. *Progress in Organic Coating*, 47:147–153, 2003.

[70] D. L. Pavia, G. M. Lampman, and G. S. Kriz. *Introduction to Spectroscopy.* Thomason Brooks/Cole, 4th edition, 2008.

[71] H. Hart, L. E. Craine, D. J. Hart, and C. M. Hadad. *Organic Chemistry: A Short Course.* CENGAGE Learning Custom Printing, 2011.

[72] T. R. Gilson and P. J. Hendra. *Laser Raman Spectroscopy.* John Wiley & Sons, 1970.

[73] E. Hecht. *Optics.* Addison Wesley, 4th edition edition, 2002.

[74] M. Bass. *Handbook of Optics; Fibreoptics & Nonlinear Optics.* Mcgraw-Hill Professional, 2000.

[75] D. A. Long. *Raman Spectroscopy.* MacGrawn-Hill, 1977.

[76] D. W. Ball. Theory of Raman spectroscopy. *Spectroscopy*, 16(11):32–34, 2001.

[77] P. J. Wheatley. *The Determination of Molecular Structure.* Oxford University Press, 1969.

[78] B. H. Stuart. *Infrared Spectroscopy: Fundamentals and Applications.* John Wiley & Sons Ltd, 2004.

[79] D. I. Bower and W. F. Maddams. *The Vibrational Spectroscopy of Polymers.* Cambridge University Press, 1992.

[80] B. C. Smith. *Fundamentals of FourierTransform Infrared Spectroscopy.* CRC Press, second edition, 2011.

[81] D. J. O'Connor, B. A. Sexton, and R. S.C. Smart, editors. *Surface Analysis Methods in Materials Science.* Springer, 2003.

[82] B. C. Smith. *Fundamentals of Fourier Transform Infrared Spectroscopy.* CRC, 1995.

[83] L. D. S. Yadav. *Organic Spectroscopy.* Springer, 2004.

[84] R. J. Gale, editor. *Spectroelectrochemistry: Theory and Practice.* Springer, 1988.

[85] V. P. Tolstoy, I. Chernyshova, and V. A. Skryshevsky. *Handbook of Infrared Spectroscopy of Ultrathin Films.* Wiley-Blackwell, 2003.

[86] G. H. Meeten. *Optical Properties of Polymers.* Elsevier, 1986.

[87] R. F. Egerton. *Physical principles of electron microscopy.* Springer, 2008.

[88] L. Reimer. *Scanning Electron Microscopy: Physics of Image Formation and Microanalysis: Physics of Image Formation and Micronanalysis.* Springe, 2010.

[89] V. Nguyen, A. S. Vaughan, P. L. Lewin, and A. Krivda. Stoichiometry and interfacial effects in epoxy based systems. *Journal of IEEE Transaction on Dielectrics and Electrical Insulation - In publication*, 2011.

[90] I. Foubert, P. A. Vanrolleghem, and K. Dewettinck. A differential scanning calorimetry method to determine the isothermal crystallization kinetics of cocoa butter. *Thermochimica*, 400:131–142, 2003.

[91] H. Li, W. Lejun, and C. P . Wong. Study of a controlled thermally degradable epoxy resin system for electronic packaging. *Electronic Components and Technology Conference*, pages 1356–1361, 2001.

[92] N. M. Alves, J. L. Gomez Ribelles, and J. F. Mano. Enthalpy relaxation studies in polymethyl methcrylate netwirjs with different crosslinking degrees. *Polymer*, 46:491–504, 2005.

[93] F. Kremer and A. Schnhals, editors. *Broadband Dielectric Spectroscopy.* Springer, 2002.

[94] T. Blythe and D. Bloor. *Electrical Properties of Polymers.* Cambridge University Press, second edition edition, 2005.

[95] P. Barber, S. Balasubramanian, T. Anguchamy, S. Gong, A. Wibowo, H. Gao, H. J. Phoehn, and HC. Loye. Polymer composite dielectric materials for pulse power energy storage. *Materials*, 2:1697–1733, 2009.

[96] L. A. Dissado and J. C. Fothergill. *Electrical Degradation and Breakdown in Polymers.* Institution of Engineering and Technology, 1992.

[97] C. C. Ku and R. Liepins. *Electrical Properties of Polymers - Chemical Principles.* Hanser Publishers, Munich, 2003.

[98] M. Cacciari, G. Mazzanti, and G. C. Montanari. Weibull statistics in short-term dielectric breakdown of thin polyethylene films. *IEEE Transactions on Dielectrics and Electrical Insulation*, 1(1):153–159, 1994.

[99] Q. Wang. *The Effect of Nano Size Fillers on Electrical Performance of Epoxy Resin.* PhD thesis, Electronics and Computer Science, 2012.

[100] A. Ash, L. Schadle, and R. Siegel. Glass transition behaviour of alumina/polymethylmecrylate nanocomposites. *Matterials Letters*, 55:83–87, 1993.

[101] T. Andritsch. *Epoxy Based Nanocomposite for High Voltage DC Applications.* PhD thesis, Delft University, 2010.

[102] G. L. Witucki. A silane primer: Chemistry and applications of alkoyl silanes. *Journal of Coatings Technology (reprint)*, pages 1–4, 1992.

[103] Z. Wang, T. Iizuka, M. Kozako, Y. Ohki, and T. Tanaka. Development of epoxy/bn composites with high thermal conductivity and sufficient dielectric breakdown strength part ii-breakdown strength. *IEEE Transactions on Dielectrics and Electrical Insulation*, 18(6):1973–1983, 2011.

[104] R. Kochetov. *Thermal and electrical properties of nanocomposites, including material processing.* PhD thesis, 2012.

[105] M. Reading, Z. Xu, A. S. Vaughan, and P. Lewin. The effect of sample thickness on the relative breakdown strength of epoxy systems. *Dielectrics 2011, The University of Kent, Cantebury*, page 1, 2011.

[106] H. Couderc, M. F. Frchette, S. Savoie, M. Reading, and A. S. Vaugha. Dielectric and thermal properties of boron nitride and silica epoxy composites. *Conference Record of the International Symposium on Electrical Insulation (ISEI)*, 2012.

[107] J. Clayden, N. Greeves, and S. Warren. *Organic Chemistry.* OUP Oxford, 2nd edition edition, 2012.

[108] R. Kochetov, T. Andritsch, U. Lafont, P. H. F. Morshuis, and J. J. Smit. Thermal conductivity of nano-filled epoxy systems. *Conference on Electrical Insulation and Dielectric Phenomena*, pages 658–661, 2009.

[109] K. Lau, M. Lu, C. Lam, H. Cheung, F. Sheng, and H. Li. Thermal and mechanical properties of single-walled carbon nanotube bundle-reinforced epoxy nanocomposites: the role of solvent for nanotube dispersion. *Composites Science and Technology*, 65:719–725, 2005.

[110] G. Socrates. *Infrared and raman Characteristic Group Frequencies.* Wiley-Blackwell, 3rd edition, 2001.

[111] J. Lu and C. P. Wong. Tailored dielectric properties of high-k polymer composites via nanoparticle surface modification for embedded passives applications. *Electronic Components and Technology Conference*, pages 1033–1039, 2007.

[112] Gelest Inc. Silane coupling agents (information sheet), 2006.

[113] T. Materne, F. Buyl, and G. L. Witucki. Organosilane technology in coating applications: Review and perspectives. *Dow Corning Corporation*, pages 1–16, 2012.

[114] L. Brown. Heterogenisation of ketone catalysts within mesoporous supports for asymmetric epoxidation. *In publication*, 3:843–850, 2013.

[115] M. Reading, Z. Xu, A. S. Vaughan, and P. L. Lewin. The thermal and electrical properties of nano-silicon dioxide filled epoxy systems for use in high voltage insulation. *Electrical Insulation Conference*, pages 493–497, 2011.

[116] M. Frchette, S. Savoie, M. Reading, and A. S. Vaughan. Dielectric and thermal properties of boron nitride and silica epoxy composites. *IEEE International Symposium on Electrical Insulation (ISEI)*, 64-68, 2012.

[117] M. F. Frchette, S. Savoie, M. Reading, A. S. Vaughan, H. Couderc, J. Castellon, and L. Banet. Surface resistance of epoxy-based composites to electrical discharge.

IEEE International Symposium on Electrical Insulation (ISEI), pages 632–636, 2012.

[118] J. P. Reithnaier, P. Paunovic, W. Kulisch, C. Popov, and P. Petkov, editors. *Nanotechnological Basis for Advanced Sensors (NATO Science for Peace and Security Series B: Physics and Biophysics)*. Springer, 2011.

[119] C. S. Reddy and C. K. Das. Hldpe/organic functionalised sio2 nanocompoites with improved thermal stability and mechanical properties. *Composite Interfaces*, 11:687–699, 2005.

[120] H. Chen, S. Zhou, G. Gu, and L Wu. Modification and dispersion of nanosilica. *Journal of Dispersion Science and Technology*, 25(6):837–848, 2004.

[121] Pike Technologies. *ATR - Theory and Applications*. Pike Technologies, 2011.

[122] PerkinElmer Life and Analytical Sciences. *FT-IR spectroscopy, Attenuated Total Reflectance (ATR) - Technical Note*. PerkinElmer, 2005.

[123] *Standard Test Method for Dielectric Breakdown Voltage and Dielectric Strength of Solid Electrical Insulating Materials at Commercial Power Frequencies*, 1992.

[124] D. H. Mills. *Electroluminescence and ageing of polyethylene*. PhD thesis, Faculty of Physical and Applied Sciences - Department of Electronics and Computer Science, April, 2012.

[125] V. Volvovek, K. Furic, L. Bistricic, and M. Leskovac. Micro raman spectroscopy of silica nanoparticles treated with aminopropylsilanetriol. *Macromolecular Symposia*, 265:178–182, 2008.

[126] P. B. Leng, H. M. Akil, and O. H. Lin. Thermal properties of microsilica and nanosilica filled polypropylene composite with epoxy as dispersing aid. *Journal of Reinforced Plastics and Composites*, 26:761–770, 2007.

[127] Y. Kobayashi, A. Kurosawa, D. Nagao, and M. Konno. Fabrication of barium titanate nanoparticles-epoxy resin composite films and their dielectric properties. *Polymer Composites*, 49(6):1179–1183, 2009.

[128] C. S. Reddy, P. Kumar Patra, and C. K. Das. Ethylene-octene copolymer-nanosilica nanocomposites: Effects of epoxy resin functionalized nanosilica on morphology, mechanical, dynamic mechanical and thermal properties. *Macromolecular Symposia*, 227:119–129, 2009.

[129] Horiba-Jobin Yvon. *Raman Data Analysis - Raman spectroscopy for analysis and monitoring.*

[130] K. J. Kingma and R. J. Hemley. Raman spectroscopic study of micro-crystalline silica. *American Miner*, 79:269–273, 1994.

[131] Y. Park and M. Nagai. Proton exchange nanocomposite membranes based on 3-glycidoxypropyltrimethoxysilane, silicotungstic acid and a-zirconium phosphate hydrate. *Solid State Ionics*, 145:149–160, 2001.

[132] M. Gnyba, M. Keranen, M. Kozanecki, and B. B. Kosmowski. Raman investigation of hybrid polymer thin films. *Material Science - Poland*, 23:31–39, 2005.

[133] B. Riegel, S. Blittersdorf, W. Kierfer, S. Hofacker, M. Muller, and G. Schottner. Kinetic investigations of hydrolysis and condensation of the glycidoxypropyltrimethoxysilane/aminopropyltriethoxy-silane system by means of ft-raman spectroscopy i. *Journal of Non-Crystalline Solids*, 226:76–84, 1998.

[134] S. M. Kang, K. M. Ahn, and B. T. Ahn. High-quality polycrystalline silicon film crystallised from amorphous silicon film using nicl2 vapour. *Journal of The Electrochemical Society*, 159:H29–H32, 2012.

[135] P. Colomban, M-P Etcheverry, M. Asquier, M. Mounichou, and A. Tourine. Raman identification of ancient stained glasses and their degree of deterioration. *Journal of Raman Spectroscopy*, 37:614–626, 2006.

[136] X. Liu and S. Zhao. Measurement of the condensation temperature of nano silica powder organically modified by a silane coupling agent and its effect evaluation. *Journal of Applied Polymer Science*, 108:3038–3045, 2008.

[137] I.D. Sideridou and M. M. Karabela. Effect of the amount of 3-

methacyloxypropyltrimethoxysilane coupling agent on physical properties of dental resin nanocomposites. *Dental Materials*, 25(11):1315–1324, 2009.

[138] S. Chen, B. You, s. Zhou, and L. Wu. Preparation and characterisation of scratch and mar resistanct waterborne epoxy/silica nanocomposite clearcoat. *Journal of Applied Polymer Science*, 112, 2009.

[139] A. Rahimi, S. Gharazi, A. Ershad-Langroudi, and D. Ghasemi. Synthesis and characterisaion of hydrophobic nanocomposite coating on glass substrate. *Journal of Applied Polymer Science*, pages 5322–5329, 2006.

[140] K. Y. Lau, A. S. Vaughan, G. Chen, I. L. Hosier, and A. F. Holt. On the dielectric response of silica-based polyethylene nanocomposites. *Journal of Phyiscs D: Applied Physics*, 46:1–9, 2013.

[141] Polytechnic of Turin Applied Sciences and Carbon Group Technology Department.

[142] Y. Zhou, F. Pervin, L. Lewis, and S. Jeelani. Experimental study on the thermal and mechanical properties of multi-walled carbon nanotube reinforced epoxy. *Materials Science and Engineering*, 452-453:657–664, 2007.

[143] K. Wang, L. Chen, J. Wu, M. L. Toh, C. He, and A. F. Yee. Epoxy nanocomposites with highly exfoliated clay: Mechanical properties and fracture mechanisms. *Macromolecule*, 38:788–800, 2005.

[144] H. Zhang, Z. Zhang, K. Friedrich, and C. Eger. Property improvements of in situ epoxy nanocomposites with reduced interparticle distance at high nanosilica content. *Acta Ma*, 54:1833–1842, 2006.

[145] Y. Okazaki, M. Kozako, M. Hikita, and T. Tanaka. Effects of addition of nanoscale alumina and silica fillers on thermal conductivity and dielectric strength of epoxy/alumina microcomposites. *International Conference on Solid Dielectrics*, pages 1–4, 2010.

[146] Z. Guo, T. Pereira, O. Choi, Y. Wang, and H. T. Hahn. Surface functionalized alumina nanoparticle filled polymeric nanocomposites with enhanced mechanical properties. *Journal of Material Chemistry*, 16:2800–2808, 2006.

[147] L. Hui, J. K. Nelson, and L. S. S. The influence of moisture on the electrical performance of xlpe/silica nanocomposites. *International Conference on Solid Dielectrics*, pages 1–4, 2010.

[148] D. Fabani, G. C. Montanari, L. Testa, R. Schifani, F. Guastavino, F. Bellucci, and F. Deorsola. Effect of water adsorption on the dielectric properties of polymer nanocomposites. *International Symposium on Electrical Insulating Materials*, pages 510–513, 2008.

[149] X. Huang, Y. Zheng, and P. Jiang. Influence of nanoparticle surface treatment on the electrical properties of cycloaliphatic epoxy nanocomposites. *IEEE Transactions on Dielectrics and Electrical Insulation*, 17:635–643, 2010.

[150] G. Chen and A. E. Davies. The influence of defects on the short-term breakdown characteristics and long-term dc performance of ldpe insulation. *IEEE Transactions on Dielectrics and Electrical Insulation*, 7, 2000.

[151] M. Preghenella, A. Pegoretti, and C. Migliaresi. Thermo-mechanical characterisation of fumed silica-epoxy nanocomposites. *Polymer*, 46:12065–12072, 2005.

[152] J. Huang, Z. Zhu, J. Yin, X. Qian, and Y. Sun. Poly(etherimide)/montmorillonite nanocomposites prepared by melt intercalation: morphology, solvent resistance properties and thermal properties. *Polymer*, 42:873–877, 2001.

[153] V. Nguyen, A. S. Vaughan, P. L. Lewin, and A. Krivda. Stoichiometry and effects of nano-sized and micro-sized fillers on epoxy based system. *Conference on Electrical Insulation and Dielectric Phenomena*, pages 302–305, 2011.

[154] J. K. Nelson Editor. *Dielectric Polymer Nanocomposites*. Springer, 2010.

[155] H. Couderc, M. Frechette, M. Reading, and A. S. Vaughan. Dielectric and thermal properties of boron nitride and silica epoxy composites. *IEEE International Symposium on Electrical Insulation (ISEI)*, pages 64–68, 2012.

[156] F. Meyer, G. Sanz, A. Eceiza, and I. Mondragon. The effect of stoichiometry and thermal history during cure on structure and properties of epoxy networks. *Polymer*, 36:1407–1414, 1995.

[157] H. Ishida and D. J. Allen. Mechanical characterization of copolymers based on benzoxazine and epoxy. *Polymer*, 37:4487–4495, 1996.

[158] V. Nguyen, A. S. Vaughan, P. L. Lewin, and A. Krivda. On the stoichiometry with space charge and breakdown behaviour of an epoxy based system with nano-sized and micro-sized fillers. *IEEE Electrical Insulation and Dielectric Phenomena*, pages 287–290, 2012.

[159] T. V. Kosmidou, A. S. Vatalis, C. G. Delides, E. Logakis, P. Pissis, and G. C. Papanicolaou. Structural, mechanical and electrical characterization of epoxy-amine/carbon black nanocomposites. *eXPRESS Polymer Letters*, 2(5):364–372, 2008.

[160] P. Pissis and D. Fragiadakis. Dielectric studies of segmental dynamics in epoxy nanocomposites. *Journal of Macromolecular Science Part B: Physics*, pages 119–136, 2007.

[161] A. K. Jonscher. Dielectric relaxation in solid. *Journal of Physics D: Applied Physics*, 32:R57–R70, 1999.

[162] L. A. Dissado and R. M. Hill. Anomalous low-frequency dispersion. *Journal of the Chemical Society, Faraday Transactions*, 80(2):291–319, 1984.

[163] W. Kasprzak, Z. Nadolny, K. Walczak, K. Siodla, W. Sikorski, K. Kozwiak, D. Pasciak, and L. Moron. The influence of barium titanate as a filler in impregnating epoxy resin on chosen electrical parameters of obtained material. *Materiials Science - Poland*, 27(4/2):1219–1227, 2009.

[164] G. Iyer, R. S Gorur, and R. Richert. Dielectric properties of epoxy based nanocomposites for high votage insulation. *IEEE Transactions on Dielectrics and Electrical Insulation*, 18(3):659–666, 2011.

[165] J. Castellon, H. N. Nguyen, S. Agnel, and A. Toureille. Electrical properties analysis of micro and nano composite epoxy resin materials. *IEEE Transactions on Dielectrics and Electrical Insulation*, 18:3, 2011.

[166] M. F. Frchette, H. D. Martinez, S. Savoie, A. Krivda, L. E. Schmidt, and D. Zegarac. Dielectric study with epoxy-based nanostructured microcomposites containing silica. *International Symposium on Electrical Insulation*, pages 1–4, 2010.

[167] I. Plesa, F. Ciuprina, and P. V Notingher. Dielectric spectroscopy of epoxy resin with and without inorganic nanofillers. *Journal of Advanced Research in Physics*, 1:1–5, 2010.

[168] F. A. Carey and R. J. Sundberg. *Advanced Organic Chemistry, Part A: Structure and Mechanisms*. Springer, 2007.

[169] M. A. Fox and J. K. Whitesell. *Organic Chemistry*. Jones and Bartlett Publishers, 2004.

[170] M. Lee, W. Kim, J. Ku, Y. D. Kin, B. H. Min, and J. H. Jim. Influence of nanoclays on electrical and morphological properties of thermoplastic polyurethane/-multiwalled carbon nanotube/clay nanocomposites. *Journal of Applied Polymer Science*, 127:4233–4240, 2012.

[171] J. V. Gulmine, P. R. Janissek, H. M. Heise, and L. Akcelrud. Polyethylene characterisation by ftir. *Polymer Testing*, 21:557–563, 2002.

[172] F. F. Lange. The interaction of a crack front with a second-phase dispersion. *Philosophical Magazine*, 22:983–992, 1970.

[173] F. F. Lange and K. C Radford. Fracture energy of an epoxy composite system. *Journal of Material Science*, 6:1197–1203, 1971.

[174] T. Kawaguchi and R. A. Pearson. The moisture effect on the fatigue crack growth of glass particle and fiber reinforced epoxies with strong and weak bonding conditions: Part 2. a microscopic study on toughening mechanism. *Composites Science and Technology*, 64:1991–2007, 2004.

[175] R. C. Smith, C. Liang, M. Landry, J. K. Nelson, and L. S. Schadler. The mechanisms leading to the useful electrical proeprties of polymer nanodielectrics. *IEEE Transactions on Dielectrics and Electrical Insulation*, 15:187–196, 2008.

[176] C. Zou and J. C. Fothergill. The effect of water absorption on the dielectric properties of epoxy nanocomposites. *IEEE Transactions on Dielectrics and Electrical Insulation*, 15:106–117, 2008.

[177] W. Yang, R. Yi, S. Hui, Y. Xu, and Z. Cao. Analysis of the dielectric spectroscopy of an epoxy-zno nanocomposite using the universal relaxation law. *Journal of Applied Polymer Science*, 127, 2012.

[178] J. C. Fothergill, J. K. Nelson, and M. Fu. Dielectric properties of epoxy nanocomposites containing tio2, alo3 and zno. *Conference on Electrical Insulation and Dielectric Phenomena*, pages 406–409, 2004.

[179] P. Maity, P. K. Poovamma, S. Basu, V. Parameswaran, and N. Gupta. Dielectric spectroscopy of epoxy resin with and without nanometric alumina fillers. *IEEE Transactions on Dielectrics and Electrical Insulation*, 16(5):1481–1488, 2009.

[180] L. A. Dissado and R. M. Hill. Anomalous low-frequency dispersion. near direct current conductivity in disordered low-dimensional materials. *Journal of the Chemical Society, Faraday Transactions 2: Molecular and Chemical Physics*, 80:291–319, 1984.

[181] D. Fragiadakis, P. Pissis, and L. Bokobza. Glass transition and molecular dynamics in poly(dimethylsiloxane)/silica nanocomposites. *Polymer*, 46:6001–6008, 2005.

[182] D. Fragiadakis and P. Pissis. Glass transition and segmental dynamics in poly(dimethylsiloxane)/silica nanocomposites studied by various techniques. *Journal of Non-Crystalline Solids*, 353:4344–4352, 2007.

[183] R. Schweitzer-Stenner. Structure and dynamics of biomolecules probed by raman spectroscopy. *Journal of Raman Spectroscopy*, 36:276–278, 2005.

[184] N. Everall. The influence of out-of-focus sample regions on the surface specificity of confocal Raman microscopy. *Applied Spectroscopy*, 62(6):591–598, 2008.

[185] S. Cînta Pînzaru, I. Pavel, N. Leopold, and W. Kiefer. Identification and characterization of pharmaceuticals using Raman and surface-enhanced Raman scattering. *Journal of Raman Spectroscopy*, 35:338–346, 2004.

[186] A. M. MacDonald, A. S. Vaughan, and P. Wyeth. Application of confocal Raman spectroscopy to thin polymer layers on highly scattering substrates: a case study of synthetic adhesives on historic textiles. *Journal of Raman Spectroscopy*, 36:185–191, 2004.

[187] R. Tabaksblat, R. J. Meier, and B. J. Kip. Confocal raman microspectroscopy: Theory and application to thin polymer samples. *Applied Spectroscopy*, 46(1):60–68, 1992.

[188] S. Michielsen. Abberations in confocal spectroscopy of polymeric materials: Erroneous thickensses and intensities, and loss of resolution. *Journal of Applied Polymer Science*, 81:1662–1669, 2001.

[189] K. J. Baldwin and D. N. Batchelder. Confocal Raman microspectroscopy through a planar interface. *Applied Spectroscopy*, 55(5):517–524, 2001.

[190] J. L. Bruneel, J. C. Lassgues, and C. Sourisseau. In-depth analyses by confocal raman microspectrometry: experimental features and modeling of the refraction effects. *Journal of Raman Spectroscopy*, 33:815–828, 2002.

[191] N. A. Freebody, A. S. Vaughan, and A. M. MacDonald. On optical depth profiling using confocal Raman spectroscopy. *Analytical and Bioanalytical Chemistry*, 396:2813–2823, 2010.

[192] N. J. Everall. Confocal raman microscopy: common errors and artefacts. *Analyst*, 135:2512–2522, 2010.

[193] N. Everall. Modeling and measuring the effect of refraction on the depth resolution of confocal Raman microscopy. *Applied Spectroscopy*, 54(6):773–782, 2000.

[194] J. Vyrykk, M. Halttunen, H. Iitti, J. Tenhunen, T. Vuorinen, and P. Stenius. Characterisation of immersion sampling technique in confocal Raman depth profiling. *Applied Spectroscopy*, 56(6):776–782, 2002.

[195] N. Everall. Depth profiling with confocal Raman microscopy, Part I. *Spectroscopy*, 19(10):22–33, 2004.

[196] N. Everall, J. Lapham, R. Adar, A. Whitley, and S. Mamedov E. Lee. Optimizing depth resolution in confocal Raman microscopy: A comparison of metallurgical, dry corrected, and oil immersion objectives. *Applied Spectroscopy*, 61(3):251–259, 2007.

[197] N. Everall. Confocal Raman Microscopy: Why the depth resolution and spatial accuracy can be much worse than you think. *Applied Spectroscopy*, 54(10):1515–1520, 2000.

[198] C. A. Froud, I. P. Hayward, and J. Laven. Advances in the Raman depth profiling of polymer laminates. *Applied Spectroscopy*, 57(12):1468–1474, 2003.

[199] A. M. MacDonald, A. S. Vaughan, and P. Wyeth. On confocal Raman spectroscopy of semicrystalline polymers: The effect of optical scattering. *Applied Spectroscopy*, 57(12):1475–1481, 2003.

[200] A. M. MacDonald and A. S. Vaughan. On confocal raman spetcroscopy of semicrystalline polymers: The effects of optical scattering. *Applied Spectroscopy*, 57(12):1475–1481, 2003.

[201] M. Van Den Brink, M. Pepers, and M. Van Herk. Raman spectroscopy of polymer latexes. *Journal of Raman Spectroscopy*, 33:264–272, 2002.

[202] A. M. MacDonald and A. S. Vaughan. Numerical simulations of confocal Raman spectroscopic depth profiles of materials: a photon scattering approach. *Journal of Raman Spectroscopy*, 38:584–592, 2007.

[203] G. Gherbaz. *Nanostructured Polymers: Morphology and Properties*. PhD thesis, School of Electronics and Computer Science, 2009.

[204] Jacqueline. I. Kroschwitz. *Concise Encyclopaedia of Polymer Science and Engineering*. WileyBlackwell, 1998.

[205] Dow Corning Corporation. *Silicone oil 200(R) fluid, 20cst material safety data sheet.*

[206] Renishaw, Wotton Ender Edge. *Renishaw Raman Imaging Microscope User Guide M/8012/1798/02*, section 4.4.4 edition.

[207] K. Chernyshov, Gen D, Y. Shemouratov, K. Prokhorov, G. Nikolacia, E. Sagitova, P. Pashinin, A. Kovalchuk, A. Klyamkina, B. Shklyaruk P. Nedorezova, and V. Optov. Raman structural study of copolymers of propylene with ethylene and high olefins. *Macromolecular Symposia*, 296:505–516, 2010.

[208] M. Veresa, M. Flea, S. Ttha, I. Pcsika, M. Kosa, A. Tthb, M. Mohaib, and I. Berttib. Raman scattering of ultra-high molecular weight polyethylene treated by plasma-based ion implantation. *Thin Solid Films*, 482:211–215, 2004.

[209] A. S. Nielsen, D. N. Batchelder, and R. Pyrz. Estimation of crystallinity of isotatic polypropylene using raman spectroscopy. *Polymer*, 43:2671–2676, 2002.

[210] Nicola Freebody. *The Use of Raman Microprobe Spectroscopy in the Analysis of Electrically Aged Polymeric Insulators.* PhD thesis, Electronics and Computer Science, 2012.

[211] F. Branda, F. Tescione, V. ambrogi, D. Sannino, B. Silvestri, G. Luciani, and A. Constantini. A new extra situ sol-gel route to silica/epoxy (dgeba) nanocomposite. a dta study of imidazole cure kinetic. *Polymer Bulletin (Heidelberg, Germany)*, 66:1289–1300, 2011.

[212] T. Nazir, A. Afzal, H. M. Siddiqi, S. Saeed, and M. Dumon. The influence of temperature and interface strength on the microstructure and performance of sol-gel silica-epoxy nanocomposites. *Polymer B*, 67:1593–1551, 2011.

[213] R. A. Pethricj, C. Miller, and I. Rhoney. Influence of nanosilica particles on the sure and physical properties of epoxy thermoset resin. *Polymer In*, 59:236–241, 2010.

[214] Princeton Instruments. Confocal raman microscopy general overview.

[215] M. Minsky. *Memoir on inventnig the confocal microscope.* Scanning, 1988.

[216] S. Hell, G. Reiner, C. Cremer, and E.H.K Stelzer. Abberations in confocal fluorescence microscopy induced by mismatches in refractive index. *The Royal Microscopy Society*, 169:391–405, 1993.

[217] L. Baia, K. Gigant, U. Posset, G. Schottner, and J. Popp W. Kiefer. Confocal micro-Raman spectroscopy: Theory and application to a hybrid polymer coating. *Applied Spectroscopy*, 56(4):536–540, 2002.

[218] J. P. Tomba, L. M. Arzondo, and J. M. Pastor. Depth profiling by confocal Raman microscopy: Semi-empirical modeling of the Raman response. *Applied Spectroscopy*, 61(2):177–185, 2007.

[219] J. P. Tomba and J. M. Pastor. Avoiding coupling fluid-sample interaction in confocal Raman depth profiling with immersion objectives. *Applied Spectroscopy*, 62(7):817–819, 2008.

[220] I. L. Hosier, A. S.Vaughan, and S. G. Swingler. Structure-property relationships in polyethylene blends: the effect of morphology on electrical breakdown strength. *Journal of Material Science*, 32(17):4523–4531, 1997.

[221] I. L. Hosier, A. S. Vaughan, and S. G. On the effects of morphology and molecular composition on the electrical strength of polyethylene blends. *Journal of Polymer Science. Part B: Polymer Physics*, 38(17):2309–2322, 2000.

[222] Y. Zhao, A. S. Vaughan, J. V. Champion, S. J. Dodd, and S. J Sutton. The structure of trees in semi-crystalline polymers. *International Conference of Dielectric Materials, Measurements and Applications*, pages 314–319, 2000.

[223] A. S. Vaughan and I. L. Hosier. The effect of dibenzylidene sorbitol on the crystallization behaviour of polyethylene. *Journal of Material Chemistry*, 48(8):2922–2928, 2008.

[224] S. Fairgrieve. *Nucleating Agents.* Smithers Rapra Press, 2007.

[225] V. M. Castano. *Performance of Plastics.* Hanser Gardner Publications, 2001.